

# Simulation of Fluid Dynamics and Particle Transport in a Realistic Human Nasal Cavity

A thesis submitted in fulfilment of the requirements for the degree of Doctor of  
Philosophy

---

Kiao Inthavong

*B. Mech. Eng. (H2A Hons.), B. Business*

School of Aerospace, Mechanical and Manufacturing Engineering  
Science, Engineering and Technology Portfolio  
RMIT University

October 2008

To my parents, who have sacrificed and given up so much to provide me with all my opportunities. Thanks to all their guidance, inspiration and encouragement.

## Author Declaration

I hereby declare that this submission is my own work and to the best of my knowledge it contains no materials previously published or written by another person, nor material which to a substantial extent has been accepted for the award of any other degree or diploma at RMIT or any other educational institution, except where due acknowledgement is made in the thesis. Any contribution made to the research by others, with whom I have worked at RMIT or elsewhere, is explicitly acknowledged in the thesis.

I also declare that the intellectual content of this thesis is the product of my own work, except to the extent that assistance from others in the project's design and conception or in style, presentation and linguistic expression is acknowledged. The content of this thesis is the result of work which has been carried out from March 2005 until October 2008. All ethics procedures and guidelines have been adhered to where appropriate. I give consent for this copy of my thesis to be made available for loan and photocopying when handed to the RMIT University Library for archiving.

.....

Kiao Inthavong

October 2008

# Acknowledgements

I would like to express my deepest gratitude to my supervisor Professor Jiyuan Tu for his encouragement, patient guidance in every aspect of my research and his support. The immense influence he presented in shaping my research attitude and approach can never be overestimated.

I would also like to express sincere gratitude to my co-supervisor, Dr William Yang of CSIRO, for his discussions and guidance into experimental research. His advice and support have helped my fine attention to details when designing and running experiments.

I would like to thank my family for all their support and love throughout my education. To the Portaro family, especially Jackie whom I would like to thank for their encouraging words and constant reviews of my work during this research. Special thanks to my wife Laura Portaro for her love, advice, patience, and support.

Finally, I would also like to thank my colleagues; Dr. Zhaofeng Tian, Dr. Krishna Mohanarangam, Akraphon Janon, Weng-Chew Chan, Lok-Tin Choi, Dr. Jian Wen, Simin Wang, Dr. Edsil Dilla, Huafeng Li, Dr. Sherman Chi-Pok Cheung, Thau Do and Gokul Rajamani for their invaluable technical guidance, lunch time soccer and basketball breaks and joyful memories throughout the research.

---

# Abstract

Traditional research methodologies into biological systems such as the human nasal cavity have always been challenging due to its invasive nature. Alternatives for human subjects have involved replicate casts to study the fluid dynamics as well as gas-particle flows for therapeutic and toxicology studies. Recent advances in the medical imaging field have allowed the reconstruction of a computational model for fluid dynamics analysis of the nasal cavity from computerized tomography (CT) scans. The locally constrained watershed approach was used for the image segmentation to acquire a cloud of data points from CT, which formed the basis for the surfaces. The final step involved creating the volumes and a computational mesh.

A range of Computation Fluid Dynamics (CFD) techniques and ideas were evaluated by applying them to solve gas-particle flows under the Lagrangian approach. The airflow was first simulated and detailed airflow structures such as local vortices, wall shear stresses, pressure drop and flow distribution were obtained. Airflow structures were found to be dependent on the nasal cavity geometry, although the pressure drop between the left and right cavity were similar. The nasal valve, which exhibits the smallest cross sectional area, was found to be a source of high resistance where the flow accelerated through. Vortices were found primarily in the upper olfactory region and just posterior to the nasal valve where the geometry begins to expand. The majority of the airflow was found close to the septum walls and only a small proportion reached the olfactory region and the outer meatus extensions that were created by the turbinate protrusions. Low flow in the olfactory region is a defence mechanism that prevents particles whose trajectories are heavily dependent on flow patterns from being deposited onto the sensitive olfactory nerve fibres, while vapours are allowed to diffuse for olfaction.

In terms of heat transfer the differences in the width of the airway especially in the frontal regions was found to be critical as the temperature difference was greatest and therefore heating of the air is expedited when the air is surrounded by the hotter walls. The air temperature in the left side was found to be hotter in the frontal regions where the airway was thinner and had a smaller cross-section compared with the right side. After the airway expansion the opposite trend occurred as the right side became warmer than the left side due to a smaller cross-sectional area.

Inhalation of foreign particles is filtered by the nasal cilia to some degree as a defence mechanism of the airway. Particles such as asbestos fibres, pollen and diesel fumes can be considered as toxic and lead to health problems. These particles were introduced and the effects of particle morphology were considered by customising the particle trajectory equation. This mainly included the effects of the drag correlation and its shape factor. Local particle deposition sites, detailed deposition efficiencies and particle trajectories were obtained. High inertial particles tended to be filtered within the anterior regions of the cavity due to a change in direction of the airway as the air flow changes from vertical at the inlet to horizontal within the main nasal passage.

It was found that major particle deposition sites include the nasal valve region and anterior section of middle turbinate. Wood dust depositing in these regions was removed slower and the layer of soft tissues in these regions may be damaged by the continuous exposure to wood particles. Pine dust had high deposition efficiency in the nasal cavity in comparison with heavy and light oak dusts, due to the fact that it comprised much larger particles. For pollen particles about 20% of 16 $\mu$ m pollen particles deposited in the main airway while for 30 $\mu$ m pollen particles, 66.2% were deposited. The rough surface characteristic of the pollen particle caused an increase in the drag coefficient when compared with spherical particles which lead to less deposition in comparison with spherical particles. For fibrous particles, it was found that asbestos had very low deposition,  $\approx 14\%$  and was independent of fibre length. In comparison, carbon fibre exhibited an increase in deposition as the fibre length increased. A parameter,  $\rho A_{cross}$  which represents the mass per unit length, was used to equate the  $d_{ae}$  for different fibre lengths.

Inhaled particles with pharmacological agents are often deliberately introduced into the nasal airway with a target delivery. The mucous lined airway that is highly vascular provides an avenue for drug delivery into the blood stream. An initial nasal spray experiment was performed to determine the parameters that were important for nasal spray drug delivery. The important parameters were determined to be the spray angle, initial particle velocity and particle swirl. It was found that particles were formed at a break-up length at a cone diameter greater than the spray nozzle diameter. The swirl fraction determined how much of the velocity magnitude went into a tangential component. By combining a swirling component along with a narrow spray into the main streamlines, greater penetration of larger particles into the nasal cavity may be possible.

These parameters were then used as the boundary conditions for a parametric study into sprayed particle drug delivery within the CFD domain. It was found that high swirl slows down the axial velocity which helps to reduce the inertia of the particle and can assist in penetrating the particles deeper past the nasal valve and into the nasal passage where the drug delivery is most effective. For a flow rate of 20 L/min 10-20 $\mu$ m particles were sensitive to initial injection velocity, insertion angle, and spray cone angle as its size increased. The deposition data from different spray parameters formulated ideas which can be used as a basis for improving the design of nasal spray devices to achieve better drug delivery such as (i) redirecting the release point of the spray (i.e. the insertion angle) to be align with the flow streamlines (ii) controlling the particle size distribution and (iii) controlling the particle's initial velocity.

---

# Work Published During Candidature

## Refereed Journal Articles

1. **K. Inthavong**, J. Wen, Z. F. Tian, J.Y. Tu, (2008) Numerical Study of Fibre Deposition in a Human Nasal Cavity, *Journal of Aerosol Science*. 39 pp.253-265  
IF: 2.952
2. J. Wen, **K. Inthavong**, J.Y. Tu, S. Wang, (2008) Numerical Simulations for Detailed Airflow Dynamics in a Human Nasal Cavity, *Respiratory Physiology & Neurobiology* 30;161(2):125-135  
IF: 2.049
3. **K. Inthavong**, J. Wen, et al. (2008). Inhalation of Toxic and Therapeutic Particles in a Human Nasal Cavity. The 2nd International Conference on Bioinformatics and Biomedical Engineering, 2008. ICBBE 2008., Shanghai, China, IEEE Transactions
4. **K. Inthavong**, Z.F.Tian, J.Y.Tu, W.Yang, (2008) Optimising Nasal Spray Parameters for Efficient Drug Delivery Using CFD, *Computers in Biology and Medicine* 38(6):713-726  
IF: 1.068
5. Z. F. Tian , **K Inthavong**, J. Y. Tu, (2007) Deposition of Inhaled Wood Dust in the Nasal Cavity, *Inhalation Toxicology* 19(14):1155-1165  
IF: 2.167
6. Z. F. Tian, **K. Inthavong**, J.Y. Tu, G.Yeoh, (2007) Numerical simulation of gas-particle flows over an in-line tube bank, *ANZIAM Journal* 48, C527-C544  
IF: 0.198
7. Z. F. Tian, **K. Inthavong**, J.Y. Tu, G.Yeoh, (2007) Numerical investigation into the effects of wall roughness on a gas-particle flow in a 90-degree bend. *International Journal of Heat and Mass Transfer* 51:1238–1250  
IF: 1.482
8. **K. Inthavong**, Z. F. Tian, H. F. Li, J.Y. Tu, W. Yang, C. L. Xue and C. G. Li, (2006) A numerical study of spray particle deposition in a human nasal cavity. *Aerosol Science and Technology*. Vol. 40, :1034-1045  
IF: 2.905
9. **K. Inthavong**, J.Y.Tu, Computational modelling of air-particle flow in the human airways. Accepted in *Journal of Computational Multiphase Flows*.



## Refereed Conference Papers

1. **K. Inthavong**, Z.F. Tian, J.Y. Tu, CFD Simulations on the Heating Capability in a Human Nasal Cavity. in the *Proceedings of 16<sup>th</sup> Australasian Fluid Mechanics Conference*, pp.842-847 (2007).
2. J.Wen, **K.Inthavong**, Z.F.Tian, J.Y.Tu, C.L.Xue and C.G.Li, Airflow Patterns in Both Sides of a Realistic Human Nasal Cavity for Laminar and Turbulent Conditions, in the *Proceedings of 16<sup>th</sup> Australasian Fluid Mechanics Conference*, pp.831-837 ( 2007).
3. **K. Inthavong**, Z. F. Tian, H. F. Li, J.Y. Tu, W. Yang, C. L. Xue and **C. G. Li**, Local deposition sites of drug particles in a human nasal cavity, Paper No. 154, in the *Proceedings of the Fifth International Conference on CFD in the Process Industries*, CSIRO, Melbourne, Australia, 13-15 December (2006).
4. **Inthavong, K.**, A Numerical Study into Local Deposition Sites in the Nasal Cavity for Therapeutic and Pollutant Inhalation, *Australasian Users Conference Proceedings 2006*, Melbourne, Australia 22-23 November (2006)
5. **K. Inthavong**, Y. Yong, S. Ding, J.Y. Tu, A. Subic, F. Thien, Airway Geometry and Inhalation Effort Comparisons in a Narrowed and Recovered Airway Caused by Acute Asthma. Paper 581 *International Conference on Audio, Language and Image Processing 2008 (ICALIP2008)* Shanghai, China 7-9 July 2008.
6. **K. Inthavong**, Y. Yong, S. Ding, J.Y. Tu, A. Subic, F. Thien, Comparison of Airway Geometries – Effect on Airflow and Particle Deposition. Submitted to *13th International Conference on Biomedical Engineering (ICBME2008)*, 3-6 December 2008.

---

# Table of Contents

<b>Acknowledgements</b>	<b>iii</b>
<b>Abstract</b>	<b>iv</b>
<b>Work Published During Candidature</b>	<b>vii</b>
<b>Table of Contents</b>	<b>ix</b>
<b>List of Figures</b>	<b>xii</b>
<b>List of Tables</b>	<b>xvii</b>
<b>Nomenclature</b>	<b>xviii</b>
<b>CHAPTER 1 Introduction</b>	<b>1</b>
1.1. Motivation	1
1.2. Objectives	3
1.3. Thesis Structure	5
<b>CHAPTER 2 Literature Review</b>	<b>7</b>
2.1. Anatomy and Physiology of the Human Nasal Cavity	7
2.2. Fluid Flow Studies in the Human Nasal Cavity	12
2.3. Particle Deposition Studies in the Human Nasal Cavity	16
<b>CHAPTER 3 Modelling the Human Nasal Cavity</b>	<b>22</b>
3.1 Nasal Replicate Reconstruction Methods	22
3.2. Developing a Computational Model of the Nasal Cavity	26
3.2.1. Medical Image Processes	26
3.2.2 MRI vs CT Scans	28
3.2.3. Image Acquisition from CT Scan	28
3.2.4. Image Processing	29
3.2.5. Segmentation	30
3.2.6. Surface Generation	31
3.3. Developing the CFD Model	32
3.3.1 Computational Mesh and Boundary Conditions	32
3.3.2 Boundary Layer Definition	35
3.3.3 Grid Independence	36

<b>CHAPTER 4 Numerical Simulation Methodology</b>	<b>38</b>
4.1. Gas Phase Modelling	38
4.1.1. General Governing Equations for Fluid Flow	38
4.1.2. Reynolds Averaged Navier-Stokes Equations	39
4.2. Gas-Particle Phase Modelling	42
4.2.1. Lagrangian Discrete Particle Tracking	43
4.2.2. Turbulent Particle Dispersion	43
4.3 Numerical Solver Procedure	45
<b>CHAPTER 5 Modelling Inhalation and Heat Transfer in the Nasal Cavity</b>	<b>47</b>
5.1. Introduction	47
5.2. Physiology of Airflow Rates in the Nasal Cavity	49
5.3. Numerical Procedure	50
5.4 Boundary Conditions	52
5.5. Results	53
5.5.1 Geometry Comparisons	53
5.5.2 Resistance and Wall Shear Stress	55
5.5.3 Path Streamlines	57
5.5.4 Airflow Analysis	59
5.5.5 Nasal Valve Flow	62
5.5.6. Middle Turbinates	65
5.5.7 Temperature Profiles	69
5.5.8 Temperatures in the Left and Right Cavities	71
5.5.9 Wall Heat Flux	73
5.6 Discussion	74
<b>CHAPTER 6 Inhalation of Toxic Particles and the Effects of Particle Morphology</b>	<b>78</b>
6.1. Introduction	78
6.1.1. Wood Dust Particles	78
6.1.2. Pollen and Rough Surfaces Modelling	79
6.1.3. Fibrous Particles	80
6.2. Numerical Considerations for Particle Morphology Differences	81
6.2.1. Spherical (Wood Dust) Particles	81
6.2.2. Pollen and Rough Surfaces Modelling	84
6.2.3. Fibre Modelling	85
6.3. Results and Discussion	87
6.3.1. Deposition Patterns of Wood Dust Particles	87
6.3.2. Deposition Patterns of Pollen and Rough Surfaces	94
6.3.3. Deposition Fibres	98
6.4. Conclusions	107
<b>CHAPTER 7 Determining Significant Nasal Spray Parameters for CFD</b>	<b>109</b>
7.1. Introduction	109
7.2. Experimental Setup	111
7.2.1 Particle Image Velocimetry (PIV)	111
7.2.2. Phase Doppler Particle Analyser (PDPA)	112
7.2.3. Experimental Test Station	114
7.3. Results and Discussion	116
7.3.1. Spray Characterisation	116

---

7.4. Conclusions	122
<b>CHAPTER 8 Inhalation of Sprayed Drug Particles</b>	<b>123</b>
8.1. Introduction	123
8.2. Numerical Procedure	124
8.2.1. Turbulent Airflow	124
8.2.2. Boundary Conditions	126
8.3. Results and Discussion	126
8.3.1. Validation using a Hybrid Method	126
8.3.2. Swirl Fraction ( $\lambda$ )	128
8.3.3. Spray Diameter at Break-up Length	131
8.3.4. Initial Particle Velocity	132
8.3.5. Insertion Angle, $\alpha$	138
8.3.6. Full Spray Cone Angle, $\beta$	143
8.3.7. Implications for Nasal Drug Delivery	147
<b>CHAPTER 9 Conclusion and Recommendations</b>	<b>148</b>
9.1. Airflow and Heat Transfer Analysis	148
9.2. Inhalation of Toxic Particles	149
9.3. Inhalation of Sprayed Particles	151
9.4. Recommendations for Further Study	153
<b>Appendix – User Defined Functions</b>	<b>155</b>
<b>References</b>	<b>158</b>

# List of Figures

Figure 2.1 Nasal cavity anatomy – adapted from the Gray's anatomy of the human body, originally published in 1918 .....	8
Figure 2.2 Nasal Cavity Geometry .....	10
Figure 2.3 Particle deposition mechanisms .....	19
Figure 2.4 Typical particle deposition curve for submicron and micron particles .....	20
Figure 3.1 Stereolithography process .....	24
Figure 3.2 Computational reconstruction methodology .....	26
Figure 3.3 (a) Computed tomography (CT) scanner and (b) CT slice concepts.....	28
Figure 3.4 CT scan of the middle turbinate region .....	29
Figure 3.5 Segmented CT slices developed from the Mumford-Shah algorithm in preparation for surface creation. ....	30
Figure 3.6 Computational model complete with surface ready for volume and mesh creation.....	32
Figure 3.7 Mesh topology used in GAMBIT.....	32
Figure 3.8 3D cell types.....	33
Figure 3.9 Nasal cavity geometry showing the computational mesh of the cross-sectional areas taken at the nasal valve, middle turbinate and nasopharynx regions.....	34
Figure 3.10 (a) Computational mesh of the anterior region (Region 1-2 – see Figure 3.9). (b) Coronal cross section of A-A showing the higher resolution at the wall surface.	36
Figure 3.11 Shear stress and velocity profiles of a coronal section near the nasal valve region for the four different cavity models.....	37

Figure 3.12 Grid independence test based on a velocity profile line taken at the posterior end of the nasal cavity. The distance and velocities are normalised by their respective maximum values of $x_{max}=96.5\text{cm}$ and $U_{max} = 1.36\text{m/s}$ .....	37
Figure 4.1 Velocity fluctuating with time at some point in a turbulent flow. ....	40
Figure 4.2 Distribution of $u',v',w'$ normalised with the friction velocity, $u_\tau$ in the vicinity of the wall (figure taken from Kreplin and Eckelmann (1978)). ....	42
Figure 4.3 Discrete Random Walk Model.....	44
Figure 4.4 Overview of the segregated solver solution steps .....	46
Figure 5.1 Airflow field through the nasal cavity.....	50
Figure 5.2 2D cross-sections of a nasal cavity of an adult male subject .....	54
Figure 5.3 The comparison of cross-sectional areas versus distance from anterior tip of nose for different geometries: (a) the cross-sectional area of the left and right side of the nose used in this paper, (b) the total cross-sectional area of both sides for different geometries.....	55
Figure 5.4 Area averaged static pressure on different coronal cross-sections versus distance from anterior tip of nose, (a) at a flow rate of 7.5 L/min (b) at a flow rate of 15 L/min.....	56
Figure 5.5 Area averaged wall shear stress on different zones surface, at flow rates of 7.5L/min and 15L/min. ....	57
Figure 5.6 Representation of flow streamlines in current nasal cavity. A comparison of streamlines produced in the literature shows similar trends Figure 5.7.....	58
Figure 5.7 Representation of flow streamlines in other nasal cavities. ....	59
Figure 5.8 Contours of axial velocity ( $x$ -direction) and streamlines of cross-flow ( $y$ - $z$ direction). Red contours represent maximum values while blue represent minimums. ....	61
Figure 5.9 Reynolds number recorded at the cross-sections depicted in figure 2. The cross-sections have been scaled to reflect their relative distances from each other across the nasal cavity. The axial distance is 0-90mm. ....	61
Figure 5.10 Velocity field in the coronal cross-section located at 2.60 cm from the anterior tip of the nose, (a), at flow rate of 7.5L/min, (b) at flow rate of 15L/min. ...	63

Figure 5.11 Velocity field in the coronal cross-section located at 3.20 cm from the anterior tip of the nose, (a), at flow rate of 7.5L/min, (b) at flow rate of 15L/min. ...	64
Figure 5.12 Velocity field in the cross-section located at 6.10 cm from the anterior tip of the nose, (a), flow rate of 7.5L/min, (b) at flow rate of 15L/min. ....	66
Figure 5.13 The coronal sections are divided into sub-sections which are indicated by letters, (a),the section is located at 6.1 cm from the anterior tip of the nose used in this paper, (b), the section is located at 6.2 cm from the anterior tip of the nose used by Keyhani et al.(1995), (C), the section is located at 6.0 cm from the anterior end of the nose used by Subramaniam et al.(1998). ....	67
Figure 5.14 Temperature profiles across the nasal cavity from the inlet. The solid black line represents a normal inhalation condition compared with experimental work. The un-coloured symbols represent the simulated results for cold dry air. ....	70
Figure 5.15 Ratio of the average temperature across the cross-sections of the left cavity with the average temperature across the cross-section of the right cavity.....	71
Figure 5.16 Contours of total temperature at cross-sections throughout the nasal cavity.	72
Figure 5.17 Wall heat flux for a cold dry air inhalation condition .....	73
Figure 6.1 Scan electron microscope image of pollen grains from a variety of common plants. Zeiss DSM 962 SEM. (Photo Courtesy of Louisa Howard and Charles Daghljan of Dartmouth College – <i>Rippel Electron Microscope Facility</i> ).....	80
Figure 6.2 Electron microscope image Amosite asbestos. (Photograph Courtesy of the U.S. Geological Survey – <a href="http://www.usgs.gov">www.usgs.gov</a> ) .....	81
Figure 6.3 Simulated particle size distribution and measured particle size distribution of dusts generated by sawing (from Chung et al. 2000). ....	83
Figure 6.4 Total deposition efficiency (DE) of monodisperse pine particles compared with other experimental investigations (Kelly et al. 2004; Pattle 1961) and numerical results (Shi et al. 2007). ....	88
Figure 6.5 (a) Local DE of all dusts; (b) Cumulative local DE of all dusts. ....	89
Figure 6.6 Local deposition patterns of wood dusts with different particle size distributions. ....	91
Figure 6.7 Particle size distribution (PSD) of deposited particles: (a) Pine dust, (b) Light oak dust. ....	93
Figure 6.8 Cumulative DE of pine and heavy oak dusts and monodisperse mean particles. ....	94

---

Figure 6.9 Cumulative deposition efficiency and regional deposition for 16 $\mu$ m and 30 $\mu$ m pollen particles. ....	95
Figure 6.10 Deposition patterns for 16 $\mu$ m and 30 $\mu$ m pollen particles. ....	96
Figure 6.11 A comparison of the variation of the local average drag coefficient variation along the horizontal axial distance for a 30 $\mu$ m pollen particle and an aerodynamic equivalent sphere. (Compare with Figure 6.12) .....	97
Figure 6.12 Fluid and particle velocity profile variation along the horizontal axial distance for a 30 $\mu$ m pollen particle. The particle Re number variation is also plotted which is a function of the velocity difference between the fluid and particle. ....	98
Figure 6.13 Fibre deposition comparison in the cavity using the two different drag correlations, HL-model and the TC-model against the experimental data. ....	99
Figure 6.14 Fibre deposition patterns for an inspiratory flow rate of 7.5L/min. Deposition fractions for each region are shown as percentages. ....	101
Figure 6.15 Total deposition efficiency for asbestos and carbon fibres at different fibre lengths. ....	102
Figure 6.16 Deposition patterns for asbestos fibres and carbon fibres at a fibre length of 100 $\mu$ m at a flow rate of 7.5L/min. ....	103
Figure 6.17 Comparison of deposition efficiencies between fibres and spherical particles using the Inertial Parameter. ....	105
Figure 7.1 Experimental PIV setup. ....	112
Figure 7.2 (a) PDPA system used at the CSIRO laser diagnostics laboratory (b) PDPA system in use. ....	114
Figure 7.3 Schematic of the experimental setup for spray visualization. ....	115
Figure 7.4 a.) Single image at the near-nozzle region showing a swirling hollow sheet of liquid. b.) Collated image from the individual single images to create the entire spray field. ....	117
Figure 7.5 Pressure Swirl Atomiser characteristics: (a) internal swirl chamber showing the tangential ports within the atomiser (b) atomisation process .....	118
Figure 7.6 Image snapshot of the spray, and the resulting PIV 2D vector plot which shows the averaged mean droplet velocity field of the spray nozzle. ....	120



Figure 8.1 Deposition efficiency for monodisperse particles released into 20L/min, 30L/min and 40L/min airflow using a hybrid tracking technique .....	127
Figure 8.2 Particle deposition within different sections of the nasal cavity. Section 1-3 is the frontal region, Section 4-7 is the middle region and Section 8-10 is the posterior region. ....	128
Figure 8.3 Particle trajectories for 10 and 20 $\mu$ m particles at different swirl fractions... 130	
Figure 8.4 Regional deposition of (a) 10 $\mu$ m particles and (b) 20 $\mu$ m released at different spray cone diameters.....	132
Figure 8.5 Total deposition in the first two zones of the nasal cavity at different particle injection velocity.....	133
Figure 8.6 Deposition patterns for (a) 10 $\mu$ m (b) 15 $\mu$ m and (c) 50 $\mu$ m particles released uniformly from the inlet surface normal to the nostril openings at $u^*=1$ and $u^*=10$ . ....	137
Figure 8.7 Side view of the nasal vestibule showing the insertion angle.....	139
Figure 8.8 Deposition in zone1 and zone2 for monodispersed particles released uniformly from the inlet surface at different insertion angles. ....	139
Figure 8.9 (a) Deposition patterns for 15 $\mu$ m particles released uniformly from the inlet surface uniformly from the inlet surface at insertion angles 100° and 90°. (b) Deposition patterns for 15 $\mu$ m particles released uniformly from the inlet surface uniformly from the inlet surface at insertion angles 70° and 30°. ....	142
Figure 8.10 $\beta$ – full spray cone angle in comparison with $\theta$ – half cone spray angle.....	143
Figure 8.11 Deposition in zone1 and zone2 for monodispersed particles released at 10m/s from a small internal diameter at different spray cone angles.....	144
Figure 8.12 (a) Deposition patterns for 15 $\mu$ m particles released at 10 m/s from a small internal diameter at the centre of the nostril inlet surface. The spray cone angles ranged from 20° and 80°. (b) Deposition patterns for 20 $\mu$ m particles released at 10 m/s from a small internal diameter at the centre of the nostril inlet surface. The spray cone angles ranged from 20° and 80°. ....	146

## List of Tables

Table 4.1	The Incompressible Full Navier-Stokes Equations in Cartesian Coordinates
Table 5.1	Velocity magnitude and geometrical details of the cross-sections depicted in Figure 5.8.
Table 5.2	Flow distribution on the plane in the middle of turbinate for flow rate of 15L/min
Table 5.3	Flow distribution on the right plane in the middle of turbinate for flow rate of 15L/min
Table 6.1	Summary of fibre their morphological characteristics, typical mean values and numerical models.
Table 6.2.	A comparison of particle deposition efficiency for 16 $\mu$ m and 30 $\mu$ m pollen particles against an aerodynamic equivalent sphere
Table 6.3	A comparison of particle deposition efficiency for Asbestos, Carbon fibre and other arbitrary fibres with varying $\lambda$ values
Table 7.1	Variables related to the actuation of a nasal spray
Table 7.2	Spray device parameters for investigation
Table 7.3	Spray device parameters for the boundary conditions in CFD analysis

# Nomenclature

$C_p$	specific heat capacity
$C_D$	drag coefficient
$C_\mu$	turbulent viscosity relationship
$d_a$	surface equivalent sphere diameter
$d_{ae}$	aerodynamic equivalent diameter
$d_{bul}$	diameter of spray at the break-up length
$d_p$	particle geometric diameter
$D$	diffusivity
$E$	energy term
$F_D$	drag force term
$F_g$	gravity force term
$h$	sensible enthalpy
$I$	inertial parameter
$J$	vapor diffusion
$k$	Turbulent kinetic energy
$\dot{m}$	mass flow rate
$P$	pressure
$P_p$	projected perimeter of the particle
Pr	Prandtl number
$Q$	air flow rate
$\dot{Q}$	heat energy transfer rate
$Re_p$	particle Reynolds number
$r$	a uniform random number between 0 and 1
$S$	source term, Strouhal number
St	Stokes number
$T$	temperature
$T_L$	fluid Lagrangian integral time
$u_\infty$	free-stream velocity
$u, u_i, u_j$	velocity, x-component velocity
$\bar{u}_i$	mean velocity
$u'_i$	fluctuating velocity
$\overline{u'_i u'_j}$	Reynolds stresses
$u^*$	ratio particle velocity to air velocity
$v$	y-component velocity
$w$	z-component velocity
$x$	distance along wall

$Y$	vapor mass fraction
$y_p$	distance to the wall from adjacent cell centroid

## Greek Letters

$\alpha$	Womersley number, or insertion angle
$\beta$	spray angle
$\Gamma$	diffusion coefficient of the scalar
$\delta_{ij}$	Kronecker's delta function
$\varepsilon$	dissipation rate of turbulent kinetic energy
$\phi$	governing scalar variable, or shape factor
$\bar{\phi}$	steady mean component of the variable
$\phi'(t)$	time varying fluctuating component of the variable
$\eta_{n,regional}$	regional deposition efficiency for the $n^{\text{th}}$ region
$\kappa$	turbulent kinetic energy
$\mu$	dynamic viscosity
$\mu_T, \mu_{eff}$	turbulent viscosity, effective turbulent viscosity
$\nu$	is the kinematic viscosity of the fluid
$\rho$	density
$\sigma$	turbulence Prandtl number
$\bar{\tau}_{ij}$	mean viscous stress tensor components
$\tau_e$	eddy life time
$\tau_{cross}$	particle eddy crossing time
$\tau_\omega$	wall shear stress
$\tau_p$	particle relaxation time
$\lambda$	swirl fraction
$\omega$	breathing frequency
$\zeta$	normally distributed random number

# CHAPTER 1

## Introduction

### 1.1. Motivation

This thesis reports the investigation of airflow and inhalation of particles in a human nasal cavity using computational fluid dynamics with additional supporting experimental work. An opportunity in computational simulations has arisen due to the increase use of such technology. Biomedical imaging techniques such as computed tomography (CT) and magnetic resonance imaging (MRI) scans coupled with 3D modelling software have allowed computational modelling of human body parts, such as the nasal cavity and upper airways for reconstruction and analysis. Detailed accurate representation of the airway geometry can be determined in greater fidelity in comparison to cast models or the examination of cadavers. Numerical simulations also allow a wider range of studies (e.g., repeatability and accuracy) based on advancements in computational models employing Computational Fluid Dynamics (CFD) techniques. include the graphical representation of results such as local particle deposition sites, particle and air flow path, velocity contours and vectors at any location. One disadvantage of CFD however, is the reliability of results, which is dependent on the correct mathematical formulation for the process under simulation, i.e., the more realistic boundary conditions imposed along with greater degree of accuracy in the numerical algorithms of the system of equations, the more precise the solution will be.

In addition, air flow studies of the nasal cavity are important in establishing the effects of airway geometry on the airflow, particularly in abnormal nasal cavity anatomies. These anomalies may impair airflow by producing narrowed or obstructed areas leading to adverse health effects. For example, spurs and deviation of the nasal septum (nasal wall that separates the left and right cavity) may impair airflow, especially if the spur or deviated septum compresses the middle airway walls (turbinates) or lateral wall of the nasal cavity, leading to obstruction of the airway and compression of the turbinates. By understanding the air flow dynamics caused by geometrical differences especially anomalies; better clinical appraisals can be delivered, leading to better informed decision-making on surgical procedures. This is critical, as it has been identified that as many as 10% of patients experience nasal obstruction following rhinoplasty (Beekhuis 1976). The computational simulation can act as a predictive or ‘virtual surgery’ tool, which will improve medical planning, patient recovery, and reduce the overall risks of surgery.

Airflow studies also further enhance understanding of the physiology of respiration. The geometric characteristics of the human nose have important features that aid in the physiological function of respiration. For example, morphological variation of the human nose has been attributed to the eco-geographic adaptation to climate (Franciscus and Long 1991; Wolpoff 1968) where nasal cavities can be broadly categorised as leptorrhines (tall and narrow) or platyrrhines (short and broad) according to their morphology. It is thought that people exposed to cold, dry environments exhibit leptorrhine features that induce turbulent flow features (Weiner 1954; Wolpoff 1968). The random and rapid fluctuation of swirling fluid from turbulent flows is beneficial for conditioning the inspired air. Those exposed to hot, humid environments however, exhibit platyrrhine features that produce more laminar flow where the conditioning of the air is less critical (Carey and Steegmann 1981; Cottle 1955; Courtiss and Goldwyn 1983). By studying the effects of the airway geometry on the airflow in detail, further physiological functions of the nasal cavity may be discovered.

During respiration, inhaled air often contains foreign particles that may be toxic to the body. The inhalation of particulate matter (PM) is a major health and safety concern. In the workplace, further exploration is relevant, particularly in industries that involve high-powered tools designed to process materials, (e.g. sanding, wood processing, concrete cutting). Everyday exposure to foreign particles however is quite common in urban

societies where air pollution is widespread especially due to vehicle exhaust and industrial release of by-products. The natural physiological function of the nose is to filter the air by trapping the particulate matter in the nasal hairs within the front nostrils (vestibule). This function is not foolproof, as some particles will pass through this region and deposit within the nasal airway, and can potentially travel through the airway to the lungs and cause severe damage. Further studies into gas-particle flows in the nasal cavity will increase understanding of what causes particles to either deposit in the vestibule or bypass the airway geometry altogether. Greater knowledge of particle dynamics may lead to safer guidelines in the context of exposure limits to polluted air.

Alternatively, inhalation of drug particles is deliberate during nasal drug delivery of which aims to deposit and prolong the residence time of the particles which is impeded by mucociliary clearance. It is a popular way to treat respiratory ailments such as congestion and allergies and has become an alternative to oral and injection routes of delivering systemic drugs for a variety of diseases. The advantages of using the nasal cavity lies in its faster onset of action, improved patient compliance and the avoidance of metabolism breakdown of the drug in the digestive system. This has driven the pharmaceutical industry into researching and developing new drugs. In fact, according to a recent report from Business Communications Company Inc., the US market alone for drug delivery systems is estimated at \$43.7 billion in 2003 and is expected to rise at an average annual growth rate of 11.3% to reach \$74.5 billion by 2008 (Orive et al. 2003). Despite this, nasal drug delivery provides only 10-20% efficiencies (Cheng et al. 2001; Suman et al. 2002) and a review by Roland et al. (2004) it was found that the extra drug load (80-90%) for certain drug types can actually cause serious side effects to patient. The efficiency of such products is measured by the amount of particles that deposit on the highly vascular mucous walls. More intimate knowledge of particle flow dynamics can help assess the likelihood of the health effects caused by the inhalation of the particle type and its deposition location.

## **1.2. Objectives**

This research focused primarily on developing useful and economically viable CFD approaches, aimed at assisting practical clinical studies where information regarding airflow structures, deposition efficiencies and deposition patterns in a nasal cavity were

presented. The objectives can be categorised into three areas: (i) airflow analysis (ii) inhalation of toxic particles – passively introduced into the airways and (iii) inhalation of drug particles from a nasal spray application – introduced deliberately into the airway. The nasal anatomy, characterised by thin airway channels does not allow direct measurements of flow patterns inside the human nose. CFD methods are advantageous in their capacity to provide detailed data that are normally difficult to produce through experiments, due to intervention and clinical risks for the volunteer. The numerical data can produce highly quantitative results, ideally complementing existing experimental data that often lack fine detail. Inter-subject variations in nasal anatomy will cause variations in nasal flow patterns, which is a concern when trying to use the results of a single model. The CFD approach therefore aimed to:

- ◆ present flow patterns between the left and right nasal cavities ;
- ◆ compare the results with experimental and numerical data that are available in literature;
- ◆ study the flow in the nasal valve and turbinate region in detail, since the airflow profiles in these regions have not been well investigated;
- ◆ provide detailed data on air flow patterns that is pertinent to the prediction of gas-particle flows and regional tissue exposure to inhaled air.

After establishing the details of the airflow, gas-particle flows were studied as inhaled air is often tainted by foreign particles such as dust, fumes and general pollutants. These studies aimed to:

- ◆ identify major deposition regions;
- ◆ compare the deposition patterns caused by different particle morphologies;
- ◆ discuss current methods in modelling non-spherical particles.

The simulated results aimed to contribute to knowledge of particle deposition patterns and to assist in risk analysis of exposure to harmful particles in industry.

Finally, particle deposition from a nasal spray was investigated. An important step in CFD is to apply correct boundary conditions. This is vital in nasal spray applications where the introduction of the sprayed particles into the nasal cavity is not straight-forward. An



experimental test station was used to identify key parameters associated with the atomisation of the drug formulation in the nasal spray. The parameters were then used as a basis for a parametric study to understand the effects. The resultant data can then be used to guide more efficient designs of nasal drug delivery systems.

### **1.3. Thesis Structure**

The rationale for conducting this research, the scope and outlines of this thesis are explained in Chapter 1.

Chapter two provides an in-depth review of the background for this research. The chapter begins with an introduction to the anatomy and physiology of the nasal cavity and is followed by a review of previous studies related to the research. This includes fluid flow studies in addition to particle deposition studies. Different methods involving experimental processes using human volunteers, replicates cast models, and numerical approaches are discussed. This literature review provides the framework and context of where the current research has developed from.

Chapter three addresses the method in which the nasal cavity is reconstructed from CT scans, producing replicate casts or computational models. The computational model includes the development of stages of extracting CT data, image processing, the geometry and mesh generation, and boundary conditions setup.

Fundamental concepts within the mathematical and numerical methodology for gas and gas-particle flows are discussed in Chapter four. The rationale for the chosen turbulence model and the related equations that are solved is discussed. This is followed by the description of the Lagrangian particle tracking model used.

The main body of this research begins in Chapter five with an analysis of airflow structures and the heat transfer capability of the nasal cavity. A discussion of the physiology of breathing is also provided. The CFD setup is described along with the resultant data, depicting the causes of airway resistance, wall shear stresses and path streamlines. These results were compared with existing experimental results. Detailed exploration into the complex flow region within the nasal valve and turbinates is also

described. The wall heat flux and the temperature contours also raised questions about the role of the turbinates and its function in heating the airflow.

Chapter six extends the analysis from the airflow to the inhalation of toxic particles and the effects of particle morphology. Specifically, particles of wood-dust, pollen with rough surfaces and fibres were modelled. The numerical treatment of each particle in of the context of its drag coefficient was modified into the commercial CFD code in Fluent.

Chapter seven moves into the development of an experimental test station to determine which nasal spray parameters are significant for the boundary conditions of CFD and discussion of measurement techniques in particle image velocimetry and phase Doppler image interferometry is undertaken. The results form the basis of boundary conditions for CFD simulations of nasal drug delivery in the following chapter.

Chapter eight applies knowledge and outcomes ascertained from the experimental work. The boundary conditions obtained (initial particle velocity, insertion angle, spray cone angle, and swirling affects) are used to study the effects of different parameters on particle flow dynamics and deposition. A turbulent model is introduced into the simulation and methodologies aimed to rectify the faults of turbulent particle dispersion are applied.

The thesis concludes within Chapter nine by summarising significant outcomes from each research section between Chapters five to eight. The deposition efficiency and deposition patterns of different particle types and their interaction with airflow structures are discussed in detail. The final sections of this chapter highlight the potential clinical significance of this study and provide recommendations for further study.

# CHAPTER 2

## Literature Review

### 2.1. Anatomy and Physiology of the Human Nasal Cavity

The human nasal cavity is an important component to the respiratory system, which performs a variety of physiological functions. It is responsible for heating and humidifying inspired air to near body core temperature with full saturation, filters the air from pollutants and toxic particles, and provides the sense of smell through olfactory recesses. Externally the nose consists of the triangular-shaped projection in the centre of the face divided into two cavities (fossae) by cartilage called the septum. This forms a curved wall internally on the medial sides of each cavity. The axial length of the nasal passage between the external and internal openings is about 10 cm in adults (Proctor 1982). The framework of the nostrils is made of cartilage, while the nasal septum, which separates the nostrils in the midline, is part bone closer to the skull and part cartilage at the outer tip (Figure 2.1).

Air enters the nose through external openings in the vestibule. The openings are called the nares or nostrils, and measure about 1.5 cm anteroposteriorly while at the back of the nose is the choanae (internal nares) measuring 2.5 cm vertically and 1.5 cm transversely which are the openings into the nasopharynx (Proctor 1982). The vestibule of the nose is the visible rounded part that contains the external nares. It is lined with a stratified squamous epithelium that is moderately keratinized, and contains a highly variable mesh of hair projecting into the air-stream (Cauna 1982; Mygind et al. 1982). The airway is largest at the nares and narrows inwards in a funnel like shape as it approaches the main entrance to the nasal passage. This entrance region is known as the nasal valve.

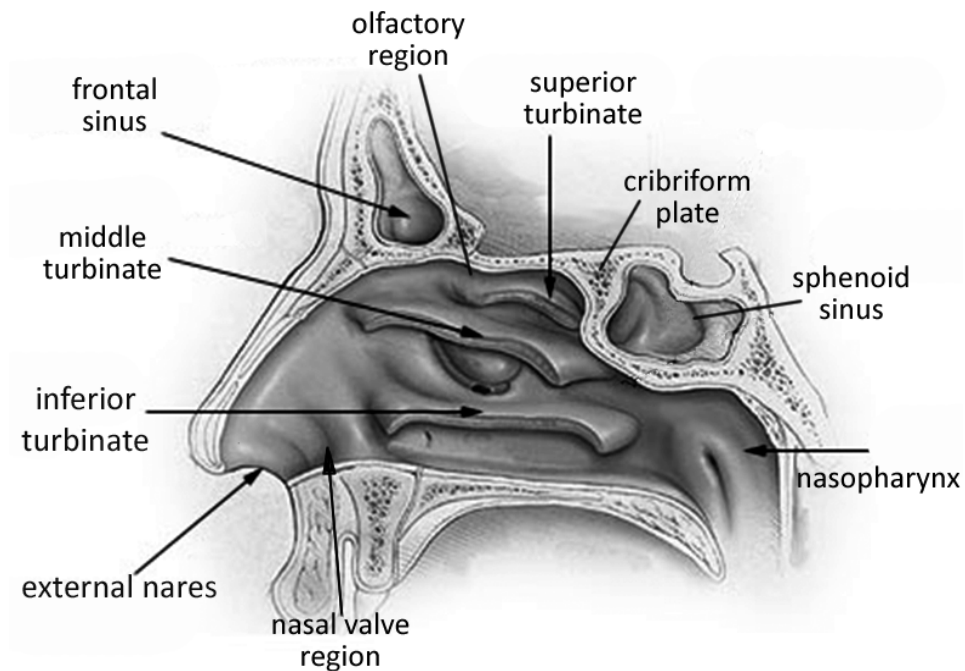


Figure 2.1 Nasal cavity anatomy – adapted from the Gray's anatomy of the human body, originally published in 1918

The nasal valve region is also referred to as the internal valve and is the region where the lower edge of the upper lateral cartilage is attached to the septum, forming an angle of approximately  $10\text{-}15^\circ$  (Bailey 1998; Kerr 1997; Myers 1993). It is shaped like a narrow slit and is prone to narrow even further at high flow rates. It is usually located less than 2 cm distal in the nasal passageway, approximately 1.3 cm from the naris. It exhibits the smallest cross-sectional area, approximately  $30\text{-}40\text{ mm}^2$  which is smaller than the total area of any other part of the respiratory tract and is the cause of the highest region of resistance (Proctor 1982). The nasal valve and the vestibule collapse at high flow rates caused by the increased pressure gradient between ambient and inhaled air. During quiet breathing, however, the dimensions of the nasal cavity are constant.

At the end of the nasal valve region the airway bends about  $90^\circ$  and expands where the cross-sectional area increases to about  $130\text{ mm}^2$  per side (Proctor 1982). This expansion is the beginning of the main nasal passage which extends 5-8cm to the choanae, is approximately 1-3mm wide (from lateral to medial sides) and 4cm high from the top to the floor of the airway. The main nasal passage is characterised by the indentations of the turbinate bones that exist on the lateral walls. The turbinates are also referred to as conchae (from the Greek word meaning shellfish) due to their small thin shell-like shapes.

Interestingly, the name turbinates is not derived from the inference that its role is to induce turbulence in the airway as suggested by Courtiss and Goldwyn (1983). In fact this phenomenon is still controversial and larger sample studies are needed (Churchill et al. 2004). Usually, individuals have 3 paired turbinates: superior, middle, and inferior. Occasionally, a fourth turbinate, the supreme turbinate, exists. The inferior turbinate is the largest, spanning nearly the entire length of the main nasal passage. The middle turbinate is almost as large while the superior turbinate is much smaller, only about half the length of the middle turbinate, and is in the posterior part of the main nasal passages. In Figure 2.2 only the middle and inferior turbinates are found at the coronal cross-section midway along the main nasal passage while the superior turbinate is located posterior to the cross-section. The large surface area of the turbinates is exposed to the passing air allowing sufficient heat and mass transfer to warm or cool the air to within 1 degree of body temperature.

The airways inferior and lateral to the turbinates are referred to as meatuses. Each meatus is named for the turbinate that lies above it eg, superior turbinate, superior meatus. The meatuses are very narrow, normally being about 0.5-1 mm wide (Proctor 1982). The airway gap in between the turbinates and the central nasal septum walls is the meatus. The walls are coated with a pseudo-stratified ciliated columnar epithelium that secretes a mucinous substance coating the walls and aiding in mucociliary clearance of small particles that are trapped on the mucosal surface by tiny hairs (cilia). Cilia beat in unison to transport the mucus from the nasal cavity and paranasal sinuses toward the nasopharynx where it is swallowed. Mucociliary clearance (i.e. cilia beating which moves the particles trapped within the mucus secretion toward the pharynx) of the deposited particles depends on their deposition site in the nasal cavity (Cheng et al. 1996; Fry and Black 1973). The anterior third of the nose is not covered by ciliated epithelium, but rather cutaneous epithelium that is like the skin.

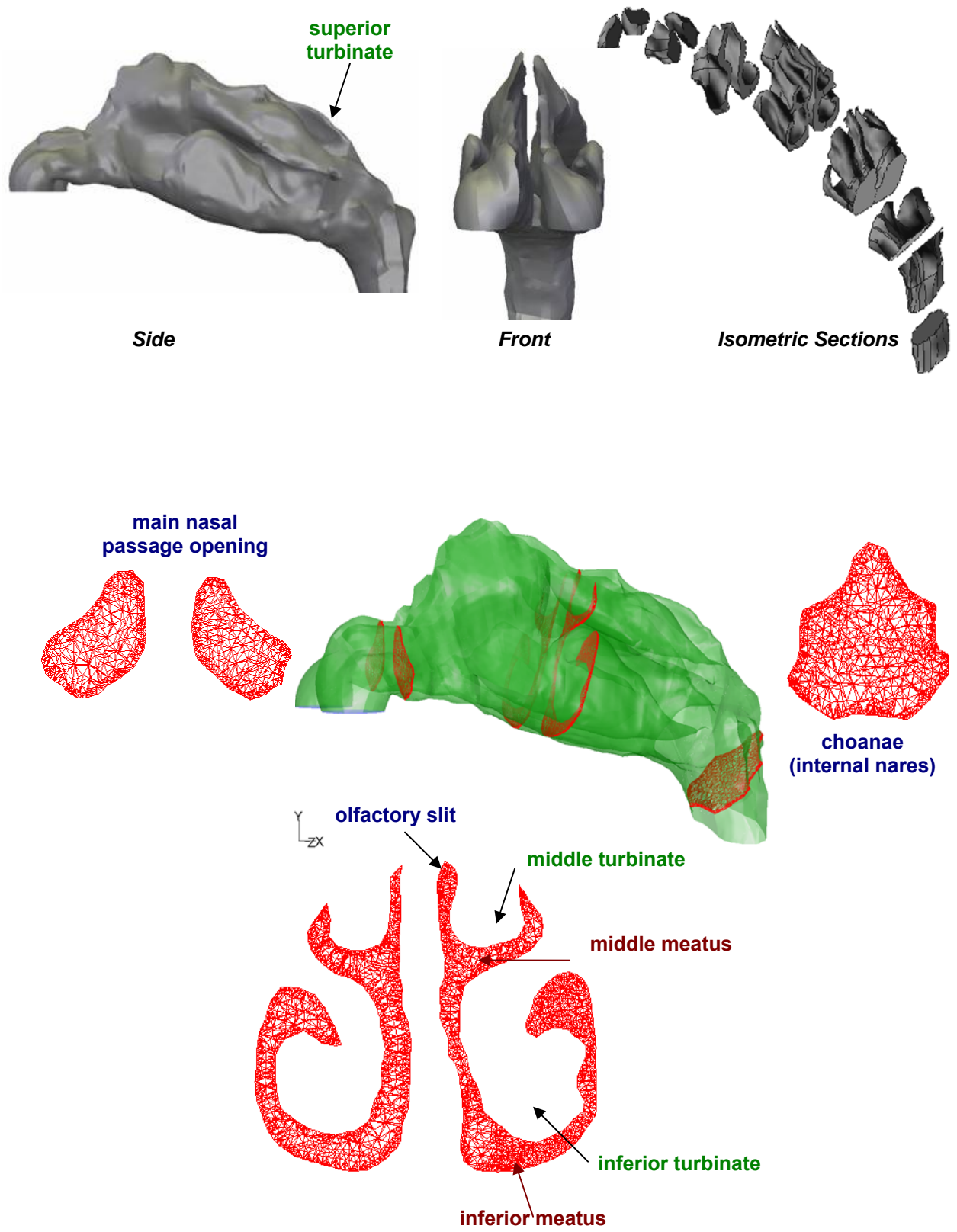


Figure 2.2 Nasal Cavity Geometry

The clearance mechanism of deposited particles in this region is thought to occur by physical means such as sneezing, wiping, and blowing (Swift and Strong 1996), which lead to a slower clearance than in the ciliated epithelium region.

At the upper region of the main nasal passage where the nasal roof is, a slit-shaped airway is contained between the superior turbinate and the septum which is the olfactory region. The sense of smell is provided by the olfactory nerves which trap odour bearing particles for olfaction. The olfactory recesses are located at the superior most portion of the nasal cavity, medial to the paired superior turbinates. Olfactory nerves are found on the superior portion of the septum, superior turbinates, and cribriform region. The width of the olfactory airway from the lateral to medial sides is 1-2 mm. The surface area of the olfactory epithelium varies somewhat from person to person, and values between 2 and 10 cm<sup>2</sup> have been reported for adults (Beidler 1980; Berglund and Lindvall 1982).

At the posterior end of the main nasal passage, the turbinates and the septum at the same point end and the two cavities merge into one. This region marks the choanae which is the beginning of the nasopharynx. The cross section area of the airway at this point is reduced to about 200 mm<sup>2</sup> from about 260 mm<sup>2</sup> which is inclusive of the two sides of the nose. The airflow changes directions about 90° downwards towards the trachea (Proctor 1982).

The nasal cavity is susceptible to anatomical anomalies especially in the complex turbinate region. Some examples of anomalies include septal deviation from the mid-line plane where ridges or spurs of bone sometimes project from the septum into one or the other fossa, enlarged turbinates turbinate hypertrophy, duplicate turbinates, and turbinate-turbinate attachment. Anatomical anomalies in their more severe form may partially or entirely block the airway in one of the nasal cavities. Non-dysfunctional morphological variation of the human nose also occurs and has been attributed to the eco-geographic adaptation to climate (Franciscus and Long 1991; Wolpoff 1968) where nasal cavities can be broadly categorised as leptorrhines (tall and narrow) or platyrrhines (short and broad) according to their morphology. It is thought that people exposed to cold dry environments exhibit leptorrhines features that induce turbulence (Weiner 1954; Wolpoff 1968). The random and rapid fluctuations of swirling fluid from turbulent flows thus is beneficial for conditioning the inspired air. Those exposed to hot humid environments however, exhibit platyrrhines features that produce more laminar flow, where the conditioning of the air is

less critical (Calhoun et al. 1990; Carey and Steegmann 1981; Cottle 1955; Courtiss and Goldwyn 1983). Geographically this has defined ethnic influences resulting in different appearances of the nose, such as: Caucasian, leptorrhine; African American, platyrrhine; Hispanic, paraleptorrhine; and Asian, subplatyrrine.

## 2.2. Fluid Flow Studies in the Human Nasal Cavity

Detailed air flow patterns can provide data that is pertinent to the prediction of gas-particle flows and regional tissue exposure to inhaled air. The nasal anatomy, characterized by thin airway channels does not allow direct measurements of flow patterns inside the human nose. Instead rigid cast models have been used to experimentally study the airflow patterns by a number of researchers. Early investigations of airflow were performed by Swift and Proctor (1977) which provided the first quantitative in vitro velocity measurements. The results showed that the majority of flow passed through the middle airway with a small fraction of the flow separated upward, forming a standing eddy in the olfactory area. The flow was found to be laminar at a flow rate of 125 ml/s. Turbulent flow was detected downstream of the nasal valve at a flow rate of 208 ml/s.

Girardin et al. (1983) used laser Doppler velocimetry, a non-invasive method of optical anemometry, to determine the velocity of water droplets suspended in air flowing through a nasal model made from a nasal cast of a cadaver. Measurements were made at five coronal cross sections of the nasal fossa for a flow rate of 166 ml/s. It was found that greater flow existed in the lower half of the fossa and closer to the septum. It was argued that the turbinates had a streamlining effect.

Hornung et al. (1987) studied the flow of  $^{133}\text{Xe}$  through a realistic life-sized plastic model of a nasal cavity generated from a nasal cast of a cadaver. This study confirmed the results of earlier visualization experiments (Masing 1967) by finding the majority of flow to be in the lower nasal airways and an increasing proportion of flow in the olfactory region at elevated flow rates. The results also showed that both catheter position and flow rate had significant and reproducible effects on the distribution of radioactivity within the model.

Schreck et al. (1993) studied the flow in a 3x enlarged plastic model generated from magnetic resonance images (MRI), spaced in 4-mm increments, of a healthy male subject. Flow visualisations were taken for flows between 50 and 1500 ml/s. It was found that two



vortices formed just posterior to the nasal valve during inspiration; a relatively large vortex formed in the upper part of the model, and a smaller one formed along the nasal floor. The majority of the flow passed through the central part of the passages, while smaller fractions passed through the meatus and the olfactory slit. Detailed flow patterns, however, were not determined.

The main problem encountered from the *in vivo* studies discussed thus far is the small size of the models which limits the resolution of the data that can be attained. This problem was addressed by Hahn et al. (1993) whom constructed a 20x scaled replica of a nasal cavity from computerised axial tomography (CAT) scans recorded in 2-mm increments from the tip of the naris to the beginning of the nasopharynx. A hot-film anemometer probe was used to measure the velocity distributions on five cross sections. Steady flow rates equivalent to 1,100, 560, and 180 ml/s through one side of the real human nose were studied. Airflows were determined to be moderately turbulent, but changes in the velocity profiles between the highest and lowest flow rates suggest that for normal breathing, laminar flow was dominant. The airflow distribution found 50% of inspired air flows through the combined middle and inferior airways and 14% through the olfactory region at all flow rates studied.

Park et al. (1997) were the first to use a two-dimensional measurement technique, digital particle image velocimetry (PIV), to study nasal airflow patterns. A 3x scaled nasal replica was generated from approximately nine coronal slices of anatomic data (from nostril to nasopharynx). Vector plots showed a significant portion of high-velocity flow in the olfactory region which is in contrast to other results in the literature.

Kelly et al. (2000) investigated two-dimensional velocity fields in parallel planes to the flow direction, throughout a nasal cavity model using particle image velocimetry (PIV). The nasal cavity was subjected to a non-oscillatory flow rate of 125 ml/s with the vector plots showing that the flow is laminar and regions of highest velocity are in the nasal valve and in the inferior airway. Relatively low flow was found in the olfactory region which suggested that it protects the olfactory bulb from particulate pollutants. Low flows were also observed in the nasal meatus whose primary function to enhance the air conditioning ability due to the increase in the surface area, was put down as a subject of debate. In these experiments a steady non-oscillatory flow was applied and the flow was considered laminar up to a flow rate of 24L/min. It was reported that approximately half of

the inspired airflow passed through the middle and inferior airways while a small fraction of the flow passed through the olfactory slit. Churchill et al. (2004) studied airflow patterns using water and dye flowing through anatomically accurate acrylic models of ten different human nasal cavities. It was found that the nasal morphological features such as the inferior orientation of the nostrils, the relative size of the nasal valve and the height of the nasal sill did not show statistically significant correlations among the ten models. However one parameter, the projection of the turbinate bones into the nasal cavity was shown to laminate the flow.

In a more recent study, Doorly et al. (2008) investigated the characteristics of the flow field using particle image velocimetry (PIV) and flow visualization. A 2x scaled model from polyvinyl acetate was constructed using a stereolithography (3D printer). Significant flow features that were found included the emergence of the jet from the internal nasal valve into the main cavity and its effect on flow instability within the turbinate region, the effectiveness of the cavity geometry in partitioning the flow into high shear zones which facilitate rapid heat transfer and humidification, and slow flow was observed in the olfactory regions to facilitate olfaction.

The increase in computational power has allowed many numerical simulations, including the work of Elad et al. (1993) which used a simplified nose-like computational model. In this simplified model, the coronal and sagittal cross-sections of the cavity were modelled as trapezoids while the inferior and middle turbinates were represented by curved plates that emerge from the lateral walls. FIDAP (Fluent Inc.) was used to simulate a steady flow which found that the flux of air tended to flow along the floor of the nasal cavity where the resistance was the lowest.

Another early study was that of Keyhani et al. (1995). A finite element mesh was constructed based on the experimental model used by Hahn et al. (1993). The steady-state Navier-Stokes and continuity equations (see Chapter 4) were solved using computational fluid dynamics (CFD) software, FIDAP (Fluent Inc.) to determine the laminar airflow patterns in the nasal cavity at quiet breathing flow rates. Their results confirmed the laminar nature of flow for quiet breathing already found experimentally. In the main nasal passages, the highest inspiratory air speed occurred along the nasal floor (below the inferior turbinate), and a second lower peak occurred in the middle of the airway (between the inferior and middle turbinates and the septum). According to this study, about 30% of

inspiratory airflow passes below the inferior turbinate and about 10% passes in the olfactory area. Secondary flows were induced by curvature and rapid changes in cross-sectional area of the airways, but the secondary velocities were small in comparison with the axial velocity through most of the main nasal passages. The flow patterns changed very little as total half-nasal flow rate varied between resting breathing rates of 125 ml/s and 200 ml/s.

Subramaniam et al. (1998) simulated the airflow under steady-state, inspiratory conditions simulating rest and light exercise (steady-state inspiratory flow rates: 15 L/min and 26 L/min, respectively) with FIDAP (Fluent Inc.). A three-dimensional, anatomically accurate representation of an adult human nasal cavity and nasopharynx was used. It was found that swirling air currents and recirculating flow existed in the nasal vestibule. The expansion at the nasopharynx gave rise to two downward, counter current, spiralling vortices. Significant lateral flow was observed mainly in the middle lateral meatus while high velocities occurred in the posterior nasal valve region. In the main nasal airway, the highest velocities occurred through the ventral and middle medial regions.

Hörschler et al. (2003) simulated a realistic model of the nasal cavity using a computational code developed at the Aerodynamisches Institut, *RWTH Aachen*, Germany. Simulations were performed for inspiration and expiration at rest with Reynolds numbers  $Re = 1560$  and  $Re = 1230$  at the nostril, respectively. The results showed one vortex located in the immediate vicinity of the turbinate tip.

Pressure–flow relationships were measured and simulated for both nasal cavities and maxillary sinuses by Croce et al. (2006). Numerical inspiratory airflow simulations were performed for flow rates up to 353 ml/s in both the nostrils using a finite volume-based method under steady-state conditions with the CFD software FLUENT (Ansys Inc., USA) using a laminar model. The main contribution to total pressure drop was localised in the nasal valve region. Airflow was found to be predominant in the inferior median part of nasal cavities. Two main vortices were observed downstream from the nasal valve and toward the olfactory region. Other studies include Weinhold and Mlynski(2004), Zhao et al. (2004), Zamankhan et al. (2006) and Shi et al. (2006) which simulated the airflow of rest and light breathing conditions (between 10L/min and 26L/min) using a laminar flow.

In summary, experimental studies of the fluid flow in the human nasal cavity have shown that greater flow existed in the lower half of the fossa and closer to the septum. Laminar flows were dominant when flow rates were 15L/min or less while the flow regime was considered turbulent for flow rates of 20L/min or more. Numerical simulations were able to identify vortices downstream from the nasal valve, where the flow accelerates and also toward the olfactory region, where low flow occurs. Overall, approximately half of the inspired airflow passed through the middle and inferior airways while a small fraction of the flow passed through olfactory slit and meatus. The relatively low flow in the olfactory region suggests that it protects the olfactory bulb from particulate matter. Low flows were also observed in the nasal meatus, whose primary function was thought to enhance the air conditioning ability due to the increase in the surface area. Therefore detailed investigation into the airflow distribution in the middle airways especially the meatus regions needs to be performed. In addition detailed flow patterns were not determined and a comprehensive comparison was not achieved. The analysis found in the studies presented focussed on one side of the nasal cavity and comparisons of the flow patterns between both nostrils were not made.

### **2.3. Particle Deposition Studies in the Human Nasal Cavity**

The inhalation of toxic particles through the nasal cavity has been found to cause adverse health responses. On the other hand, it also provides an alternative route for drug delivery due to the highly vascularised mucosal walls that provide improved speed of pharmacological action and retention of the drug composition, which is often destroyed when drugs are digested. Particle deposition in human nasal cavity has been studied by *in vivo* measurements (Etherington et al. 1998; Heyder and Rudolf 1977; Hounam et al. 1971; Keck et al. 2000b; Kesavanathan et al. 1998; Pattle 1961; Wiesmiller et al. 2003) and many others). The work by Kesavanathan et al. (1998) determined the effect of particle size, flow rate, nostril shape, and nasal passage geometry on nasal particle deposition efficiency in ten healthy volunteers. Three constant flow rates of 15, 25, and 35 l/min were used in this study. An empirical correlation was devised to curve fit the deposition efficiency based on the particle aerodynamic diameter, flow rate, nostril length to width ratio (ellipticity,  $E$ ), and minimum nasal cross-sectional area ( $A_{\min}$ ). However there still

remained a large intersubject variation in deposition despite the inclusion of the above factors.

Keck et al. (2000b) studied the deposition efficiency of the particles during normal respiration of eleven human volunteers. It was found that 1–3  $\mu\text{m}$  sized particles had a deposition efficiency of about 60% during respiratory conditions of  $V_t = 0.75$  L (tidal volume) and a frequency of 15/s. This compared with 4–30  $\mu\text{m}$  particles having around 90% deposition. Between 80% and 90% of the particles retained in the nasal cavity were deposited at the anterior nasal segment. Wiesmiller et al. (2003) compared the deposition of the particle during inspiration and expiration among nine human volunteers. A deposition of 46% was found for nose-only inhalation while for nose-in/mouth-out breathing, 33% deposition was found. The results suggest that intranasal particle deposition takes place during inspiration as well as during expiration which is important in cleansing of respiratory air.

A major problem associated with *in vivo* studies is the highly invasive nature such as the use of probes or radio-labelled particles which usually require large amounts of radioactivity. To avoid these problems and to obtain more reproducible results, *in vitro* studies using replicate casts have been carried out (Cheng et al. 1998; Gradon and Podgorski 1992; Guilmette et al. 1994; Häußermann et al. 2001; Itoh et al. 1985; Kelly et al. 2004; Swift 1991; Zwartz and Guilmette 2001).

Swift (1991) studied particle deposition in a replica based on MRI scans of the nose of an adult and an infant over a range of particle sizes of 1–4 $\mu\text{m}$  and flow rates of 7–50 L/min. Deposition in the child nasal passage was greater than the adult at the same flow rate, but was similar in efficiency for equivalent states of rest or exercise breathing.

Guilmette et al. (1994) examined inertial depositions in a nasal replica that was based on the same MRI data used by Swift (1991). Flow rates ranged from 10 to 40 L/min and particle mass median diameters were about 0.6–12 $\mu\text{m}$ . Zwartz and Guilmette (2001) constructed another replica of the human nasal cavity with improved accuracy in manufacturing. A number of deposition efficiency measurements were made for 5.5  $\mu\text{m}$  particles and flow rates ranging from 10 to 40 L/min

Häußermann et al. (2002) used monodisperse droplets (1.7 $\mu\text{m}$  to 10 $\mu\text{m}$ ) under different breathing patterns. It was found that breathing patterns influence the total amount of nasal

deposition and suggested that it probably also affected the deposition sites. The total deposition for constant flow was significantly higher than that of human breathing. It is suggested that the impaction factor (a parameter used in deposition by impaction studies) is not applicable for constant flow in the cast, but is better for the human breathing pattern. However it was found that there were small differences in deposition efficiencies when the impaction factor was high (i.e. the differences become less pronounced with increasing particle size).

Cheng(2003) summarized the particle deposition mechanisms in the extrathoracic region, including both nasal and oral airways. It was concluded that depositions in the nasal and oral airways are dominated by the inertial mechanism for particles  $>0.5 \mu\text{m}$  and by the diffusion mechanism for particles  $<0.5 \mu\text{m}$ . Kelly et al. (2004) investigated the impact of differently manufactured nasal replicas on both inertial particle and ultrafine particle deposition efficiencies. They found that the inertial nasal particle deposition is significantly influenced by small geometric differences and even wall roughness, but such effects are minor for nanoparticles. The simulation of nanoparticle deposition was performed by Zamankhan et al. (2006) under steady laminar conditions where diffusion was the dominant deposition mechanism for the smallest range of particles (1–30 nm).

Shi et al. (2006) numerically simulated the transport and deposition of nanoparticles,  $d_p=1-2 \text{ nm}$  and ultrafine particles,  $d_p=5 \text{ nm}$  under a transient laminar flow in a representative human nasal cavity. The cyclic airflow patterns as well as local and overall nanoparticle deposition patterns were computationally simulated and analysed. It was found that about one-half of a percent of the inhaled nanoparticles passed through the recesses of the olfactory region as the main airflow bypasses these recesses. In a follow up study by the same authors (Shi et al. 2007) inertial particles in the human nasal cavity were simulated, where the wall roughness of the nasal cavity was taken into account. They found that the wall roughness can influence the particle deposition on the premise that a large fraction of particles are likely to travel near airway surfaces and that particles with  $d_p >4\mu\text{m}$  are consequently trapped by surface roughness or small bumps.

In terms of sprayed particle deposition for drug delivery applications, various studies adopting human subjects or nasal cavity replicas have found relationships for particle deposition efficiencies with nasal spray parameters such as spray cone angle and the particle size distribution produced (Cheng et al. 1996; Cheng et al. 2001; Suman et al.

2002). Kimbell et al. (2004) simulated particle deposition by releasing particles from different planes in order to imitate the nasal spray delivery. Schroeter et al. (2006) employed CFD to analyse particle deposition in the nasal cavity particularly in the turbinate and olfactory region. They found high deposition efficiency in the nasal valve region, medium deposition efficiency in the turbinate region and very low deposition efficiency in the olfactory region. In a follow-up paper by the same research group (Kimbell et al. 2007), particles were released from different locations of the nostrils to characterise the deposition efficiencies and patterns from nasal sprays. However the particles were released passively into the nasal cavity and the effects of the particles' boundary conditions caused by the atomisation of the drug was not included.

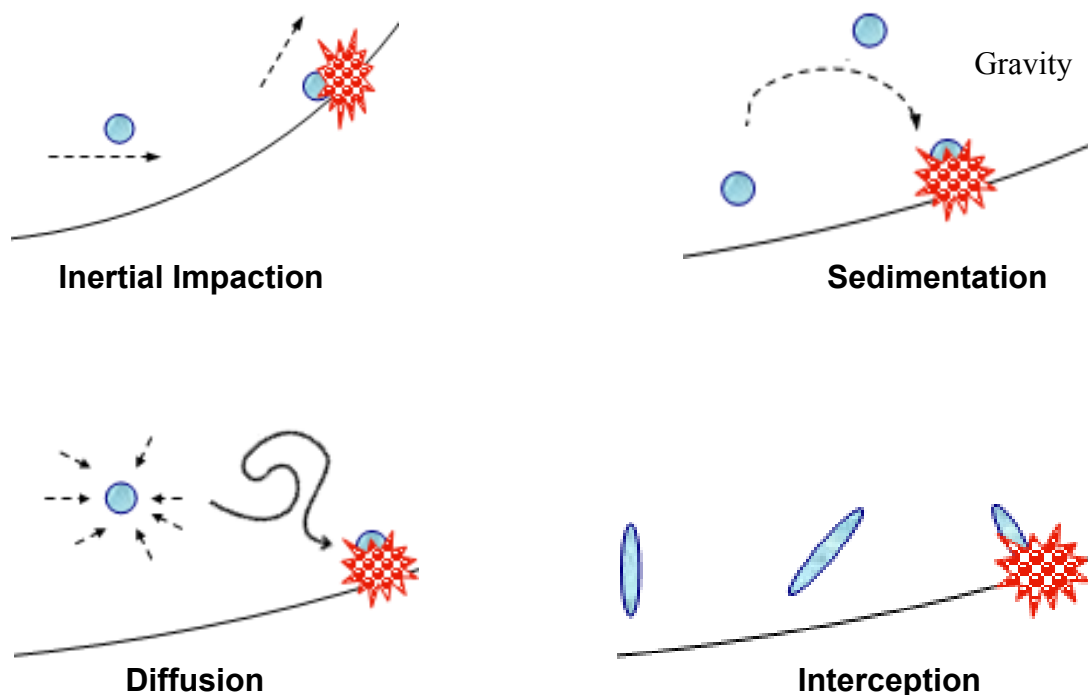


Figure 2.3 Particle deposition mechanisms

In addition, Lippman et al. (1993) discusses three main mechanisms for deposition of inhaled drug particles: inertial impaction, gravitational sedimentation, and Brownian diffusion, while it is apparent that elongated shapes such as fibres may induce higher interception Figure 2.3. Particles in the submicron range will deposit by Brownian diffusion (Gonda and Gipps 1990). In the submicron range, as the particle size approaches 1nm the effects of Brownian diffusion becomes increasingly dominant (Figure 2.4). For micron ranged particles, typically larger than  $1\mu\text{m}$ , the effects of particle inertia become important and deposition by inertial impaction becomes dominant.

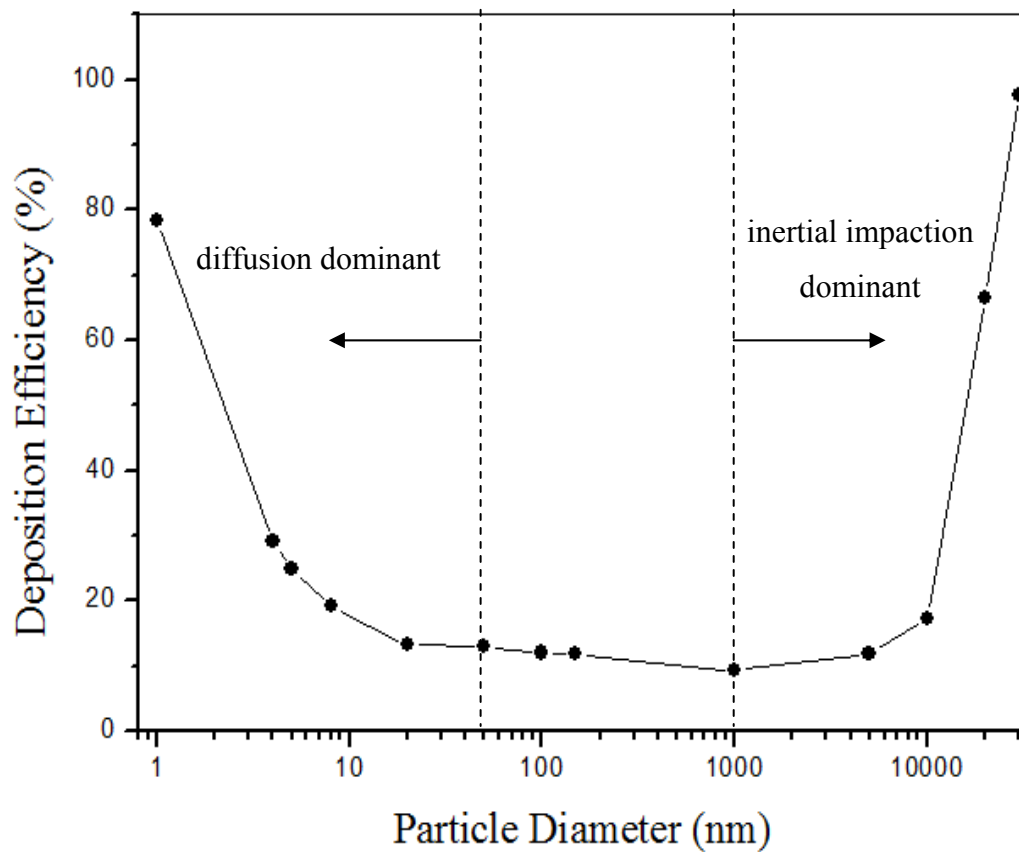


Figure 2.4 Typical particle deposition curve for submicron and micron particles

The inertial impaction parameter is defined as,

$$I = d_{ae}^2 Q \quad (2.1)$$

where  $d_{ae}$  is the aerodynamic equivalent diameter in microns and  $Q$  is the flowrate usually taken with units of  $\text{cm}^3/\text{s}$ . Further studies from Kelly et al. (2004) and Eck et al. (2000) show high deposition efficiencies ( $> 95\%$ ) for inertial parameter values greater than  $3 \times 10^4 \mu\text{m}^2 \text{cm}^3/\text{s}$ .

In summary, these studies showed that particle deposition in the nasal cavity is strongly influenced by three major factors: particle physical factors including particle diameter, shape and density; physiological factors such as respiratory ventilation and pattern; and nasal morphological factors such as airway passage geometry, and nostril shape and size. Generally, particle deposition was either dominated by Brownian diffusion (submicron particles) or by inertial impaction (micron particles). Small micron particles ( $< 5 \mu\text{m}$ ) had



an approximate deposition efficiency of 60% while 5-30  $\mu\text{m}$  particles had around 90% deposition. A large proportion of this deposition occurred in the anterior nasal region. In addition, particle deposition can take place during inspiration as well as during expiration which has important implications for cleansing of the respiratory air. The studies focussed on particle deposition due to spherical particles and the effects of particle shape and morphology were not considered. Particulate matter, especially toxic fibres, pollen and fumes may exist in different forms and consequently its interaction with the airflow field is indeed different. These effects are needed to be considered. In the pharmaceutical industry, particle deposition from nasal spray devices have been investigated, but are few in numbers. Nasal spray parameters, such as spray cone angle, and particle size and their effect on deposition have been identified. Some conflicting results have been produced regarding the spray cone angle and this may be attributed to the high variability associated with experimental testing. Further investigations are needed to provide deeper knowledge of nasal spray characteristics and hence provide accurate boundary conditions for CFD simulations of sprayed particles in the nasal cavity.

## CHAPTER 3

# Modelling the Human Nasal Cavity

## 3.1 Nasal Replicate Reconstruction Methods

In general there are three methods in gas and gas-particle studies of the nasal cavity: i) human subjects, ii) replicate casts, iii) numerical simulations. Because of the intrusive nature, ethical issues, and health risks to the volunteers (e.g. measurements of regional deposition in the nose require relatively large amounts of radioactivity leading to a high radiation dose for the participants), alternative methods are often utilised. The following sections provide a description of alternative methods to using human volunteers.

Swift and Proctor (1977) provided the first quantitative in vitro velocity measurements by inserting a miniature Pitot device into the flow passage of a model that was made from the nasal cast of a cadaver. Dye was injected outside the nostril into a steady flow of water while a transparent, flat, plastic plate was used in place of the nasal septum to allow observations to be made.

Girardin et al. (1983) constructed a normal sized nasal cavity model and used Laser Doppler Velocimetry to measure the velocity fields of the nasal fossa under flow rates of 167 and 560 ml/s. This method was significant for its time as it was one of the first studies to implement a non-invasive method of optical anemometry to provide quantitative analysis.

Hornung et al. (1987) studied the flow of  $^{133}\text{Xe}$  through a realistic life-sized plastic model of a nasal cavity generated from a nasal cast of a cadaver. A needle catheter was used to

infuse the radioactive xenon into a continuous flow of room air maintained through the model by a variable vacuum source connected to the nasopharynx. The radioactive gas was infused at one of five release sites in the nostril, and the distribution of the radioactivity was imaged in the sagittal plane with a scintillation camera. The data was organized to show the activity in six contiguous regions of the midnose. For each catheter, release site activity patterns were determined for three flow rates.

Swift (1991) went on to construct a plastic replica of the nasal cavity based on magnetic resonance images (MRI) scans of the nose from the external nares to the end of the nasopharynx. The replica was assembled from 3-mm thick plastic sandwich elements that were carved by hand with a high-speed cutting tool. Tracings of airway outlines on the plastic elements were used for guidance in the hand-carving process.

Schreck et al. (1993) studied the flow in a x3 enlarged plastic model generated from MRI, spaced in 4-mm increments, of a decongested subject. Templates were formed from scaled MRI data and were cut into Plexiglas plates, which were assembled to form the nasal model. Pressure measurements, flow visualization, and hot-wire anemometry studies were performed at different flow rates. The influence of nasal congestion and the collapse of the external nares were examined by using clay to simulate local constrictions in the cross section. The nasopharynx was modelled as a sharp bend in a circular duct.

Hahn et al. (1993) constructed a 20X enlarged model of the right nasal cavity from coronal Computed Tomography (CT) scans (2mm apart) from a human volunteer that had no abnormalities. The outlines of scaled CT scan data were cut out from Styrofoam slabs, which were then glued together to form the nasal model. The surface of the interior cavity on each section was coated and smoothed with casting plaster and holes were drilled through the sides of the block to allow the insertion of a hot-film anemometer probe to measure velocities of the air flowing inside the model.

Cheng et al. (2001) obtained coronal plane images of 3-mm thickness from MRI of a non-smoking healthy adult male volunteer. The entire nasal airway length was imaged from the external nares to the posterior nasopharynx. A replica model was constructed by milling 77 acrylic plastic sections at 1.5 mm-thick using a computer-controlled micro milling machine. Plates in the anterior one-third and the posterior one-third of the model were coated with a very thin layer of vacuum grease to seal the model while the middle

turbinate region was covered with a layer of clear book tape to provide the seal. A constant flow of air was sucked through from the nasopharynx region at a flow rate of 20 L/min.

More recently a replicate has been produced through stereolithography such as the construction by Kelly et al. (2004). Stereolithography (SL) is a manufacturing method where a design is created from CAD and converted into a compatible SL format (i.e., a file with extension .stl). SL uses a laser beam to build 2-D layers by curing a photopolymeric liquid resin (Figure 3.1). On each layer, the resin solidifies as it is polymerised by exposure to the laser beam which traces out the cross-sectional pattern. The surface of the layer is then coated with a liquid resin and the SL apparatus descends by a single layer thickness, typically 0.05 mm to 0.15 mm to begin the next layer. This continues until a complete 3-D part is formed. The model, which was fabricated from 26 computed tomography scans by using rapid prototyping techniques, is a scaled replica of a human right nasal cavity.

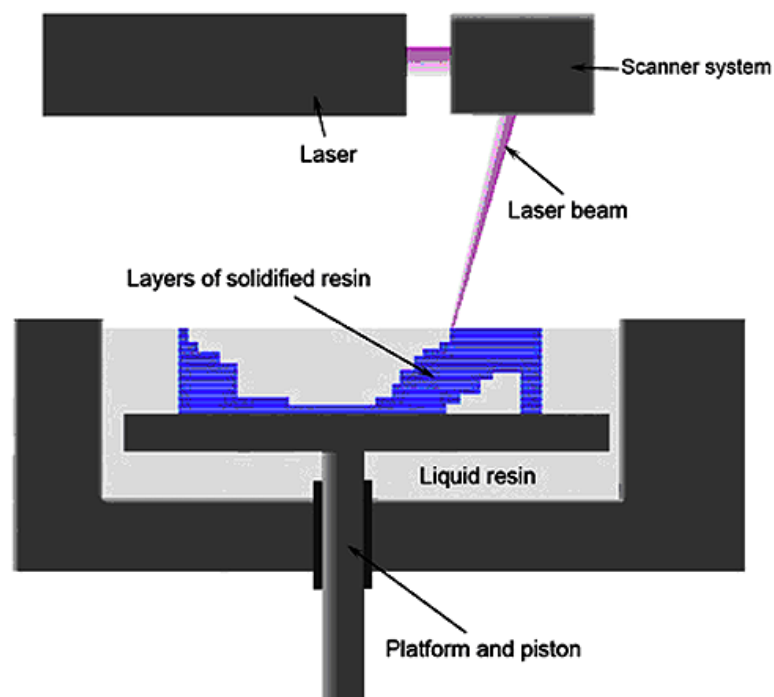


Figure 3.1 Stereolithography process

In a comprehensive study of the effects of nasal cavity geometry on airflow dynamics Churchill et al. (2004) ten replicate cast models were constructed from direct casting of the upper respiratory passageways of cadavers, ranging in age at death from 41–88 (mean

age at death =  $68.1 \pm 18.9$ ) years. Each head was sagittally sectioned roughly 5 mm lateral of the midsagittal plane so as to preserve the nasal septum on one side. The posterior nasopharynx was occluded with modelling compound and a molten metal alloy was poured into the nostril to fill the passageway. This formed the cast which acrylic plastic would polymerize around. Dye was introduced into the model to allow visualisation of the flow field.

In these studies, the effect of post mortem changes such as shrinkage of the mucosa is to be expected in cadavers (thus the models reflect a decongested or even hypercongested condition) and the introduction of an artificial septum are common issues associated with replicate cast models. Although these studies provide valuable descriptive and quantitative information on air flow patterns and deposition rates in the nasal passages, the methods are time consuming and expensive. The resolution of the measurements can also be poor because of the small size of the cast model and therefore scaled-up physical models are required. An alternative is the use of computational models to perform the analysis by numerical methods. This provides the advantages of repeatability, a larger number of tests, fine detailed solutions, and greater control of variables at low cost and quick turn around times.

## 3.2. Developing a Computational Model of the Nasal Cavity

The construction of the computational model can be divided into four stages: image acquisition, data conversion, segmentation and surface reconstruction (Figure 3.2) which are discussed in the following sections.

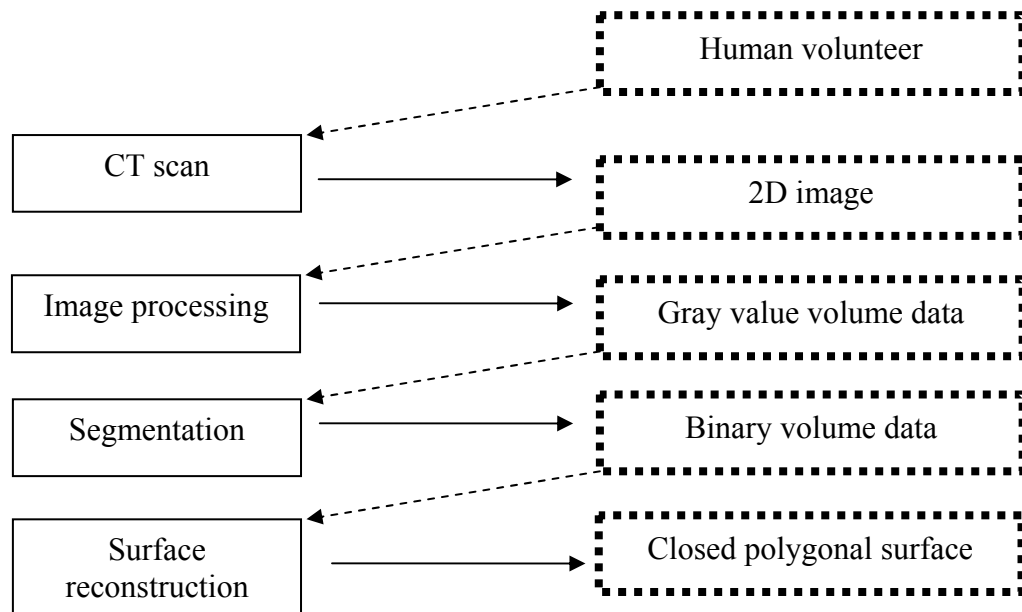


Figure 3.2 Computational reconstruction methodology

### 3.2.1. Medical Image Processes

The development of a computational model of the human nasal cavity begins firstly with medical imaging taken from the human volunteer. Medical images can be obtained from various sources, yet all provide essentially similar information: a 3D matrix (or series of 2D matrices) of volume elements (voxels), in which tissues and structures are distinguished from one another by differences in brightness or greyscale. Visualization and reconstruction of morphological structures contained within these images is an area of active research. In general, there are two imaging techniques that are currently in favour, MRI and CT. Each technique has its own advantages and downfalls. A brief description follows.

Magnetic resonance (MR) imaging essentially provides a distribution map of hydrogen nuclei (found in water). A large magnet (typically 1.5 Tesla, which is approximately

50,000 times greater than the Earth's magnetic field) is used to align dipole magnetic moments of protons within the object of interest. An electro-magnetic radio frequency (RF) pulse is then applied to induce a  $90^\circ$  offset (spin echo). Following the pulse, the magnetic moments of the protons return to equilibrium or relaxation. There are two relaxation times of interest: longitudinal relaxation (T1) is the time for approximately 63% of protons to realign with the magnetic field along the longitudinal axis; transverse relaxation (T2) is the time for approximately 63% of protons to precess out of phase. Different tissues exhibit different T1 and T2 relaxation times, which results in high-contrast images. The contrast is provided by saturating the imaging plane with radio-frequency energy. Air that moves into the plane provides fresh spins and appears bright in the image, in contrast to the saturated tissues surrounding the airway.

Computed tomography (CT) is the combination of mechanical and computer engineering which was first developed in 1972 by Sir Godfrey Hounsfield (Richmond 2004). During a typical CT procedure, the patient is placed on a table. The table then moves the patient through the gantry (a donut-shaped device), which houses an X-ray tube and detector array. For each image acquired, the X-ray tube rotates around the patient and the X-rays pass through the patient to the detector array, and thousands of X-ray measurements are acquired. The computer then processes this information and displays the corresponding images on a computer screen (Figure 3.3). This imaging technique avoids any superimposition of organs or tissues upon one another that might occur during other types of X-ray tomographic studies. The CT exam creates images analogous to a single slice of bread from a whole loaf or a slice from an orange. Hence, the word 'slice' is often used to describe a view of patient anatomy. Each CT image consists of large number of small picture elements (pixels). Each pixel is assigned a numerical value (gray scale), based on the degree to which the tissue corresponding to that pixel attenuates the X-Ray beam.

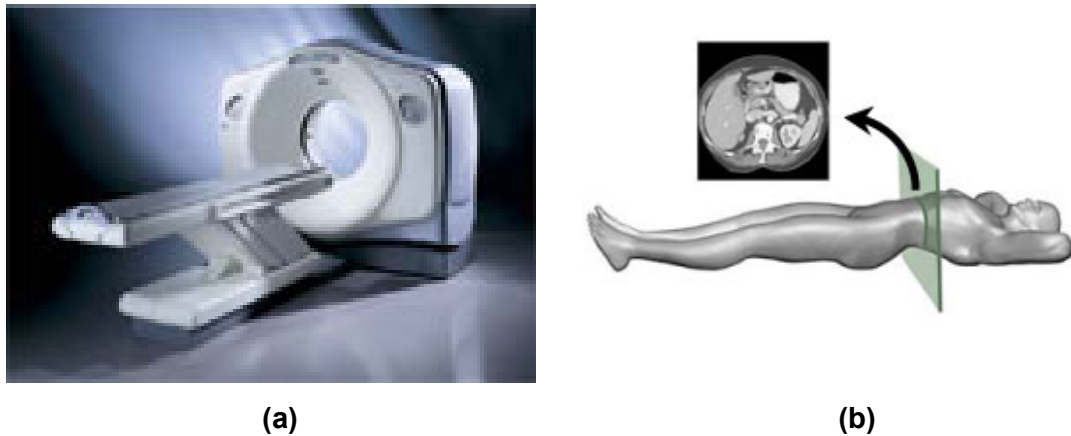


Figure 3.3 (a) Computed tomography (CT) scanner and (b) CT slice concepts

### 3.2.2 MRI vs CT Scans

Although both MRI and CT images provide 3D volumetric data sets, in this study, they are viewed as a series of stacked 2D pixels which have an associated depth, or slice thickness. In addition CT images produce matrices of voxel greyscale values determined by the CT number of the voxel tissue. Since different tissues have different attenuation characteristics, the resulting image distinguishes different tissues by greyscale. This allows good detection bone structures which is an advantage over MRI. However dental metallic devices are one of the most problematic issues with CT scan quality. These devices cause considerable streak artefacts that obscure the nasal cavity and sinus anatomy. In terms of the nasal cavity, MRI distinguishes mucosal structures well, although the turbinate cartilage location has to be inferred from its surrounding mucosa, since actual bone structures may not be visible. Despite the advances of MRI, insufficient tissue, plus the problems of susceptibility due to the air-containing passages, makes MRI a less effective method for obtaining nasal cavity geometries (Zinreich et al. 1988). Although both methods can provide the necessary data, this research chose CT scans for its availability and its ability to distinguish air passages more clearly.

### 3.2.3. Image Acquisition from CT Scan

In this research a nasal cavity geometry was obtained through a CT scan of the nose (Figure 3.4) of a healthy 25 year old, non-smoking Asian male (170 cm height, 75 kg mass). The CT scan was performed using a CTI whole body scanner (General Electric). The single-matrix scanner was used in helical mode with 1 mm collimation, a 40-cm field of view, 120 kV peak, and 200 mA. The scans captured outlined slices in the x–y plane at



different positions along the z axis from the entrance of the nasal cavity to just anterior of the larynx at intervals of 1 to 5 mm depending on the complexity of the anatomy.



Figure 3.4 CT scan of the middle turbinate region

### 3.2.4. Image Processing

The data obtained from CT scan was a series of cross sectional images which contains different gray scale information with respect to different organs or tissues. The original set of CT images is converted into a file format compatible with the package Mimics® (Materialise NV), a 3D imaging software that generates and modifies surface 3D models from stacked medical images such as CT and MIR through image segmentation done in the STL format. The program allows image enhancement by rescaling the grey-level histogram to 1-200 and remapping the image volume to an 8-bit/pixel depth file. The image processing step included the following:

- ◆ Sub-image creation, which extracts a new volume from the original image. The sub-image extraction had a twofold purpose: (a) to reduce both the amount of calculations needed in the further processing steps and computational time and memory resources; and (b) to remove the noisy regions out the airway;
- ◆ 3D convolution with a Gaussian kernel, which reduces the background noise present in the images. Because of its isotropic shape, the Gaussian filter has optimal properties such as smoothing mask, removing small-scale texture and noise, which altered the regional segmentation, without distorting lower spatial frequencies.

- ◆ Filtering was applied in three dimensions in order to obtain a smoothed CT image volume also along the axial direction. Such a procedure attenuates the spatial discontinuities among the slices introduced during acquisition, as an effect of the slice thickness.

### 3.2.5. Segmentation

A 2D segmentation is used to detect and extract, slice by slice, the walls of the airway. For the segmentation process, a region growing algorithm, based on the Mumford-Shah algorithm (Mumford and Shah 1989) found in Mimics is used. Regional segmentation was applied as it allows the tracking only of the domains of interest, even in the presence of noise. A first regional segmentation with a greater number of partitioning regions than necessary is performed on each single slice. This allows the algorithm to detect the walls even in severely disturbed images. A threshold binarisation process is then applied in order to remove sub-regions unrelated to the airway, which typically present a lower intensity value with respect to the signal. In this study, the threshold was empirically chosen and represents 45% of the maximum grey-level value of the study.

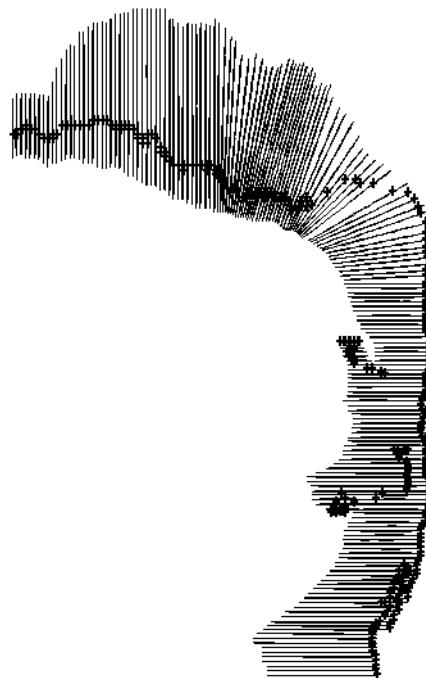


Figure 3.5 Segmented CT slices developed from the Mumford-Shah algorithm in preparation for surface creation.

The airway contours may exhibit some irregularities due to the image discretisation, such as harsh corners, which may cause severe distortions in the flow field values, when the

model is used in fluid-dynamic simulation. To avoid this effect a moving average between the spatial co-ordinates confining the airway lumen is performed. The number of average operations ( $n$ ) is imposed by the user, so that the function executes  $n$ -times the computations. As an optimal trade-off between removing contour irregularities and preserving a suitable spatial resolution, moving average step was applied twice. The algorithm provided the outlines of every slice (in X-Y plane) respected to its vertical position (Z location of the slice) in a 3-D space in which was stored as IGES file (Initial Graphics Exchange Specification).

### 3.2.6. Surface Generation

Generation of a surface from the 2D contour data began with the translation of the segmented, modified and smoothed contour points into a data series that was read into the computer program Geomagic Studio (Geomagic U.S.). The obtained data points that lie on the airway surfaces were fitted by applying the NURBS (Non-Uniform Rational B-Splines) approach (Piegl and Tiller 1995) and the resultant file stored as an IGES file (Initial Graphics Exchange Specification). Based on the IGES file, the commercial software CATIA (Computer Aided Three dimensional Interactive Application, by Dassault Systemes) was used to finish the surface model. The file (Figure 3.6) is then ready to be imported into the appropriate CFD software to define the airflow domain and volume mesh.

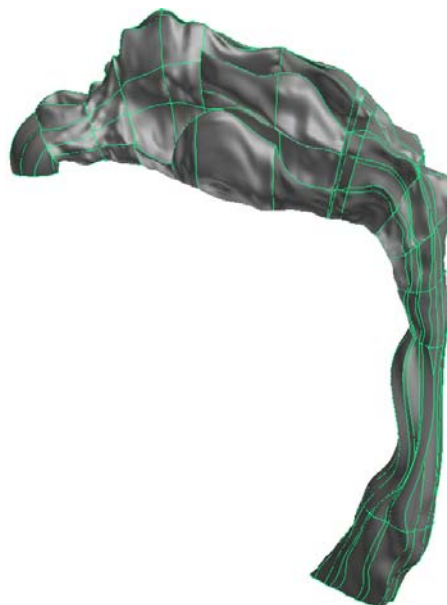


Figure 3.6 Computational model complete with surface ready for volume and mesh creation.

## 3.3. Developing the CFD Model

### 3.3.1 Computational Mesh and Boundary Conditions

The computational mesh topology hierarchy used in GAMBIT includes:

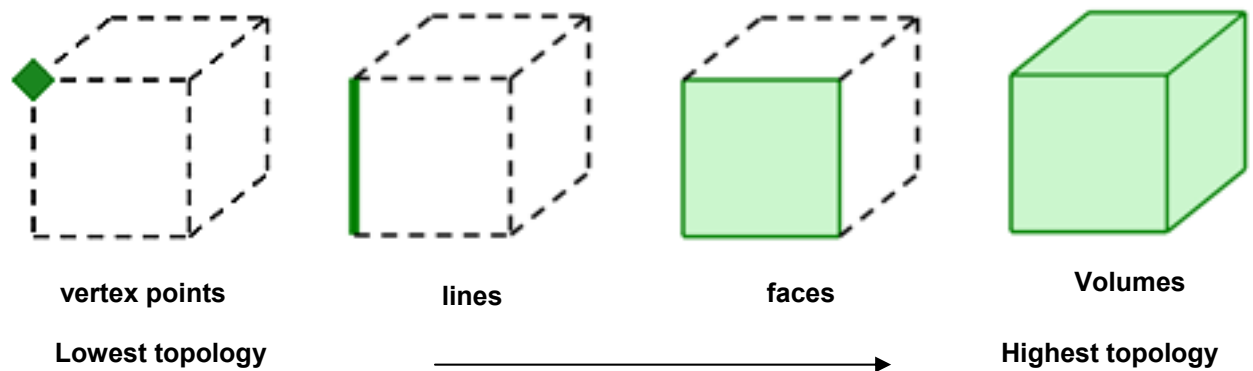


Figure 3.7 Mesh topology used in GAMBIT

A higher topology assumes the existence of the topologies underneath it (Figure 3.7). For example, the creation of volume cell automatically inherits the lower topologies (i.e. a volume cell contains face, line and vertex structures). For a complex geometry such as the nasal cavity, an unstructured mesh was used as it is very time consuming if not impossible to achieve as a structured mesh. Unstructured meshes may involve the use of hexahedral, tetrahedral, pyramid, and wedge cells (Figure 3.8) in combination, whereas a structured mesh is more reliant on hexahedral cells or the use of block-structured grids.

An advantage in using an unstructured mesh for complex geometries is that the use of tetrahedral cells allows far fewer cells than an equivalent mesh consisting of hexahedral elements since the tetrahedral cells can be controlled in terms of clustering them in regions of the flow domain where they are needed. In contrast structured hexahedral cells will generally force cells to be placed in regions where they are not needed. However, one problem with tetrahedral cells is that their grid designs are prone to high aspect ratios which affect the skewness of the cell. Additionally tetrahedral cells can never be aligned with the flow direction. These two problems can impede convergence and lead to numerical diffusion. Numerical diffusion is a common source of error and is also called *false diffusion* because it is a product of numerical error and does not represent a physically occurring phenomenon. A few techniques may be applied to minimise the likelihood of false diffusion such as choosing higher order discretisation schemes (see Section 4.3) and increasing the resolution of the mesh (see Section 3.3.3).

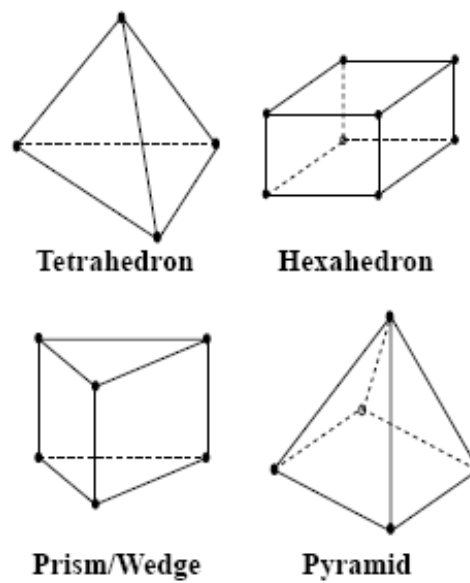


Figure 3.8 3D cell types

The computational model constructed from Section 3.2.5 in IGES format is imported into GAMBIT where the surfaces generated are detected as faces. Individual faces were given a name according to their axial position from one to ten (one being the nostril end, and ten being the nasopharynx end). At the nasopharynx, a long tubular extension was included in the geometry to allow for an outflow Neumann boundary condition. For this condition, the flow at the exit assumes a fully developed condition and zero normal gradients exist for all flow variables except pressure (i.e.  $\frac{\partial \phi}{\partial n} = 0$ ). This type of outflow boundary condition is convenient as it allows the modelling of flow exits where the details of the flow velocity and pressure are not known prior to solution of the flow problem. The faces are then stitched together to form a complete volume which acts as the airflow domain that is to be simulated. The computational domain with its ten sections were categorised into regions (Figure 3.9). The anterior airway of the nasal airway can be regarded as regions 1–4, the middle airway as regions 5–8, and the posterior airway is taken as regions 9–10. The two nostrils were defined as velocity inlets where the velocity magnitude and direction or their velocity components can be defined. Additional scalar properties can also be defined for this boundary condition.

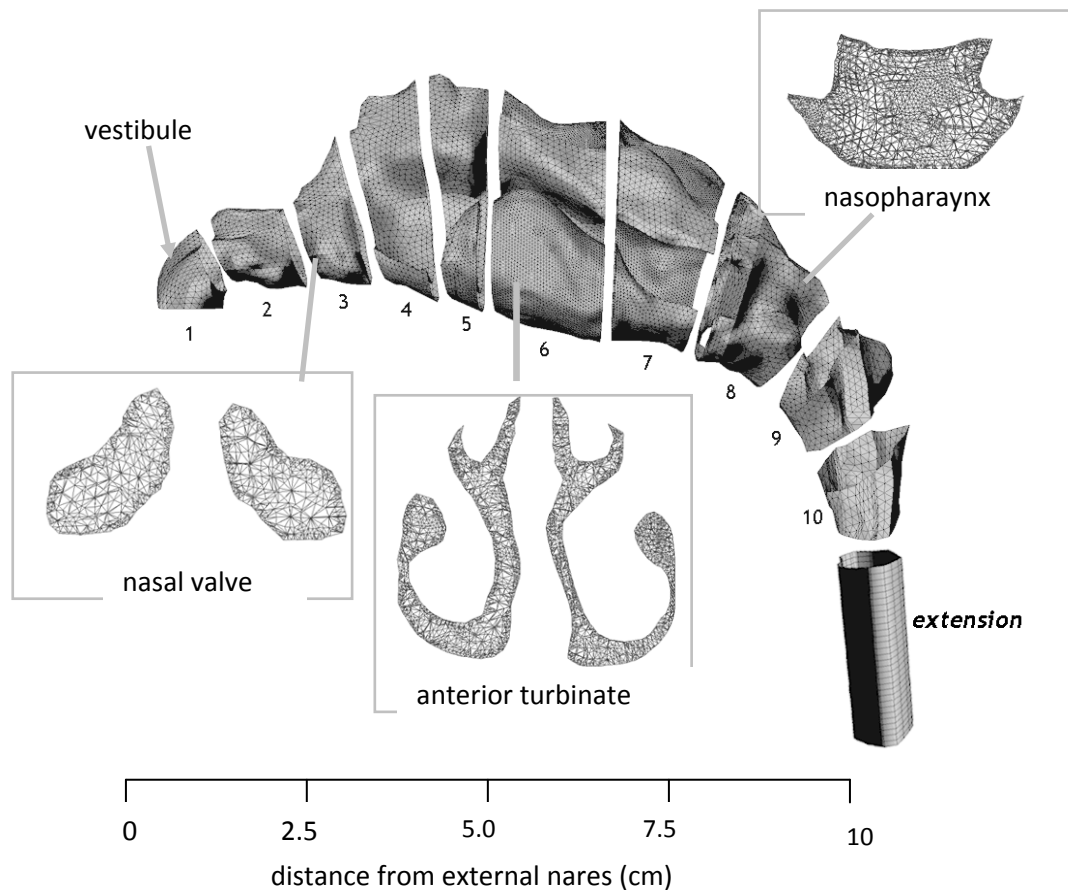


Figure 3.9 Nasal cavity geometry showing the computational mesh of the cross-sectional areas taken at the nasal valve, middle turbinate and nasopharynx regions.

### 3.3.2 Boundary Layer Definition

In general, CFD simulations of the human airway experience high velocity gradients near the wall due to the presence of viscous boundary layers in which the velocity varies from zero (at the wall) to high values in the bulk flow region. To resolve these high velocity gradients boundary layers of thin elements near the wall are used to increase the resolution of the computational cells. This ensures greater accuracy and obtains better convergence of the CFD solver. Flow field quantities such as wall-shear stresses, are computed by spatial differentiation of the near-wall velocity field, which requires the generation of boundary layers of proper thickness (Figure 3.10). This means that meshing stage begins by imposing a boundary layer at the wall surfaces. Lines are then meshed with a concentration grading so that the mesh joining the boundary layer is of similar distance. Meshing of the line topology sets the foundations for the face mesh and finally the volume

cells are meshed based on the face mesh. The distance of the first grid point to the wall in the boundary layer region should meet the following criteria (Schlichting 1979)

$$y_p \sqrt{\frac{u_\infty}{\nu \cdot x}} \leq 1 \quad (3.1)$$

Where  $y_p$  is the distance to the wall from the adjacent cell centroid,  $u_\infty$  is the free-stream velocity,  $\nu$  is the kinematic viscosity of the fluid, and  $x$  is the distance along the wall from the starting point of the boundary layer. To check this criterion, the first model created is simulated in FLUENT to obtain a tentative flow field solution. The criterion is inputted into FLUENT's "Custom Field Function" and applied to cells that lie along the wall. Because the mesh was unstructured, the cells varied in their values and an average value was taken over a nominal region. It was found that the anterior region needed to be refined the most to satisfy the criterion. From the initial model Equation 3.1 gave values around 3. This was refined and the near wall mesh was satisfied by the third refinement. Further refinement of the mesh also included that of grid independence, discussed in the next section.

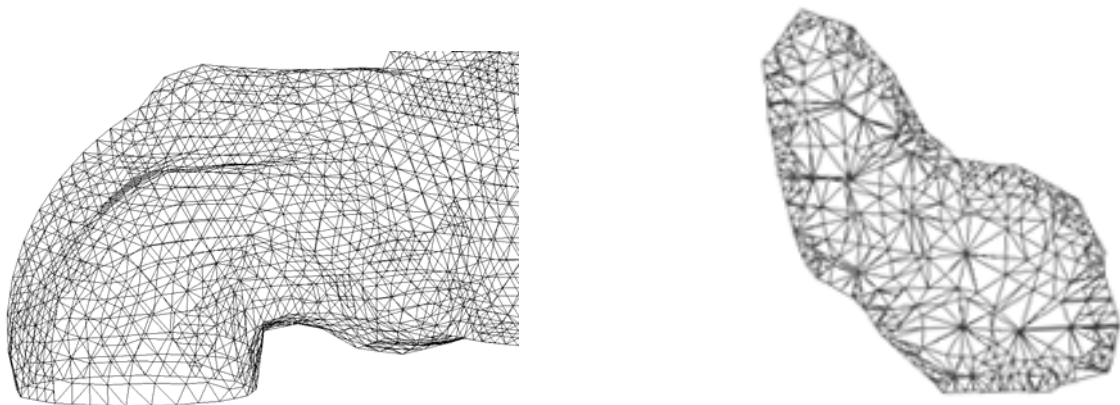


Figure 3.10 (a) Computational mesh of the anterior region (Region 1-2 – see Figure 3.9).  
(b) Coronal cross section of A-A showing the higher resolution at the wall surface.

### 3.3.3 Grid Independence

In regions of large gradients, as in shear layers or high acceleration in the nasal valve region, the grid should be fine enough to minimize the change in the flow variables from

cell to cell. However in some regions the large gradients in the flow field are not apparent without analysing the flow field. Grid adaption methods are applied to refine the mesh to increase or decrease the grid density where they are needed based on the flow field data. This leads to a mesh that has optimised and hence is grid independent for the flow field where a compromise between computational resources and accuracy has been made.

A model with 82,000 unstructured tetrahedral cells was initially used to solve the air flow field at a flow rate of 7.5L/min. The model was then improved by cell adaptation techniques that included refining large volume cells, cells that displayed high velocity gradients and near wall refinements. From each refinement a new model with a higher cell count was produced. This process was repeated twice, with each repeat producing a model with a higher cell count than the previous model. Subsequently four models were produced, 82000, 586000, 950000 and 1.44million cells. A grid independence test shown in Figure 3.11 and Figure 3.12, found the results for average velocity and the wall shear stress converge as the mesh resolution approached 950,000 cells. In order to make a compromise between the result's accuracy and computational cost, a model with 950,000 elements was used in this study.

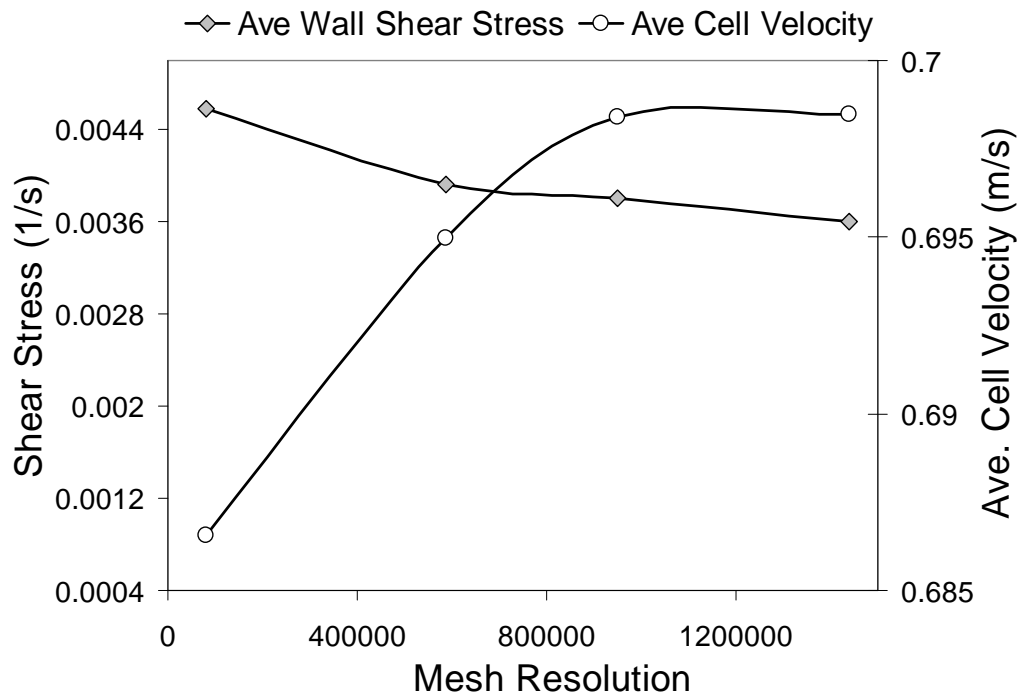


Figure 3.11 Shear stress and velocity profiles of a coronal section near the nasal valve region for the four different cavity models.



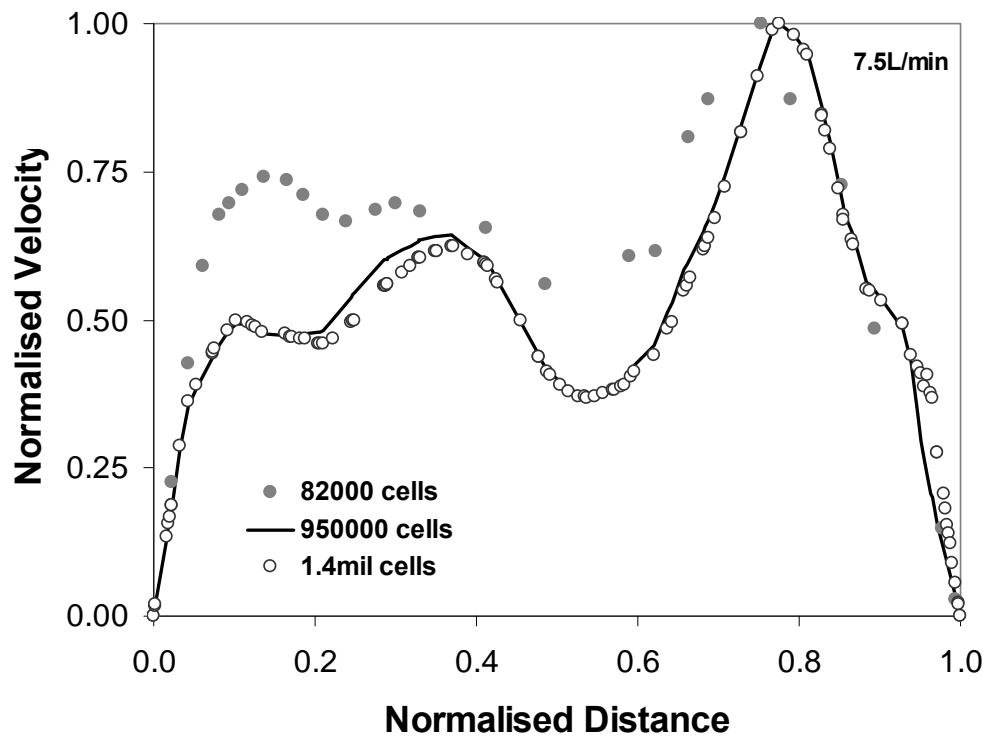


Figure 3.12 Grid independence test based on a velocity profile line taken at the posterior end of the nasal cavity. The distance and velocities are normalised by their respective maximum values of  $x_{max}=96.5\text{cm}$  and  $U_{max} = 1.36\text{m/s}$ .

# CHAPTER 4

## Numerical Simulation Methodology

### 4.1. Gas Phase Modelling

This chapter provides the mathematical equations and numerical models used for the numerical simulations. However, the details of setting the boundary conditions and the particle phase modelling method are not discussed in this chapter. Instead they are described within separate chapters that pertain to their own analysis (Chapter 5, 6 and 8) which covers the different aspects of particle modelling.

#### 4.1.1. General Governing Equations for Fluid Flow

CFD is fundamentally based on the governing equations of fluid flow and heat transfer. They are mathematical statements of the conservation laws of physics, consisting of a continuity equation, three momentum equations and an energy equation which are also called the full Navier-Stokes equation. The airflow in the respiratory system is regarded as a continuum where the effects on a molecular scale may be ignored. The behaviour of the air is then described in terms of its macroscopic fluid properties such as velocity, pressure, density, temperature and their space and time derivatives. For a general fluid property defined by  $\phi$ , the governing equations of fluid flow for an incompressible fluid, such as the airflow in the respiratory system, can be cast into the so-called transport equation form as:

$$\underbrace{\frac{\partial \phi}{\partial t}}_{\text{local acceleration}} + \underbrace{\frac{\partial(u\phi)}{\partial x} + \frac{\partial(v\phi)}{\partial y} + \frac{\partial(w\phi)}{\partial z}}_{\text{advection}} = \underbrace{\frac{\partial}{\partial x} \left[ \Gamma \frac{\partial \phi}{\partial x} \right] + \frac{\partial}{\partial y} \left[ \Gamma \frac{\partial \phi}{\partial y} \right] + \frac{\partial}{\partial z} \left[ \Gamma \frac{\partial \phi}{\partial z} \right]}_{\text{diffusion}} + \underbrace{S_\phi}_{\text{source term}} \quad (4.1)$$

where  $t$  is time,  $u$ ,  $v$  and  $w$  represents velocity components,  $\Gamma$  is the diffusion coefficient, and  $S_\phi$  which is a general source term that may represent external variables. These source terms may include pressure and non-pressure gradient terms, gravity that influence the fluid motion and heat sources or sinks within the flow domain, to name a few. Equation 4.1 represents the transport process of the fluid properties and hence is also known as the transport equations.

In words, Equation 4.1 can be read as:

$$\begin{array}{ccccccc}
 \textit{Rate of increase of} & & \textit{Net rate of flow of} & & \textit{Rate of increase} & & \textit{Rate of increase} \\
 \textit{\phi in a fluid element} & + & \textit{\phi through a fluid} & = & \textit{of \phi due to} & + & \textit{of \phi due to} \\
 & & \textit{element} & & \textit{diffusion} & & \textit{additional} \\
 & & & & & & \textit{sources} \\
 \textbf{local acceleration} & & \textbf{advection} & & \textbf{diffusion} & & \textbf{source terms}
 \end{array}$$

This equation is commonly used as the starting point for computational procedures in either the finite difference or finite volume methods. By setting the property  $\phi$  equal to 1,  $u$ ,  $v$ ,  $w$  and  $T$ , and selecting appropriate values for the diffusion coefficient  $\Gamma$  and source terms  $S$ , one can obtain the partial differential equations for the conservation of mass, momentum and energy as shown in Table 4.1.

#### 4.1.2. Reynolds Averaged Navier-Stokes Equations

For turbulent flows, a direct numerical solution (DNS) of the time-dependent Navier-Stokes equations for highly complex geometries where all scales of motion such as Kolmogorov scales, are resolved are unlikely to be attainable for some time to come because of the extreme computing requirements. Alternatively, turbulent models based on an ensemble average of the Navier-Stokes equations, which avoid the need to predict all the effects of each and every eddy in the flow are used. Osborne Reynolds first introduced the concept of Reynolds decomposition (Figure 4.1) which defines  $\phi$  as the sum of a steady mean component  $\bar{\phi}$  with a time varying fluctuating component  $\phi'(t)$  superimposed on it as:

$$\phi(t) = \bar{\phi} + \phi'(t) \quad (4.7)$$

**Table 4.1** The incompressible full Navier-Stokes equations in cartesian coordinates**Conservation of mass** ( $\phi = 1$ )

$$\frac{\partial u}{\partial x} + \frac{\partial v}{\partial y} + \frac{\partial w}{\partial z} = 0 \quad (4.2)$$

**Conservation of Momentum** ( $\phi = u, v$  or  $w$ )

$$\frac{\partial u}{\partial t} + \frac{\partial(uu)}{\partial x} + \frac{\partial(vu)}{\partial y} + \frac{\partial(wu)}{\partial z} = -\frac{1}{\rho} \frac{\partial p}{\partial x} + \frac{\partial}{\partial x} \left[ \nu \frac{\partial u}{\partial x} \right] + \frac{\partial}{\partial y} \left[ \nu \frac{\partial u}{\partial y} \right] + \frac{\partial}{\partial z} \left[ \nu \frac{\partial u}{\partial z} \right] + S_u \quad (4.3)$$

$$\frac{\partial v}{\partial t} + \frac{\partial(uv)}{\partial x} + \frac{\partial(vv)}{\partial y} + \frac{\partial(wv)}{\partial z} = -\frac{1}{\rho} \frac{\partial p}{\partial y} + \frac{\partial}{\partial x} \left[ \nu \frac{\partial v}{\partial x} \right] + \frac{\partial}{\partial y} \left[ \nu \frac{\partial v}{\partial y} \right] + \frac{\partial}{\partial z} \left[ \nu \frac{\partial v}{\partial z} \right] + S_v \quad (4.4)$$

$$\frac{\partial w}{\partial t} + \frac{\partial(uw)}{\partial x} + \frac{\partial(vw)}{\partial y} + \frac{\partial(ww)}{\partial z} = -\frac{1}{\rho} \frac{\partial p}{\partial z} + \frac{\partial}{\partial x} \left[ \nu \frac{\partial w}{\partial x} \right] + \frac{\partial}{\partial y} \left[ \nu \frac{\partial w}{\partial y} \right] + \frac{\partial}{\partial z} \left[ \nu \frac{\partial w}{\partial z} \right] + S_w \quad (4.5)$$

**Energy Equation** ( $\phi = T$ )

$$\frac{\partial T}{\partial t} + \frac{\partial(uT)}{\partial x} + \frac{\partial(vT)}{\partial y} + \frac{\partial(wT)}{\partial z} = \frac{\partial}{\partial x} \left[ \left( \frac{\nu}{\text{Pr}} \right) \frac{\partial T}{\partial x} \right] + \frac{\partial}{\partial y} \left[ \left( \frac{\nu}{\text{Pr}} \right) \frac{\partial T}{\partial y} \right] + \frac{\partial}{\partial z} \left[ \left( \frac{\nu}{\text{Pr}} \right) \frac{\partial T}{\partial z} \right] + S_T \quad (4.6)$$

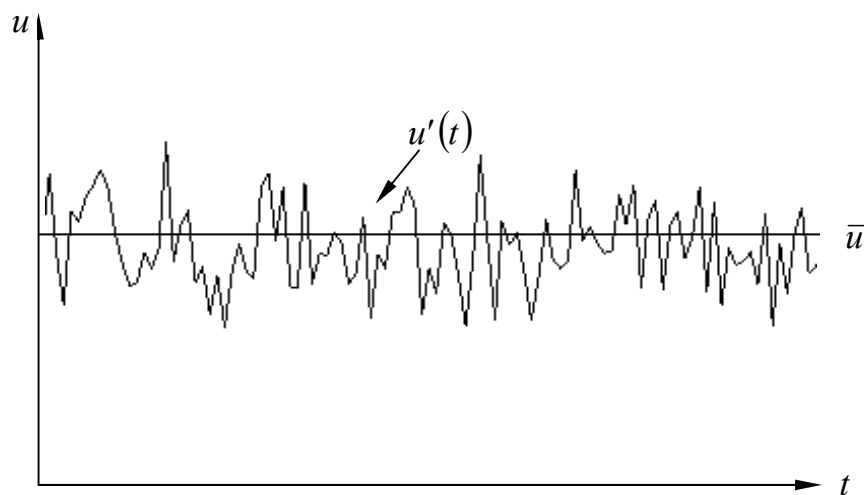


Figure 4.1 Velocity fluctuating with time at some point in a turbulent flow.

Applying equation (4.7) to the Navier-Stokes equations in Table 4.1 produces the Reynolds Averaged Navier-Stokes (RANS) equations – a detailed derivation can be found in Wilcox (1993). Turbulence models using the RANS equations are classified on the basis of the number of additional transport equations (Equation 4.1) that need to be solved. In the case of the  $k$ - $\varepsilon$  models, two additional transport equations (for the turbulence kinetic energy  $k$ , and the turbulence dissipation rate,  $\varepsilon$ ) are solved. This model is discussed later in the relevant section where the model is used (Chapter 8).

The RANS equations are provided below in tensor form for brevity:

$$\frac{\partial \bar{u}_j}{\partial x_j} = 0 \quad (4.8)$$

$$\frac{\partial (\bar{u}_i)}{\partial t} + \frac{\partial (\bar{u}_j \bar{u}_i)}{\partial x_j} = -\frac{1}{\rho} \frac{\partial \bar{p}}{\partial x_i} + \frac{\partial}{\partial x_j} \left( \nu \frac{\partial \bar{u}_i}{\partial x_j} \right) + \frac{\partial \bar{\tau}_{ij}}{\partial x_j} - \frac{\partial (\overline{u'_i u'_j})}{\partial x_j} \quad (4.9)$$

$$\frac{\partial \bar{T}}{\partial t} + \frac{\partial (\bar{u}_i \bar{T})}{\partial x_i} = \frac{\partial}{\partial x_i} \left( \frac{k}{\rho C_p} \frac{\partial \bar{T}}{\partial x_i} \right) - \left( \frac{\partial \overline{u'_i T'}}{\partial x_i} \right) \quad (4.10)$$

where  $\bar{u}_i$  and  $u'_i$  are the mean velocity and fluctuating velocity, respectively.  $\bar{\tau}_{ij}$  is the mean viscous stress tensor components:

$$\bar{\tau}_{ij} = \nu \left( \frac{\partial \bar{u}_i}{\partial x_j} + \frac{\partial \bar{u}_j}{\partial x_i} \right) \quad (4.11)$$

As a result from the Reynolds averaging, there are more unknowns than there are equations due to the presence of the Reynolds stresses,  $\overline{u'_i u'_j}$  in Equation (4.9). Turbulence models are used to predict the Reynolds stresses by applying the Boussinesq assumption first proposed in 1877, which relate the Reynolds stresses to the mean velocity gradients (Hinze 1975).

$$-\rho \overline{u'_i u'_j} = \mu_T \left( \frac{\partial u_i}{\partial x_j} + \frac{\partial u_j}{\partial x_i} \right) - \frac{2}{3} \rho k \delta_{ij} \quad (4.12)$$

One advantage of the Boussinesq assumption is the relatively low computational cost associated with the computation of the turbulent viscosity,  $\mu_T$ , although this comes with the disadvantage that  $\mu_T$  is assumed to be an isotropic scalar quantity, which in general is not valid. This fluctuating velocity components  $u'$ ,  $v'$  and  $w'$  are derived from the same quantity,

$$u' = v' = w' = \sqrt{\frac{2k}{3}} \quad (4.13)$$

The isotropic assumption is found to be sufficient for free shear flows and within the bulk flow regions. Its validity however, is undermined at near wall regions where the normal velocity component ( $v'$ ) is found to be much smaller than its counterparts (Figure 4.2).

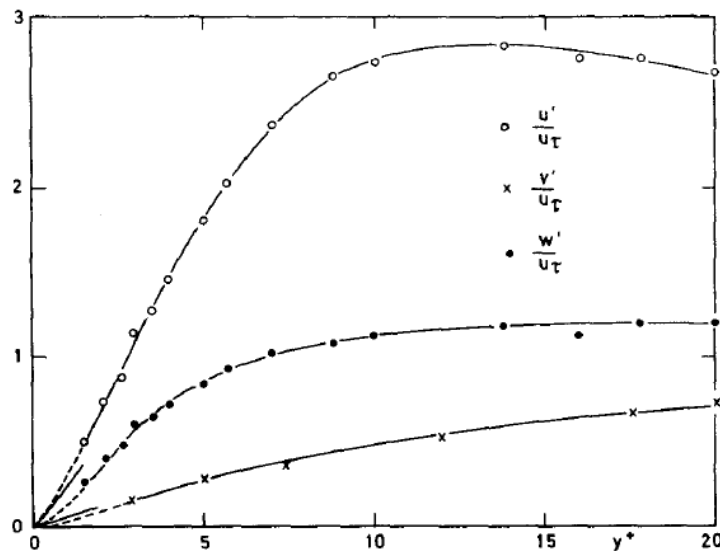


Figure 4.2 Distribution of  $u'$ ,  $v'$ ,  $w'$  normalised with the friction velocity,  $u_\tau$  in the vicinity of the wall (figure taken from Kreplin and Eckelmann (1978)).

## 4.2. Gas-Particle Phase Modelling

In general, gas-particle flows can be studied by employing either a Eulerian–Lagrangian, Eulerian–Eulerian or a single phase Eulerian particle transport model that treats the particles as a dilute chemical species in a multi-component mixture model. Only the Eulerian–Lagrangian model was used in this research.

### 4.2.1. Lagrangian Discrete Particle Tracking

The Lagrangian particle tracking method within FLUENT is used to trace the dispersion of particles about the trajectory. The scheme is most popular in engineering applications for the prediction of particle flows because it can easily be combined with a stochastic Discrete Random Walk (DRW) scheme, albeit with high computational costs (Tu 2000). For a low volume fraction of dispersed phase (particles), as found in the case of particle suspension in nasal inhalation, the Lagrangian approach with one-way coupling is used, i.e. the airflow transports the particles, but the effect of particles movements on the flow was neglected. In this approach, the airflow field is first simulated, and then the trajectories of individual particles are evaluated using particle equation of motion. The equation of motion involves a force balance of the particle inertia and the forces acting on the particles, which is written as,

$$\frac{du_i^p}{dt} = F_{D,i} + F_{g,i} + F_{s,i} \quad (4.14)$$

where  $F_g$  is the gravity term, which is defined as

$$F_{g,i} = \frac{g(\rho_p - \rho_g)}{\rho_p} \quad (4.15)$$

and  $\rho_p$  and  $\rho_g$  denotes the density of particle material and air, respectively.  $F_D$  is the drag force per unit particle mass, and  $F_i$  is an additional force (force/unit particle mass) term that is added accordingly. These forces are discussed in the relevant chapters pertaining to the morphology of the particles (Chapter 6). In addition the turbulent dispersion of particles in the Lagrangian reference frame is also discussed in the relevant chapters (Section 8.2.2).

### 4.2.2. Turbulent Particle Dispersion

The CFD code, FLUENT, handles the turbulent dispersion of particles by integrating the trajectory equations for individual particles, using the instantaneous fluid velocity  $u_i^g + u_i'(t)$ , along the particle path during the integration process. The fluctuations from the turbulence are accounted for within the so-called ‘Discrete Random Walk’ model (DRW) (Macinnes and Bracco 1992). This method is also called the Eddy Interaction Model (EIM)

(Figure 4.3). Within this model the fluctuating velocity components  $u_i'$  that prevail during the lifetime of the turbulent eddy are sampled by assuming that they obey a Gaussian probability distribution, so that

$$u_i' = \zeta \sqrt{u_i'^2} \quad (4.16)$$

where  $\zeta$  is a normally distributed random number and the remaining right-hand side is the local root mean square (RMS) velocity fluctuation can be obtained (assuming isotropy) by:

$$\sqrt{u_i'^2} = \sqrt{2k_g/3} \quad (4.17)$$

The interaction time between the particles and eddies is smaller of the eddy lifetime  $\tau_e$  and the particle eddy crossing time  $\tau_{cross}$ . The characteristic lifetime of the eddy is defined as:

$$\tau_e = -T_L \log(r) \quad (4.18)$$

where  $T_L$  is the fluid Lagrangian integral time,  $T_L \approx 0.15k_g / \varepsilon_g$ .

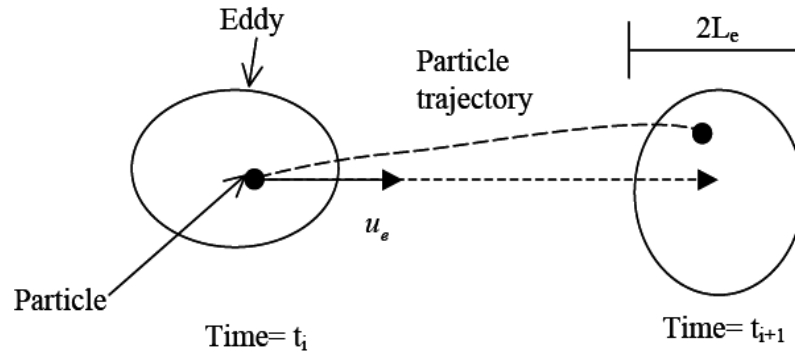


Figure 4.3 Discrete Random Walk Model

The variable  $r$  is a uniform random number between 0 and 1. The particle eddy crossing time is given by:

$$t_{cross} = -t_p \ln \left[ 1 - \left( \frac{L_e}{t_p |u_i^g - u_i^p|} \right) \right] \quad (4.19)$$



where  $t_p$  is the particle relaxation time ( $\rho_p d_p^2 / 18 \rho_p \nu_g$ ),  $L_e$  is the eddy length scale and  $|u_i^g - u_i^p|$  is the magnitude of the relative velocity. The particle interacts with the fluid eddy over the interaction time. When the eddy lifetime is reached, a new value of the instantaneous velocity is obtained by applying a new value of  $\zeta$  in Equation 4.16.

However there are known problems with the DRW method as it is often coupled with a RANS turbulence model. In this situation the isotropic assumption becomes important as the flow in a nasal cavity is a wall bounded type flow. The isotropic assumption (i.e.  $u' = v' = w'$ ) leads to an overestimation of the normal fluctuating velocity component (see Figure 4.2) in the near wall region. This causes an overestimation of deposition for the smaller range of particles ( $\ll 10\mu\text{m}$ ) (Macinnes and Bracco 1992; Wang and James 1999; Zhang et al. 2004). This overestimation at the near wall region increases in sensitivity for smaller particles that have a shorter relaxation time. The effect is compounded by the geometry, which is similar to that of very narrow duct flows where the effects of the walls are emphasized. An improved model for the random walk method is proposed by Wang and James (1999). However, limitations in accessing and making the necessary modifications to the commercial code FLUENT restricts the evaluation of this method. As Tu et al. (2004) mentions, there is an urgent need for a more manageable, user-friendly, defined function model in FLUENT in order to incorporate and assess other phenomenological models such as that proposed by Wang and James (1999). A work around method is provided as an alternative in Section 8.3.1

### 4.3 Numerical Solver Procedure

The equations given in Table 4.1 are converted into their corresponding integral form which is a requirement for control volume based CFD solvers such as FLUENT. The domain is then discretised into control volumes based on the designed mesh from Chapter 3. The governing equations given in Table 1 are rearranged into an integral form to allow integration of the equations on each individual control volume cell within the mesh. A set of algebraic equations for dependent variables such as velocities, pressure and temperature are then set up and solved. The segregated solver within FLUENT was chosen which solved the governing equations sequentially (i.e., segregated from one another). The flow chart of the procedure is shown in Figure 4.4.

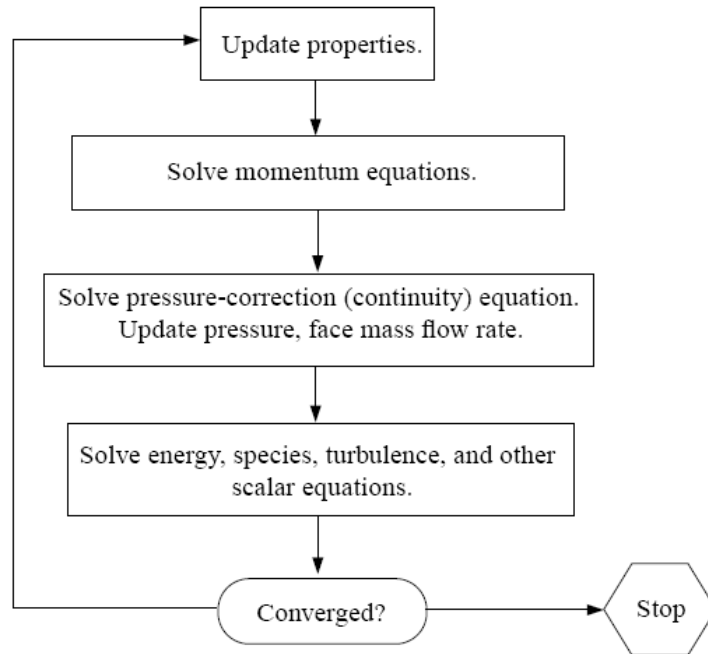


Figure 4.4 Overview of the segregated solver solution steps

The third order accurate QUICK scheme, based on a weighted average of second-order-upwind and central interpolations of the variable (Leonard and Mokhtari 1990) was used to approximate the momentum equation while the SIMPLE algorithm (Vandormaal and Raithby 1984) was used to obtain the relationship between velocity and pressure corrections to enforce mass conservation and also to obtain the pressure.

# CHAPTER 5

## Modelling Inhalation and Heat Transfer in the Nasal Cavity

### 5.1. Introduction

Individual aspects of the nasal cavity such as the geometry and flow rate collectively affect nasal function such as the filtration of foreign particles by bringing inspired air into contact with mucous-coated walls, humidifying and warming the air before it enters the lungs and the sense of smell. To better understand the physiology of the nose, modelling the inhalation of airflow by CFD methods can provide details of flow patterns between the left and right nasal cavities. Because of the inter-subject variations inherent between nasal cavity geometries, the numerical results herein can be compared with experimental data available in literature to complement the current knowledge base. In this chapter CFD simulations were performed using a steady laminar flow for flow rates of 7.5L/min and 15L/min. General agreement of gross flow features were found that included high velocities in the constrictive nasal valve region, high flows near the septum walls, and vortex formations posterior to the nasal valve and olfactory regions. The differences in the left and right cavities were explored and the effects it had on the flow field were discussed especially in the nasal valve and middle turbinate regions. Geometrical differences were also compared with models that have been studied in the literature. The variations in flow patterns and flow features such as pressure drop, wall shear stress, velocity, and flow distribution between the left and right cavity as well as different geometries are also

presented. The flow in the nasal valve and turbinate region was studied in particular detail, since the airflow profiles in these regions have not been well investigated.

Furthermore, the air conditioning capability of the nose in terms of its heat transfer was simulated for a flow rate of 15 L/min. A major physiological function of the human nasal cavity is to condition the inhaled air to body core temperature with full saturation to prevent damage to the alveolar epithelium in the lungs. The air conditioning capability of the nose is dependent on the nasal mucosal temperature and the airflow dynamics caused by the airway geometry. Morphological variation of the human nose has been attributed to the eco-geographic adaptation to climate. This interesting phenomenon provides the suggestion that the airway geometry is a major influence on the heat transfer capability of the nose (see Section 2.2).

Past experimental studies that have been performed in order to achieve a relationship between nasal morphological features and the flow regime, have produced mixed results. For example Proetz (1951) and the work by Courtiss and Goldwyn (1983) state that the role of the turbinates is to induce turbulence, while Scherer et al. (1989) and Elad et al. (1993) state that the turbinates laminate the flow by introducing streamlines. In a separate study, Naftali et al. (1998) found that the turbinates increase the rate of local heat and moisture transport by narrowing the passageways for air and by induction of laminar swirls downstream of the turbinate wall. It is suggested that during breathing via the human nose provides ample time for heat and water exchange to near alveolar conditions under normal and extreme conditions.

The work by Churchill et al. (2004) was the first to consider multiple morphological parameters (naris angle, nasal sill height, nasal valve, inferior turbinate and middle turbinate) and its effects on the induction of turbulence at different flow rates. It was found that the projection of the inferior turbinates was the only significant parameter and that a greater projection of the inferior turbinate bone laminated the flow by simply decreasing the cross-sectional area of the passageway while larger passageways, with a greater hydraulic diameter, would experience more turbulent flow.

Without considering humidity and water exchange, Lindemann et al. (2004) numerically simulated the temperature distribution during inspiration in an anatomically realistic nasal

cavity. Their simulations used a constant inspiratory flow rate of 2.6 m/s (25 L/min) with a constant mucosal wall temperature of 34°C throughout and found that the inspired air (20°C) was heated to 33.9°C at the nasopharynx. Compared with in-vivo measurements, the numerical simulation by Lindemann et al. (2004) successfully visualized the close relationship between the intranasal air temperature and airflow pattern. Similarly Naftali et al. (2005) and Wolf et al. (2004) simulated an unsteady laminar flow using a constant mass diffusivity for the transport of airflow through an idealised cavity model. A periodic inlet of air (25°C, air flux = 7.5 L/min) was heated by a constant mucosal wall temperature of 37°C. It was found that the simulation produced a higher temperature profile compared with their in-vivo experiments. This may be attributed to the higher constant mucosal wall temperature used, since it was found by Lienar et al. (2003) that the end-expiratory nasal mucosal wall temperature varied between 32.3°C to 34.7°C after exposure to 25°C inspired air.

## 5.2. Physiology of Airflow Rates in the Nasal Cavity

In the following descriptions, the +X coordinate axis is from the anterior tip of the nostril inlet to the nasopharynx which is referred to as the axial direction. The nose can be divided axially into four regions: the vestibule, the nasal valve, the turbinate and the nasopharynx regions. The first three-quarters of the nasal cavity are divided into the left and right cavity separated by the nasal septum wall. Air enters each cavity through the oval shaped external nostrils into the vestibule. The flow changes direction, 90° towards the horizontal, before entering the nasal valve region (Figure 5.1). The flow increases in this region where the cross-sectional area is smallest causing an acceleration of the air. At the end of the nasal valve region the cross-sectional area of the nasal cavity increases suddenly. This expansion is the beginning of the turbinate region where the profile is complicated and asymmetrical. Finally, at the nasopharyngeal region, the left and right cavities merge together causing the flow in this region to mix intensely.

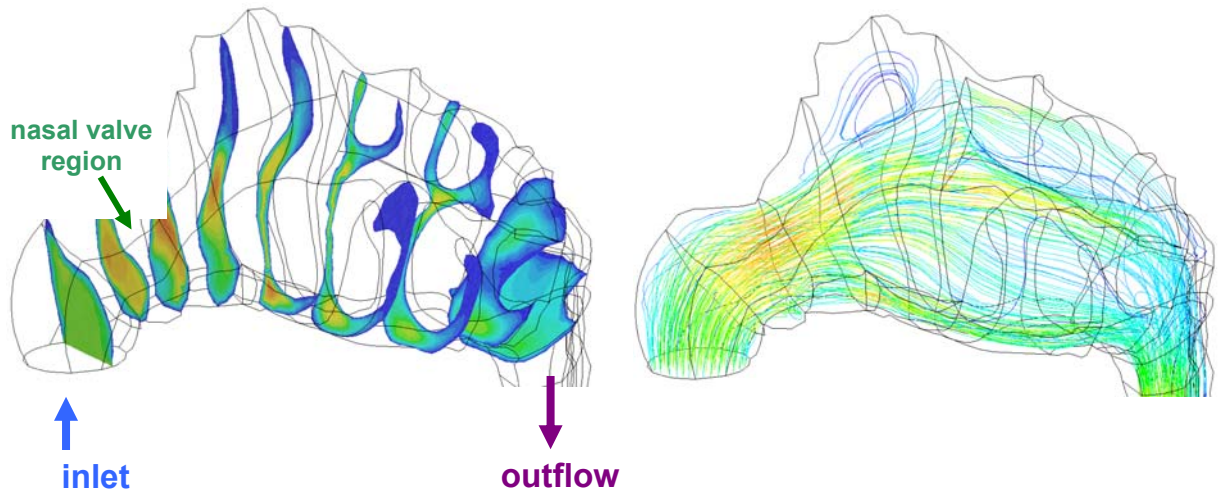


Figure 5.1 Airflow field through the nasal cavity

The main factors that contribute to the airflow patterns are the nasal cavity geometry and the flow rate. For a realistic human nasal cavity, the left and right sides of the nasal cavity differ geometrically while nasal morphological differences can be found between individuals. The inspiratory flow rates for adults can range between 5-12 L/min for light breathing and 12-40L/min for non-normal conditions such as during exertion and physical exercise. Usually breathing switches from pure nasal flow to oral-nasal flow at this higher range. Additionally flow rates for extreme forced inhalation conditions have been found to reach 150L/min (Robert 2001).

### 5.3. Numerical Procedure

Flow rates of 7.5L/min and 15L/min. were used to simulate light adult breathing while the heat transfer simulation was performed under 15 L/min only. At these flow rates, the flow regime has been determined to be laminar (see Section 2.2). A steady flow rather than a cyclic unsteady flow was used in this case to allow the results to emphasize the airflow dynamics and patterns independent from cyclic conditions. Moreover the significance of the fluctuating sinusoidal pattern of the inhalation-exhalation breathing cycle on the nasal airflow can be estimated by examining the Womersley number,  $\alpha$  and the Strouhal number,  $S$ . The calculated Womersley number,

$$\alpha = \frac{D}{2} \left( \frac{\omega}{\nu_g} \right)^{0.5} \quad (5.1)$$

was 1.68 while the Strouhal number,

$$S = \frac{\omega D}{u_{ave}} \quad (5.2)$$

was 0.01.  $D$  is equal to 0.01m and is the characteristic length which was taken as the average hydraulic diameter of thirty cross-sections taken throughout the nasal cavity.  $\nu_g$  is the kinematic viscosity of air and  $\omega$  is the breathing frequency equal to  $\omega = 2\pi f = 1.57s^{-1}$  and  $u_{ave}$  is the average velocity through the nasal passage under the flow rate of 15 L/min which is equal to 0.9m/s. Although the Womersley number is greater than 1, it is not much greater, while the low value for  $S$  suggests that the flow may be assumed to be quasi-steady. It has however, been shown experimentally that the oscillatory effects are not present until  $\alpha \Rightarrow 4$  (Isabey and Chang 1981). Additionally other studies have also concluded that under most conditions especially low flow rates, the nasal airflow can be considered quasi-steady (Chang 1989; Hahn et al. 1993; Sullivan and Chang 1991).

In addition to the continuity, momentum, and energy equations from Equations 4.1-4.6, additional equations were considered. The mass transfer equation for water vapour can be written as:

$$\frac{\partial(\rho Y u_i)}{\partial x_i} = - \frac{\partial J_i}{\partial x_i} \quad (5.3)$$

where  $Y$  is the vapor mass fraction and  $J$  is the vapor diffusion flux which arises due to concentration gradients. For a laminar flow:

$$J_i = -\rho D \frac{\partial Y}{\partial x_i} \quad (5.4)$$

where  $D$  is the diffusivity which varies with temperature and is expressed by the semi-empirical correlation from Vargaftik (1975):

$$D = 2.16e^{-5} (T / 273.15)^{1.8} \quad (5.5)$$

which is implemented into FLUENT through the user-defined functions.

## 5.4 Boundary Conditions

For the boundary conditions, a no slip flow velocity on the passage surfaces was assumed. At the nostril, a uniform flow perpendicular to the inlet was specified which is a reasonable approximation. Keyhani et al. (1995) specified the velocity profile at the nostril based on experimental data which showed that for a given flow rate the downstream flow field is not significantly affected by the details of the velocity profile at the nostril. Additionally the flow rates of left and right nostrils are assumed to be the same. This does not simulate real breathing perfectly since the flow is induced at the larynx drawing the air from the nostrils which is affected by geometrical differences leading to varied flow rates between the cavities. However for this research, the focus was to present the ability of CFD to capture the micro fluid structures that exist in flow patterns within the left and right cavities under a steady state solution whilst being able to compare these results against available experimental data that are based on a fixed flow rate through each cavity (Keyhani et al. 1995; Subramaniam et al. 1998). Therefore it was important to maintain similar settings and to keep the flow rates the same between the two cavities.

The critical flow rate at which the flow changes from a laminar to a turbulent flow regime is difficult to succinctly define due to the complexity of the airway which has led to some debate concerning the type of airflow regime to implement for numerical simulations. Experimental studies by Swift and Proctor (1977) and Kelly et al. (2000) have suggested that a laminar flow regime dominates for low flow rates around 10 L/min. While Hahn et al. (1993)'s results also concur, it is mentioned that the flow is a disturbed laminar regime. The work by Churchill et al. (2004) also showed that even at the lowest flow rates, 1.5 L/min, small local turbulent characteristics were present. However it is pointed out that some of the turbulence observed reflects local flow regimes that have little effect on the bulk flow through the nose. For the ten nasal replicates compared, the average rate at which flow switched from transitional to turbulent was 11 L/min. Despite this a survey of more recent numerical simulations of realistic nasal airways show a consensus among researchers in using a laminar flow for flow rates less than 20 L/min (Croce et al. 2006; Garcia et al. 2007; Naftali et al. 2005; Schroeter et al. 2006). In this study a flow rate of 7.5 L/min was used with a prescribed laminar flow regime.



Two climatic conditions were used for the inspired ambient air; normal air conditions (25°C, 35% relative humidity) that match with experimental data (Keck et al. 2000a) and a cold dry condition, (12°C, 13% relative humidity). The inner mucosal walls which are covered by a wet mucus layer are assumed to be fully saturated with water vapour and have an unlimited supply of heat and water. Lienar et al. (2003) were able to measure local nasal mucosal wall temperatures after exposure to air at different climatic conditions, which ranged from 32.3°C – 34.7°C for normal air conditions and 30.6°C – 33.7°C for cold dry air. Therefore a value of 33.5°C and a value of 32.1°C were applied for the normal air and the cold dry air case respectively.

## 5.5. Results

### 5.5.1 Geometry Comparisons

Fourteen cross-sections evenly spaced apart in the  $x$ -direction (Figure 5.2) were created and used to calculate the averaged flow properties. The cross-sectional areas versus distance from the anterior tip of the nose of the left and right cavities were compared (Figure 5.3). In the anterior region of the nasal cavity ( $x < 26$  mm) and the posterior turbinate region ( $x > 44$  mm), the cross-sectional area of the right cavity is larger than that of the left, while in the middle region the right side is smaller than the left.

The present computational model was also compared with other nasal cavities where existing data were available (Figure 5.3). Although inter-subject variations in nasal cavity geometries exist, a general trend can be observed on a macro level. For example a local minimum is found for all profiles just after the inlet where the nasal valve region exists.

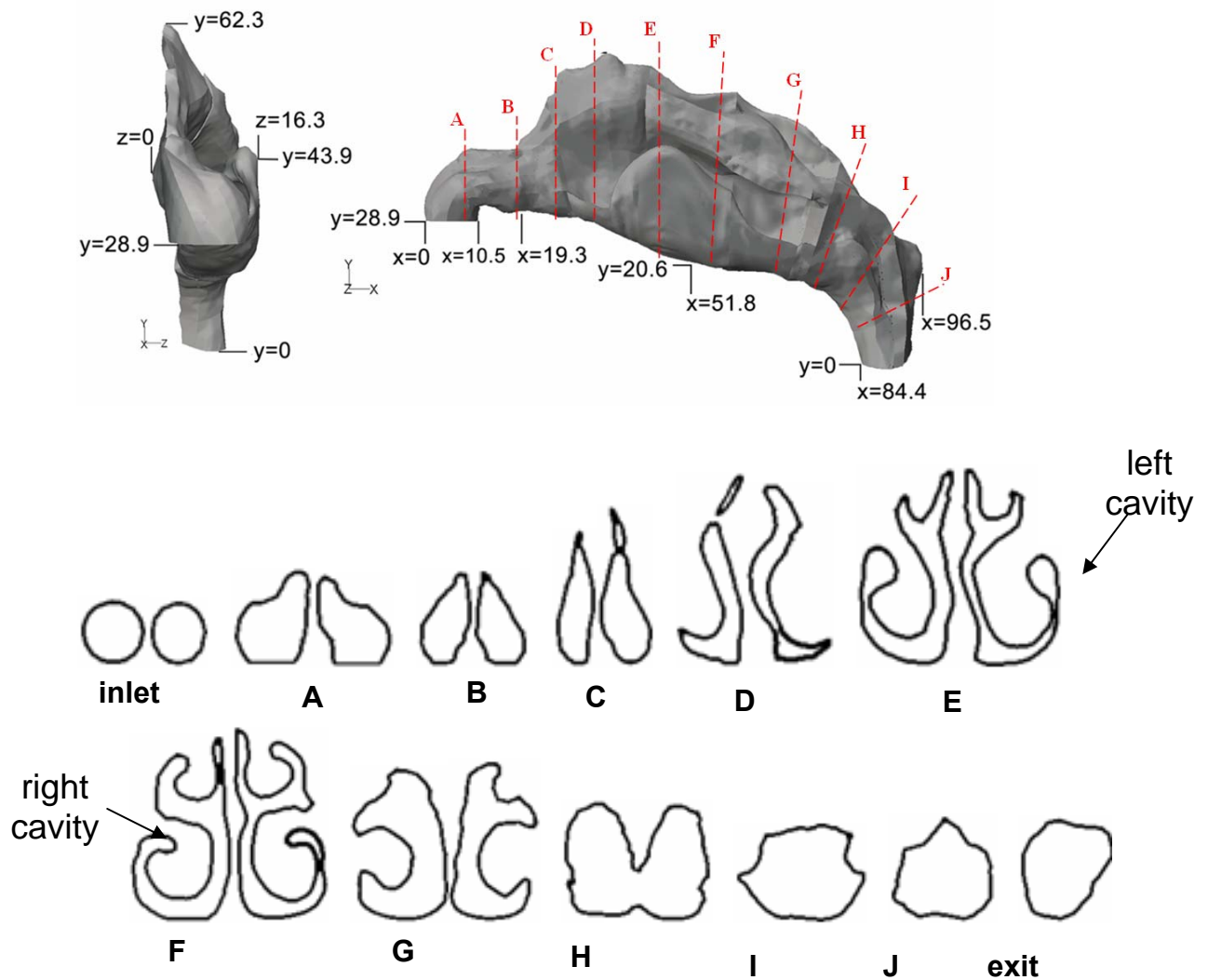


Figure 5.2 2D cross-sections of a nasal cavity of an adult male subject

The nasal valve is the narrowest region where the cross-sectional area was found to be  $1.4\text{cm}^2$  which compares with  $1.6\text{cm}^2$ ,  $1.9\text{cm}^2$  and  $2.0\text{cm}^2$  for Subramanian et al. (1998), Cheng et al. (1996) and Keyhani et al. (1995)'s models respectively. At the anterior turbinate region the airway expands to accommodate the olfactory sensors and the turbinate bone projections. This is reflected by an increase in the cross-sectional profiles which is observed immediately after the nasal valve region. For the current geometry, the nasal valve region is located about 2.0cm from the anterior tip of nose, which compares with the other models that are all located around 3.0cm away from the anterior tip of nose (Figure 5.3).

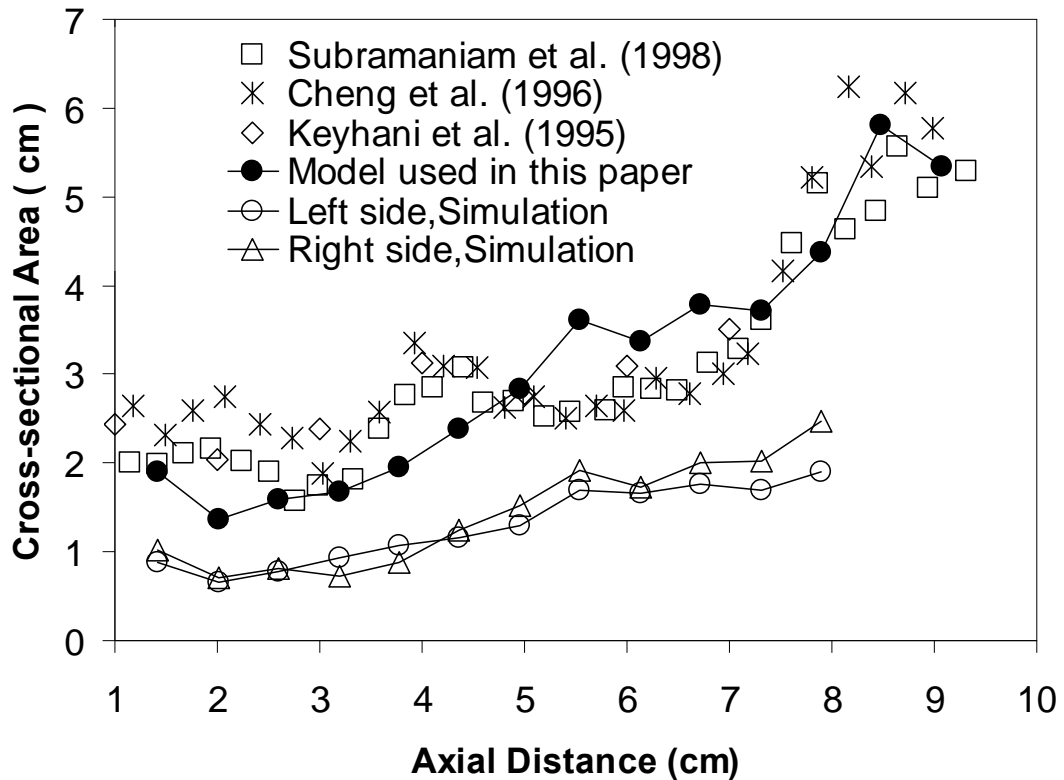


Figure 5.3 The comparison of cross-sectional areas versus distance from anterior tip of nose for different geometries: (a) the cross-sectional area of the left and right side of the nose used in this paper, (b) the total cross-sectional area of both sides for different geometries.

### 5.5.2 Resistance and Wall Shear Stress

Nasal resistance is an important factor in considering airway resistance. In adults, nasal resistance can contribute up to half of the total airway resistance (Bailey 1998). As shown in Figure 5.4, the static pressure profile decreases as the distance from the anterior nose increases. Less resistance is found for the left side where the pressure decrease is not as great as found in the right side. The influence of geometrical variations was found to produce dramatic increases in the resistance when the cross-section was reduced. In the frontal regions where  $x$  is less than 2.66mm, the majority of the nasal resistance to airflow is produced. The average wall shear stress for each subdivided zone (see Figure 3.9) was calculated by summing the local shear stress at each surface and dividing by the total number of surfaces within each zone.

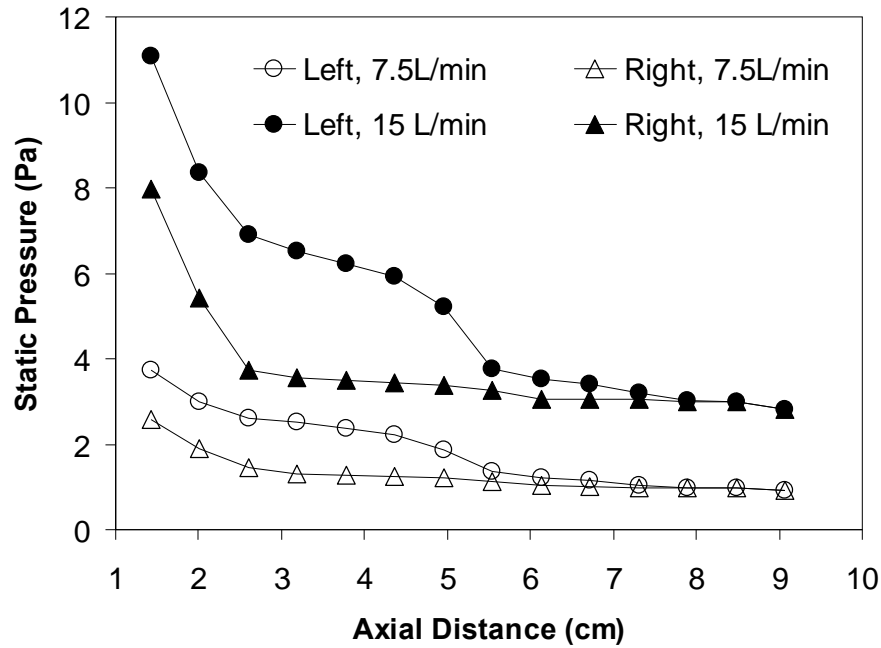


Figure 5.4 Area averaged static pressure on different coronal cross-sections versus distance from anterior tip of nose, (a) at a flow rate of 7.5 L/min (b) at a flow rate of 15 L/min.

For a Newtonian fluid, the average wall shear stress induced by the flowing air on the gas-wall interface is given by,

$$\tau_{ave} = \frac{\sum_{i=1}^a \left( \mu \frac{\partial U}{\partial n} \right)}{a} \quad (5.6)$$

where  $\mu$  is the gas viscosity,  $a$  is the number of cells along a wall and  $n$  is the unit vector normal to the cavity surface. The general trend for the wall shear stress at different rates is similar (Figure 5.5).

The highest wall shear stresses are found in Zone2 where the nasal valve exists. Additionally the flow in this region has changed direction from vertically aligned to a horizontal direction (Figure 3.9) which causes the high stresses. The wall shear stress decreases gradually corresponding to the airway expansion in the middle region where the velocity decreases. Minimum values are found in Zone8 before increasing again. The increase is caused by the two cavities merging and a change in the flow direction at the nasopharynx where the air travels downwards towards the lungs.

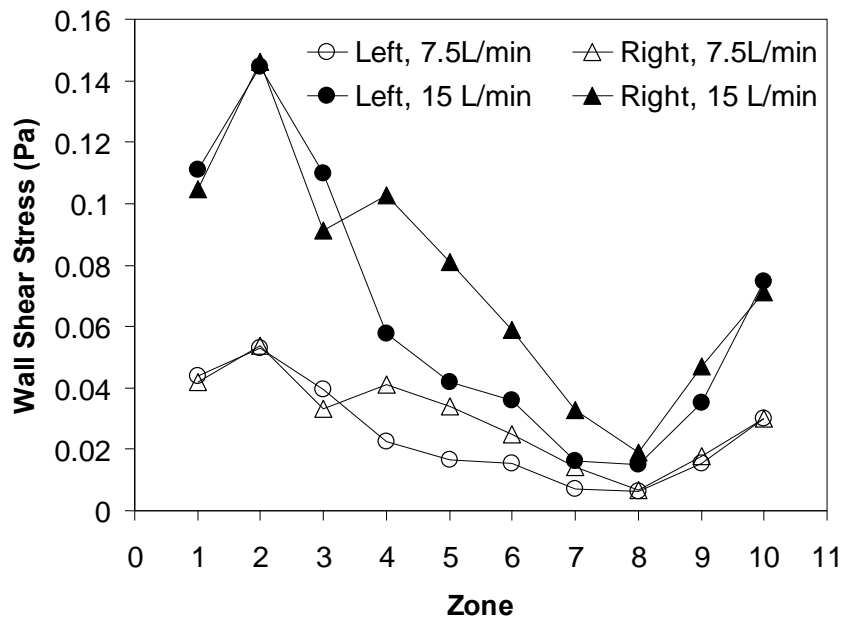


Figure 5.5 Area averaged wall shear stress on different zones surface, at flow rates of 7.5L/min and 15L/min.

### 5.5.3 Path Streamlines

Path streamlines were released from the nostril inlet to provide qualitative visualisation of the flow field. The streamlines in the left nasal cavity at a flow rate of 7.5L/min show flow separation and reversed flow just posterior to the narrowest valve (Figure 5.6a). A vortex in the upper anterior part of the cavity was prominently formed. This vortex is a result of the adverse pressure gradient caused by the abrupt increase in the cross-sectional area from the nasal valve to the main nasal passage. A similar trend was found in the experimental work of Weinhold and Mlynski (2004) and Kelly (2000). As the flow rate increases to 15L/min (Figure 5.6c), the vortex moved posteriorly to the middle region of turbinate and was smaller. The streamlines in the right cavity at a flow rate of 7.5L/min (Figure 5.5b), showed no recirculation and most of the streamlines are concentrated in the middle and lower regions of the nasal cavity. At a flow rate of 15L/min (Figure 5.6d), two vortices are found. The bigger vortex is just posterior to the nasal valve while the smaller vortex is found in the posterior turbinate region. Both vortices are found in the upper region of the nasal cavity.

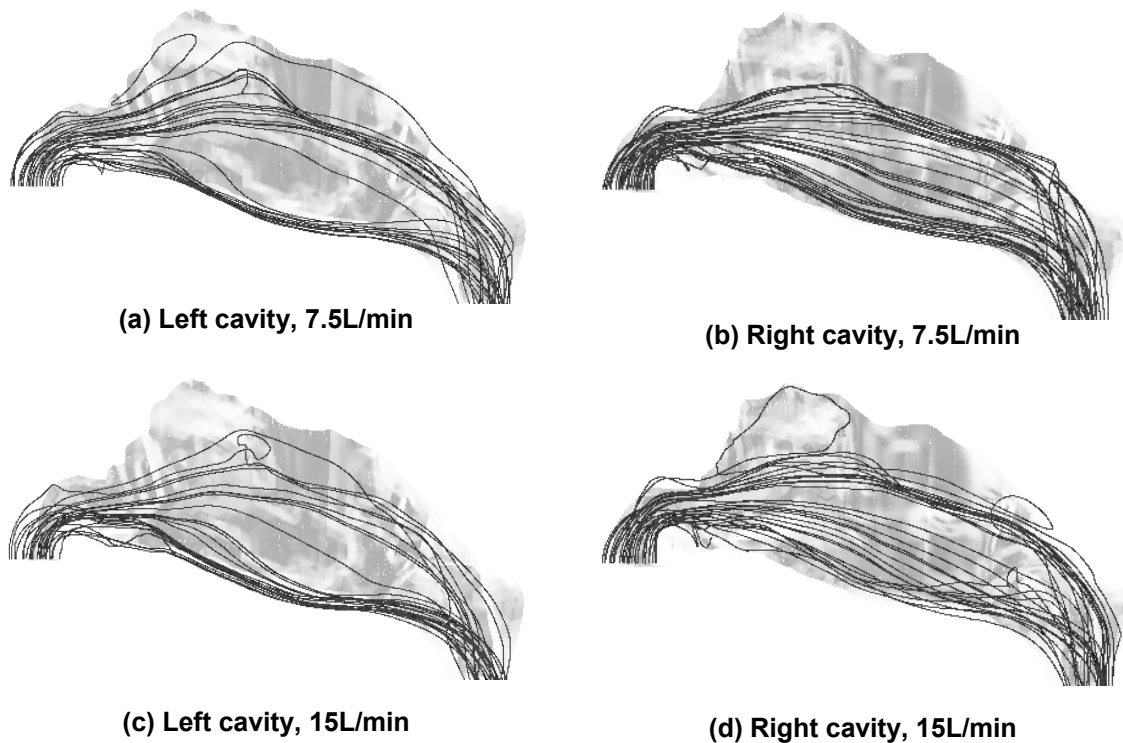
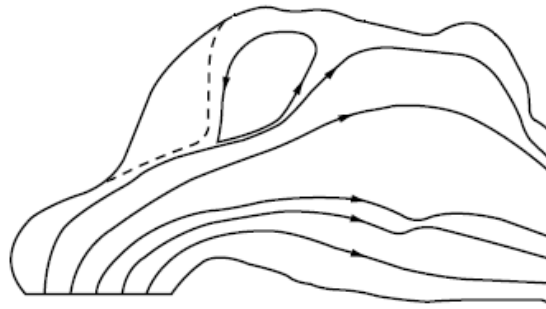


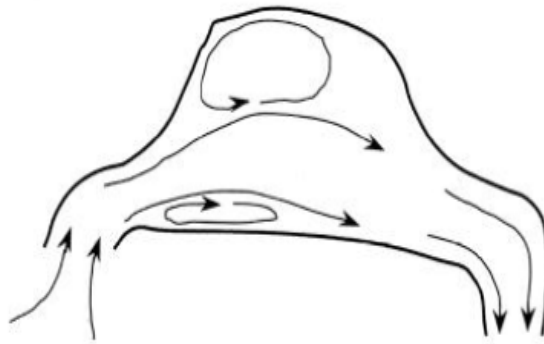
Figure 5.6 Representation of flow streamlines in current nasal cavity. A comparison of streamlines produced in the literature shows similar trends Figure 5.7.

The simulated results were then compared with data available from the literature (Figure 5.7). Keyhani et al. (1997) found a recirculating zone downstream of the airway. The vortex extends up to the anterior end of the middle turbinate but does not reach the olfactory slit. The larger vortex is found in the upper region while a smaller vortex is found near the floor of the airway.

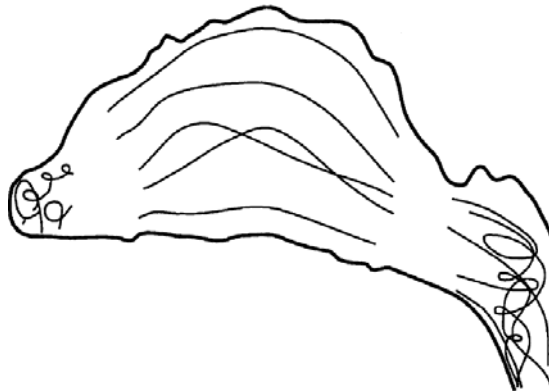
This smaller vortex occurs directly after the nasal valve region where a favourable pressure gradient promotes flow separation. These disturbances are also found in the current simulation where the streamlines are erratic but do not reach the same magnitudes as the vortex found by Schreck et al. (1993). The simulations by Subramaniam et al. (1998) is most different where prominent recirculating streams are found in the vestibule and complex spiralling flow patterns are found in the nasopharynx. There is no obvious recirculation zone inside this nasal cavity.



(a) Keyhani et al. (1997)



(b) Schreck et al. (1993)



(c) Subramaniam et al. (1998)

Figure 5.7 Representation of flow streamlines in other nasal cavities.

#### 5.5.4 Airflow Analysis

The effects of the airflow due to the asymmetry of the left and right side of the cavity is shown in Figure 5.8 which combines contours of the axial velocity ( $x$ -component of velocity) with streamlines of secondary flow ( $y$ - $z$  component of velocity). The red contours suggest the bulk flow region since the direction of flow is in the  $x$ -axis.

Conversely the blue contours show low flow in the  $x$ -axis. At the beginning of the flow at  $A$ , air flows upwards depicted by the streamlines pointing in the positive  $y$  direction. No cross flow in the  $z$ -direction is found. The flow accelerates at  $B$  as the airway decreases in area where the nasal valve begins to form. At this cross-section, the flow has changed directions about  $90^\circ$  from the inlet and coupled with the narrowed region, cross flows in the  $y$  and  $z$  directions are more prevalent especially in the left side. Additionally the bulk flow begins to split into two directions with the majority flowing upwards and a smaller proportion flowing downwards.

The geometry continues to become thinner and this accelerates the bulk flow through the middle of  $C$ . The flow away from the centre of the airway is moving away from the septum walls and splitting upwards and downwards coinciding with the vertically expanding geometry. This flow feature continues through section  $D$  as the meatus forms. At the turbinate region  $E, F, G$  the main axial flow remains close to the septum walls and little flow reaches the outer meatus region. As the geometry begins to curve downwards, the flow streamlines reflect this by pointing in the negative  $y$ -direction.

Comparisons of the Reynolds number showed that both cavities exhibit similar values, except in the front regions of the airway especially at section  $C$  (Figure 5.9). The left cavity has a higher Re number ( $Re = 496$ ) compared with the right cavity ( $Re = 355$ ). This difference is due to the greater velocity found in the left cavity (Table 5.1). Although the hydraulic diameters are similar, the cross-sectional area of the right-side is greater than the left-side. This suggests that the left-side has a narrower cross-section compared to the right-side which causes the airflow to accelerate and increases the Reynolds number. In the turbinate regions at sections  $E$ ,  $F$ , and  $G$ , there are some differences in the airway geometry as well as the flow velocity. The right side experiences a greater velocity due to a narrow cross-section which produces a higher Reynolds number.



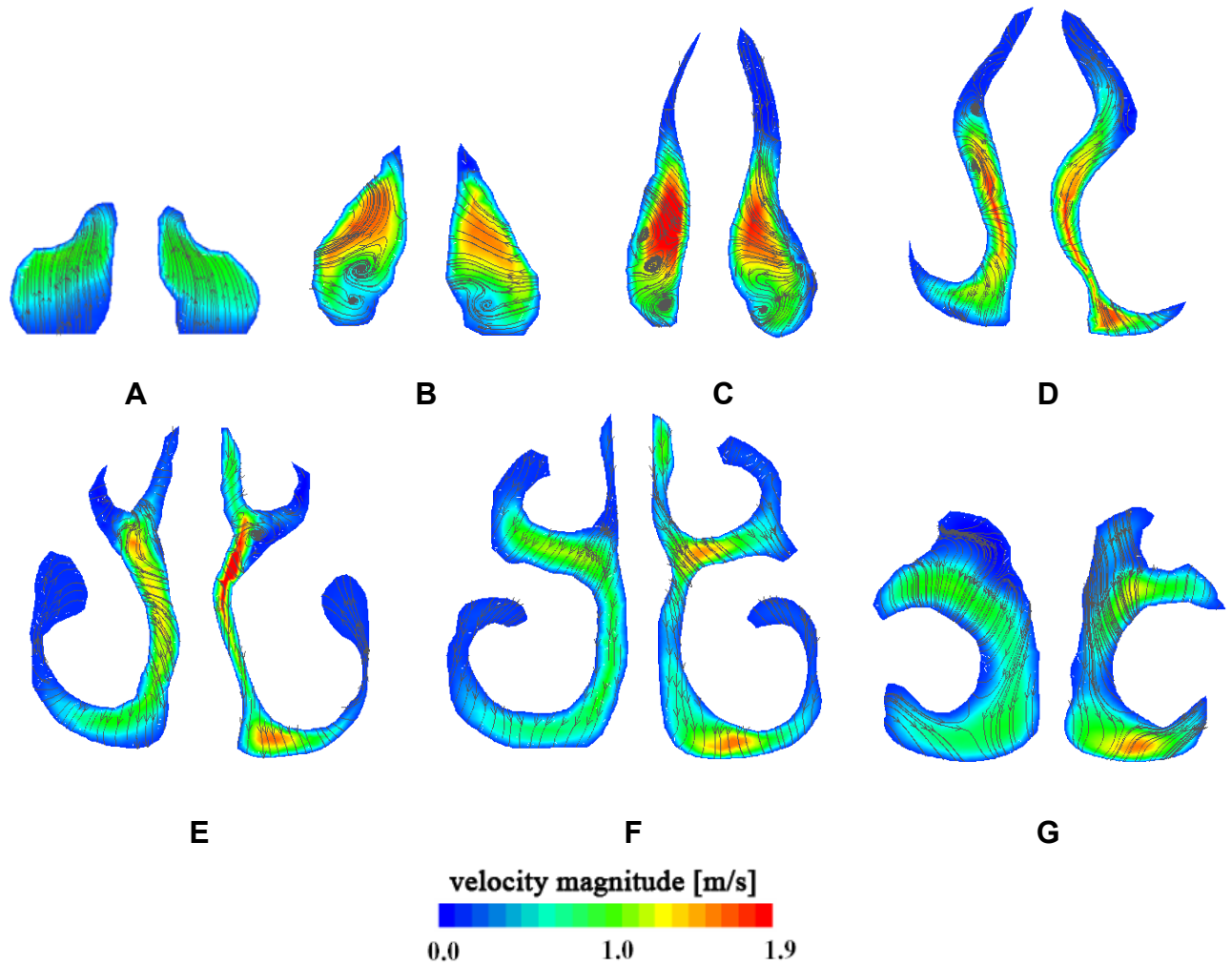


Figure 5.8 Contours of axial velocity ( $x$ -direction) and streamlines of cross-flow ( $y$ - $z$  direction). Red contours represent maximum values while blue represent minimums.

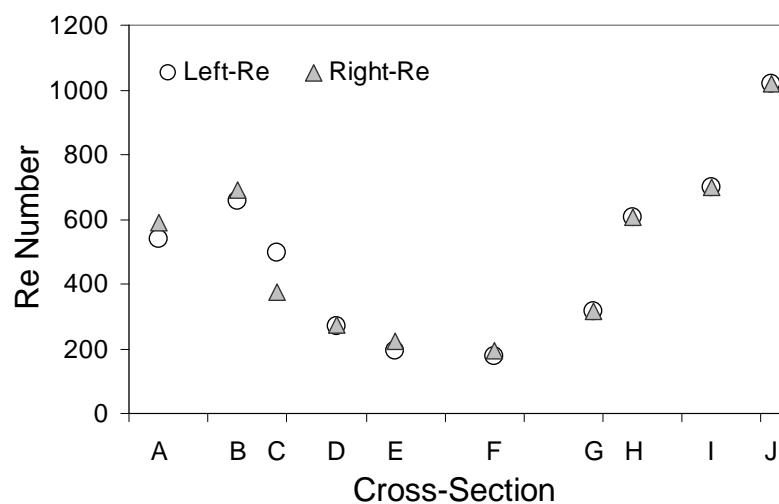


Figure 5.9 Reynolds number recorded at the cross-sections depicted in figure 2. The cross-sections have been scaled to reflect their relative distances from each other across the nasal cavity. The axial distance is 0-90mm.

**Table 5.1** Velocity magnitude and geometrical details of the cross-sections depicted in Figure 5.8.

<b>LEFT</b>	<b>Area (mm<sup>2</sup>)</b>	<b>Hyd Diam. (mm)</b>	<b>Velocity</b>
A	67	7.6	1.06
B	65	7.7	1.29
C	93	7.0	1.13
D	140	5.2	0.79
E	180	5.5	0.53
F	216	5.9	0.46
G	248	11.0	0.43

<b>RIGHT</b>	<b>Area (mm<sup>2</sup>)</b>	<b>Hyd Diam. (mm)</b>	<b>Velocity</b>
A	76	8.3	1.09
B	74	8.4	1.24
C	105	7.1	0.80
D	119	4.9	0.85
E	147	4.8	0.70
F	184	6.3	0.47
G	193	10.5	0.46

<b>COMBINED</b>	<b>Area (mm<sup>2</sup>)</b>	<b>Hyd Diam. (mm)</b>	<b>Velocity</b>
H	551	22.5	0.41
I	338	16.0	0.66
J	230	16.2	0.95

### 5.5.5 Nasal Valve Flow

Two cross-sectional areas located proximal to the anterior nasal valve at 2.6cm and 3.2cm were chosen to reflect the rapid changes in the flow field. The nasal valve is located 2cm posterior to the anterior nares. The naming convention used for the left and right cavity takes on the side that the cavity sits anatomically. The cross-section shown in Figure 5.10 is from a frontal perspective (positive flow into the paper) and therefore the right cavity is depicted on the left side. A contour plot of the axial velocity ( $x$ -component of velocity) is combined with streamlines of secondary flow ( $y$ - $z$  component of velocity).

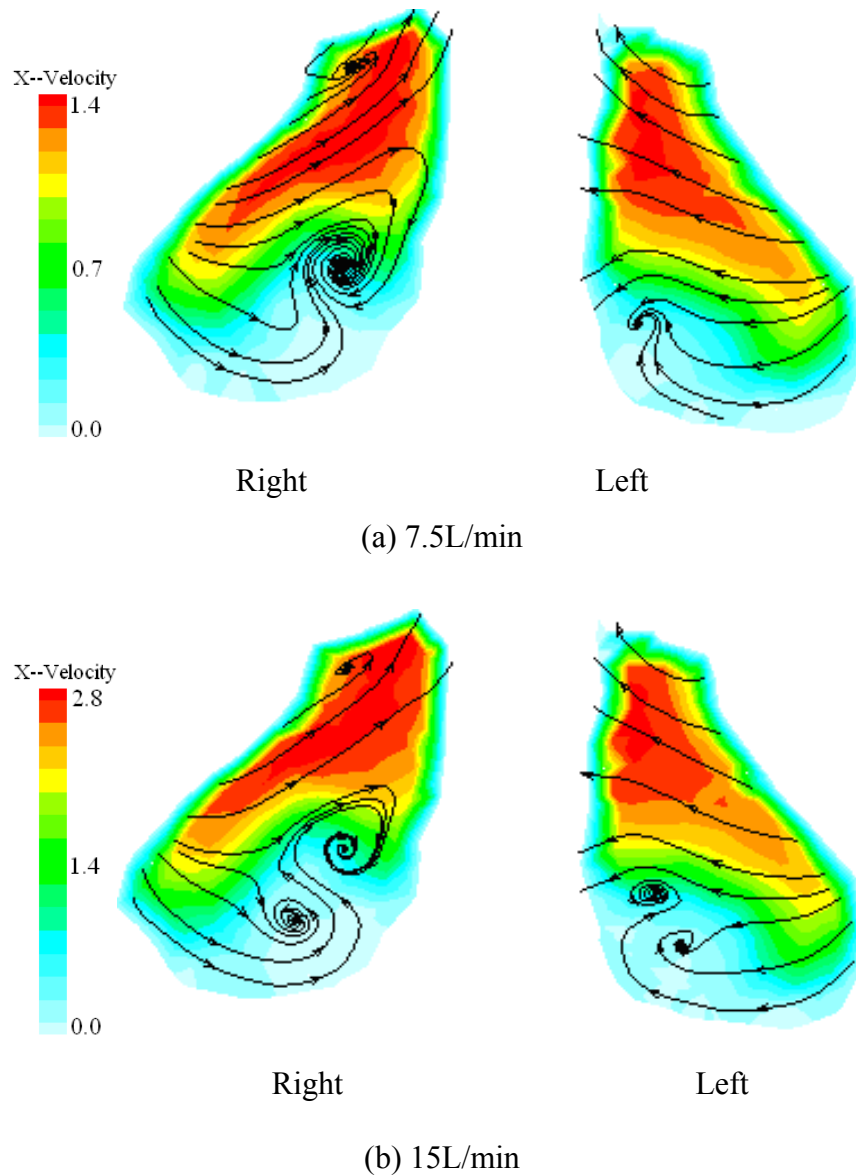


Figure 5.10 Velocity field in the coronal cross-section located at 2.60 cm from the anterior tip of the nose, (a), at flow rate of 7.5L/min, (b) at flow rate of 15L/min.

The air enters the vestibule region with a vertical direction. As the distance increases from the anterior tip of the nostrils, the nasal geometry becomes narrow as the airflow turns posteriorly, approximately  $90^\circ$  towards the nasopharynx. This transition along with the narrowing geometry forces the flow to emerge from the outer walls from the septum and directed inwards. The presence of the wall along with the bulk flow that exists in the upper regions produces low flow near the floor of the airway (light blue colour) and forces the flow to recirculate forming vortices in this region. For the cross-section located at 2.6cm from the anterior tip of the nose, two vortices in the right cavity and one in the left are found for a flow rate of 7.5L/min (Figure 5.10a).

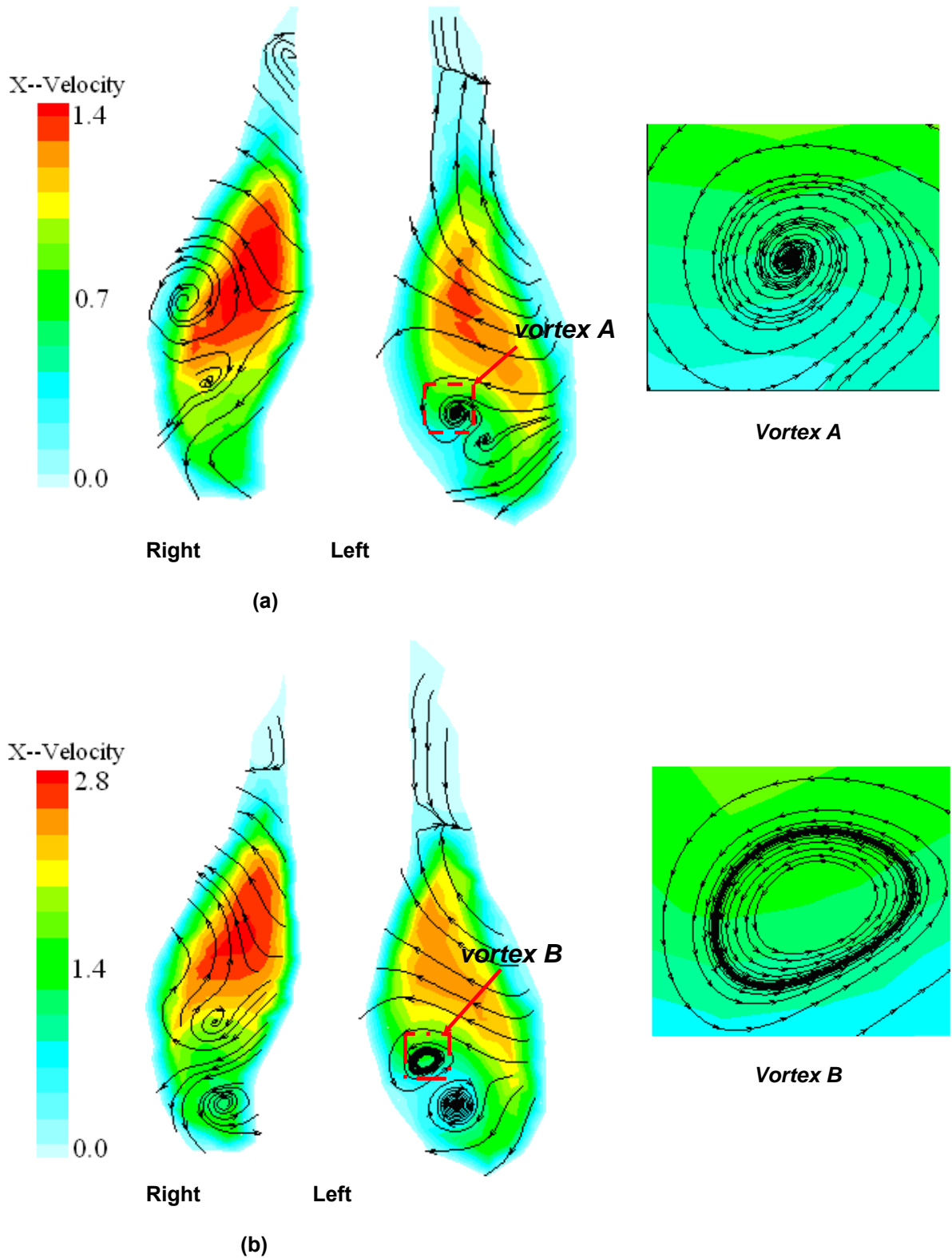


Figure 5.11 Velocity field in the coronal cross-section located at 3.20 cm from the anterior tip of the nose, (a) at flow rate of 7.5L/min, (b) at flow rate of 15L/min.

When the flow rate increases to 15L/min, the number of vortices in both of the cavities increases in the low flow regions and the streamlines are more dispersed (Figure 5.10b).

At the cross-section located at 3.2cm from the anterior tip of the nose the bulk flow is concentrated more centrally as the air stream is developing (Figure 5.11). At a flow rate of 7.5L/min, there are two vortices in the left cavity while in the right cavity some recirculation occurs forming weaker vortices (Figure 5.11a). The direction of the streamlines in vortex *A* all point to the centre of the vortex, which demonstrates that the axial velocity gradient is positive and the pressure gradient is negative along the axial direction (Escudier 1988; Stabl 1992). As the flow rate increases to 15L/min, the magnitude of the recirculation and hence the vortices increase (Figure 5.11b). The direction of all the vortices except for the upper vortex in the left cavity (vortex *B*) all point inwards. Vortex *B* shows the outer streamlines of the vortex directed inwards while the inner streamlines are directed outwards from the centre. This streamline feature is a case of a Hopf bifurcation from bifurcation theory which suggests that the positive velocity gradient changes from positive to a negative gradient (Escudier 1988).

### 5.5.6. Middle Turbinates

The same contour-streamline plot was applied to the middle turbinate area located at 6.10 cm from the anterior nares. The streamlines show that flow is directed downwards with the bulk flow concentrated in the upper and lower region close to the septum walls. There are no visible vortices but some weak recirculation occurs, possibly due to the narrow geometry (Figure 5.12). Velocities in this region are lower than in the nasal valve region as the geometry has expanded. The downwards direction is due to the airway which is now heading towards the nasopharynx. Therefore the overall flow path undertakes a U-turn shape where the flow entered upwards, travelled horizontally and ending downwards towards the lungs.

To further study and compare the distribution of airflow in the turbinate region with other work in the literature, the cross-section in the middle turbinate region was subdivided into separate regions and labelled from *A* through to *E*.

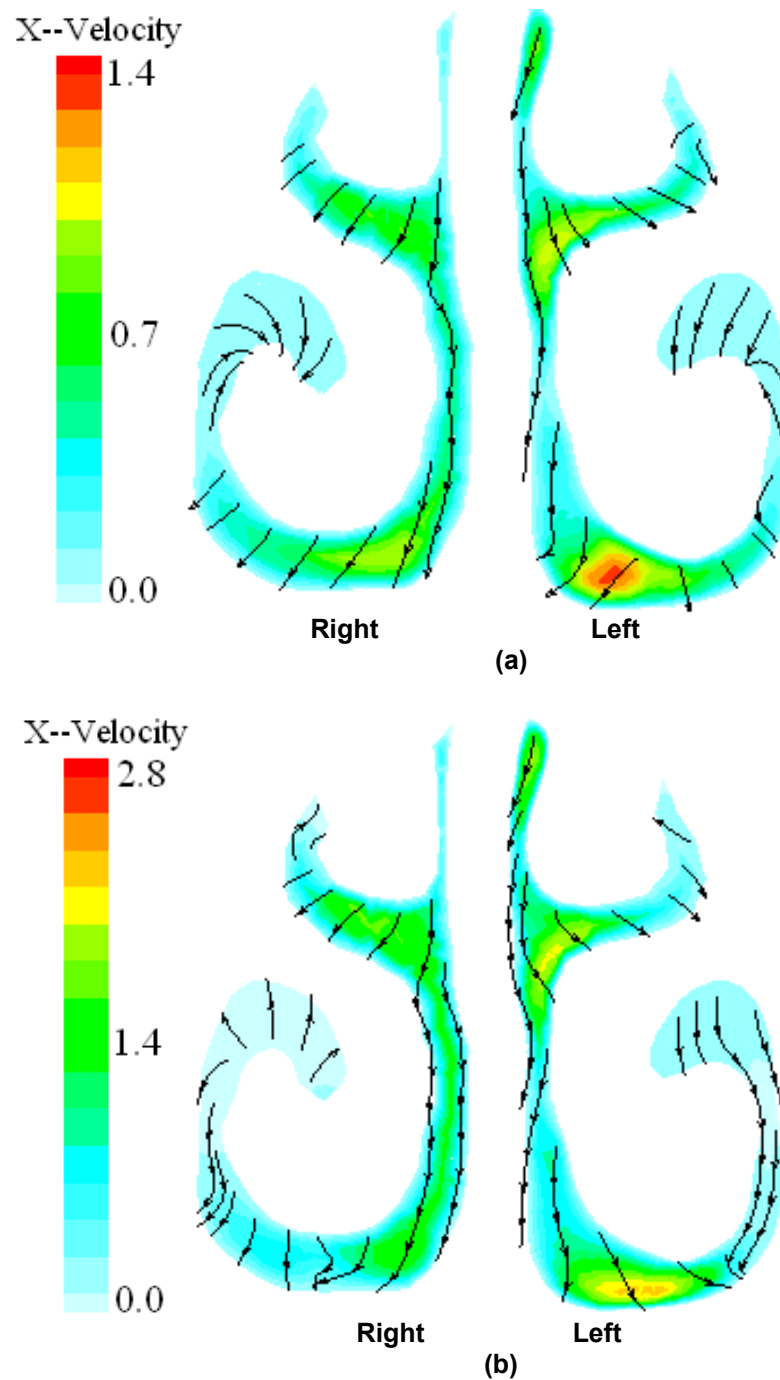


Figure 5.12 Velocity field in the cross-section located at 6.10 cm from the anterior tip of the nose, (a), flow rate of 7.5L/min, (b) at flow rate of 15L/min.

This enabled measurements of the local distribution (Figure 5.13). Local volumetric flow was determined by integrating the velocity component normal to the plane over the cross-sectional area of each region. The results of the airflow distribution at a flow rate of 15L/min for left and right sides are given in Table 1. There are obvious differences

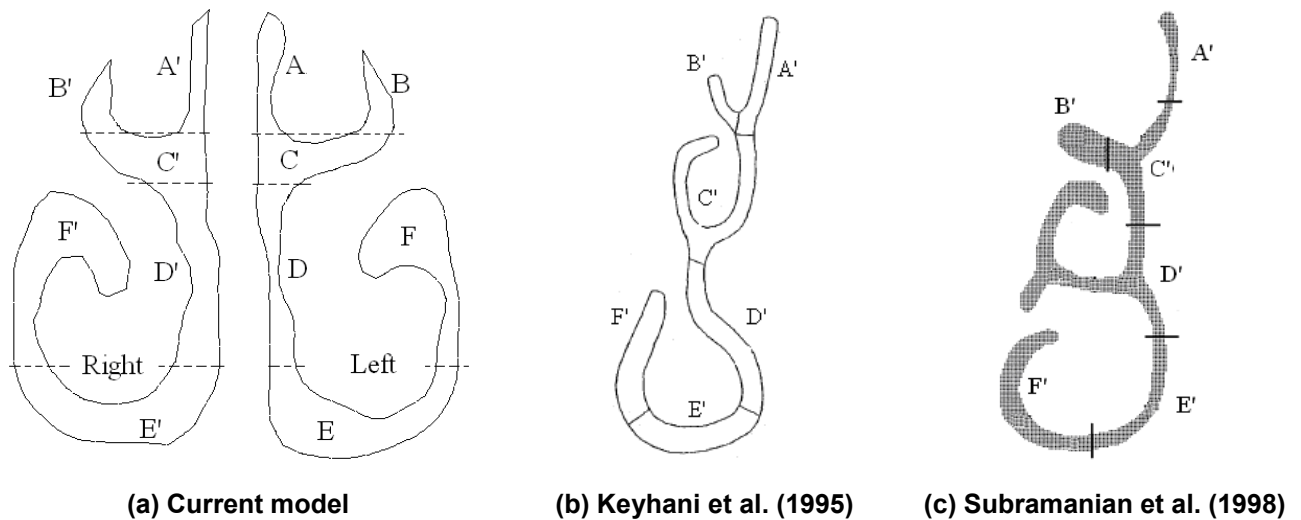


Figure 5.13 The coronal sections are divided into sub-sections which are indicated by letters, (a), the section is located at 6.1 cm from the anterior tip of the nose used in this paper, (b), the section is located at 6.2 cm from the anterior tip of the nose used by Keyhani et al. (1995), (c), the section is located at 6.0 cm from the anterior end of the nose used by Subramanian et al. (1998).

between the comparative geometries of Keyhani et al. (1995), Subramanian et al. (1998) and the current model in this study (Figure 5.13). The most obvious difference is that the current model only has two meatus extensions ( $B'$  and  $F'$ ) in comparison with the other models that have three meatus extensions:  $B'$ ,  $C'$ ,  $F'$  for Keyhani et al. (1995) and  $B'$ ,  $D'$ ,  $F'$  for Subramanian et al. (1998). The cross-sections are all located at a similar region in the nasal airway - in the middle of nasal turbinate. The location of our model is located at 6.1 cm away from the anterior tip of nose while for Keyhani et al. (1995) (Figure 5.13b) and Subramanian et al. (1998) (Figure 5.13c) the locations are 6.2 cm and 6.0 cm, respectively. The  $\%Q_{total}$  describes the proportion of flow as a percentage of the total flow rate. The main flow direction is not easily specified for complex geometries such as that of the nose. Therefore the average velocity magnitudes  $U = (u_x^2 + u_y^2 + u_z^2)^{1/2}$  and  $U_x$  in the  $x$ -direction (axial) are used for analysis.

The flow analysis through the left cavity (Table 5.2) shows that 85% of the air passes through the superior medial airway (region  $C$ ), the middle medial airway (region  $D$ ) and the ventral medial airway (region  $E$ ). These regions cover 59% of the entire cross-section. The right cavity is slightly wider and the regions  $C'$ ,  $D'$  and  $E'$  take up 61.6% of the right section while the  $\%Q_{Total}$  is 94%. Despite the small difference in area coverage, region  $D$  in the left cavity exhibits a small constricting section which causes a higher resistance in

the flow and hence the smaller proportion of air flow through *C*, *D* and *E*. For Keyhani et al. (1995) model, the majority of the flow occurs in *C'* and *E'* (56% in total) which are the central and lower passages. The flow also dominates in similar regions *D'* and *E'* for Subramanian et al. (1998) totalling 71% (Table 5.3).

**Table 5.2** Flow distribution on the plane in the middle of turbinate for flow rate of 15L/min

Region	LEFT					RIGHT				
	A (mm <sup>2</sup> )	Q (ml/s)	% Q <sub>tot</sub>	U (m/s)	U <sub>x</sub> (%)	A (mm <sup>2</sup> )	Q (ml/s)	% Q <sub>tot</sub>	U (m/s)	U <sub>x</sub> (%)
A'	13.7	13.9	11.6	1.3	78.1	10.4	3.1	2.5	0.42	70.5
B'	9.7	1.4	1.2	0.2	62.6	8.6	1.6	1.3	0.24	75.6
C'	23.2	25.6	21.4	1.4	79.2	29.1	28.5	23.7	1.12	87.1
D'	21.6	24.4	20.3	1.2	90.8	36.9	34.7	28.8	1.00	94.2
E'	50.3	52.4	43.7	1.1	95.8	50.5	50.2	41.7	1.06	93.8
F'	42.8	2.2	1.8	0.1	80.0	53.5	2.5	2.1	0.11	41.8
<b>Total</b>	<b>161.3</b>	<b>119.9</b>				<b>189.0</b>	<b>120.5</b>			

**Table 5.3** Flow distribution on the right plane in the middle of turbinate for flow rate of 15L/min

Region	Keyhani et al. (1995)					Subramaniam et al. (1998)				
	A (mm <sup>2</sup> )	Q (ml/s)	% Q <sub>tot</sub>	U (m/s)*	U <sub>x</sub> (m/s)	A (mm <sup>2</sup> )	Q (ml/s)	% Q <sub>tot</sub>	U (m/s)	U <sub>x</sub> (%)
A'	15.6	14.1	11.4	-	0.91	7.9	2.1	1.9	0.51	52.9
B'	6.0	3.8	3.0	-	0.63	15.4	2.1	1.9	0.24	58.3
C'	35.5	34.2	27.3	-	0.96	20.8	12.9	11.3	0.78	79.5
D'	27.9	22.8	18.3	-	0.82	54.8	53.2	46.7	1.20	87.5
E'	27.9	35.9	28.7	-	1.29	20.5	27.8	24.4	1.39	97.8
F'	26.5	14.1	11.3	-	0.53	28.9	15.8	13.9	0.79	69.6
<b>Total</b>	<b>139.4</b>	<b>124.9</b>				<b>148.3</b>	<b>113.9</b>			

\* data not available



The flow in the left cavity stays close to the wall while its distribution is mainly in the middle sections and more dominant in the lower sections while a small percentage (11.6%) is found in the upper section. This pattern was also observed in the work by Hahn et al. (1993) and in Keyhani et al. (1995)'s model. In the right cavity the flow is concentrated within the middle sections. The flow in the left olfactory slit (section  $A$ ) is found to be larger than that of the right side (zone  $A'$ ). The axial flow values were represented by the  $x$ -component of velocity  $U_x(\%)$  as a percentage of the total velocity magnitude  $U$  was high which implies that the flow is dominant in the  $x$ -direction. Low velocity regions found in  $B'$  and  $F'$  for all the models show a much lower axial velocity. These regions become susceptible to recirculating flows as they are far away from the bulk flow regions.

### 5.5.7 Temperature Profiles

Temperature profiles were obtained from an averaged temperature at each cross-section throughout the airway for a breathing rate of 15 L/min. The results for the normal air condition were compared with experimental work (Keck et al. 2000a; Keck et al. 2000c) whose results were averaged from a population of 50 and 23 volunteers respectively. The profile showed good agreement in the frontal regions of the nasal airway, while a small discrepancy is observed in the back regions towards the nasopharynx. The profile converged to a steady value at a distance of 40mm from the inlet, suggesting that the air is conditioned early in the front region.

The profiles for the inhalation of cold dry air were recorded for the left and right sides of the nasal cavity and also shown in (Figure 5.14). The temperature profiles converge to a peak value of 30.7°C for the last ten measurements away from the inlet. This compares with the inhalation of normal air which has a value of 33.3°C for the last ten measurements. The distance at which the profile converged to a steady value is 71-mm from the inlet which is the location where the left and right cavities begin to merge together.

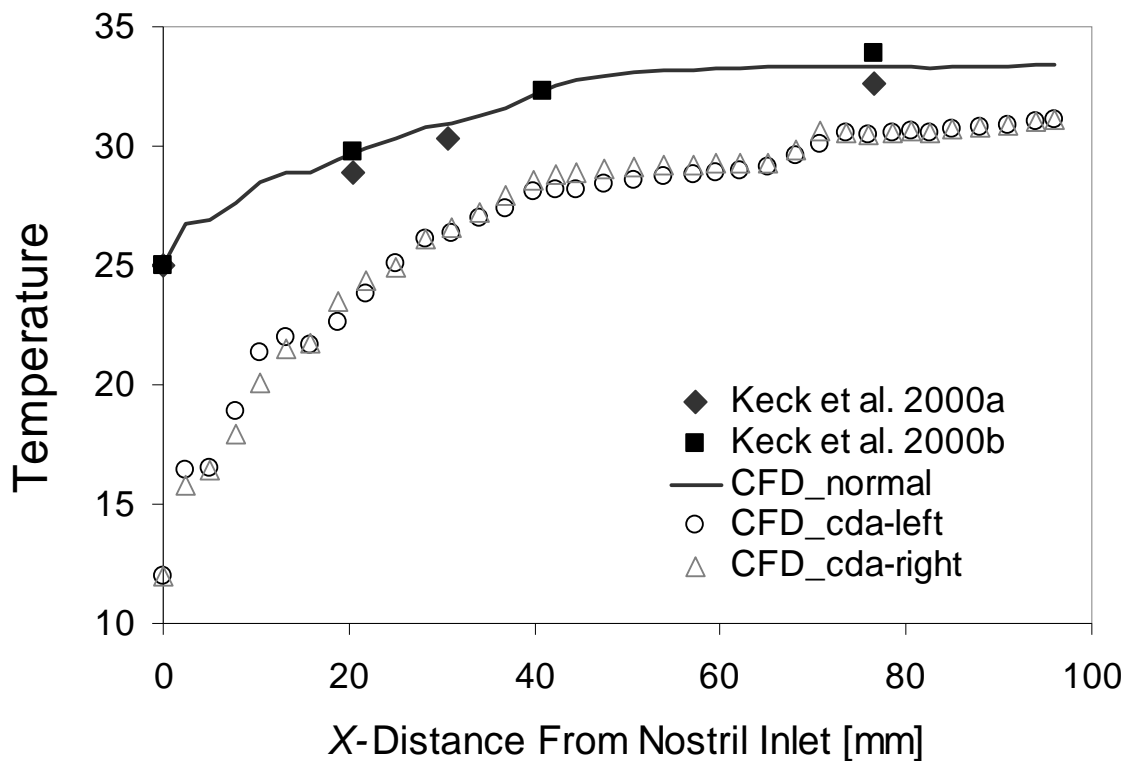


Figure 5.14 Temperature profiles across the nasal cavity from the inlet. The solid black line represents a normal inhalation condition compared with experimental work. The un-coloured symbols represent the simulated results for cold dry air.

For normal air conditions (25°C, 35%RH) heating of the inhaled air is dominant in the frontal region of the airway. The temperature difference is stable after the anterior turbinate region and the heat transfer is minimal. One of the roles of the turbinate region that has been suggested is its enhancement to condition the inhaled air due to an increase in the contact surface area of the meatus passageway. In the case of normal air conditions, the turbinate region does not actually apply much heat transfer to the inhaled air since the inhaled air has been conditioned close to the body temperature before it reaches the turbinates. The majority of the temperature change of the inhaled air occurs in the frontal regions where the temperature difference is greatest. For the cold dry air case, the temperature profile follows a similar curve, but had lower temperatures.

### 5.5.8 Temperatures in the Left and Right Cavities

Given that other dependent variables, such as wall temperature and a steady air flow were kept constant in this study, the effects of the nasal geometry differences on the airflow field and heat transfer ability could be isolated for analysis. For this comparison, the differences between the left and right cavities can be used. The averaged temperatures at different cross-sections shown in Figure 6 were recorded and compared. The left cavity produces higher temperatures in the front regions before the airway expands just after cross-section *B* ( $x \approx 19\text{mm}$ ), however after the airway expansion the right cavity produces higher values.

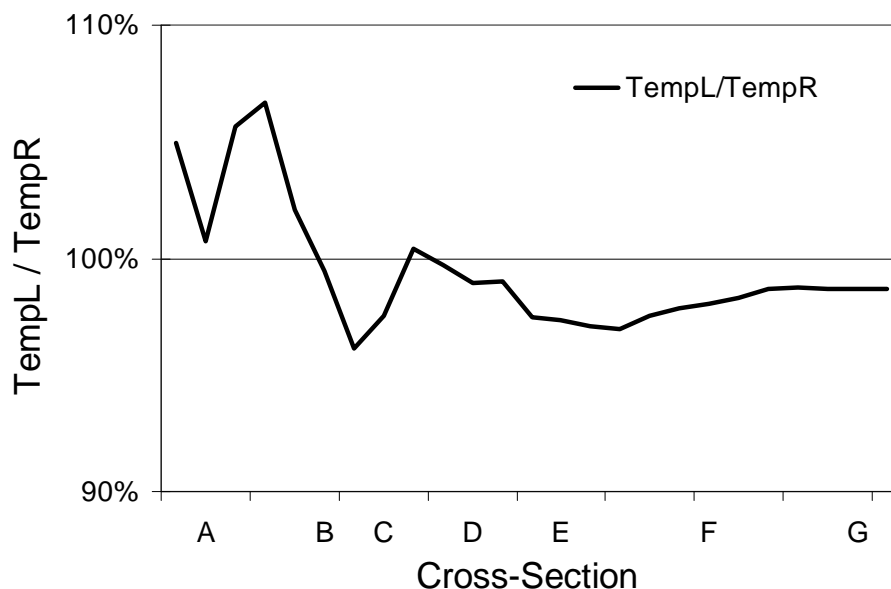


Figure 5.15 Ratio of the average temperature across the cross-sections of the left cavity with the average temperature across the cross-section of the right cavity.

The contour plots reveal that the cooler air is found at the central locations of each cross section furthest from the wall. The temperatures at the olfactory regions (top of section *D,E*) remain high as there is little airflow that reaches this upper region and the region is heated by the near surrounding walls. This is an important feature of the human body as the olfactory epithelium is lined with delicate olfactory receptor neurons which need to be void of any cold dry air exposure to prevent any damage. At section *C*, the left-side is thinner; however the bulk flow remains in the middle region which accelerates through. The bulk flow regions are the last to be heated up to a peak value of  $30.7^{\circ}\text{C}$ . A comparison

of the temperature contour plots in Figure 5.16 with the axial velocity contours in Figure 5.8 shows that at high axial velocity regions, the temperature is at its lowest. This is due to the finite heat source provided by the constant wall temperature where the heating of the cold air is dependent on the mass flow rate as depicted by the thermodynamic balance equation:

$$\dot{Q} = \dot{m}C_p(T_{wall} - T_{air}) \quad (5.8)$$

This implies that the flow residence time,  $\dot{m}$  is critical for the inhaled air to be heated, given that the heat source is driven by the difference in the constant wall temperature and the inhaled air.

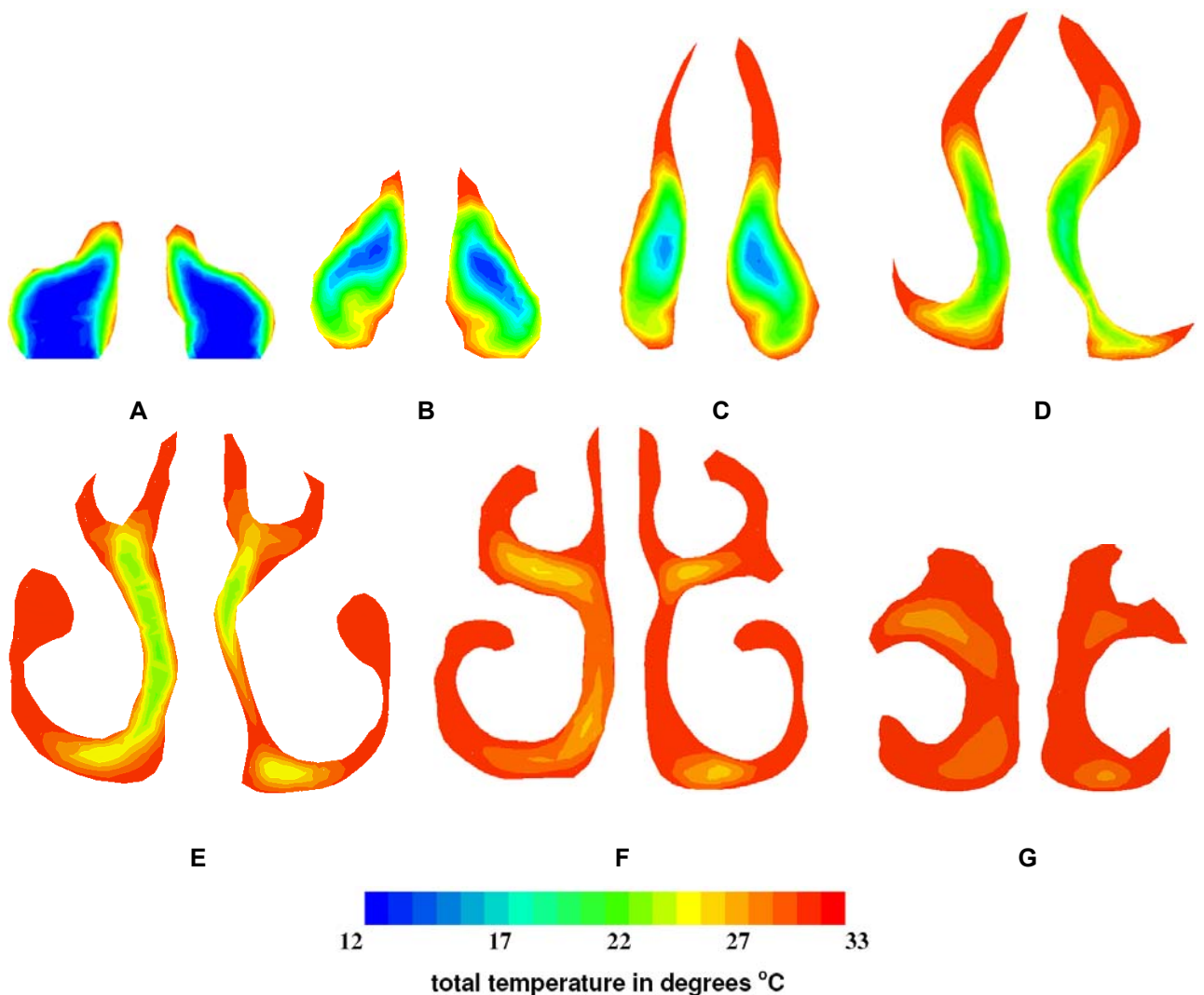


Figure 5.16 Contours of total temperature at cross-sections throughout the nasal cavity.

### 5.5.9 Wall Heat Flux

The wall heat flux was mapped for the entire airway however only the region up to section *F* is shown since the region thereafter showed little change. The heat flux is greatest at the frontal regions where the temperature gradients are greatest (Figure 5.17). The lower and upper sections of the airway exhibit low fluxes, since the flow of the inhaled air is minimal in those regions. At the anterior turbinate region the protruding meatus regions do not show any heat flux. The main airway attached to the septum walls show that heat is being transferred. The region after the anterior turbinates show no heat flux which means that the inhaled air adjacent to the walls has reached body core temperatures. Further heating becomes dependent on the airflow especially for the air which requires convective movements to enhance heat transfer. An increase in the velocity magnitude will not necessarily enhance the heat transfer due to the shorter residence time, but rather an increase in the cross-flow in the *y-z* directions is required to promote mixing and the convective heat transfer.

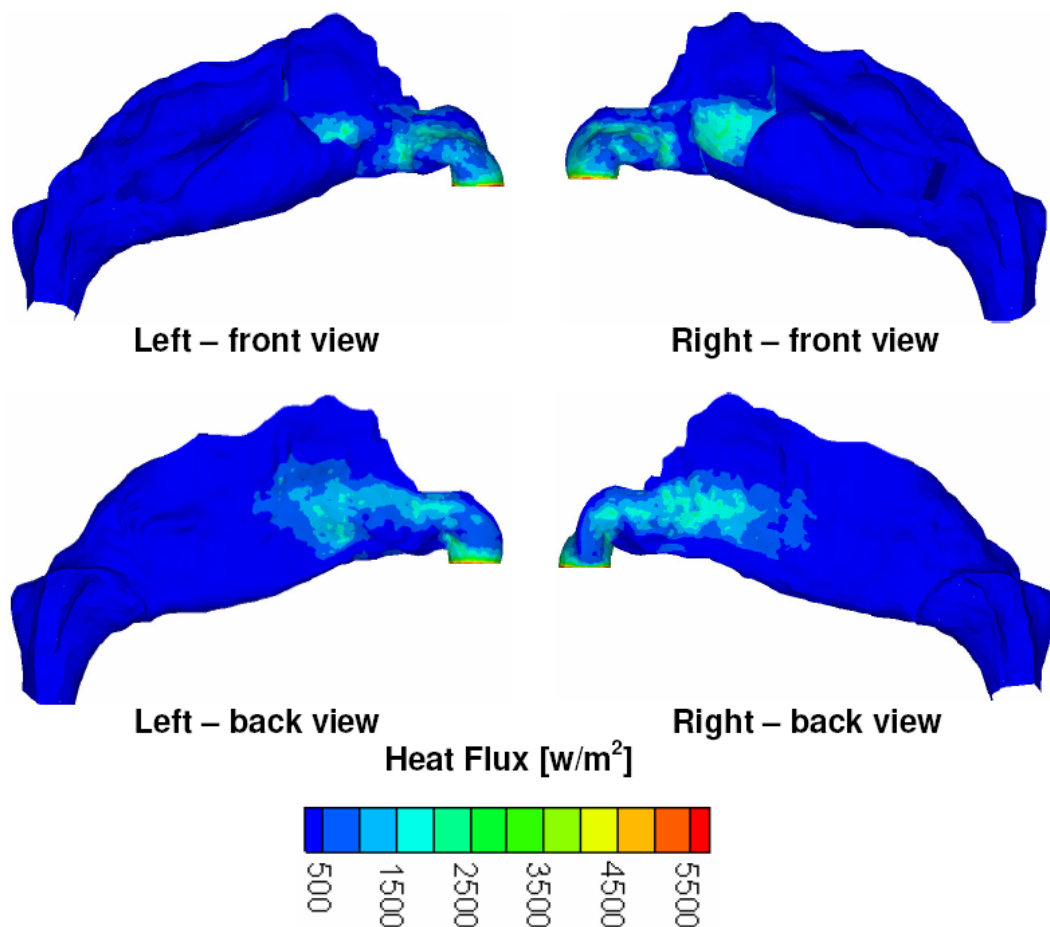


Figure 5.17 Wall heat flux for a cold dry air inhalation condition

## 5.6 Discussion

The main distinctions of the reconstructed nasal cavity used in this paper in comparison with others are: (i) a narrower nasal valve region, (ii) wider turbinates and (iii) a shorter length. Our model exhibited the smallest cross-sectional area for the nasal valve region but had the largest cross-sectional area in the turbinate region when compared with other models. The differences in geometry for the left and right sides as well as the intersubject variations, provided differences in the airflow patterns. For example an increase in the flow rate resulted in higher wall shear stresses while also magnifying the local differences between the left and right cavities, where they exist (e.g. Zone 4-6). As shear stresses are linearly related to the local velocity, these values significantly increase as breathing efforts increase. High shear stresses that are concentrated locally may cause irritation of the blood vessels within that area. Maximum shear stresses have been found in the range of 0.2 Pa (Elad et al. 1993) on the septal wall across the inferior turbinate at near peak inspiration of 20L/min, which compares with stresses in uniform regions of large arteries which exist in the range of 1.5-2 Pa (Nucci et al. 2003). The maximum shear stresses that occurred in the nasal valve region and to a lesser extent in Zone3 and 4, may lead to dysfunctional effects on nasal sensation of airflow and may play a role in the well-being of nasal breathing. By mapping out the distribution of external stresses on the nasal cavity walls, predictions of the mechanoreceptor response may be estimated.

Path streamlines were investigated and compared. This provided a pictorial view of macro flow features in terms of the recirculation zones that is important in the study of gas-particle flows within the airway. It was found that recirculation was prevalent in the olfactory region and in the nasal valve region where the flow experiences sharp changes in the flow conditions. There were some differences in the size and location of the vortices between the models compared which may be attributed to geometrical differences such as an increase in airway height that was found to promote separation by Keyhani et al. (1997).

The internal nasal valve is considered as a region rather than a single cross-section of the nasal passageway and resembles a constriction-expansion region which causes the majority of the total airflow resistance. The streamlines in the anterior nasal valve are all directed from the outer wall towards the inner septum wall (Figure 5.10). In the right cavity however, the opposite occurs (Figure 5.11). The flow is directed from the inner side,

outwards. Further examination of the streamlines in cross-sections further downstream reveal that the secondary flow direction in the left cavity indeed changes similar to the right cavity. Therefore the authors believe that the flow development in the right cavity is quicker than the left in this instance. As the air enters the nasal valve region after the 90° turn, the transition coupled with the narrowing geometry forces a majority of the flow direction to come from the opposite side of the septum walls. This is consistent with the larger contour areas (red-colour) of high velocity found for the right cavity. After the flow is aligned and the airway begins to expand the resistance at the walls causes the flow to rebound and flow in the opposite direction. For particle deposition studies this flow feature is important as it allows better prediction of deposition sites. The direction of the streamlines that initially accelerate from the outer wall will enhance the deposition of inhaled particles onto the inner nasal septum wall side rather than on the outer surfaces. The complex flow in the nasal valve region therefore acts as a filtration device for particle deposition – a fact that is positive for toxic inhalation but a problem for drug delivery.

The turbinate region consists of a narrow curled bone that protrudes into the main airway. The middle and inferior turbinate is an important structure for filtration, heating and humidification where the mucosal wall surface area is increased. However, only a small percentage of air reaches this outer surface area within the meatus region ( $F$ ). The surface area of the turbinates that is in contact with the airflow affects less than 2% of the flow field in terms of for heating and humidification. Therefore the efficiency of the turbinates to heat and humidify the air through the increase in surface area of the meatus regions is very low. This suggests that the role of the turbinates to condition the air may not be solely reliant on the surface area contact but may in fact be influenced by the nature of the flow that the turbinates cause. For example, the protrusions create narrow meatus airways which affect the flow regime (laminar or turbulent) and hence the heating capability. Intersubject geometric variation is thought to arise from eco-geographic adaptation to climate. Some researchers have proposed that people exposed to cold dry environments exhibit leptorrhine features that induce turbulence, while those exposed to hot humid environments however, exhibit platyrrhine features that produce more laminar flow, where the conditioning of the air is less critical (see Section 2.1). The airflow distribution results obtained confirm this idea however further studies involving a larger sample of geometries are needed to confirm this hypothesis.

The high flow rates found in region  $A$  and  $A'$  may be considered as undesirable since it can lead to damage to the olfactory regions. Normally low flow characteristics are required in the olfactory region as it is a defence mechanism that prevents particles whose trajectories are heavily dependent on flow patterns from being deposited onto the sensitive olfactory nerve fibres, while vapours are allowed to diffuse for olfaction.

In terms of the heat transfer, the airflow analysis was found to be linked with the temperature contours in that, regions of high velocity was correlated with lower temperatures. The contour and streamline plots of the airflow revealed that the nasal valve region, which exhibits the smallest cross-section not only acts as a filter to restrict foreign particles but also creates complex flow patterns such as vortices and recirculation. Additionally the reduced cross-section forces the airflow closer to the walls, exposing them to the warmer surface; although this is offset by an acceleration of the air in this region.

The temperature profiles showed that the air was heated to its near maximum value by the time it reached the turbinate region. This suggests that the heat transfer process is more dominant in the anterior regions of the nasal cavity rather than in the turbinate regions. The temperature difference is stable after the anterior turbinate region and the heat transfer is minimal. One of the roles of the highly vascularised turbinate region that has been widely discussed is to condition the inhaled air. However in the case of normal air conditions, the turbinate region does not actually apply much heat transfer but rather acts as a heat source through its constant temperature maintained by the bed of capillary blood that provides the walls with this energy to maintain. The majority of the temperature increases occurs in the frontal regions where the temperature difference is greatest. For the cold dry air case, the temperature profile follows a similar curve, but shifted downwards to accommodate the temperature decrease. As discussed earlier, only a small percentage of air reaches this outer meatus region ( $F$ ) the heating and humidifying ability of the turbinates affects less than 2% of the flow field. Therefore the role of the turbinates to condition the air may not be solely reliant on the surface area contact but may in fact be influenced by the nature of the flow that the turbinates cause. Further studies into this phenomenon are therefore needed.



---

Having the airflow field established allows an understanding of how the particles will be transported through the nasal cavity. For example, the significant gross features of nasal cavity airflow have been identified as the 90-degree bend at the nostril entrance into a narrowing nasal valve region before expansion into the main nasal passage. Within this anterior region, local recirculating regions will form where flow separation occurs due to the bend as well as the converging-diverging nasal valve region. Using Lagrangian tracking, the particles are individually tracked and their fate can be determined by setting boundary conditions at the surfaces of the nasal cavity to terminate the particle trajectory. With this in mind, it is anticipated that larger particles that exhibit high inertia will deposit at the 90-degree bend due to its inability to its momentum exceeding the flow field vectors. The nasal valve region exhibited complex flow patterns involving vortices which will have an interesting effecting on the particle transport. The following chapters (6-8) will describe the transport of inhaled particles. The inhaled particles are categorised into two types: involuntary inhalation of suspended particles found in the air (e.g. pollen, fibres, dust) and deliberate inhalation of particles (nasal spray delivered particles). The different characteristics of the particles due to their morphology and the numerical considerations for this are discussed. In addition the resulting deposition patterns of the particles in the nasal cavity are presented.

CHAPTER **6**

# Inhalation of Toxic Particles and the Effects of Particle Morphology

## 6.1. Introduction

During normal respiration, inhaled air often contains foreign particles such as dust, fumes and general pollutants. Additionally drug delivery via the nasal cavity has seen the study of drug particles suspended in the airflow become more prominent. The introduction of particles to the airflow involves a secondary solid phase to be present in conjunction with the gas phase, leading into the field of multiphase flows. This chapter presents different modelling strategies required to account for a variety of particles that include spherical, fibrous, and rough surface particles. A brief description of these particle types follows.

### 6.1.1. Wood Dust Particles

Spherical particle modelling is quite common as it allows a simplified drag correlation. This advantage often outweighs the need to consider all the physics involved with non-spherical particles, since approximate values can provide sufficient accuracy for common engineering problems. One example of its extensive use is within the nasal drug delivery studies. Numerical simulations have made use of spherical particles to represent the characteristics of general aerosols (Zhang et al. 2004; Zhang et al. 2005; Zhang et al. 2002) while Schroeter et al. 2006) used spherical particles to represent drug particles for nasal drug delivery. In this chapter, the application of spherical particles was applied to wood

dust particles. This work came about as a result of occupational injury to woodturners who encountered frequent nose bleeds during their time spent at the '*Peninsula Woodturners Guild Incorporated*'<sup>1</sup> in Victoria, Australia.

The processing of raw timber from the use of high-powered reciprocating tools such as sanding and sawmills generates large quantities of fine, inhalable wood dust. Direct contact with the wood dust leads to inhalation of the particles via the nasal cavity. It is not surprising then, that significant health effects have resulted from direct contact of inhaled wood dust with tissues of the respiratory tract. While ingestion is also common, no health effects have been reported. The effects from deposited wood particles in the nasal cavity have been found to be a potential cause of respiratory diseases including allergic rhinitis, nasal mucociliary stasis, and asthma. Three wood dusts, pine dust, heavy oak dust, and light oak dust, defined by a particle size distribution generated by machining (Chung et al. 2000), were simulated at a flow rate of 10 L/min.

### **6.1.2. Pollen and Rough Surfaces Modelling**

The symptoms of hay fever (allergic rhinitis) caused by airborne pollen have been well established while more recently its relationship to asthma has been proposed (Bousquet et al. 2001). The morphology of pollen come in various shapes, diameters and densities as shown in Figure 6.1 which pertain to different aerodynamic properties. One particular pollen grain that is highly allergenic is ragweed pollen which is a primary cause of hayfever. Its geometric diameter generally ranges from 16-27 $\mu\text{m}$  (Crowder et al. 2002), has low densities and exhibits spiny protrusions that sit on a spherical surface base. The nasal airway acts as an air filter for the respiratory system where high inertial particles readily deposit onto the nasal walls by impaction leading to inflammation of the mucosa and other effects of hay fever. The inertial property of the pollen is affected by its lower density and therefore will lower the aerodynamic diameter but this may be countered with the protrusions that will alter its drag coefficient.

---

<sup>1</sup> Peninsula Woodturners Guild Incorporated Member – Bill Munt (billmunt@bigpond.net.au)

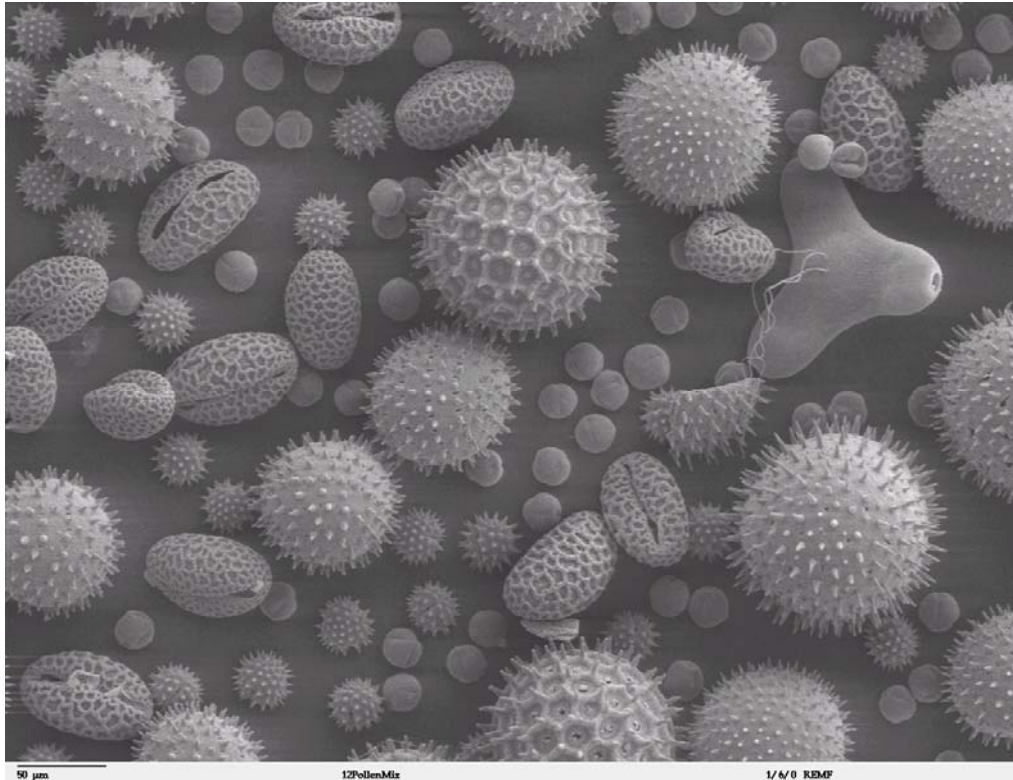


Figure 6.1 Scan electron microscope image of pollen grains from a variety of common plants. Zeiss DSM 962 SEM. (Photo Courtesy of Louisa Howard and Charles Daghlian of Dartmouth College – *Rippel Electron Microscope Facility*)

### 6.1.3. Fibrous Particles

Inhalation of fibrous materials, such as asbestos is one case that has been identified in the workplace as hazardous. Asbestos (Figure 6.2) was once popular among manufacturers and builders in the late 19th century due to its resistance to heat, sound absorption and tensile strength. However since the inhalation of asbestos fibres was found to cause serious illnesses such as asbestosis and mesothelioma, the use of asbestos was banned in many countries. Despite this the risk of exposure still exists mainly through the demolition of older buildings and materials where the fibres become airborne. The alternative for asbestos fibres is the use of man-made vitreous fibres (MMVFs) using inorganic materials such as glass, natural rock and amorphous silicates. MMVFs themselves are not free from toxic properties. The levels of toxicity vary and this is dependent on the fibre length and their biopersistence in the lungs (Lippman 1990; Timbrell 1982).

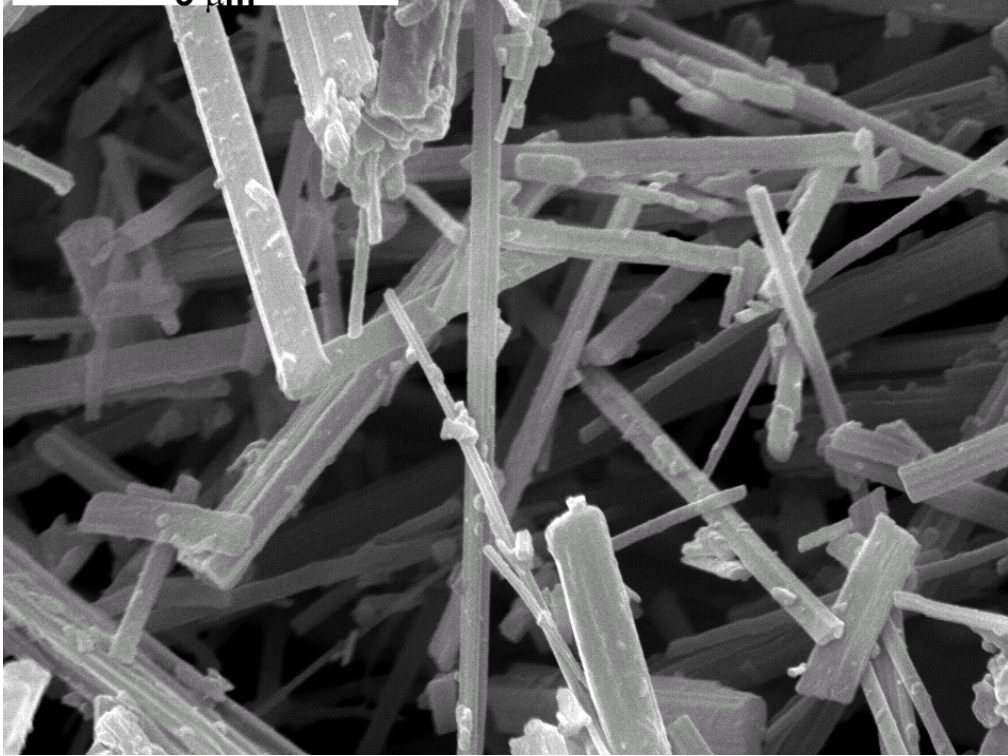


Figure 6.2 Electron microscope image Amosite asbestos. (Photograph Courtesy of the U.S. Geological Survey – [www.usgs.gov](http://www.usgs.gov))

## 6.2. Numerical Considerations for Particle Morphology Differences

### 6.2.1. Spherical (Wood Dust) Particles

Trajectories of individual particles can be calculated by integrating the force balance equations on the particle:

$$\frac{\partial u_p}{\partial t} = F_D(u_g - u_p) + \frac{g_i(\rho_p - \rho_g)}{\rho_g} \quad (6.1)$$

where  $u_p$  presents the particle velocity and  $\rho_p$  is the particle density. Additional source terms for the particle equation such as Brownian force and Saffman lift force were not included as the particles concerned were larger than submicron particles that are influenced by their mean free path. Additionally, wood particles were far denser than air,

causing terms that depend on the density ratio, such as the pressure force, buoyancy force, virtual mass effect and Basset force to be very small.  $F_D(u_g - u_p)$  in Equation 4 is the drag force per unit particle mass and  $F_D$  is given by:

$$F_D = \frac{18\mu_g C_D \text{Re}_p}{\rho_p d_p^2} \quad (6.2)$$

where  $d_p$  is the particle volume equivalent diameter.  $\text{Re}_p$  is the particle Reynolds number, which is defined as:

$$\text{Re}_p \equiv \frac{\rho_p d_p |u_g - u_p|}{\mu_g} \quad (6.3)$$

It is noted that the gravity term, 'g' was taken as  $-9.81\text{m/s}^2$  taken in the Y-axis and hence is applicable for an upright position. The drag coefficient  $C_D$  is given by Morsi and Alexander (1972) as:

$$C_D = a_1 + \frac{a_2}{\text{Re}_p} + \frac{a_3}{\text{Re}_p^2} \quad (6.4)$$

where the  $a$ 's are empirical constants for smooth spherical particles over several ranges of particle Reynolds number.

Dusts from pine (softwood) and from light and heavy oak (hardwood) were simulated where their respective densities are  $560 \text{ kg/m}^3$ ,  $590 \text{ kg/m}^3$ , and  $930 \text{ kg/m}^3$ . A study carried out by Chung et al. (2000) examined the particle size distribution of dusts during sawing and sanding of pine and oak. Oak dust generated by sawing exhibited smaller particle sizes than the pine dust, while similar size distributions were found for both pine and oak dust when generated by sanding. Therefore, only nasal depositions of wood dust with size distributions from sawing were investigated herein. Figure 6.3 illustrates the measured and simulated particle size distribution of both pine and oak. It is noted that the particle size distributions were based on the particle number fraction and not volume fraction nor mass fraction. Both heavy oak dust and light oak dust were assumed to have the same size distribution. All particles in this study were assumed to be spherical.

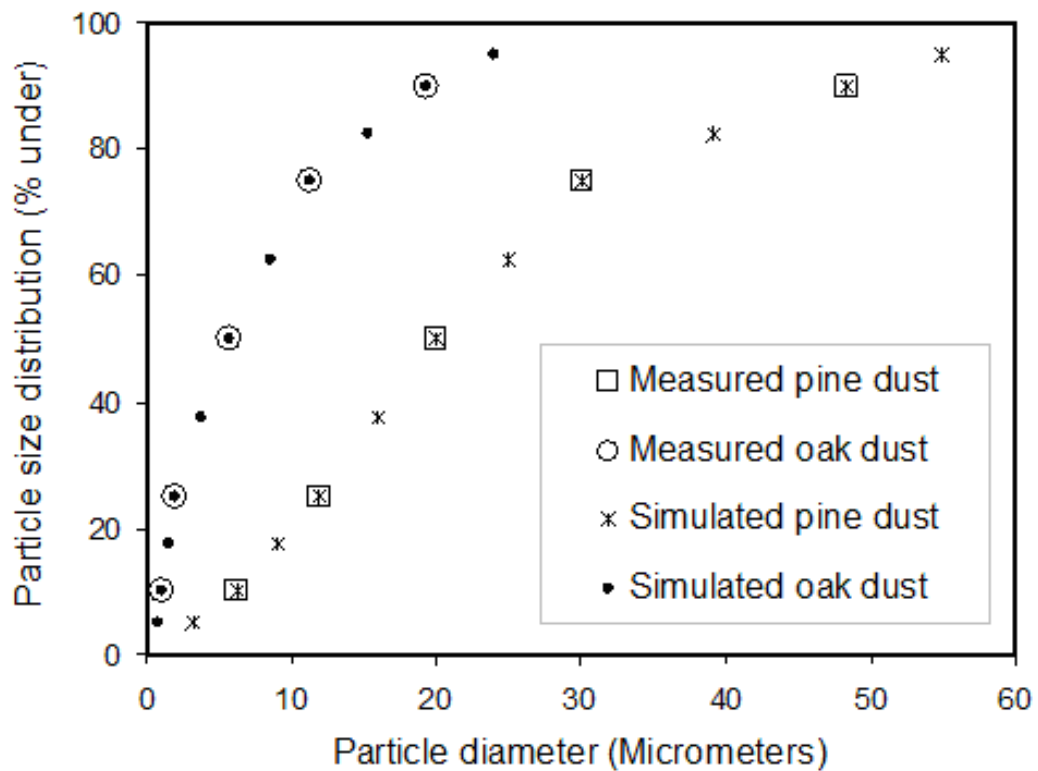


Figure 6.3 Simulated particle size distribution and measured particle size distribution of dusts generated by sawing (from Chung et al. 2000).

The equivalent aerodynamic diameter,  $d_{ae}$ , is defined as,

$$d_{ae} = d_p \sqrt{\rho_p / 1000} \quad (6.5)$$

In still air, particles with  $d_{ae}$  that are smaller than 1  $\mu\text{m}$  are likely to be found suspended in the air, while particles with  $d_{ae}$  from 1  $\mu\text{m}$  to 10  $\mu\text{m}$  tend to settle by gravity. However, normal air movements that are typically found in indoor workshops have been shown to make all particles suspend in the air for a long period of time. This includes particles with  $d_{ae}$  larger than 10  $\mu\text{m}$  that have been found suspended in the air near the dust source and under strong wind conditions (ASHRAE 2001). Moreover, the study of the inhalability of ultralarge particles in still air conducted by Dai et al. (2006) confirmed that the “cutoff” particle size for nasal inhalation is approximately 135  $\mu\text{m}$ . Therefore, particles with  $d_{ae}$  of 10  $\mu\text{m}$  and greater were also considered for investigation for the case of wood dust deposition when the dust source is near, such as the common scenario of wood workshops and other secondary wood industries. For pine dust with density of 560  $\text{kg}/\text{m}^3$  and size range of 3–55  $\mu\text{m}$ , this equates to a range of 2–41  $\mu\text{m}$ . For oak dusts with a size

distribution from 1  $\mu\text{m}$  to 24  $\mu\text{m}$ , the corresponding  $d_{ae}$  is 0.94 to 23  $\mu\text{m}$  for heavy oak while the  $d_{ae}$  range is 0.76 to 19  $\mu\text{m}$  for light oak.

In this study, three particle deposition efficiencies were used to quantitatively present the simulation results: the total deposition efficiency  $\eta_{total}$ , the regional deposition efficiency  $\eta_{n,regional}$ , and the cumulative deposition efficiency  $\eta_{n,cumulative}$ . The total deposition efficiency  $\eta_{total}$  is defined as:

$$\eta_{total} = \frac{N_{totaldep}}{N_{totalin}} \times 100 \quad (6.6)$$

Here,  $N_{totaldep}$  is the total number of particles deposited in the whole nasal cavity while  $N_{totalin}$  is the total number of particles released at the nostrils. The regional deposition efficiency for the  $n$ th region (regional numbers are shown in Figure 1),  $\eta_{n,regional}$  is calculated as:

$$\eta_{n,regional} = \frac{N_{n,deposition}}{N_{totalin}} \times 100 \quad (6.7)$$

Here,  $N_{n,deposition}$  is the number of particles deposited in the  $n^{\text{th}}$  region. The cumulative regional deposition efficiency for the  $n$ th region,  $\eta_{n,cumulative}$  is given as

$$\eta_{n,cumulative} = \sum_{i=1}^n \eta_{i,regional} \quad (6.8)$$

### 6.2.2. Pollen and Rough Surfaces Modelling

For non-spherical particles, considerable development in formulating a single correlation for any shape and orientation have been performed, notably by Haider and Levenspiel (1989) which has been proven to provide accurate representation for a wide range of shape factors. Their correlation defines the  $C_D$  as a function of the particle Reynolds number and a shape factor which is given as:

$$C_D = \frac{24}{\text{Re}_p} \left(1 + a \text{Re}_p^b\right) + \frac{c \text{Re}_p}{d + \text{Re}_p} \quad (6.9)$$

where



$$a = \exp(2.3288 + 6.4581\phi + 2.4486\phi^2)$$

$$b = 0.0964 + 0.5565\phi$$

$$c = \exp(4.905 - 13.8944\phi + 18.4222\phi^2 - 10.2599\phi^3)$$

$$d = \exp(1.4681 + 12.2584\phi - 20.7322\phi^2 + 15.8855\phi^3)$$

and the shape factor  $\phi$  is defined as:

$$\phi = \frac{A_s}{A_p} \quad (6.10)$$

where  $A_s$  is the surface area of a sphere having the same volume as the particle, and  $A_p$  is the actual surface area of the particle.

### 6.2.3. Fibre Modelling

It has been reported that the accuracy of the Haider-Levenspiel method (Equation 6.9) decreases as the shape factor decreases (Gabbitto and Tsouris 2007). A different and novel approach is by Tran-Cong et al. (2004) which defines the fibre by spherical aggregate particles clustered into a cylindrical bar configuration. This correlation will be referred to as the TC-model while the method given in Equation 6.9 is referred to as HL-model. Two equivalent diameters and a shape factor called the ‘degree of circularity’ (Wadell 1933) are used for the drag correlation. The volume equivalent sphere diameter, also known as the nominal diameter, is defined as

$$d_n = \sqrt[3]{6V/\pi} \quad (6.11)$$

where  $V$  is the particle volume. The surface equivalent sphere diameter is defined as

$$d_A = \sqrt{4A_p/\pi} \quad (6.12)$$

where  $A_p$  is the projected area of the sphere. The shape factor used is based on the surface sphericity and is defined as

$$c = \pi(d_A/P_p) \quad (6.13)$$

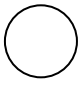
where  $P_p$  is the projected perimeter of the particle in its direction of motion. The empirically defined correlation for the drag coefficient is given as:

$$C_D = \frac{24}{\text{Re}} \frac{d_A}{d_n} \left[ 1 + \frac{0.15}{\sqrt{c}} \left( \frac{d_A}{d_n} \text{Re} \right)^{0.687} \right] + \frac{0.42 \left( \frac{d_A}{d_n} \right)^2}{\sqrt{c} \left[ 1 + 42500 \left( \frac{d_A}{d_n} \right)^{-1.16} \right]} \quad (6.14)$$

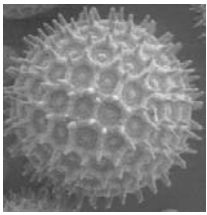
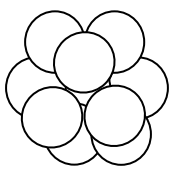
The correlation was implemented into FLUENT via the User-Defined Function allowing a customised drag correlation. In summary the morphological characteristics, typical mean values and numerical models to account for the different particle types are shown in Table 6.1.

**Table 6.1** Summary of fibre their morphological characteristics, typical mean values and numerical models.

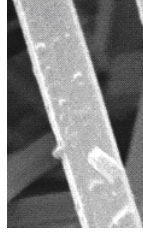

**Wood particles**

Shape	Typical size range	Density	Model
Sphere	5-60µm <i>Chung et al. (2000)</i>	Pine - 560 kg/m <sup>3</sup> Light Oak - 590 kg/m <sup>3</sup> Heavy Oak - 930 kg/m <sup>3</sup>	 <i>Morsi and Alexander(1972)</i>

**Ragweed Pollen**

Shape	Typical size range	Density	Real Image	Modelled Image
Sphere with rough surface	16-30 µm <i>Crowder et al. (2002)</i>	550 kg/m <sup>3</sup> <i>Crawford (1949)</i> 840–1320 kg/m <sup>3</sup> <i>Harrington and Metzger (1963)</i>	 <i>Photo Courtesy of Dartmouth College Rippel Electron Microscope Facility</i>	 <i>Agglomerates of spheres method by Tran-Cong et al. (2004)</i>

**Fibre**

Shape	Typical size range	Density	Real Image	Modelled Image
Elongated cylinders	Asbestos Diameter (FD) < 3 μm	Asbestos 260-400 kg/m <sup>3</sup>	 <p>Photograph Courtesy of the U.S. Geological Survey</p>	 <p>Elongated cylinder method by Haider and Levenspiel (1989)</p>
	Carbon Diameter (FD) ≈ 2-15 μm	Carbon 1830kg/m <sup>3</sup> <i>Su and Cheng (2005)</i>		
	Fibre Length > 5 μm  Aspect Ratio > 3			

### 6.3. Results and Discussion

#### 6.3.1. Deposition Patterns of Wood Dust Particles

*Validation*

The total deposition efficiency of monodisperse pine particles in a range of 3-55 μm was investigated. For each discrete particle size as defined by a size distribution (Figure 6.3), 11,100 particles were released from both nostrils. Particle deposition was found to converge at 11,100 for the spherical wood dust. A sensitive study found there was negligible difference in comparison with a doubling of the number of particles. A smaller number of particles can usually be applied when the particle tracking is a non-stochastic process which is normally applied in turbulent dispersions. Figure 6.4 compares the predicted total deposition efficiency in relation to the inertial parameter. The inertial parameter,  $d_{ae}^2 Q$  is ideal for normalising particle deposition that is dominated by impaction (Equation 2.1). The current CFD techniques captured the trend of total deposition efficiency by predicting the curve reasonably. The differences in deposition may be attributed to the inter-subject variability between the nasal cavity models obtained by Kelly et al. (2004) – 53 year-old non-smoking Caucasian male), with the model used in

the present study – 25 year-old Asian male. Häußerman (2001) also states that nasal cavity replicate casts with wider airways can cause less deposition due to secondary flow.

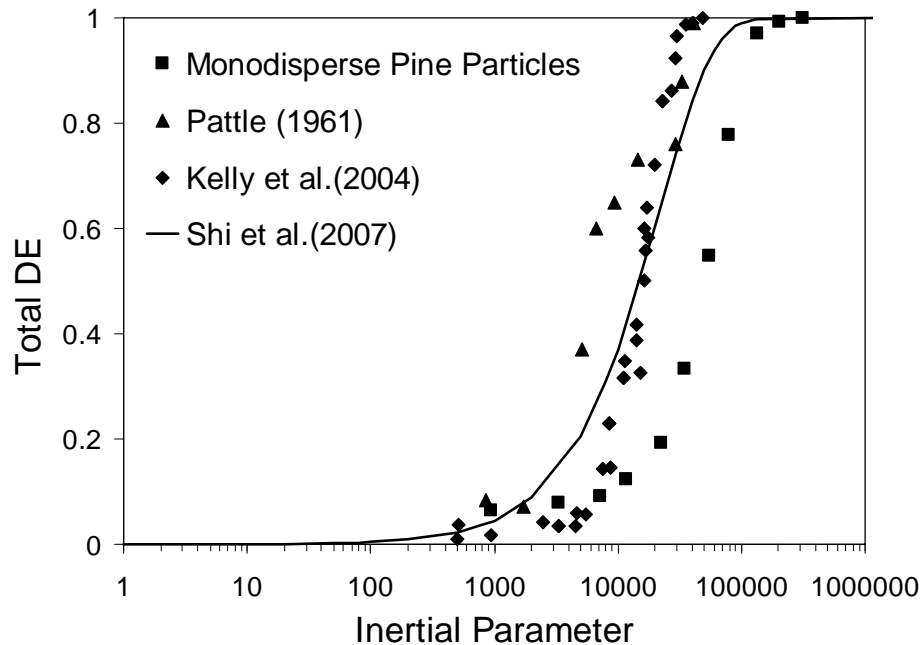
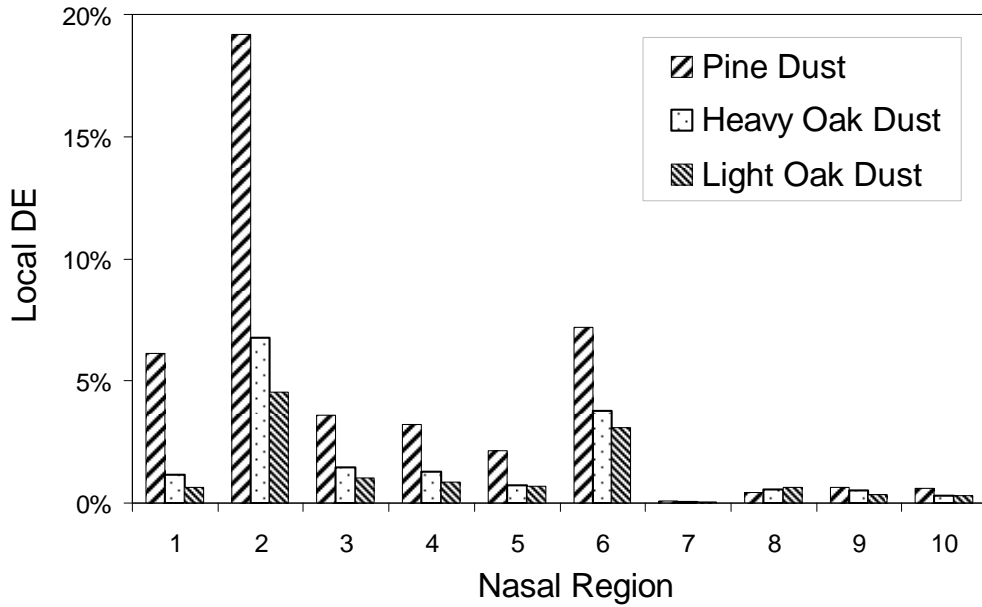


Figure 6.4 Total deposition efficiency (DE) of monodisperse pine particles compared with other experimental investigations (Kelly et al. 2004; Pattle 1961) and numerical results (Shi et al. 2007).

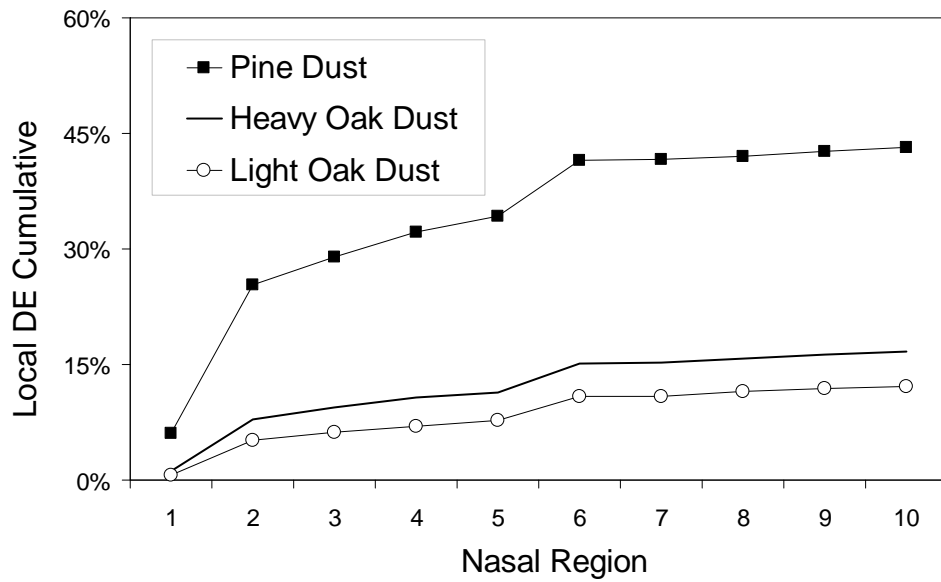
Furthermore, Kelly et al. (2004) points out, that differences in comparison of particle inertial deposition with different nasal cavity models can be explained by inertial impaction considerations. For  $d_{ae}^2 Q$  values less than  $2000 \mu\text{m}^2\text{cm}^3/\text{s}$  particles have a short relaxation time, which allows the particles to adjust to flow streamlines and hence the effect of different geometries is less significant. Accordingly the comparison between the deposition curve of the CFD simulation and the experimental data is fairly similar at this lower range. As the value of  $d_{ae}^2 Q$  increases the particles relaxation time increases and the particles are more likely to continue a linear trajectory that deviates from a curving streamline. The differences in geometries that cause curvatures in streamlines are therefore more significant for larger inertial particles and greater deviation between different geometries is reasonable. Therefore, when neglecting the experimental uncertainties and differences in geometry, the characteristics of the CFD results correspond to the experimental data reasonably well. In addition Häußermann et al. (2001)'s study showed that a lower flow rate (i.e. 10L/min) had lower deposition efficiencies than a higher flow rate (i.e. 20L/min) for the same inertial parameter.

**Deposition Patterns of Dusts with Particle Size Distribution Generated by Sawing**

Deposition patterns of pine and oak dusts with particle size distribution generated by sawing (Figure 6.3) were simulated.



(a)



(b)

Figure 6.5 (a) Local DE of all dusts; (b) Cumulative local DE of all dusts.

Figure 6.5a compares the regional deposition efficiency of dusts in the nasal cavity, while Figure 6.5b gives the cumulative regional deposition efficiency. Figure 6.6 a,b,c displays the deposition patterns of different dusts in the nasal cavity. It is clearly shown that the anterior nasal segment (region 1-5) was the most preferred region of particle deposition for all dusts. This is consistent with experimental observations of Keck et al. (2000a), and Fry and Black (1973). In between region 2 and 3 lies the nasal valve that plays a major role in particles depositing in the anterior nasal segment, as it has the smallest cross-section area. The nasal valve accounts for approximately half of the total airway resistance and has been considered a major obstruction to the delivery of inhaled pharmaceuticals by nasal sprays (Schroeter et al. 2006). Beyond the nasal valve, particles are found to deposit in region 3 (Figure 6.6) on the septum walls of both sides of the nasal cavity. The second highest concentration of particle deposition of all wood dusts is found on the anterior parts of the middle turbinates in region 6 while a small portion of particles deposited at the back of the nasal cavity where the flow changes direction from horizontal to vertically downwards. The change in the flow direction at the nasopharyngeal region again acts like an inertial impactor, filtering out high inertial particles.

There are two major clearance mechanisms of inhaled wood particles in the nasal cavity: the mucociliary mechanism and by physical means. Particles deposited on the ciliated epithelium of the nose are cleared by the mucociliary action, i.e. cilia beating that moves the mucus secretion to remove particles towards the pharynx. The anterior one-third of the nose is not covered by ciliated epithelium, but cutaneous epithelium that is like the skin. The clearance mechanism of deposited wood particles in these region is assumed to be by physical means such as sneezing, wiping and blowing (Swift and Kesavanathan 1996), which leads to a slower clearance than in the ciliated epithelium region. In a study of wood dust deposition in the nose of furniture workers (Hadfield 1972), wood particles were found to accumulate in two major regions: (i) in a small oval-shaped area on the anterior part of the nasal septum near the floor of the nose, and (ii) on the anterior part of the middle turbinate. It is noticeable that these regions also exhibit high particle deposition efficiency through the current CFD study. Inhaled wood dust depositing on these regions is retained and any toxic substance which it may contain remains in contact with this part of the epithelium for a longer time than on other regions that are covered by the ciliated epithelium (Fry and Black 1973), and therefore damages the exposed layer of soft tissues.

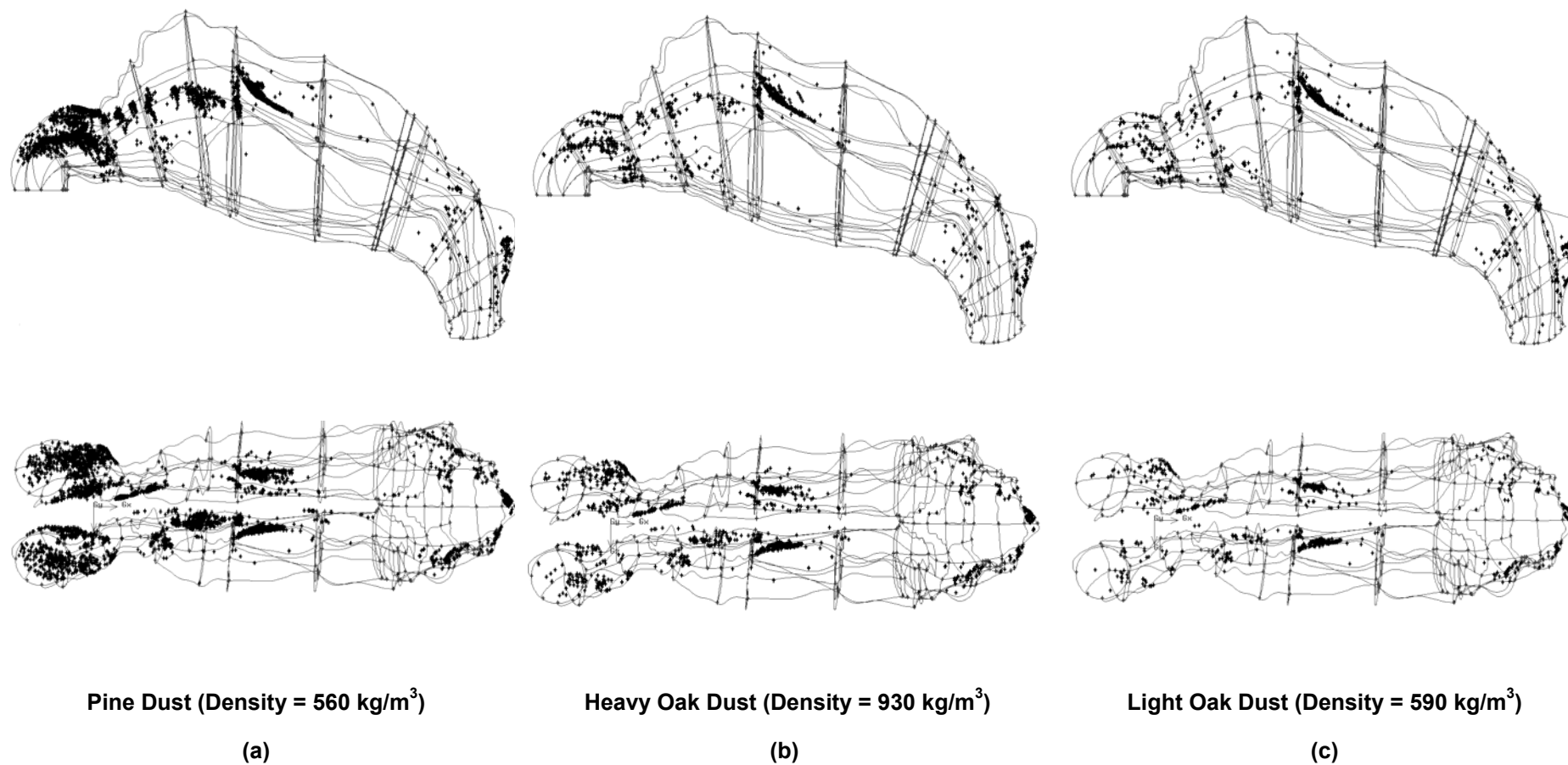


Figure 6.6 Local deposition patterns of wood dusts with different particle size distributions.

This has been confirmed by observations by Hadfield (1973) where the deposited particles washed away from the anterior end of the middle turbinate for a large number of furniture workers under investigation, produced a rough granular appearance to the naked eye, which could be surmised as a premalignant lesion.

Pine dust had much higher deposition efficiency than oak dusts in the anterior nasal segment, as it comprised much larger particles. On the other hand, oak dusts consisting of smaller particles, lead to a lower deposition. Compared with heavy oak dust, light oak dust had a lower deposition efficiency, though it had the same particle distribution as heavy oak dust. This was due to a lower material density that light oak dust exhibited and consequently a lower Stokes number.

### Particle Size Fraction Analysis of Deposited Dusts

The particle size fractions of deposited polydisperse pine particles and polydisperse light oak particles were analysed. Here, the fraction of particles with a size of  $d_p$  deposited in the  $n^{\text{th}}$  region,  $F_{n,d_p}$ , is defined as

$$F_{n,d_p} = \frac{N_{n,d_p}}{N_{n,dep}} \times 100\% \quad (6.15)$$

where  $N_{n,d_p}$  is the number of particle with a size of  $d_p$  deposited in the  $n^{\text{th}}$  region and  $N_{n,depo}$  is the number of particles deposited in the  $n^{\text{th}}$  region. Figure 6.7a and b, shows the particle size fraction of deposited pine dust and light oak dust, respectively. In Figure 8a, larger particles ( $d_p \geq 16 \mu\text{m}$ ) account for a large proportion of regional deposition in regions 1–5. Larger particles exhibit higher Stokes numbers which prevents the particles from following the curved streamlines.

As a result, most large particles deposited in the region 1-5 due to nasal valve and curved geometry where flow suddenly changes direction. Particles smaller than  $20 \mu\text{m}$  account for a very small portion of deposition in these regions due to the fact that small particles are able to follow the gas phase flow. In region 6, most deposited particles were in the range of  $16\text{-}48 \mu\text{m}$ . It is noticeable that there is a reduction in the deposition of  $55 \mu\text{m}$  particles, since most  $55 \mu\text{m}$  particles had deposited in region 1-5. A similar trend can be found for light oak dust in Figure 6.7b where deposition of large particles ( $d_p \geq 16 \mu\text{m}$ )



were dominant in region 1-6, while medium size particles had high deposition concentrations in region 7-10.

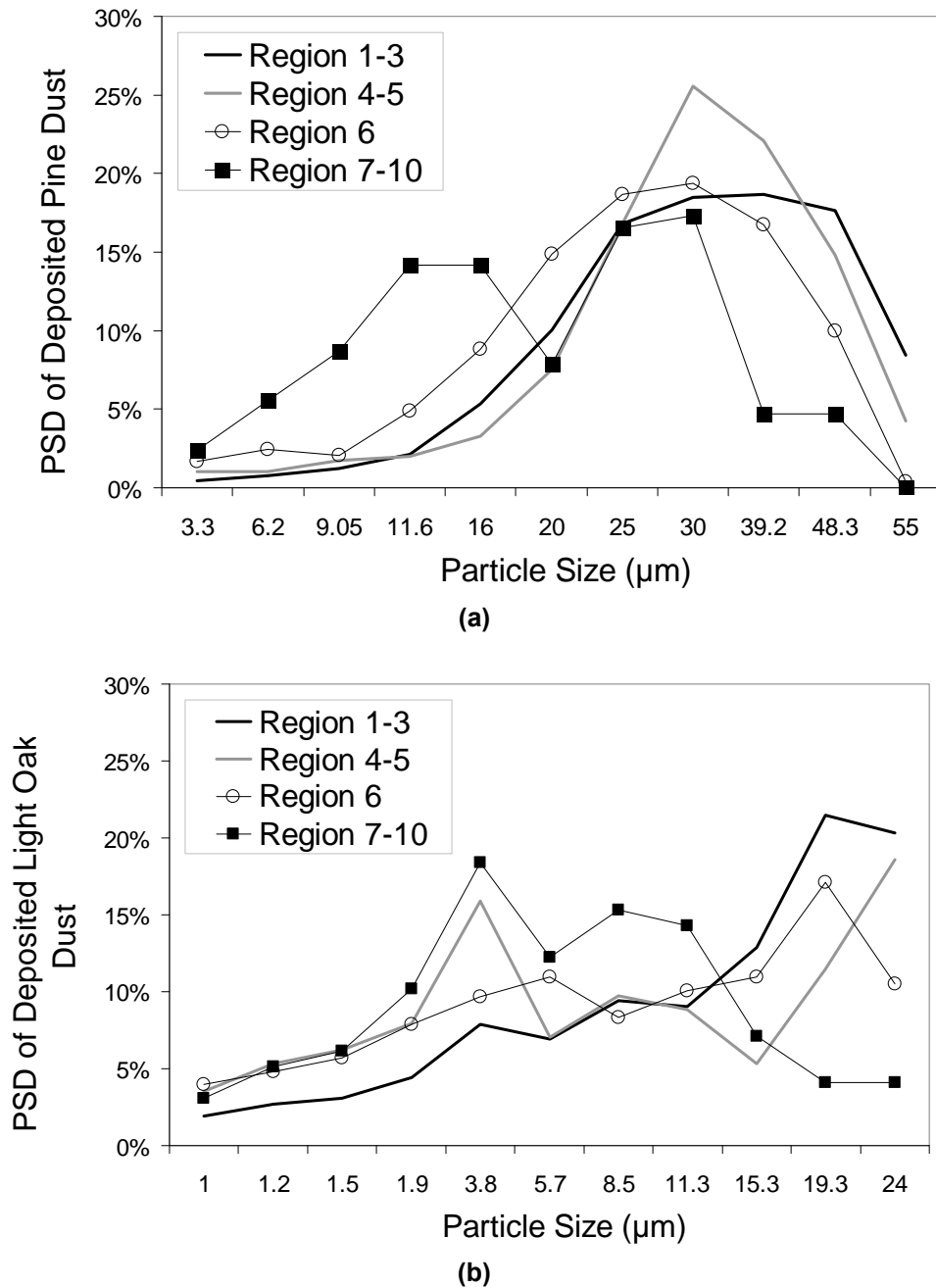


Figure 6.7 Particle size distribution (PSD) of deposited particles: (a) Pine dust, (b) Light oak dust.

Besides the particle size distribution of the pine and oak dusts generated by sawing, Chung et al. (2000) also measured their mean particle size to be 18.6 $\mu\text{m}$  and 4.9 $\mu\text{m}$  respectively. Figure 6.8 compares the cumulative regional deposition efficiency of polydispersed particles with the particle size distribution defined in Figure 6.3 compared with

monodispersed particles with size of 18.6  $\mu\text{m}$  for pine particles and 4.9  $\mu\text{m}$  for heavy oak particles. For 18.6  $\mu\text{m}$  pine particles and 4.9  $\mu\text{m}$  heavy oak particles representing the mean particle size of the pine and oak wood dust, 11,700 monodisperse particles were released spaced evenly from both nostrils with zero initial velocity. It is clear that the deposition using a polydisperse size distribution is much higher than the mean particle deposition efficiency, indicating that the mean particle diameter is not suitable for representative deposition studies.

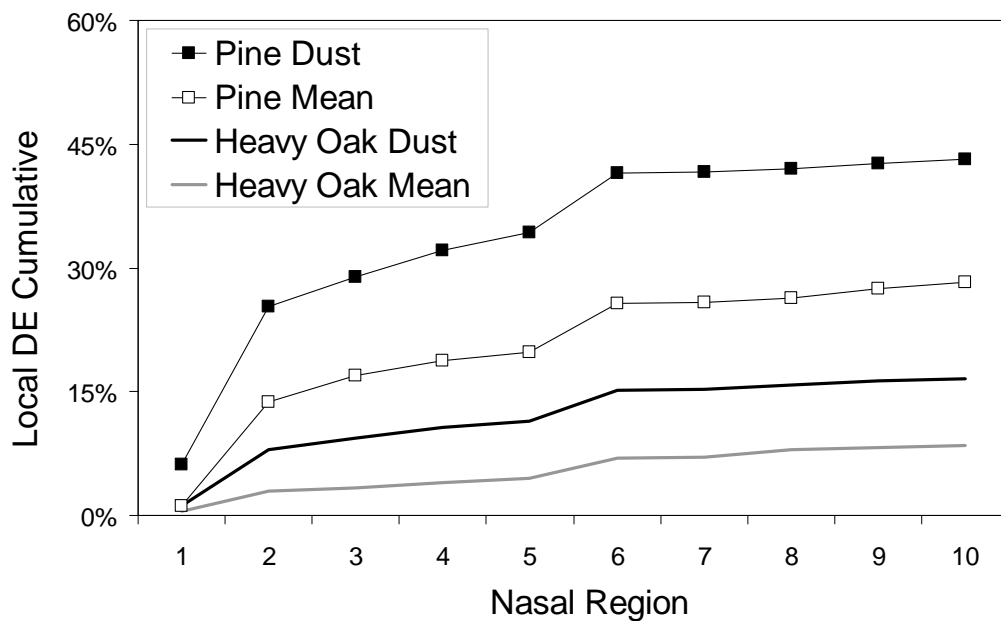


Figure 6.8 Cumulative DE of pine and heavy oak dusts and monodisperse mean particles.

### 6.3.2. Deposition Patterns of Pollen and Rough Surfaces

Pollen can be defined as a sphere-like particle with a rough surface, especially allergenic kinds such as ragweed. It may be modelled as a cluster of spheres to form a rough surface and the technique developed by Tran-Cong et al. (2004) is adopted herein. During the pollen season, pollen in the air can either be wet or dry according to the stage of pollen development. The dry pollen lacking water content was found to have a density of 550kg/m<sup>3</sup> (Crawford 1949) while wet pollen with moisture has a density of 1320kg/m<sup>3</sup> (Harrington and Metzger 1963). In the current simulation only dry pollen was considered as this is more justifiable in terms of the developed drifting pollen in the air. As aforementioned, it can be envisaged that the effects of a higher density lead to an increase

in the inertial property, enhancing the impactability of the particle and increasing the deposition.

Two pollen sizes 16 $\mu\text{m}$  and 30 $\mu\text{m}$  were investigated and the fate of each pollen was individually tracked. It was found that high deposition occurs in the frontal regions within the nasal vestibule (Figure 6.9). In between Region 2-3 lies the nasal valve region which is known to have the smallest cross-sectional area, thus causes acceleration of the fluid flow and particles. Beyond the nasal valve the particles are seen to deposit in the upper region of the nasal cavity, due to the momentum of the particles exiting the nasal valve. The deposition of particles in Region 6 may also be the cause of irritation and inflammation to the mucosal walls. Further along the nasal cavity, deposition is also seen at the nasopharynx (back of the nasal cavity) where the flow changes direction at 90° degrees, which suggests that the particle's inertia is too high to negotiate such a sharp turn and that the nasopharynx serves as an additional air filtration system for large particles (Figure 6.10).

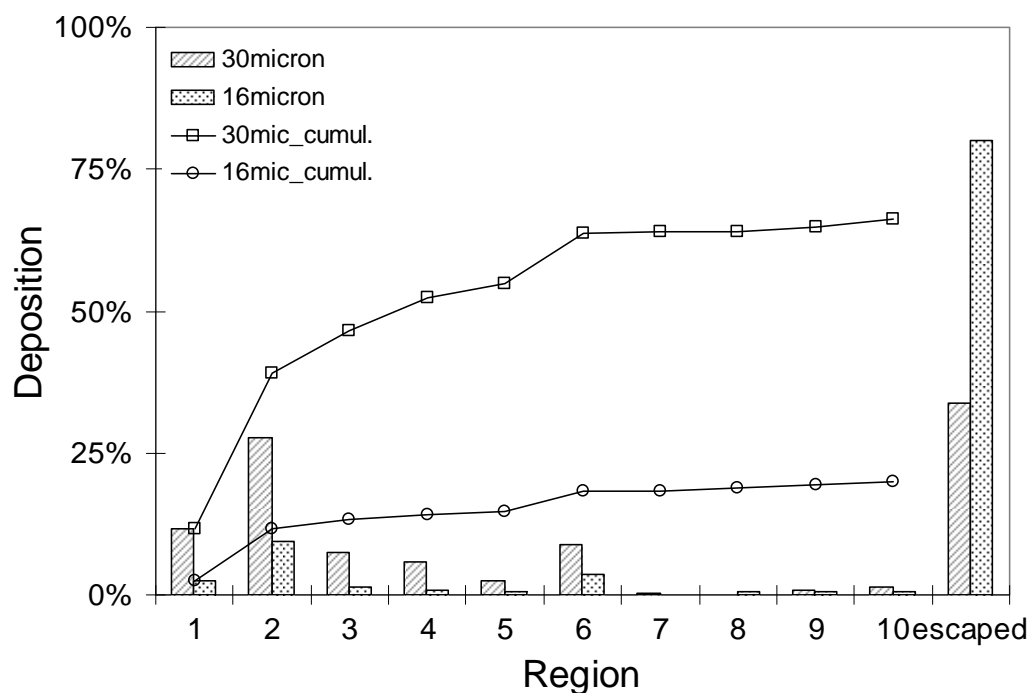


Figure 6.9 Cumulative deposition efficiency and regional deposition for 16 $\mu\text{m}$  and 30 $\mu\text{m}$  pollen particles.

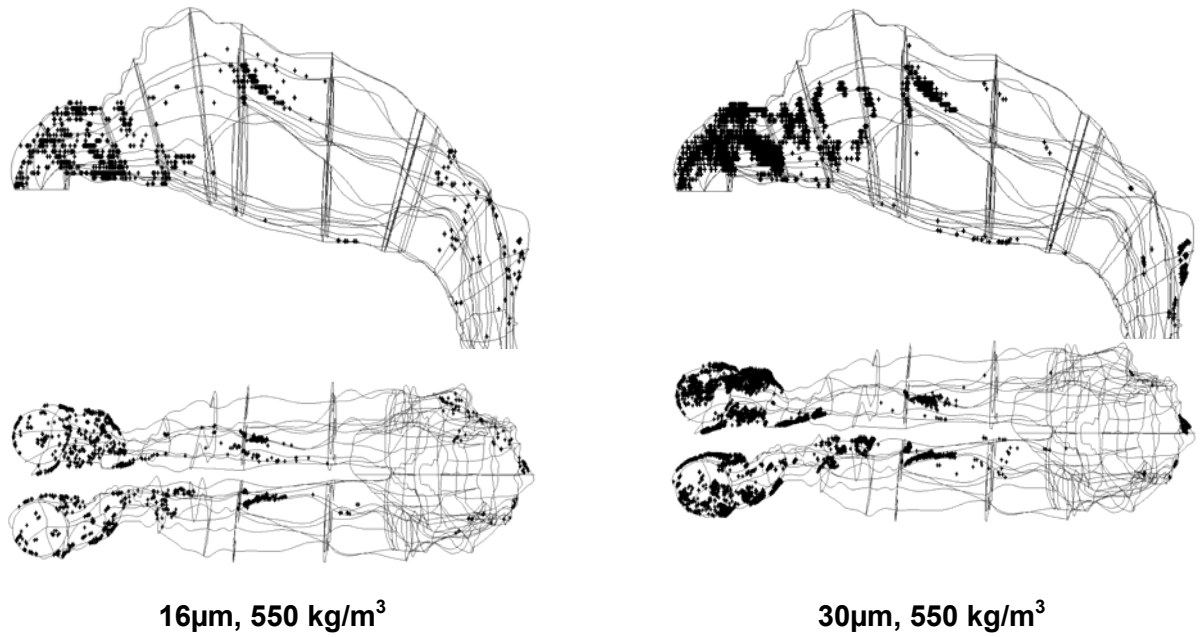


Figure 6.10 Deposition patterns for 16 $\mu$ m and 30 $\mu$ m pollen particles.

A comparison with a normal spherical particle having the same aerodynamic diameter can be made through the inertial parameter. Table 6.2 shows that a higher deposition occurs for spherical particles in comparison with near-spherical particles, although they exhibit the same inertial parameter. This is a consequence of the increased drag coefficient pertaining to the Tran-Cong et al. (2004) correlation which is higher than the drag coefficient of a spherical particle.

**Table 6.2.** A comparison of particle deposition efficiency for 16 $\mu$ m and 30 $\mu$ m pollen particles against an aerodynamic equivalent sphere.

Density	$d_{g,p}$	$d_{a,p}$	Inertial Parameter (IP)	Deposition % <i>sphere</i>	Deposition % <i>pollen</i>
550	16	11.86	23,443	30.3%	19.9%
550	30	22.25	82,500	86.0%	66.2%

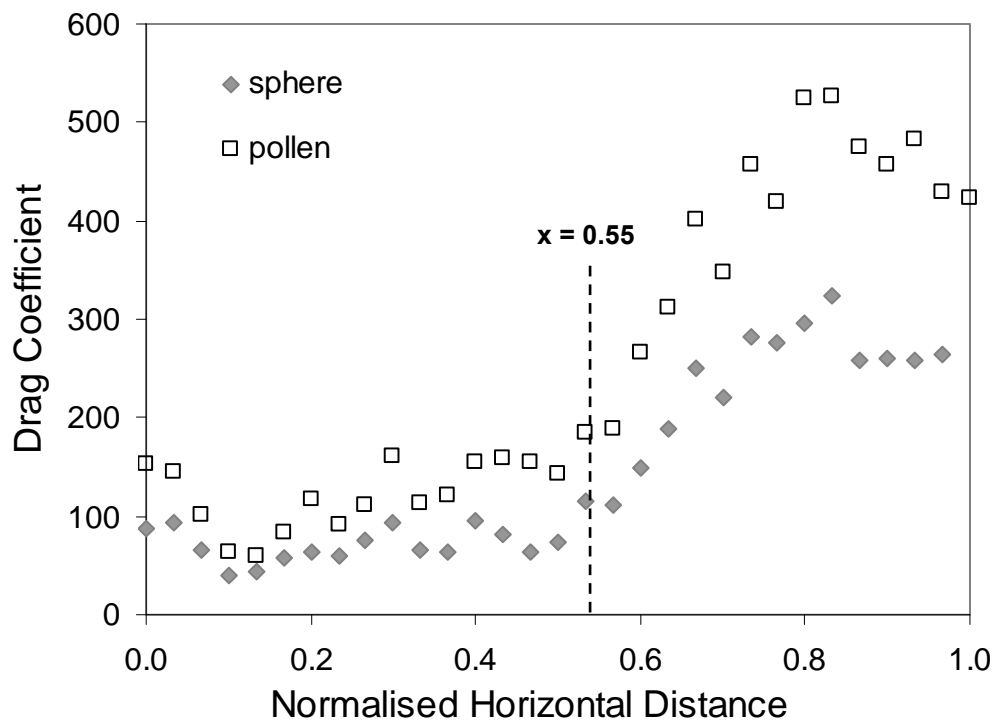


Figure 6.11 A comparison of the variation of the local average drag coefficient variation along the horizontal axial distance for a 30 $\mu\text{m}$  pollen particle and an aerodynamic equivalent sphere. (Compare with Figure 6.12)

A comparison of the drag coefficient for the pollen and sphere found that near the entrance of the airway, the drag coefficient is low for both particles and steadily increases and reaches large values near the nasopharynx region (Figure 6.11). This may be attributed to the particle Reynolds number which is dependent on the slip velocity between the particle and the fluid velocity (Figure 6.12). The increased drag coefficient assists in slowing down the particle's momentum and thus reducing the particle relaxation time (i.e Stokes number) required by the sudden changes in the flow field. The slip velocity is reduced and significant effects occur after the normalised  $x$ -position of  $x=0.55$ , around the middle region. The reduction in the slip velocity in turn reduces the particle Reynolds number, thus increasing the drag coefficient where a very small amount of deposition, is found in this later region. Additionally at  $x=0.63$ , the fluid velocity is slowed down until it is less than the inlet velocity which is due to the pressure drop associated with internal flows and the geometry of the airway.

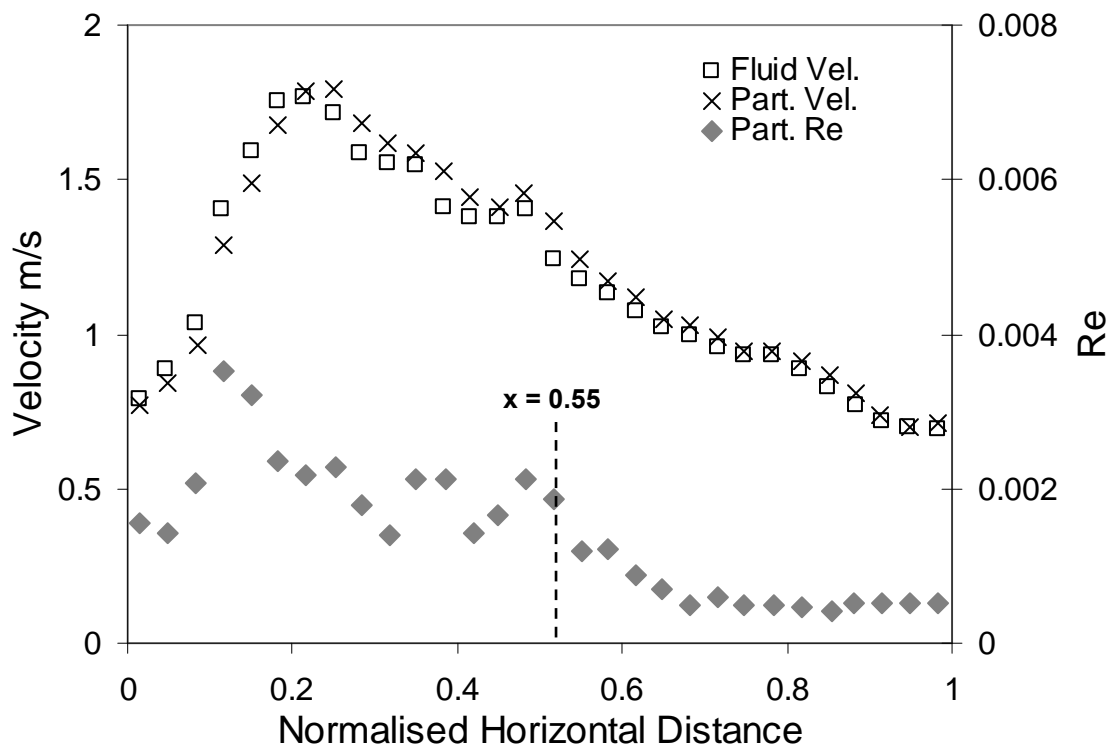
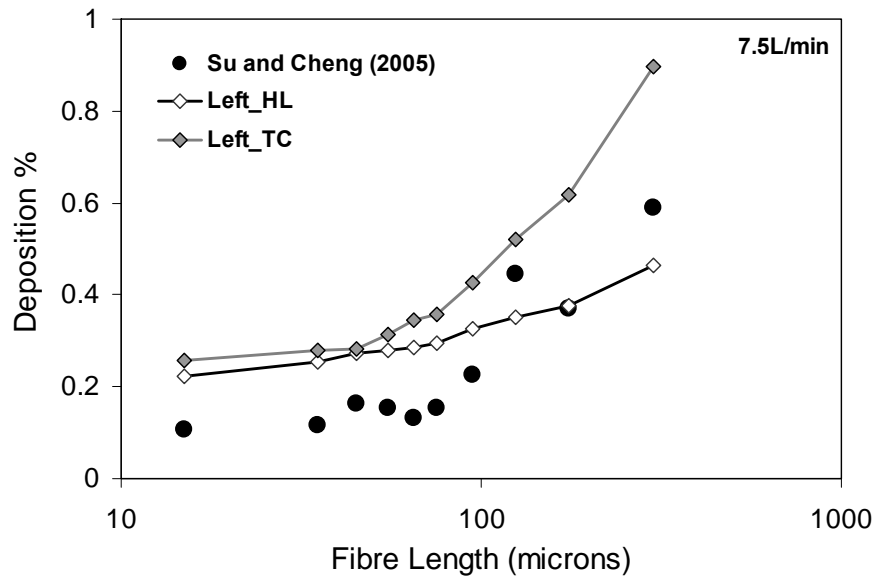


Figure 6.12 Fluid and particle velocity profile variation along the horizontal axial distance for a 30 $\mu$ m pollen particle. The particle Re number variation is also plotted which is a function of the velocity difference between the fluid and particle.

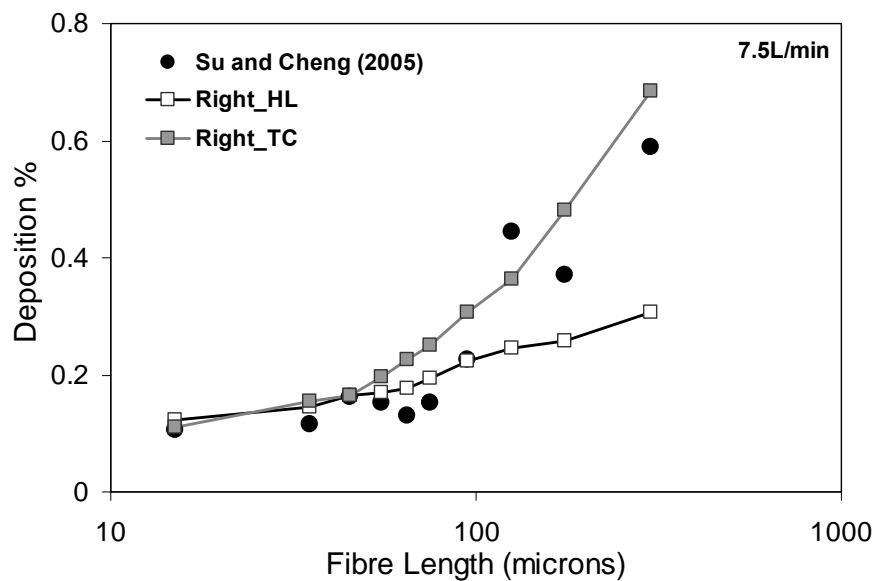
### 6.3.3. Deposition Fibres

#### Carbon Fibre Deposition

Monodisperse carbon fibres with a diameter of 3.66 $\mu$ m, density at 1.83g/cm<sup>3</sup> and varying lengths were simulated through the left and right nasal cavities at a flow rate of 7.5 L/min. The two approaches, HL-model and TC-model (see Section 6.2.4) in modelling the aerodynamic flight of the fibres were used. The simulation found close agreement between the experimental data with the deposition values of the cavity using the TC-model (Figure 6.13). At short fibre lengths the deposition difference between the two models are similar while for long fibre lengths a difference of 37% is observed.



(a)



(b)

Figure 6.13 Fibre deposition comparison in the cavity using the two different drag correlations, HL-model and the TC-model against the experimental data.

The differences between the two models are consistent and it is the handling of the drag coefficient through the model correlations that provide the variances in the particle trajectory. The HL-model uses a shape factor to define the fibre elongation where, according to its definition (Eqn.8), the shape factor of a sphere is equal to 1. The greater the aspect ratio and hence the greater length to diameter ratio, the lower the shape factor

becomes. For isometrically shaped particles the shape factor is considered the best single parameter for describing the shape of falling particles, however at low shape factors, the accuracy becomes compromised (Haider and Levenspiel 1989). On the other hand the TC-model uses a circularity parameter that has the advantage of allowing the correlation of flow dependence on particle orientation (Equation 6.14). The other major cause of deposition differences is in the nasal geometry variations between subjects as well as the differences in left and right cavities. This factor is discussed in the next section.

The drag coefficient is inherently linked to the particle Reynolds number ( $Re_p$ ) through the slip velocity from the aerodynamic flight of the particles in relation to the fluid velocity. For the velocity ( $10^{-1}$ ), particle size ( $10^{-6}$ ) and viscosity ( $1/10^{-6}$ ) scales involved, the calculated  $Re_p$  is in the range of 0.02 to 1. A longer fibre length causes greater elongation and therefore the drag coefficient increases due to the non-spherical shape. For long fibre lengths the shape factor and circularity values decrease. The differences between the two models are greatest at the longest fibre lengths where the empirical correlations become less accurate. At shorter lengths the models have closer agreement to each other and provide more accurate data fits (Haider and Levenspiel, 1989).

### **Carbon Fibre Deposition Comparisons**

The deposition fractions for the front, middle and back regions of the left and right nasal cavities were obtained and compared with experimental data (Su and Cheng 2005) from a different airway model (Figure 6.14). The deposition patterns indicate that most of the fibres pass through the nasal cavity, potentially reaching the lungs. The number of fibres passing through the cavities decrease as the fibre length increases implying that longer fibres enhance deposition. As discussed earlier, the left cavity shows greater deposition, while the right cavity produced more similar results to the experimental data. In nearly all the cases, deposition is dominant in the anterior regions. This region is characterised by the convergent-divergent shape of the nasal valve. The narrowing anterior nasal valve accelerates the bulk flow through the cross-sectional centres while localised pockets of low flow regions form around it. Posterior to the nasal valve the airway diverges and expands causing a favourable pressure gradient that induces flow separation and vortices. The nasal valve region causes violent flow patterns that enhance the fibre deposition. The middle regions generally exhibit lower deposition except for the case with fibre lengths equal to  $175 \mu\text{m}$  in the left cavity.



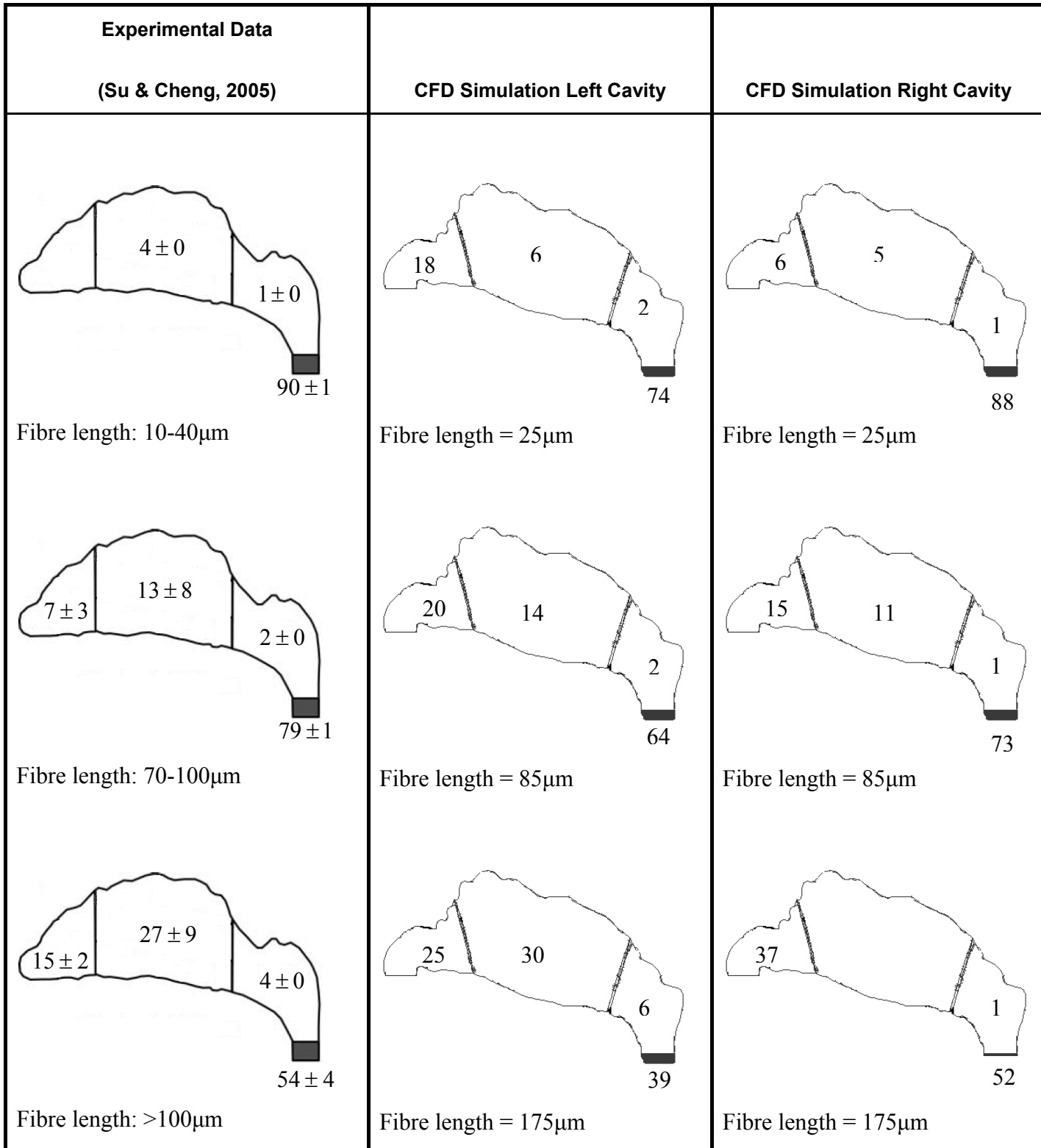


Figure 6.14 Fibre deposition patterns for an inspiratory flow rate of 7.5L/min. Deposition fractions for each region are shown as percentages.

### Asbestos Fibre Deposition

Typical values for carbon and asbestos fibres found in literature are summarised in Table 6.1. The toxicity of the fibres has been linked to its length where fibre deposition in the lungs can be carcinogenic. The CFD simulated deposition values shown in Figure 6.15 is the average deposition from the left and right cavities. The effects of fibre length on the two fibre types are markedly different. Deposition of asbestos fibres in the nasal airway is low and exhibits little variation despite the significant variation in length. The low deposition rates (14%) suggest that inhalation of the asbestos fibres will lead to deep respiratory deposition such as the lungs. In contrast the carbon fibres increase from 18% to 80% in deposition as the fibre length increases from 10 to 300  $\mu\text{m}$ . The cross-sectional diameter for the carbon fibres is approximately three times that of asbestos while the density is six times as great. The length for carbon therefore becomes more significant due to a greater mass per unit length.

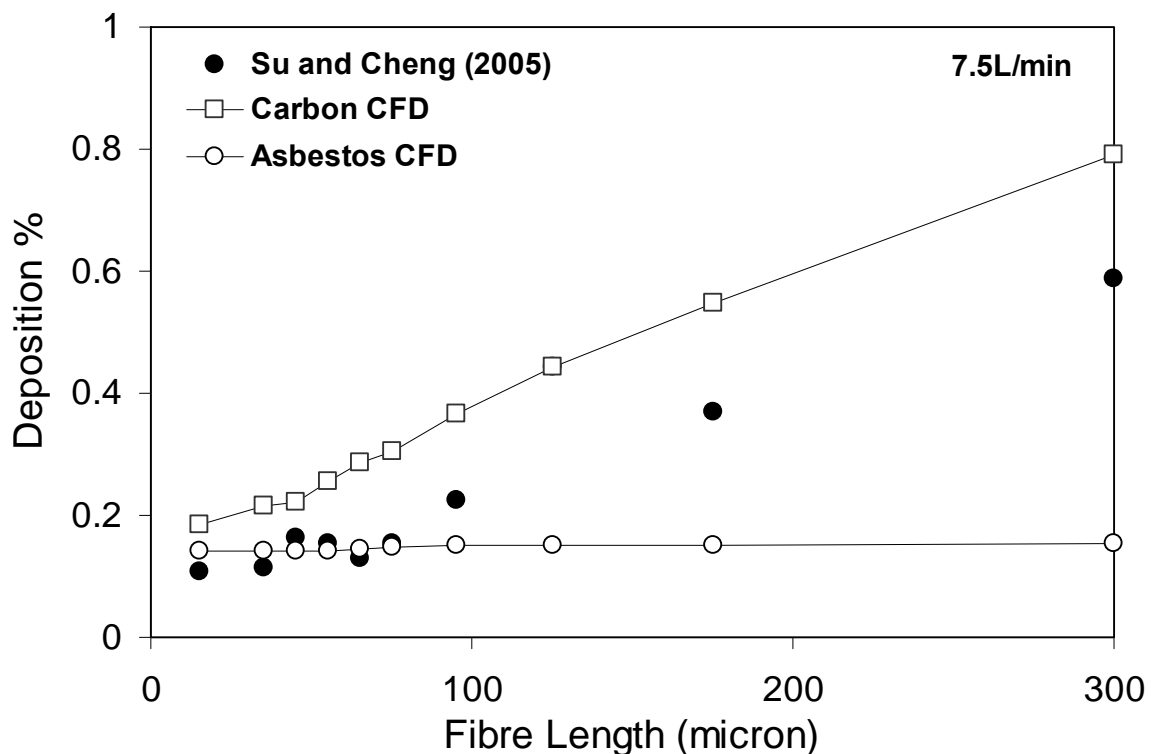


Figure 6.15 Total deposition efficiency for asbestos and carbon fibres at different fibre lengths.

The deposition patterns produced for the two different fibres show very sparse deposition for asbestos (Figure 6.16). The main deposition regions for both fibre types are found in the middle airway at the inner septum walls and also at the back region at the nasopharynx region. High deposition is also found near the nasal valve region where flow acceleration and deceleration occurs. Due to the Lagrangian tracking methodology the deposition sites shown consider only particle deposition by inertial impaction, where it was found by Su and Cheng (2005) that fibre deposition in the nasal airway is mainly due to impaction and that short fibres could have the same deposition fraction as long fibres in a specific nasal airway region or subregion, as long as the inertial parameter for both fibres are in the same range. However for asbestos ( $d_{ae} \approx 1\mu\text{m}$ ) at low flow rates such as 7.5 L/min the inertial parameter is low and deposition by interception may have a slight increase for very long fibre lengths. Deposition by interception can occur if the particle travels close enough to a surface of the airway passages where an edge of the particle touches the surface. Usually the fibre length determines whether the particle will be intercepted. Typical fibres with a diameter of  $1\mu\text{m}$  and a length of  $200\mu\text{m}$  have been found to deposit in the bronchial tree (Sussman et al. 1991). Although the nasal airway is more treacherous in comparison to the tracheobronchial airway, the nose is much larger in size and the effects of deposition of long fibre lengths would be marginal.

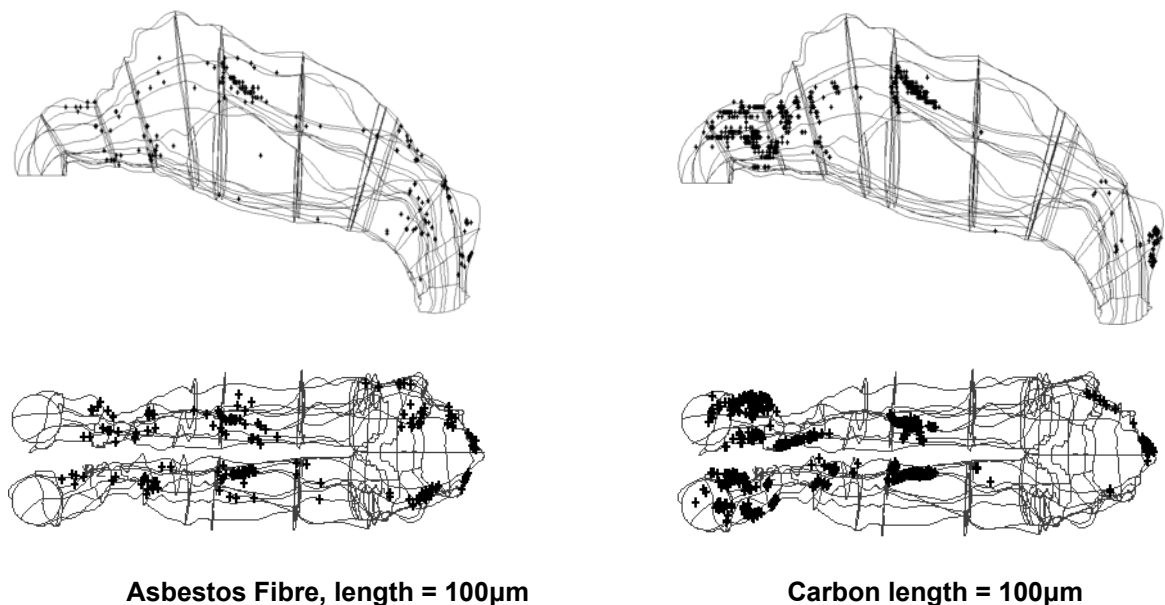


Figure 6.16 Deposition patterns for asbestos fibres and carbon fibres at a fibre length of  $100\mu\text{m}$  at a flow rate of 7.5L/min.

### Comparison of Fibre and Spherical Particle Deposition

Normalisation of the fibres can be performed through correlations from Stöber 1972) for an equivalent aerodynamic diameter ( $d_{ae}$ ) given as:

$$d_{ae} = d_{ve} \sqrt{\frac{\rho}{1000 \cdot \kappa}} \quad (6.16)$$

where  $d_{ve}$  is the volume equivalent diameter,  $\rho$  is the density of the fibre and  $\kappa$  is the dynamic shape factor for a prolate spheroid. The dynamic shape factor taking the length oriented perpendicular to the flow is given as:

$$\kappa_{\perp} = \frac{\frac{8}{3}(\beta^2 - 1)\beta^{1/3}}{2\beta^2 - 3 \sqrt{\beta^2 - 1} \ln(\beta + \sqrt{\beta^2 - 1}) + \beta} \quad (6.17)$$

and also for the length oriented parallel to the flow is given as:

$$\kappa_{\parallel} = \frac{\frac{4}{3}(\beta^2 - 1)\beta^{1/3}}{2\beta^2 - 1 \sqrt{\beta^2 - 1} \ln(\beta + \sqrt{\beta^2 - 1}) - \beta} \quad (6.18)$$

where  $\beta$  is the aspect ratio and is defined as the ratio of the fibre length to the diameter. For random orientation of the fibre, the shape factor is a combination of the two orientations and is given as:

$$\frac{1}{\kappa_R} = \frac{1}{3\kappa_{\parallel}} + \frac{2}{3\kappa_{\perp}} \quad (6.19)$$

Taking the random orientation for the dynamic shape factor, the equivalent aerodynamic diameter range for carbon fibre is 7.6-12.8  $\mu\text{m}$  for lengths of 10-300  $\mu\text{m}$  respectively. For asbestos fibres at the same length range, the  $d_{ae}$  range is 1.0-1.6  $\mu\text{m}$ . This is due to the properties of asbestos exhibiting a smaller density and a small cross-sectional diameter causing the  $d_{ae}$  to be independent of its length.

The deposition of the carbon and asbestos fibres over a range of the inertial parameter (Equation 6.15), is used to compare against previous studies of total deposition efficiencies of monodispersed spherical particles over the nasal cavity as an entire unit (Figure 6.17). The deposition efficiency increases as the inertial parameter increases. The range in which the deposition efficiency reaches 90% or more is from 20,000 (Cheng et al. 2001) to 50,000 (Su and Cheng 2005). The simulation results used the TC-model and

show the combined deposition efficiency for the left and right cavity. For  $IP < 10,000$  the deposition efficiency is higher for the simulation than for Su and Cheng (2005). The higher values for the smaller inertial particles may be improved by the addition of a wall roughness model (Shi et al., 2007). An empirical correlation by Kelly et al. (2004) to curve fit their experimental data was given as,

$$\eta = 1 - \exp\left(-(\alpha \cdot d_{ae}^2 Q)^\beta\right) \quad (6.20)$$

where the coefficients are,  $\alpha = 5.86e-5$ ,  $\beta = 2.1892$ .

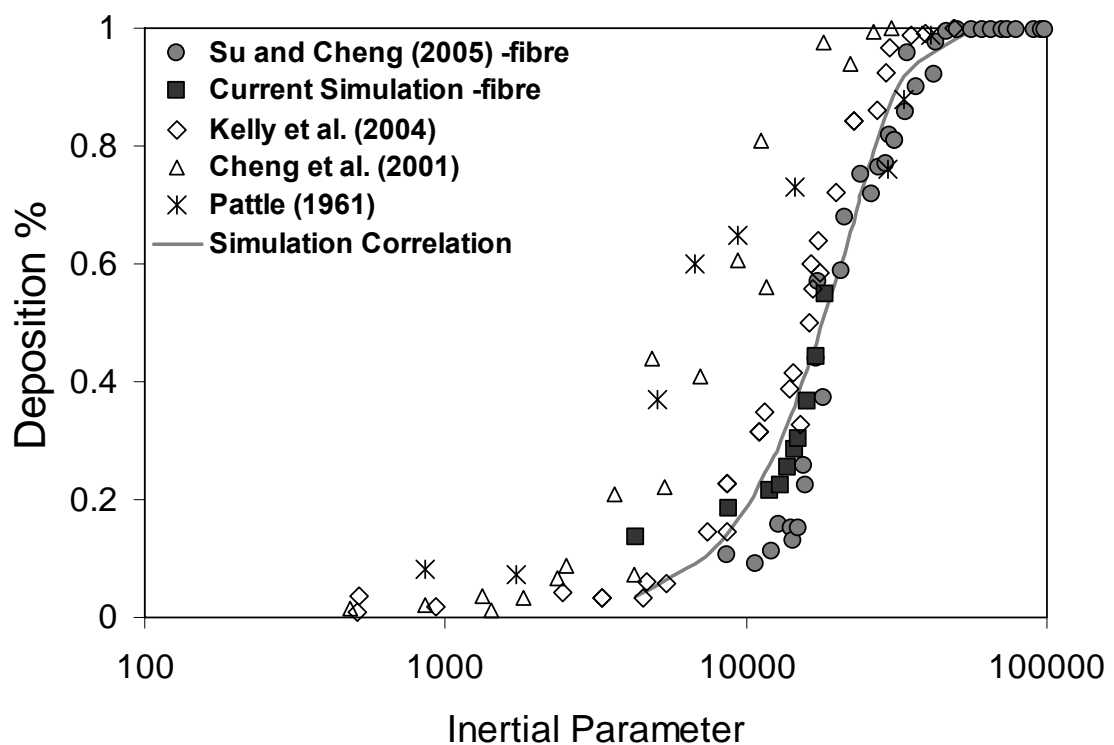


Figure 6.17 Comparison of deposition efficiencies between fibres and spherical particles using the Inertial Parameter.

Similarly a correlation for the fibre deposition efficiency was found using MatlabR2006b (Mathworks USA) software to program the Levenberg-Marquardt algorithm for constant determination. The coefficients for the correlation given in Equation 6.21 are  $\alpha = 4.654e-5$ ,  $\beta = 2.054$ .

The deposition efficiency curves helps to predict the deposition for a given aerodynamic diameter and flow rate. With the production of man-made fibres, there is an opportunity to

control properties of the fibre that may lead to adverse health effects such as the fibre length. In the case of carbon fibres, the longer fibre lengths helped increase deposition within the nasal cavity thereby reducing the potential deep lung inhalation. Conversely deposition of asbestos fibres was found to be independent of their lengths given the lighter density and smaller diameters. By taking the product of the density with the cross-sectional area, the parameter of mass per unit length,  $\rho A_{cross}$  [kg/m], is used to define the resulting  $d_{ae}$ . Table 6.3 shows the significance of the fibre lengths on the effects of  $d_{ae}$  for different  $\rho A_{cross}$  values. The deposition of the fibres can then be predicted by using the resultant  $d_{ae}$  for the fibre in question and applying the deposition efficiency curve correlation (Equation 6.21). The  $\rho A_{cross}$  value for asbestos and carbon fibre is 300 and 19390, respectively. As  $\rho A_{cross}$  increases,  $d_{ae}$  increases as expected but is most significant in the smaller length range.

**Table 6.3** A comparison of particle deposition efficiency for Asbestos, Carbon fibre and other arbitrary fibres with varying  $\rho A_{cross}$  values.

	Density (kg/m <sup>3</sup> )	Diameter ( $\mu$ m)	$\rho A_{cross}$ (kg/m)	Length ( $\mu$ m)	$d_{ae}$ ( $\mu$ m)	Equivalent $d_{ae}$ total deposition (%)
<b>Asbestos</b>	300	1	300	10	1.09	0.00
				100	1.44	0.01
				300	1.59	0.02
<b>Carbon fibre</b>	1830	3.66	19390	10	7.60	10.1
				100	11.38	42.8
				300	12.84	60.1
<b>Fibre 1</b>	1000	3.56	10000	10	5.49	2.8
				100	8.20	13.5
				300	9.25	21.2
<b>Fibre 2</b>	3190	4	40000	10	10.69	35.1
				100	16.18	90.7
				300	18.31	98.1

## 6.4. Conclusions

The effects of particle morphology on deposition patterns and deposition efficiencies were found to be significant for nasal airway deposition. In the human nasal cavity, the dominant mechanism of deposition is by inertial impaction, especially for particles greater than  $5\mu\text{m}$  at low flow rates (7.5-15L/min). Under these conditions, the inertial parameter is a useful tool that allows comparisons between particles that exist in this inertial framework. Thus aerodynamic factors pertinent to the particle morphology such as the shape factor must be accounted for through the drag coefficient. Appropriate empirical correlations were utilised to consider the aerodynamic flight of the typical inhalants.

Wood dust was modelled as a spherical particle where the major particle deposition sites included the nasal valve region and anterior section of middle turbinate. Pine dust had high deposition efficiency in the nasal cavity in comparison with heavy and light oak dusts, due to the fact that it comprised much larger particles in its particle size distribution. On the other hand, this indicates that dusts with a large amount of fine particles, such as those generated by fine sanding, may penetrate the nasal cavity and travel further into the lung. Allergenic ragweed pollen and toxic asbestos fibres were also considered. It was found that about 20% of  $16\mu\text{m}$  pollen particles deposited in the main airway while for  $30\mu\text{m}$  pollen particles, 66.2% deposited. These values are smaller when compared with a sphere having the same aerodynamic diameter which indicates that the drag coefficient for pollen is greater than for a spherical particle. For asbestos fibres, where the density and cross-sectional diameter is small, the fibre length is seen to be insignificant for the deposition efficiency. It was seen that the deposition increased from 8.7%-9.6% for an increase in fibre length of  $10\mu\text{m}$  to  $300\mu\text{m}$ . Conversely, carbon MMVFs with higher density and larger cross-sectional diameter exhibits greater mass per unit length, thus its deposition increased from 14%-50% over the same fibre length range. This comparison supports the current practice of replacing asbestos with carbon MMVFs in building materials in the prevention of respiratory diseases, where deposition of the fibres in the nasal cavity is increased, reducing deep lung deposition. It is imagined that these results may assist in the design of new aerosols and guide practical clinical tests for toxicological.

The geometry of the nose and the physiological mucociliary (nasal hair) movement acts as a filtering function to prevent foreign particles entering the main nasal passage. Hence this

may be the product of evolutionary change in producing such a geometry. While harmful particles are best kept out of the nasal cavity, drug particles delivered into the airway needs to deposit in the highly vascularised mucus walls to allow the absorption of the drug composition into the blood stream. Therefore the delivery of the drug particles must overcome the evolutionary developments of the nasal cavity. The following two chapters aim to obtain knowledge of nasal spray atomisation and how the parameters associated with the atomisation will affect the initial particle conditions that are required for the CFD simulations.



# CHAPTER 7

## Determining Significant Nasal Spray Parameters for CFD

### 7.1. Introduction

Nasal drug delivery provides an alternative approach to traditional delivery methods such as oral drug routes that fail in the systemic delivery of compounds due to its dissociation by the digestive system. The nasal airway is dominated by the nasal turbinates; that are lined with highly vascularised mucosa that contain openings to the paranasal sinuses. Because of these characteristics it is hypothesised that drug delivery to combat health problems such as lung diseases, cancers, diabetes, sinus infections etc. may be viable if the drug formulation can be deposited in the turbinate region (Kimbell et al. 2004). However this requirement tends to be poorly implemented where a large proportion of the drug particles are known to deposit in the anterior regions of the nasal vestibule, attributed to the sprayed particles existing in a high inertial regime (Inthavong et al. 2006; Kelly et al. 2004; Zwartz and Guilmette 2001). Therefore studies into local particle deposition becomes of great significance in the delivery of drugs via the nasal airway. Knowledge of initial conditions from the atomised drug particles introduced into nasal cavity as well as the deposition mechanisms caused by the interaction of drug particles with the air flow field is required in order to develop optimised delivery devices (nasal sprays) and correct drug formulations.

The function of the delivery device is to atomise the liquid formulation into a fine spray made up of small micron sized particles. Although the physics of sprays and atomisation has been studied quite extensively the majority of the research has focussed on industrial applications, such as fuel injectors (Gao et al. 2005) and spray dryers (Straatsma et al. 1999), resulting in a lack of experimental data for nasal spray applications. Moreover there exists a great difficulty in the ability to capture detailed measurements of the dense spray found at the near-nozzle region which has hindered the understanding of the atomisation process. Despite this, there have been experimental studies documenting nasal particle deposition in the inertial regime by *in-vivo* (Kesavanathan et al. 1998; Newman et al. 1998) as well as *in-vitro* (Kelly et al. 2004; Swift 1991; Zwartz and Guilmette 2001) methods. From these studies, deposition efficiencies were correlated with an inertial parameter that is a function of the flow rate, particle diameter and density. However these studies investigated the natural inhalation of suspended particles from the surrounding air which was drawn into the nasal cavity through an extended pipe connected to the nares.

Nasal particle deposition delivered by a spray device was performed by (Cheng et al. 2001) using a multi-sectional nasal airway replica model and found deposition patterns from four different nasal spray pumps. The results showed the particles deposited mainly in the anterior and turbinate regions and that deposition in the anterior region increased with an increase in spray cone angles and larger particles. (Suman et al. 2002) investigated deposition patterns in relation to *in-vitro* measurements of two different nasal spray pumps having different performance characteristics. It was found that spray characteristics, such as spray angle and plume geometry did not affect the distribution of droplets in the nose. The discrepancy between the two correlations may be attributed to numerous variations that exist in nasal spray applications that are hard to quantify experimentally (Table 7.1). Furthermore *in-vivo* methods are not able to provide precise and detailed information regarding initial particle conditions and its relationship to the specific deposition site within the nasal passage.

**Table 7.1** Variables related to the actuation of a nasal spray

Consumer Variables	Parameter affected
Increased / Decreased inhalation:	Air flow rate

---

Nostrils opened (one or two):	Air flow pattern
Head tilt back/forward:	Insertion angle inwards
Spraying away from septum walls:	Insertion angle sideways
Strength of actuation:	Particle size and velocity
Speed of actuation:	Particle size and velocity
Insertion location:	Surrounding geometry

---

## 7.2. Experimental Setup

### 7.2.1 Particle Image Velocimetry (PIV)

Particle Image Velocimetry (PIV) is a technique that allows for the instantaneous measurement of two components of fluid velocity within a plane defined by a laser sheet. PIV has very recently matured and proven to be a powerful tool for studying a wide range of fluid flows. In this section, a brief introduction to PIV system is presented.

PIV is a technique that measures the instantaneous velocity field within an illuminated plane of the fluid field using light scattered from particles seeded into the fluid. The light scattered from these particles is collected and imaged using a camera at two separate times so that the displacement of the particles can be measured Figure 7.1. Using a laser as a light source, it is possible to very accurately locate and shape this illuminated plane so that one can make measurements within a very thin measurement volume. One of two methods is generally used to control this timing of image acquisition. The two images may be obtained using a continuous laser sheet and a regulated shutter on the camera. Alternatively, the camera can gather scattered light over an extended period while the pulsing light source controls the precise timing of the particle images. Using a pulsed laser, it can be ensured that each of these image pairs may be obtained at an effectively instantaneous time and that the precise time separation between the two images of the pair is known. During the time between these two images, the particles within the fluid will move a distance that is proportional to the fluid velocity. After obtaining the images, the

local fluid velocity,  $u$ , is found from  $u = \delta/\Delta t$  where  $\delta$  is the particle displacement and  $\Delta t$  is the time between the two images.

PIV systems use digital cameras and computers to perform the image acquisition and measurement the particle displacement. Successive image pairs of the particles within a laser plane are captured with a high-speed digital CCD (Charge-Coupled Device) camera. Using a pulsed laser, each of these image pairs is obtained at an effectively instantaneous time. As the precise time separation between the images pair is known, it is possible to calculate the local velocity at any sub-region of these acquired images by measuring the distance that particles have traveled between these images.

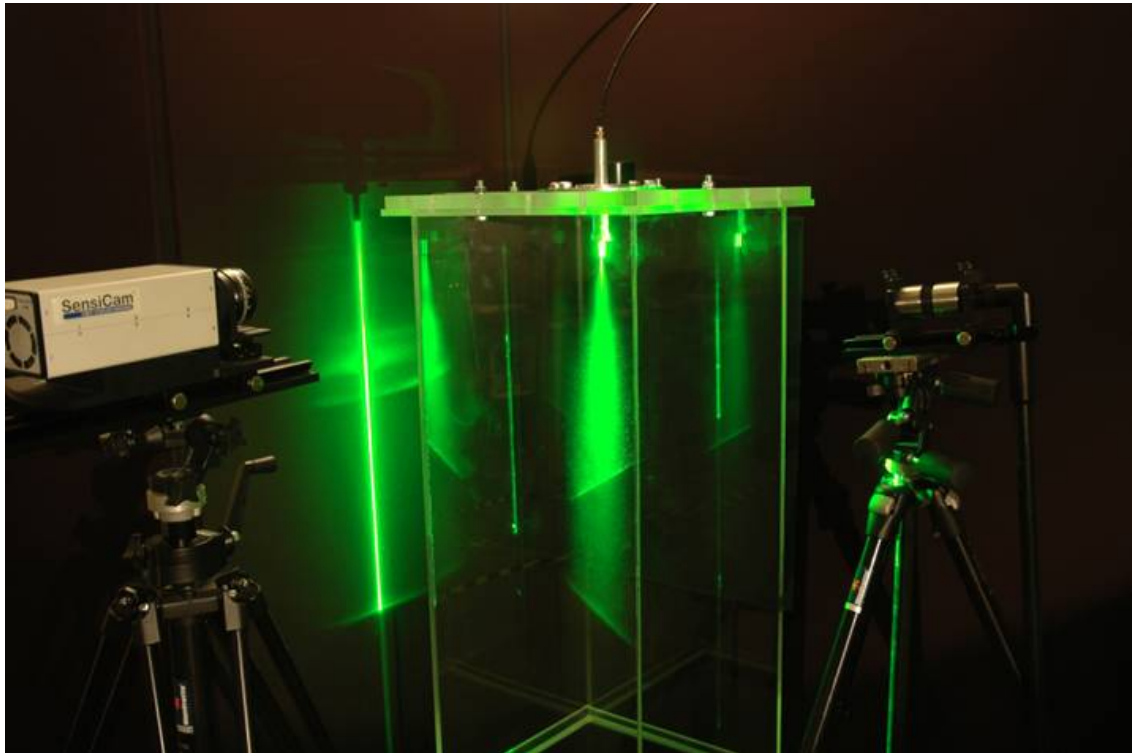
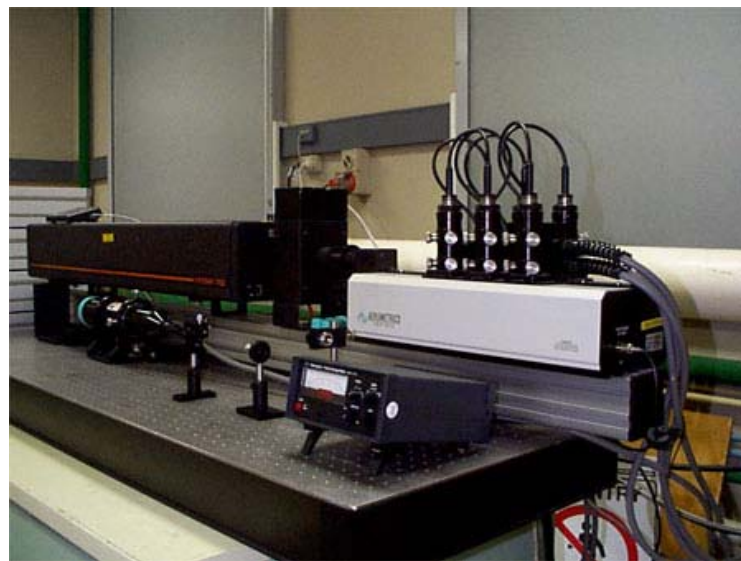


Figure 7.1 Experimental PIV setup

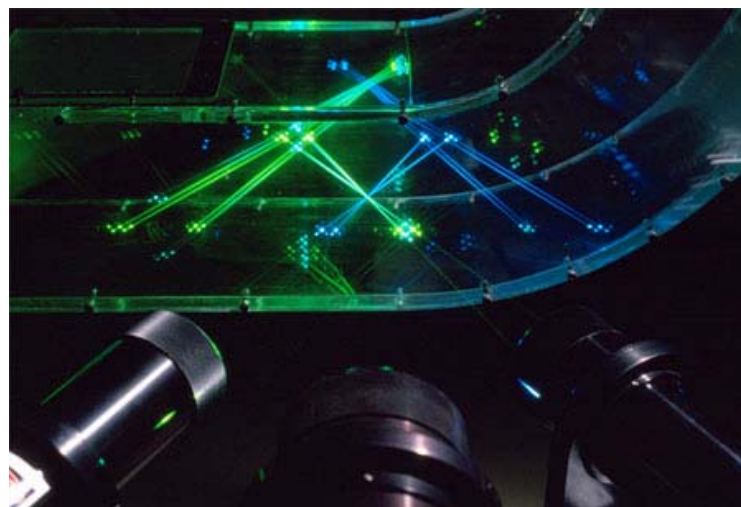
### 7.2.2. Phase Doppler Particle Analyser (PDPA)

The Phase Doppler Particle Analyser is based upon the principles of light scattering interferometry. The laser beam pairs intersect into a single point at the sample volume

location forming an interference fringe pattern. When a drop passes through the interference fringe patterns of the two laser pairs, the scattered light sweeps past the receiver aperture at the Doppler difference frequency, which is directly proportional to the drop velocity. The spatial frequency shift of the fringe pattern is inversely proportional to the drop diameter. Typically sampling rates can reach up to 800MHz. The PDPA analyser rejects signals, which do not meet a series of threshold values that are set as criteria. These settings are critical to the accuracy of the data analysis routine. A data analysis routine is used to convert the raw data into meaningful drop size distributions. Typical PDPA analysers measure sizes in the range of  $0.5\mu\text{m}$ - $10,000\mu\text{m}$ .



(a)



(b)

Figure 7.2 (a) PDPA system used at the CSIRO laser diagnostics laboratory (b) PDPA system in use.

### 7.2.3. Experimental Test Station

The experimental setup employed for this study is shown in Figure 7.3 which includes a test chamber, a pressurised water supply system, a liquid collection system and a visualization system. The test chamber was constructed of clear perspex box enclosing the spray nozzle that pointed downwards. Water was stored in a pressure tank and was fitted with a pressure line that had an allowable maximum operating pressure of 600kPa, at one end and a pressure regulator fitted at the outlet end. The maximum pressure was applied at the upstream and a pressure regulator was used to monitor a constant pressure in the system. The pressure at the spray nozzle would be slightly smaller than the reading at the regulator due to head losses, however this was not significant as the primary aim was to obtain qualitative images. Two visualization systems were employed: i) particle image velocimetry (PIV) which will provide an approximate velocity field ii) a phase doppler particle anemometry (PDPA) which enables detailed imaging of the spray and the formation of droplets. An ILA 2D PIV system was used, consisting of a SensiCam 12-bit digital CCD camera (1280×1024 pixels), which was synchronised with a New Wave 120 mJ double-cavity Nd:YAG Laser.

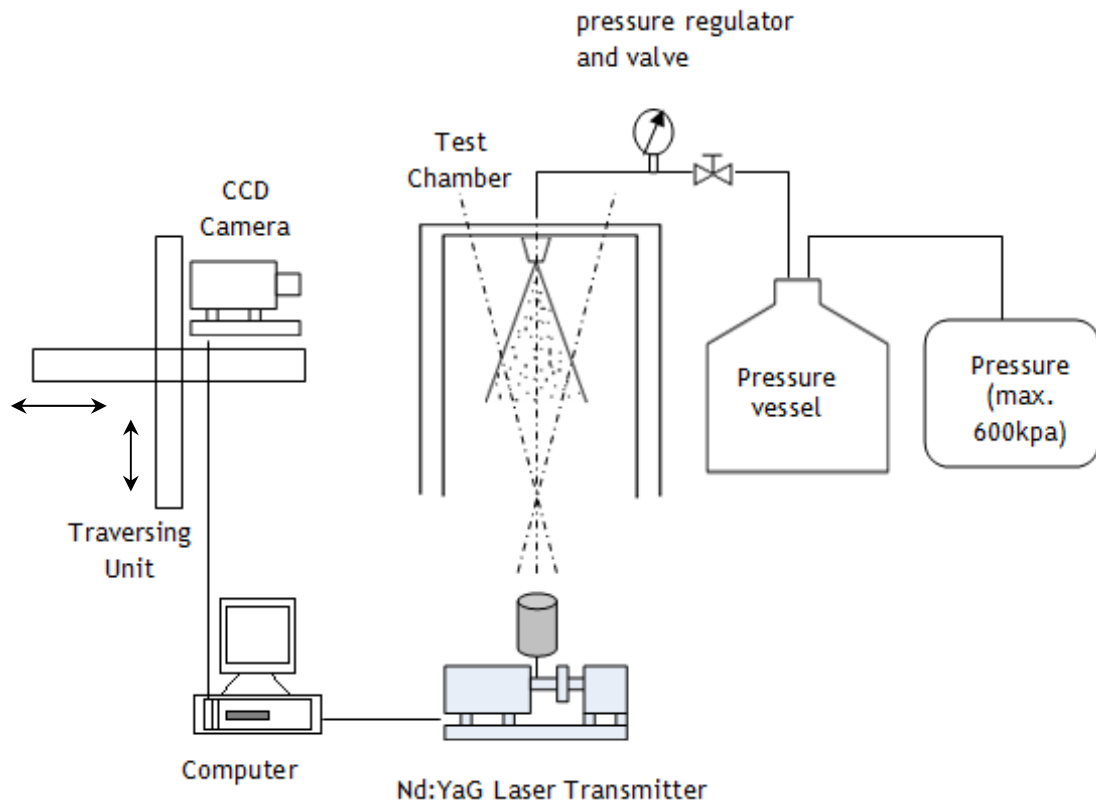


Figure 7.3 Schematic of the experimental setup for spray visualization.

In the PIV measurement, 800 pairs of successive images were taken at the laser repetition rate of 4 Hz (Figure 7.1). Hence, a mean velocity flow pattern was obtained by statistically averaging 800 successive instantaneous velocity vector maps over approximately three minutes. For capturing of the spray, an Oxford Laser PDPA system was used. The CCD camera was situated approximately 10cm from the test chamber which was dependent on the camera focal length. A long distance microscope lens provided a magnification of 2.46 offering a resolution of approximately  $3.01 \mu\text{m}/\text{pixel}$ . Thus each image, at  $1280 \times 1024$  pixel resolution was only able to capture a physical region of  $3.85\text{mm} \times 3.08\text{mm}$ . The camera was mounted on a traversing unit which allowed precise movements in all three coordinates to reposition the camera in order to capture the spray in full. A constant upstream pressure of 600kPa was applied and the water was released through a pressure regulator-valve and allowed to reach steady conditions before the images were taken. A single run was limited to approximately three minutes in order to avoid pressure variations associated with a decreasing liquid volume within the pressure tank. The spray nozzle

used in the present study was a nasal spray device kindly provided by Saint-Gobain/Calmar, Product Number 43110-016.

## 7.3. Results and Discussion

### 7.3.1. Spray Characterisation

Figure 7.4 shows two images of the spray that include (a) a single image at the near-nozzle region and (b) a portrait of the spray from the merging of all single images taken at different areas of the spray. It was observed that the pressure induced by the nasal spray actuation caused the liquid to emerge from the orifice under the action of both radial and axial forces. A swirling thinning sheet of liquid was formed which was unstable, breaking up into ligaments before forming particles at a distance, called the break-up length, from the nozzle (Figure 7.4b).

A hollow spray cone was produced at the break-up length with the majority of particles located at the periphery of the hollow cone (Figure 7.5). This atomisation process is typically found through the use of pressure-swirl type atomisers that are contained within the spray nozzle. Theory of pressure-swirl atomisation have been studied extensively for the last century with the vast majority of literature focussed on high pressure applications, such as fuel injectors found in the automotive industry.



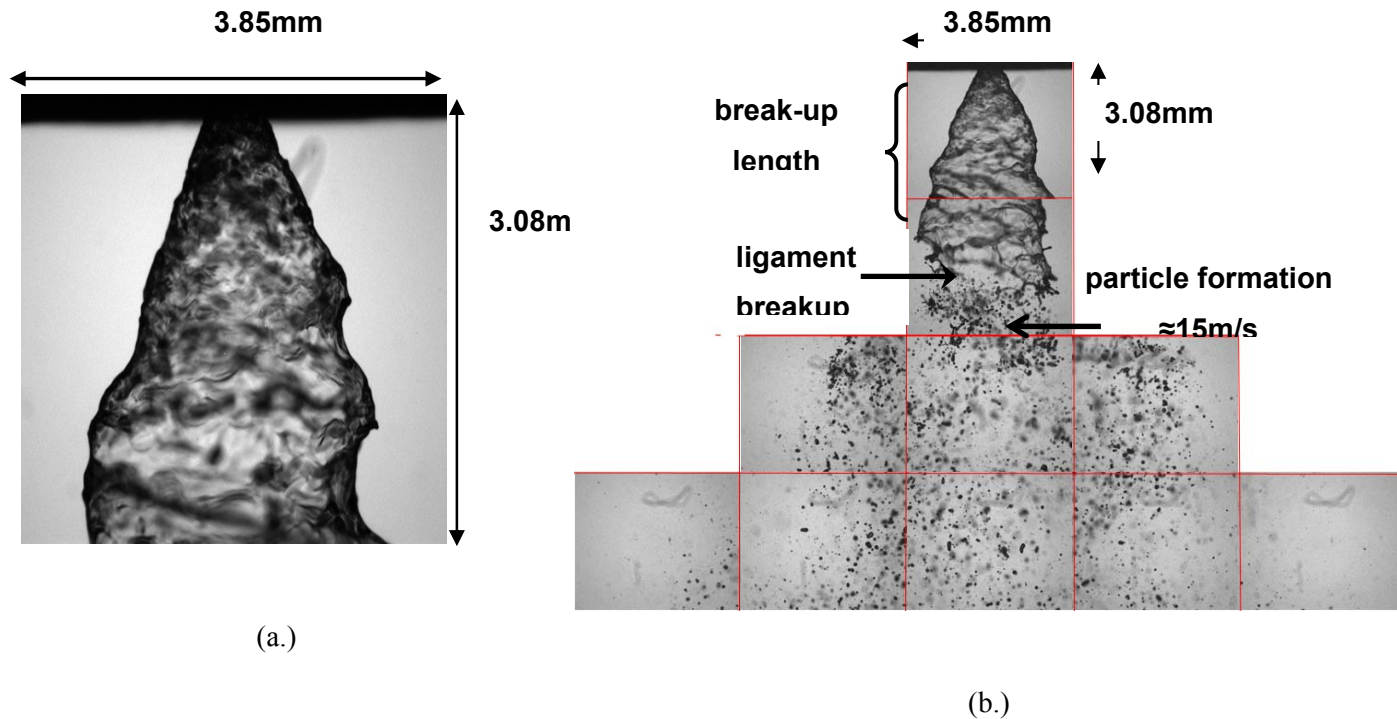


Figure 7.4 a.) Single image at the near-nozzle region showing a swirling hollow sheet of liquid. b.) Collated image from the individual single images to create the entire spray field.

Although little has been researched on nasal spray applications it is evident that the key parameters that may influence nasal drug deposition are: nozzle diameter, spray cone angle, swirl effects and break-up length. The diameter at the break-up length is important in terms of particle initialisation in the computational model as the particles need to be defined at the break-up length rather than at a point source at the nozzle exit.

This can be approximated by

$$d_{bul} = 2(d_n + L_{bu} \tan \phi) \quad (7.1)$$

where  $d_{bul}$  is the diameter at the break-up length,  $\phi$  is the half angle between the spray sheet and the spray centreline (Figure 7.4a),  $L_{bu}$  is the break-up length and  $d_n$  is the nozzle diameter. However this linear approximation doesn't take into account any momentum losses during the entire spray penetration and gives an over-prediction of the diameter as  $L_{bu}$  is further downstream. Because of sensitive information regarding corporate patents over the design of nasal spray devices, detailed information is not attainable to quantify some of the design parameters such as the nozzle diameter, pressure-swirl chambers and

cone angles. By applying the camera magnification ratio  $1\text{pixel}:3\mu\text{m}$  to the images, and using imaging analysis software (Adobe Photoshop CS) measurements for the cone angle, nozzle diameter and break-up length were ascertained and is summarised in Table 7.2.

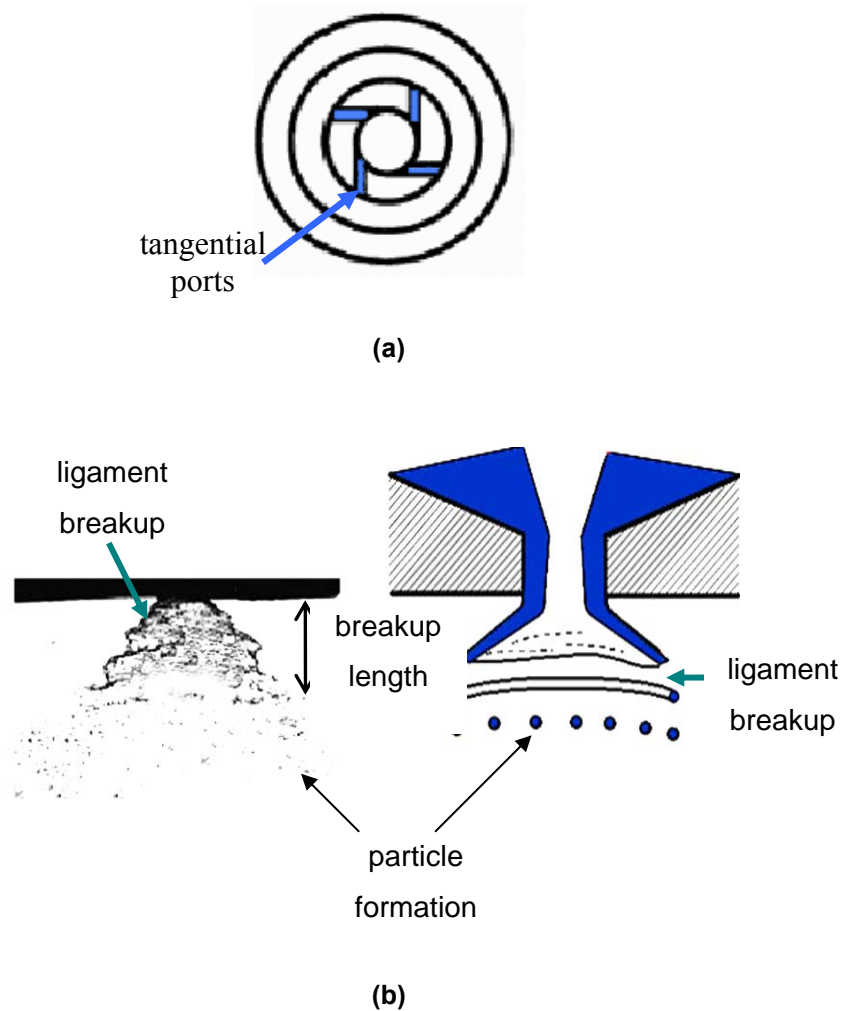


Figure 7.5 Pressure Swirl Atomiser characteristics: (a) internal swirl chamber showing the tangential ports within the atomiser (b) atomisation process

**Table 7.2** Spray device parameters for investigation

Measured Parameters	Value
Nozzle diameter	$\approx 0.5$ mm
Diameter at break-up length	$\approx 4$ mm
Spray cone angle	$\approx 30^\circ$
Initial particle velocity	$\approx 15$ m/s

---

Break-up length  $\approx 3.5$  mm

---

The 2D velocity field produced by the PIV system found that the exit velocity from the nozzle was approximately 15m/s. The maximum velocity reached 17m/s in the region around 0.1m downstream (Figure 7.6). It should be noted that this value is a consequence of a continuous spray which induces a continuous momentum force applied to the bulk spray flow caused by the upstream pressure. For nasal spray applications where the upstream pressure is applied in a short instance, the continuous momentum does not exist. The development of the spray is therefore an unsteady characteristic which is beyond the scope of this investigation. The initial velocity however is more applicable as the atomisation near the nozzle is the same for a continuous spray as it is for a pulsed spray. This is due to the atomisation dependence on the hydraulics of the flow within the atomiser, which governs the emerging liquid stream and the final disintegration into droplets.

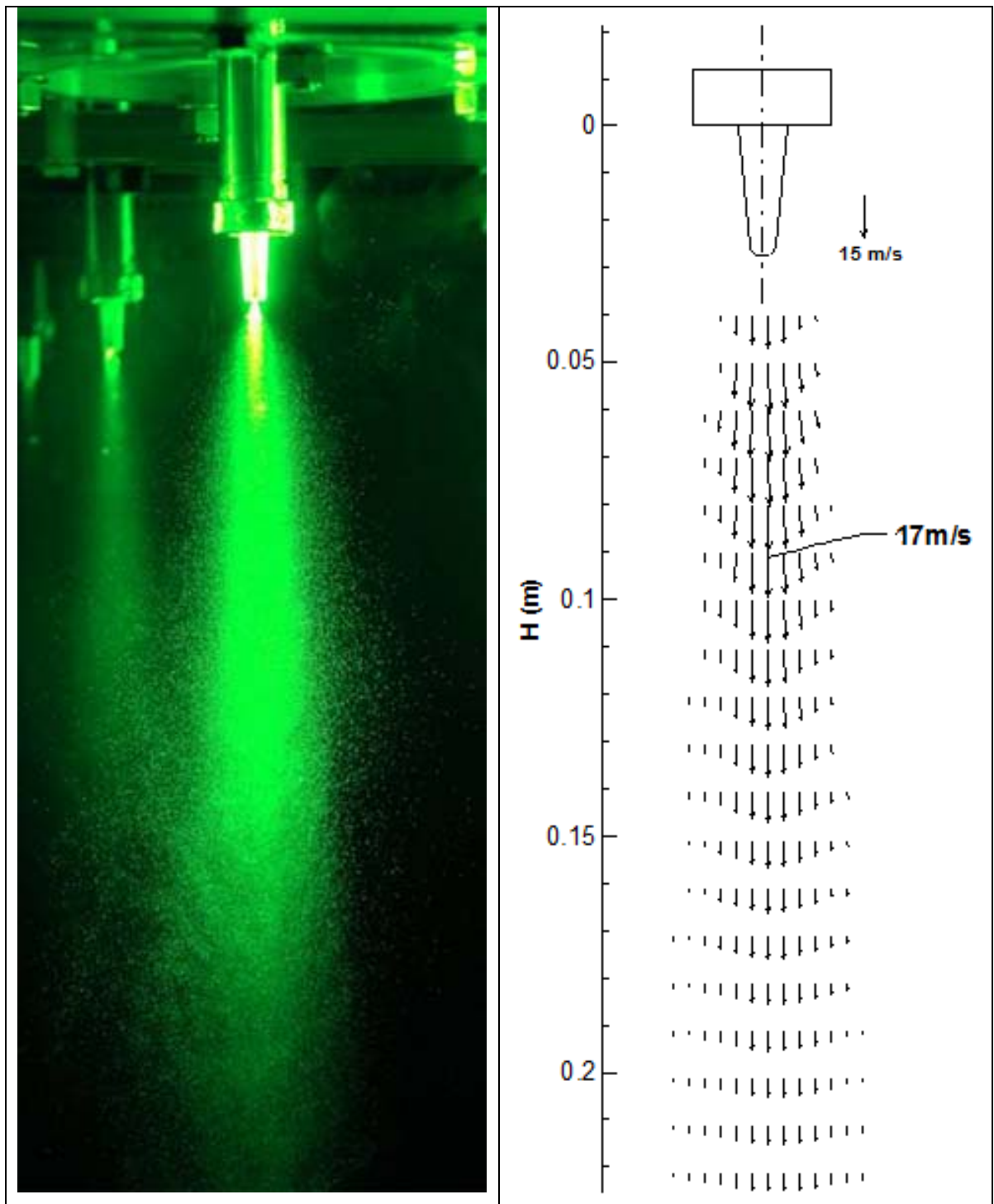
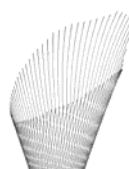
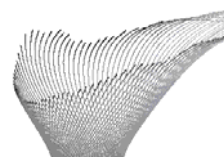





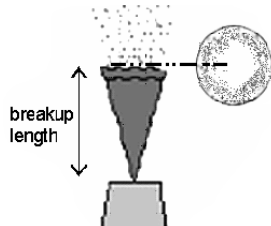
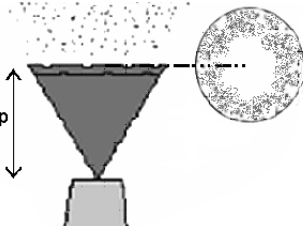


Figure 7.6 Image snapshot of the spray, and the resulting PIV 2D vector plot which shows the averaged mean droplet velocity field of the spray nozzle.

The measured values along with the observed images from Figure 7.4 enabled confidence in determining the appropriate parameters and setting a corresponding range of realistic values. The parameters determined from the experimental data to be important for CFD analysis were the swirl fraction, particle size, spray cone angle and the spray diameter at break-up length. The experimental data allowed a realistic range of values to be ascertained and this is summarised in Table 7.3. The swirl fraction parameter was included as the amount of swirl exerted onto the particles can be controlled by the internal swirl chamber design of a pressure-swirl atomiser (Lefebvre 1989).

**Table 7.3** Spray device parameters for the boundary conditions in CFD analysis

Parameter for Investigation	Values		
<i>Swirl fraction</i>	0.1 	0.5 	0.9 
<i>Particle size</i>	10 $\mu\text{m}$ 		20 $\mu\text{m}$ 
<i>Spray cone angle</i>	20 $^{\circ}$ 		60 $^{\circ}$ 
<i>Spray diameter at break-up length</i>	2mm 		4mm 

The swirl fraction sets the fraction of the velocity magnitude to go into the swirling component of the flow where the direction of the swirl component is defined using the right-hand rule about the axis (a negative value for the swirl fraction can be used to reverse the swirl direction).

The spray cone angle defines the degree of dispersion of the spray into the airway. Studies have shown that the spray angle is influenced by the nozzle dimensions, upstream pressure, liquid properties and the density of the medium into which the liquid is sprayed (Babu et al. 1982; Rizk and Lefebvre 1985). For the numerical simulation monosized particles were released as a hollow spray cone from the centre location of the each nostril. The spray cone angle was fixed at  $40^\circ$  and the distance of the release location from the nostril inlet was approximately 3mm which assumes that the nasal spray device is actuated at the inlet. Different locations as well as different insertion angles and spray cone angles will also have an effect and this variable is also investigated.

## 7.4. Conclusions

An experimental test station was designed and the atomisation of the drug spray was captured through PIV and high speed PDPA. The relevant parameters that affected the spray atomisation were identified. These were: spray cone angle which defines the degree of dispersion of the spray into the airway; swirl fraction which defines the fraction of the velocity magnitude to go into the swirling component of the flow; particle size; break-up length; and spray diameter at break-up length. This data plays an important role in allowing intelligent settings for the CFD initial particle boundary conditions. A study into the effects of different parameters on the spray performance and finally the particle deposition patterns can then be more accurately modelled. The following chapter provides the application of the parameters determined from these experiments.

## CHAPTER 8

# Inhalation of Sprayed Drug Particles

## 8.1. Introduction

Drugs delivered using a nasal spray device are inefficient as discussed earlier (Section 1.1 and 7.1). Using CFD to analyse and track the particles' trajectory through the nasal cavity can provide information that will lead to more efficient nasal spray designs. In this chapter the simulation of sprayed particles is discussed. The main difference between the inhalation of sprayed drug particles and that of inhaled aerosols in Chapters 5 and 6 is the initial velocity of the particles introduced into the nostrils. This boundary condition is critical and has a significant effect on the deposition patterns. Other parameters that govern the boundary conditions of sprayed particles have been established in Chapter 7 and these parameters are studied over a realistic range. The effects of each parameter is analysed by showing the deposition efficiencies and deposition patterns. This information can be exploited by engineers in designing the atomiser inside the nasal spray to control the desired parameters that gives the best deposition patterns and efficiencies.

Spray particle deposition is determined by several parameters: (i) deposition mechanisms involving the interaction between particles and its continuum; (ii) gas phase flow field such as velocity and turbulence effects; (iii) particle material properties and initial spray conditions such as particle density, size and spray cone angle. The first two, gas flow field due to the nasal cavity and deposition mechanisms have been determined in Chapter Two and Chapter Five respectively. Particle material properties and initial spray conditions are determined from the drug composition and the nasal spray device which initialises the

drug delivery process. Recent studies have measured spray characteristics, such as particle size and spray cone angle (Dayal et al. 2004; Eck et al. 2000; Suman et al. 2002). A nasal spray produces drug particles in the range of  $5\mu\text{m}$  up to  $200\mu\text{m}$  with a mean of  $45\text{-}65\mu\text{m}$  and spray cone angles ranging from narrow sprays at  $35^\circ$  to wide sprays at  $70^\circ$ . It was found that an increase in spray cone angle from  $35^\circ$  to  $60^\circ$  showed a reduction in size of the deposition area as less of the spray was able to penetrate the narrow nasal valve (Newman et al. 1998). Cheng et al. (2001) found that deposition in the anterior region increased with an increase in cone angles. In contrast, Suman et al. (2002) found that there wasn't a significant difference in deposition patterns with respect to spray cone angles. It is argued that the changes in spray angle is unlikely to alter the distribution of droplets in the nose due to the narrow passageway of the nasal valve, compared with the spray plumes which are ten times greater. Thus the emitted plumes never have the opportunity to freely develop in the nasal cavity as they would in an unconfined space. The differences in arguments stem from the numerous variations that exist in studying nasal spray deposition efficiencies. Moreover, the effects of the insertion angle of the spray device, the location of the insertion and the initial particle velocity were not discussed.

## 8.2. Numerical Procedure

### 8.2.1. Turbulent Airflow

The presence of turbulent flow has been confirmed in the human nasal cavity at flow rates of  $20\text{L}/\text{min}$  and the  $k\text{-}\varepsilon$  turbulence model used (Keyhani et al. 1995; Yan et al. 2004). The  $k\text{-}\varepsilon$  turbulence models are the most commonly used turbulence model, based on the assumption of isotropic turbulence and a single eddy viscosity for all three components of the velocity vector. This can cause inaccuracies for flows with high swirling action which makes the turbulence anisotropic. However for flows in the small narrow nasal cavity that exhibit low levels of swirl the  $k\text{-}\varepsilon$  approximation may be sufficient given the low computational costs compared with more sophisticated approaches such as Large Eddy Simulations and the Reynolds Stress Model. The gas phase Reynolds-Averaged conservation equations along with the equations for the turbulent kinetic energy and its dissipation rate can be cast in the general form:



$$\frac{\partial}{\partial x_j}(A_i \phi) - \frac{\partial}{\partial x_j}(\Gamma \frac{\partial \phi}{\partial x_j}) = S \quad (8.1)$$

continuity equation ( $\phi = 1$ )

$$A_i = \rho_g u_j^g \quad \Gamma = 0 \quad S = 0 \quad (8.2)$$

momentum equation ( $\phi = u_i^g$ )

$$A_i = \rho_g u_j^g \quad \Gamma = \rho_g v_{g,t} \quad S = -\partial P / \partial x_j; \quad (8.3)$$

turbulent kinetic energy equation ( $\phi = k_g$ )

$$A_i = \rho_g u_j^g \quad \Gamma = \rho_g v_{g,t} / \sigma_k \quad S = P_k - \rho_g \varepsilon_g; \quad (8.4)$$

dissipation equation ( $\phi = \varepsilon_g$ )

$$A_i = \rho_g u_j^g \quad \Gamma = \rho_g v_{g,t} / \sigma_k \quad S = C_1 \rho_g (2S_{ij}^2)^{1/2} - C_2 \rho_g \frac{\varepsilon_g^2}{k_g + \sqrt{\nu \varepsilon_g}} \quad (8.5)$$

where

$$S_{ij} = \frac{1}{2} \left( \frac{\partial u_i^g}{\partial x_j} + \frac{\partial u_j^g}{\partial x_i} \right) \quad (8.6)$$

The realizable  $k$ - $\varepsilon$  model (Shih et al. 1995) was intended to address deficiencies experienced in the Standard and RNG  $k$ - $\varepsilon$  models. The term “realizable” means that the model satisfies certain mathematical constraints on the normal stresses, consistent with the physics of turbulent flows. The development involved the formulation of a new eddy-viscosity formula involving the variable  $C_\mu$  in the turbulent viscosity relationship:  $\nu_{g,t} = C_\mu k_g^2 / \varepsilon_g$  and a new model for the  $\varepsilon$ -equation based on the dynamic equation of the mean-square vorticity fluctuation. The variable constant  $C_l$  can be expressed as:

$$C_l = \max \left[ 0.43, \frac{\eta}{\eta + 5} \right] \quad \text{and} \quad \eta = \frac{\kappa_g}{\varepsilon_g} (2S_{ij}^2)^{1/2} \quad (8.7)$$

The variable  $C_\mu$ , no longer a constant and is computed from:

$$C_\mu = \frac{1}{A_0 + A_s \frac{\kappa_g U_*}{\varepsilon_g}}; \quad U_* \equiv \sqrt{S_{ij}^2 + \tilde{\Omega}_{ij}^2}; \quad \tilde{\Omega}_{ij} = \Omega_{ij} - 2\varepsilon_{ijk} \omega_k; \quad \Omega_{ij} = \bar{\Omega}_{ij} - \varepsilon_{ijk} \omega_k \quad (8.8)$$

while the model constant  $A_0$  and  $A_s$  are determined by:

$$A_0 = 4.04; \quad A_s = \sqrt{6} \cos\varphi; \quad \varphi = \frac{1}{3} \cos^{-1}(\sqrt{6}W); \quad W = \frac{S_{ij}S_{jk}S_{ki}}{\tilde{S}^3}; \quad \tilde{S} = \sqrt{S_{ij}^2} \quad (8.9)$$

Other constants in the turbulent transport equations are  $C_2 = 1.9$ ,  $\sigma_\kappa = 1.0$  and  $\sigma_\varepsilon = 1.2$ .

The numerical description of the turbulent dispersion is given in Section 4.2.2

## 8.2.2. Boundary Conditions

The nasal cavity was subjected to constant air flow rates of 20-40 L/min. The internal walls were modelled using an “enhanced wall treatment” function to consider the no-slip condition on the air flow. The particles adopted the properties of spherical water droplets, as most drug formulations are diluted with water. Initial particle conditions are assumed by analytical methods due to a lack of experimental data. The conditions for the release of particles into the constant flow rate differed for the parameter under investigation and are elucidated upon, within the relevant sections. The internal walls of the nasal cavity were set to a “trap” condition, meaning that particles touching a wall, deposit at that location.

## 8.3. Results and Discussion

### 8.3.1. Validation using a Hybrid Method

Monodispersed particles in the range of  $1\mu\text{m}$  to  $30\mu\text{m}$  were initially tested at gas flow rates, 20L/min and 40L/min. Two tracking methods, DRW tracking and mean flow tracking (which infers no turbulent particle dispersion) were applied. The results found were qualitatively similar to that found in Zhang et al. (2004). The DRW tracking grossly overestimates particle deposition for an inertial parameter (IP)  $< 10,000$  and underestimates deposition for IP  $> 20,000$ , whilst the mean flow tracking overestimates particle deposition for IP  $< 8,000$  and underestimates deposition for IP  $> 10,000$ . It is suggested that a hybrid tracking method be used where the DRW tracking is used for larger particles where IP  $> 10,000$  and a mean flow tracking be used for IP  $< 10,000$ , (Figure 8.1), equivalent to  $d_p \approx 5.5\mu\text{m}$  for a flowrate of 20L/min. This ideal model is sufficient for the study of nasal spray particles that have mean particle sizes in the range of

50 $\mu\text{m}$ -70 $\mu\text{m}$  (Cheng et al. 2001), which is much larger than the critical size for the applicable use of the DRW tracking method. Thus further analysis of deposition of particles will focus on particles  $\geq 10\mu\text{m}$ .

Differences in the comparison of particle deposition with the inertial parameter is discussed by Häußermann et al. (2001), such as the limitation of the inertial parameter not taking into account the changes in airway geometry. This constant air flow rate is a measure of the average impactability of the particle over the entire domain, as it doesn't factor in the changes in velocity which is significant when the geometry under consideration is highly convoluted, narrow and complex. Furthermore, nasal cavity replicate casts with wider airways as in Swift (1991)'s case might cause less deposition due to secondary flow (Häußermann et al. 2001). Additional differences between deposition efficiency curves are discussed in Section 6.3.1.

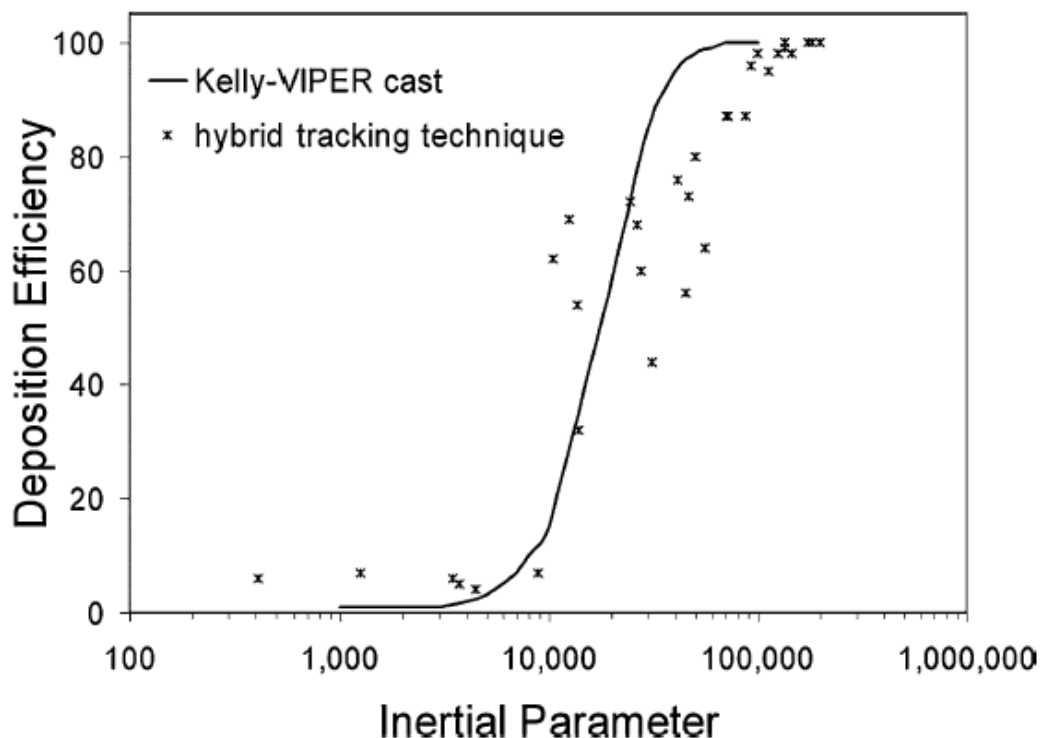


Figure 8.1 Deposition efficiency for monodisperse particles released into 20L/min, 30L/min and 40L/min airflow using a hybrid tracking technique

### 8.3.2. Swirl Fraction ( $\lambda$ )

The swirl fraction sets the fraction of the velocity magnitude to go into the swirling component of the flow, thus a higher fraction will produce a greater tangential velocity component. This increases the time taken to travel a given axial distance as the particle is swirling more and its residence time becomes longer. Additionally the induced drag from the cross-flow of air helps to reduce the initial high momentum of the particle and the chances of particles travelling through the frontal regions of the nasal cavity increases. Figure 8.2 shows high deposition of particles occurring in the frontal regions (Region 1-3).

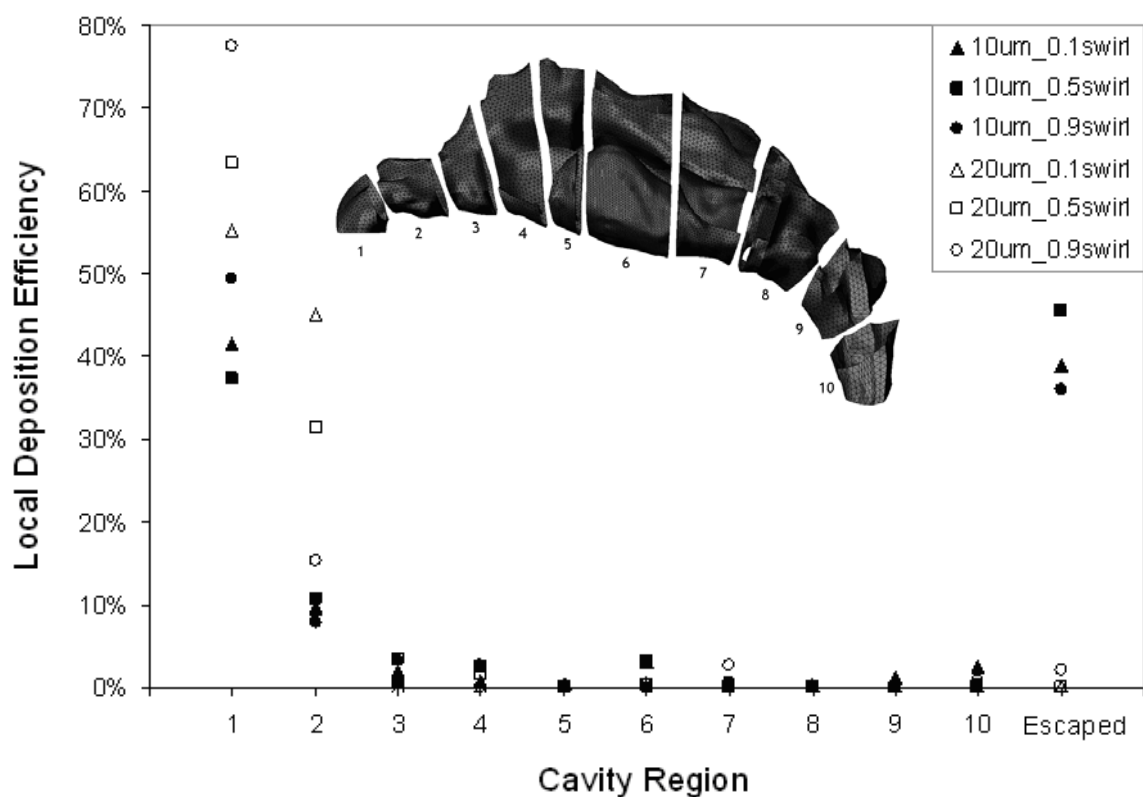


Figure 8.2 Particle deposition within different sections of the nasal cavity. Section 1-3 is the frontal region, Section 4-7 is the middle region and Section 8-10 is the posterior region.

The amount of swirl has a different effect for the two different particle sizes. For 10µm particles with  $\lambda = 0.9$  deposition in the frontal zones increases, while for  $\lambda = 0.5$ , a higher percentage of particles escape. Conversely for 20µm particles an increase in the swirl fraction decreases the deposition in the frontal zones. Some deposition in the middle zones occurs and 2.2% escape when the  $\lambda = 0.9$ . The reason for these local deposition patterns

can be better understood by observing the particle trajectories (Figure 8.3). It is known that larger particles that possess high inertia (i.e. Stokes number characteristics) need to be aligned with the flow streamlines to avoid impaction. This implies that the particles need to be projected at a clear unobstructed path in the nasal airway rather than be projected at walls.

When  $\lambda \rightarrow 0$ , the velocity magnitude is entirely composed of axial velocity, which projects the particles vertically. High inertia particles are directed at the roof of the nasal vestibule and do not have enough time to slow down and adapt to the gas phase streamlines. However smaller inertia particles can adapt to the flow streamlines more readily. One idea to overcome this is to insert the nasal spray at an angle (insertion angle) that would provide such alignments with the flow streamlines (Inthavong et al. 2006). However this technique is dependent on the user upon the application of the nasal spray device as well as the precise location of the nozzle.

When  $\lambda \rightarrow 1$ , the velocity magnitude is entirely composed of a tangential velocity and the particles are projected at a tangential direction to the nasal spray insertion angle. For  $10\mu\text{m}$  particles, deposition increases in the frontal zones as more particles are pushed towards the wall. For  $20\mu\text{m}$  particles this is also the case, however instead of impaction into the upper roof when  $\lambda = 0.1$ , impaction is on the side walls. The horizontal projection of a small proportion of particles is then enhanced by the gas phase velocity which carries the particles along the floor of the nasal cavity. Without any obstructions to the flow, the particles are transported through to the nasopharynx area. A small increase in deposition within the middle and anterior regions are observed. At the nasopharynx, the flow changes direction at  $90^\circ$  which acts as another filter to capture high inertia particles that impact at the back. Although a swirl fraction of 1 is extreme and indeed unrealistic to achieve practically within the atomiser design, its use in the present investigation provides a deeper understanding of the effects of the swirl fraction. The particle trajectories demonstrate that the swirling motion decreases the particles' initially high inertia due to the difference in the air and particle velocities.

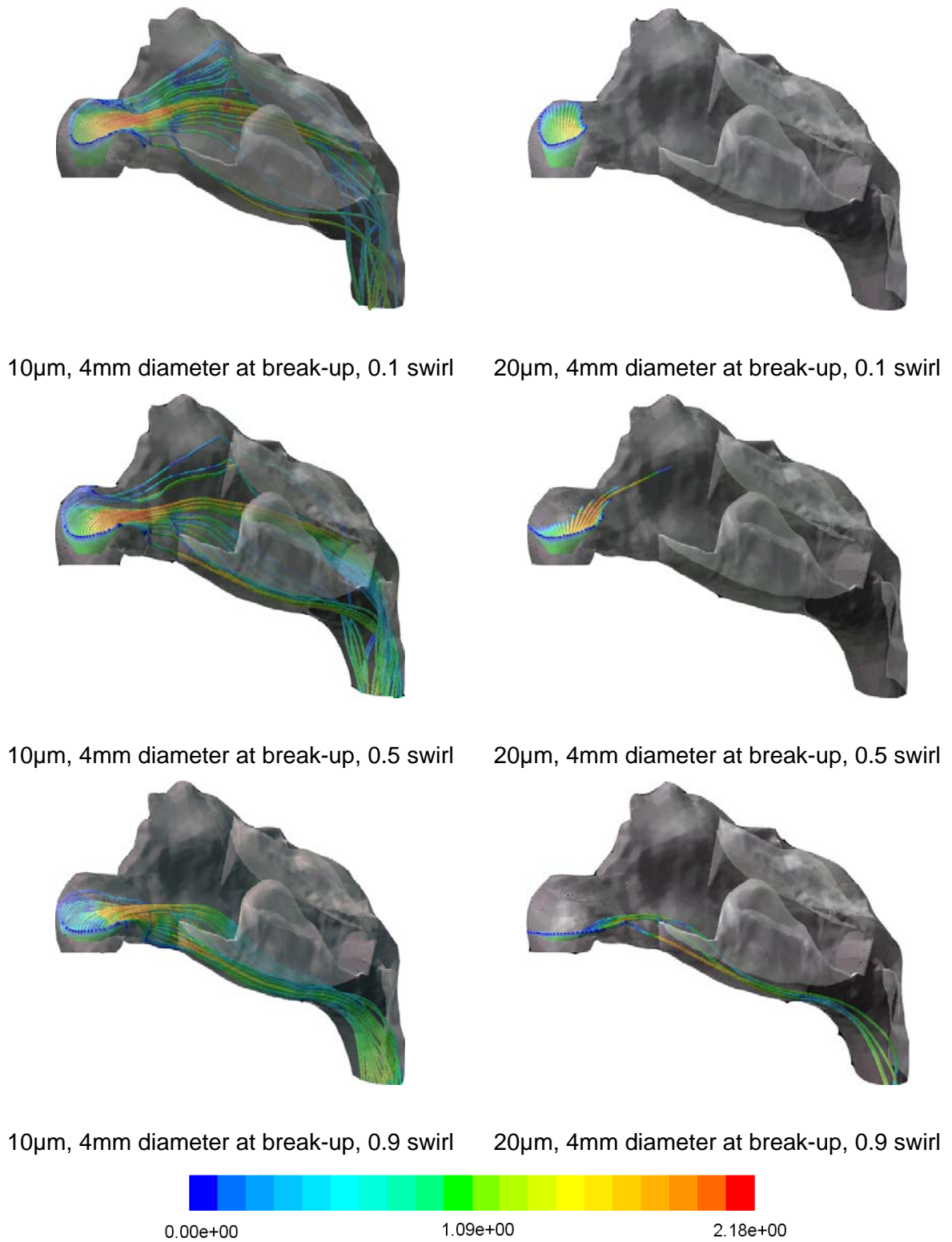
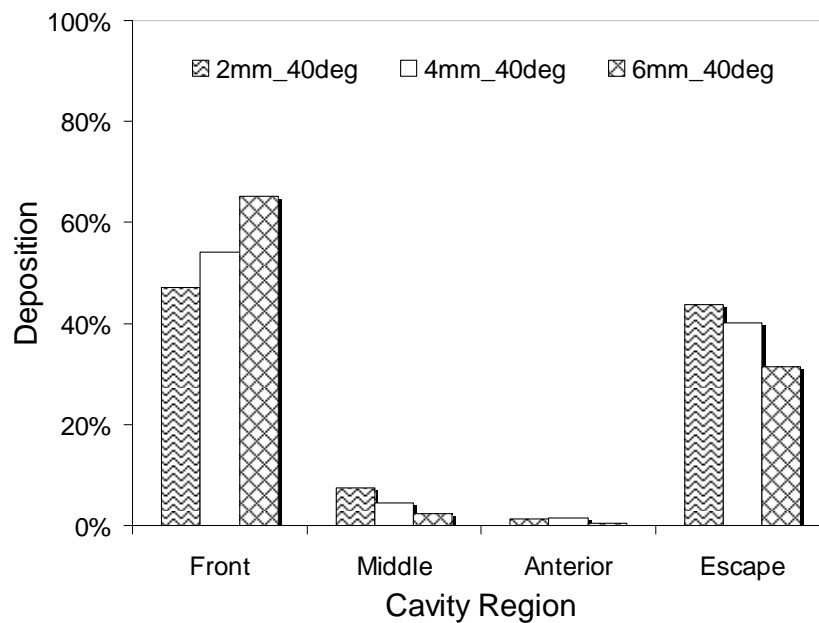


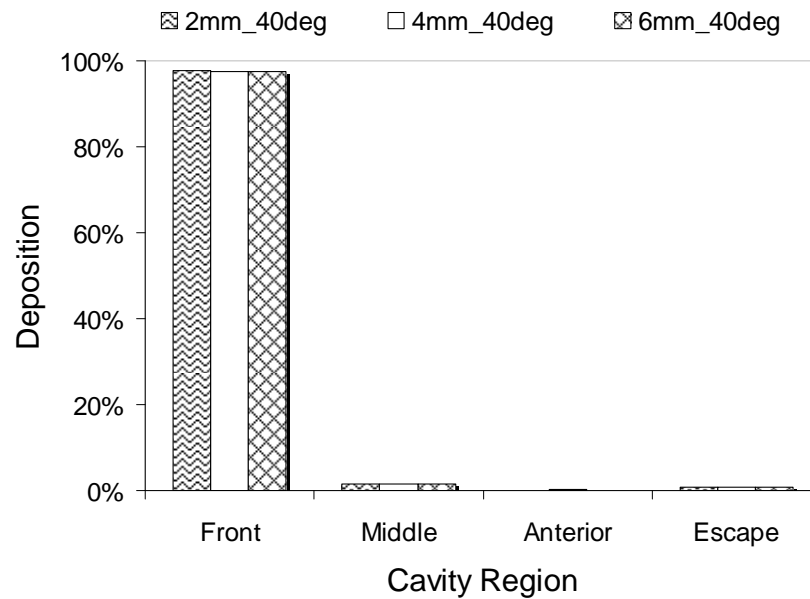
Figure 8.3 Particle trajectories for 10 and 20µm particles at different swirl fractions.

### 8.3.3. Spray Diameter at Break-up Length

The diameter of the spray cone at the break-up length can be controlled by the design of the atomiser. For example the spray formation having a shorter/longer break-up length would produce a smaller/larger diameter at break-up. Additionally the design of the nozzle diameter and spray cone angle produced from the nozzle has an effect on the spray diameter at break-up. For  $10\mu\text{m}$  particles, a larger diameter is shown to increase deposition in the frontal sections (Figure 8.3). As a result deposition in the middle and sections decreases as well as the number of particles escaping which is brought about by the initialized particles existing closer to the walls. This effect is similar to the spray cone angle effects where particles are projected outwards. Therefore a design that couples a wide spray cone angle with a large spray diameter at break-up would bring about high frontal deposition. For  $20\mu\text{m}$  particles, the high inertial properties of the particle dominate the effect of the diameter at the break-up length and negligible change occurs (Figure 8.4).



(a)



(b)

Figure 8.4 Regional deposition of (a) 10µm particles and (b) 20µm released at different spray cone diameters.

### 8.3.4. Initial Particle Velocity

The initial particle velocity can be controlled in many ways such as changing the nozzle diameter and the actuation mechanism. Monodispersed particles were released uniformly in a normal direction to the inlet surface of each nostril and the average deposition within the left and right nasal cavity was recorded. Injected particle velocities were chosen to reflect a real nasal spray application. Velocities were calculated based on mass conservation, assumed nasal spray geometries and our own preliminary experimental work on nasal spray nozzles, which found velocities ranging between 10m/s to 20m/s for 200kpa to 500kpa pressure actuations, respectively. Quantitatively, the results obtained by using a uniform surface injection, normal to the nostril inlets, will differ from a real nasal spray application that possesses an injection from a very small diameter. However, qualitatively, it provides a basis for the impactability of specific particles at different injection velocities.

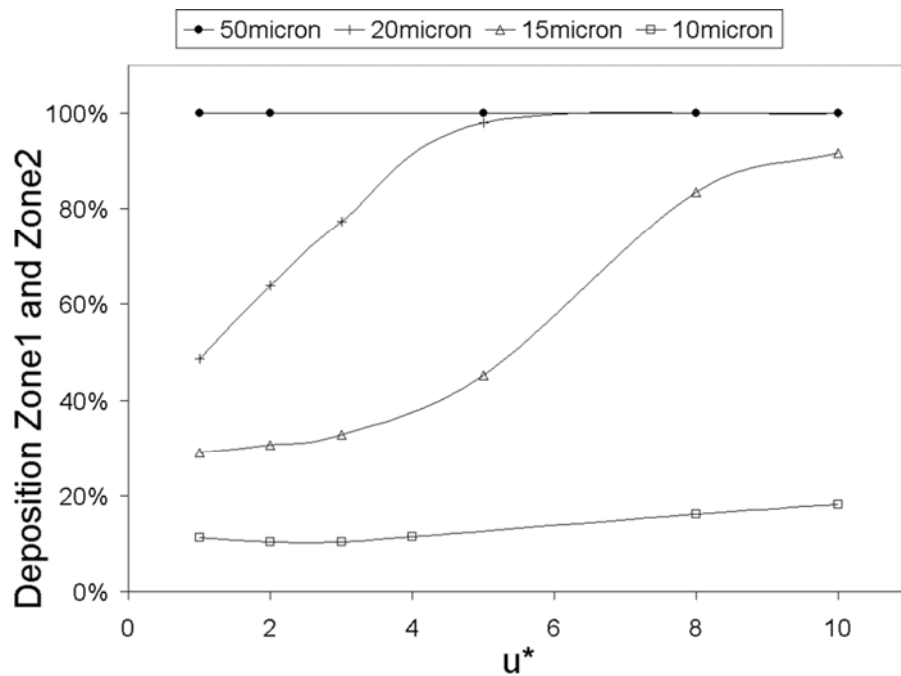
The injected particles gain an increase in their kinetic energy, resulting in an initially higher momentum to travel in the intended trajectory. However this energy is degenerated by the drag force acted on by the gas phase. The amount of influence of the gas on the



particle is dependent on the particle Stokes number. The relationship for the particle-gas velocity ratio as a function of the Stokes number is (Crowe et al. 1998):

$$u^* = \frac{u_p}{u_g} \approx \frac{1}{1 + St} \quad (8.10) \quad \text{where} \quad St = \frac{\rho_p d_p^2 U}{18\mu_g D} = \tau \frac{U}{D} \quad (8.11)$$

Which suggests that for small Stokes numbers (i.e.  $St \rightarrow 0$ ), the particle velocity approaches the gas phase velocity quickly. For large Stokes numbers (i.e.  $St \rightarrow \infty$ ) suggesting that  $u^*$  approaches zero. This means that the particle velocity is unaffected by the gas.



where  $u^* = u_p / u_g$

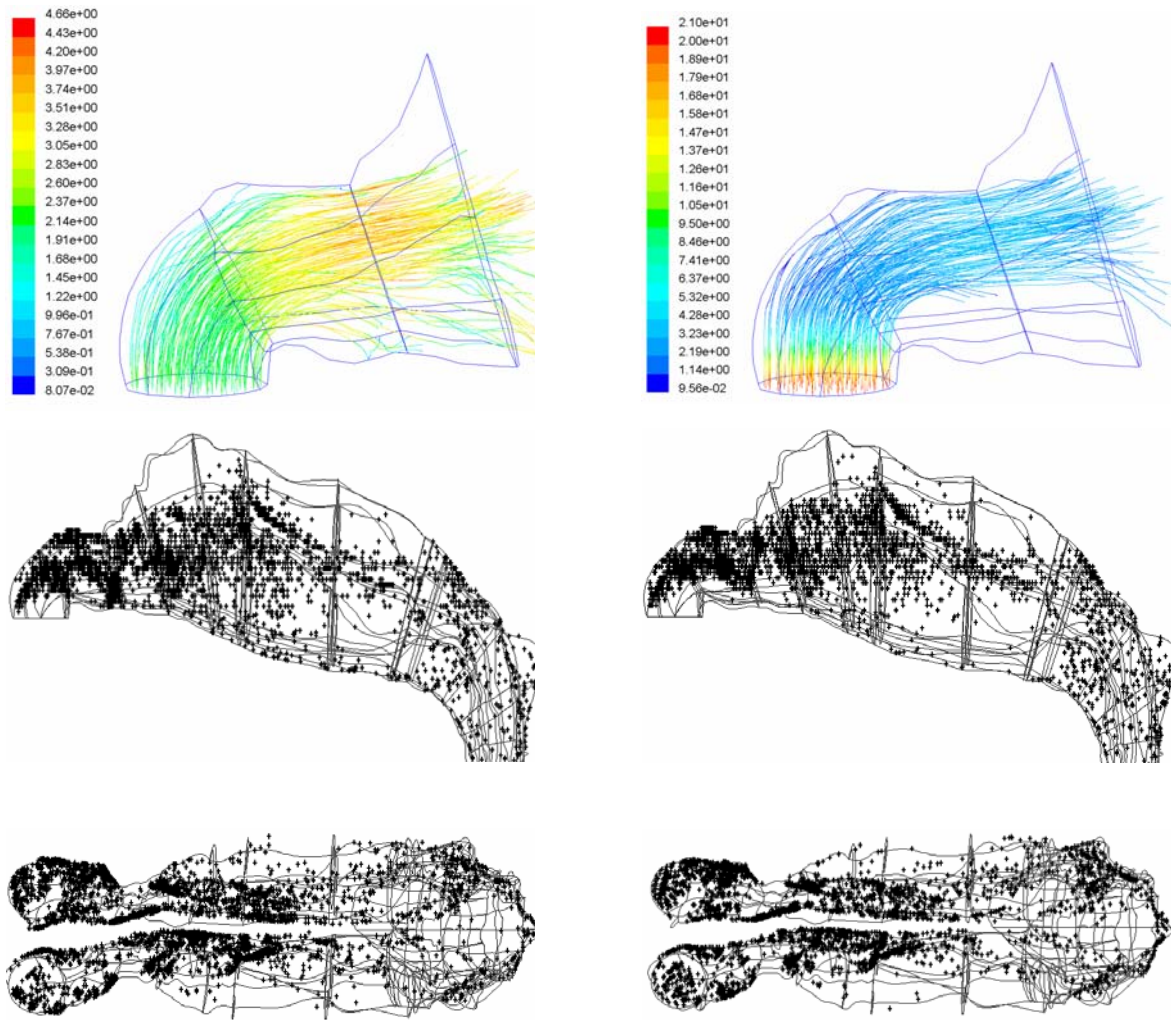
Figure 8.5 Total deposition in the first two zones of the nasal cavity at different particle injection velocity.

Thus it is expected that the dynamic change in the particle velocity will occur within the anterior section of the nasal cavity. The anterior third of the nasal cavity is divided into three zones and particle flow visualization and deposition patterns within this region are observed with results displayed in Figure 8.5 and Figure 8.6a, b, and c.

Figure 8.5 shows the total particle deposition in the first two zones of the nasal cavity at different particle injection velocity. Zones are shown graphically Figure 3.9. A small

influence on the impactability of a  $10\mu\text{m}$  particle is observed when there is an increase in the initial particle velocity and is seen by the slight increase in deposition. The low Stokes number brings about a rapid decrease in velocity and the particle assumes the gas phase velocity before the change in direction of the flow. The influence of  $u^*$  amplifies as the particle size increases, where a large proportion of particles deposit more readily in the two frontal zones. The geometry of the frontal section of the nasal cavity conforms to that of a  $90^\circ$  bend where the particle Stokes number is of importance. The larger particles exhibit much higher Stokes numbers which prevents the particles from following the curved streamlines. It is observed that  $50\mu\text{m}$  particles entrained in the flow ( $u^*=1$ ) is an example of this. Therefore an injected  $50\mu\text{m}$  particle ( $u^*=10$ ) exhibiting a greater amount of initial momentum will only exacerbate the linear projectile motion of the particle.

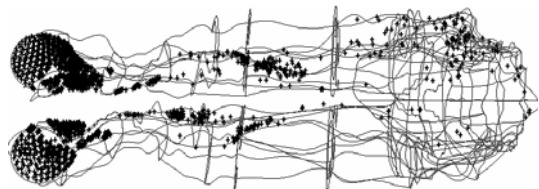
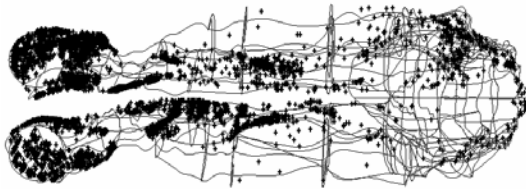
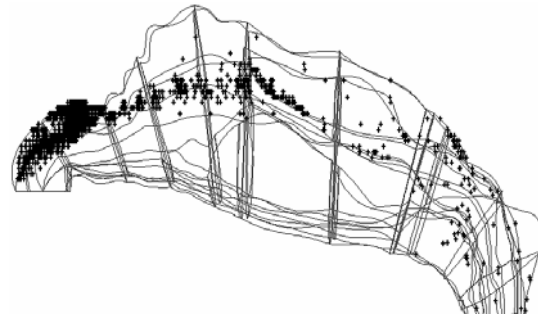
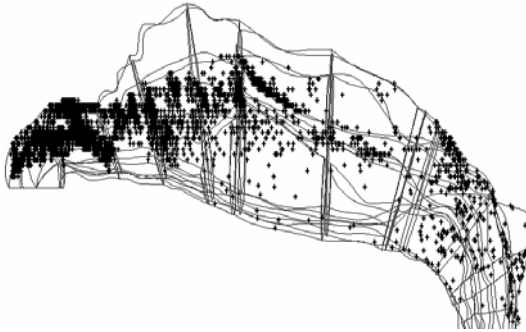
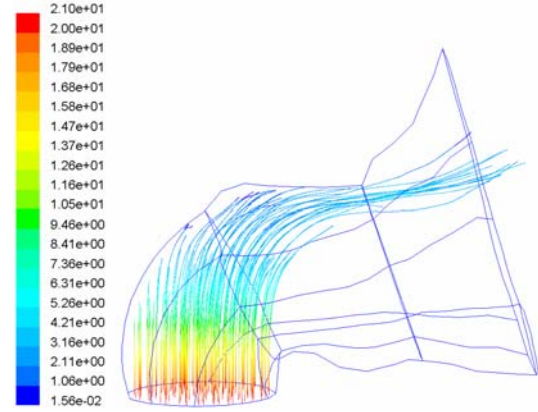
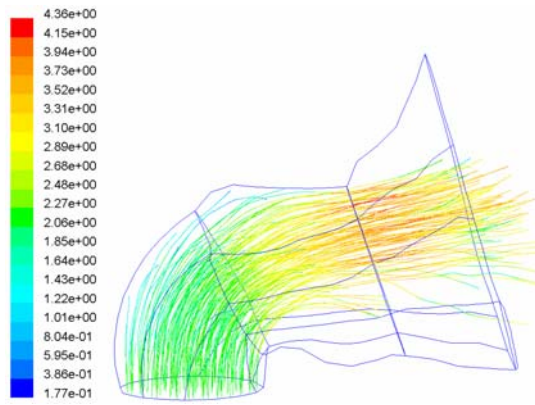
About 70% of  $15\mu\text{m}$  particles are able to follow the curved streamlines when  $u^*=1$  as particle impactability is governed by the Stokes number only. However significant deposition increases when  $u^* > 4$ . The Stokes number, a ratio of the particle's relaxation time to the flow characteristic time, indicates how long it takes for the particle to adjust to the gas phase conditions. For a fixed distance (nostril opening to the top of the vestibule), an increase in  $u^*$  will decrease the time taken to cover this distance. This leads to a shorter time and distance for the particle to adapt to the gas phase conditions and presents a higher impactability than that calculated by the Stokes number alone. The influence of the injected particle velocity then, is still felt as the gas phase begins to curve. As particle size increases, so does the relaxation time that the particle needs, to adapt to flow changes. As a result significant deposition increases occur at lower  $u^*$  values for larger Stokes numbers.



*10µm at injection velocity  $u^* = 1$*

*10µm at injection velocity  $u^* = 10$*

(a)



$15\mu\text{m}$  at injection velocity  $u^* = 1$

$15\mu\text{m}$  at injection velocity  $u^* = 10$

(b)

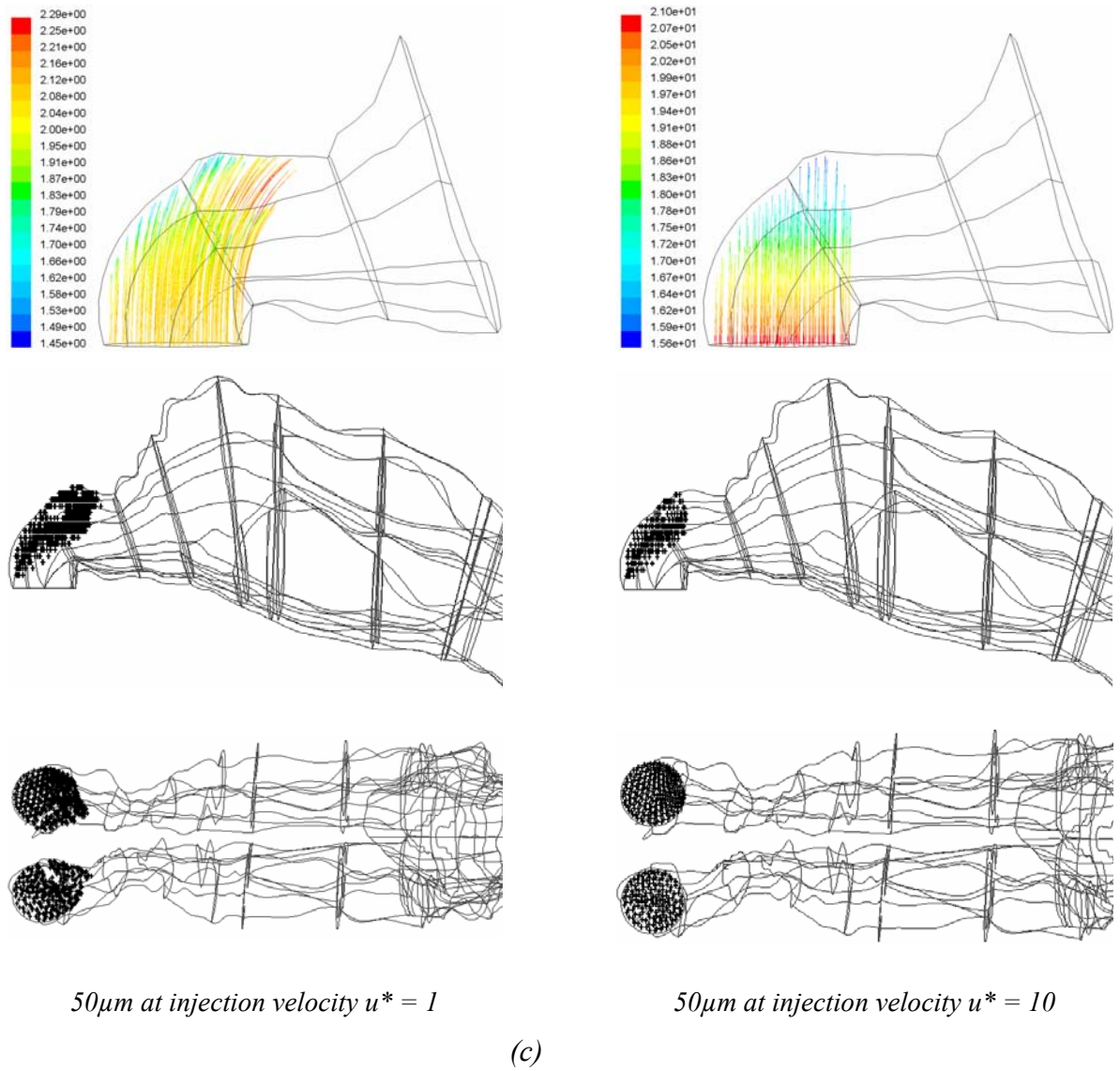


Figure 8.6 Deposition patterns for (a) 10 $\mu\text{m}$  (b) 15 $\mu\text{m}$  and (c) 50 $\mu\text{m}$  particles released uniformly from the inlet surface normal to the nostril openings at  $u^*=1$  and  $u^*=10$ .

Figure 8.6 displays the deposition sites for the two extreme cases,  $d_p = 10\mu\text{m}$  and  $d_p = 50\mu\text{m}$  and a mid-range particle,  $d_p = 15\mu\text{m}$  subjected to  $u^*=1$  and  $u^*=10$ .  $50\mu\text{m}$  particles impact at the top of the vestibule at  $u^*=10$ , and at  $u^*=1$ , only a small proportion begin to curve albeit for a short distance before impaction. In contrast  $10\mu\text{m}$  particles are barely affected by the increase in injection velocity with local deposition sites being concentrated near the nasal valve region and septum walls which is a qualitatively similar to Zwartz and Guilmette (2001). The difference in deposition occurs at the entrance region where entrained particles released near the wall deposit readily through fluctuations in the flow whereas particles at higher velocities overcome this region. The particle flow for  $u^*=10$  enable the particles to travel further linearly which is evident in the particles adapting to the flow changes at a later stage than particles at  $u^*=1$ . This later adaptation to the flow causes the particles to assume those streamlines closer to the ceiling of the nasal cavity compared with particles at  $u^*=1$ . Beyond the first two zones of the nasal cavity deposition sites are similar, locally.

Deposition of  $15\mu\text{m}$  particles at  $u^*=1$  are mainly concentrated within the vestibule, nasal valve regions and along the septum walls. Differences appear between the left-side and right-side of the cavity which is due to anatomical variations. The concentration of particles within the middle passage of the nasal cavity is lighter than that shown in  $10\mu\text{m}$  particles as the larger particles have a higher concentration within the anterior section of the nasal cavity. When  $u^*$  is increased to 10 the particle is no longer just governed by its Stokes number, but also by the driving force of the initial injected velocity that adds initial momentum to the particle. This increase in momentum is dissipated by the difference in velocities of the gas and particle phase. The particles travel further linearly, in the normal direction to the nostril inlet with 88% impacting at the top of the vestibule. Only 12% of particles are able to adjust to the curvature in time and these particles remain in the upper regions of the nasal cavity throughout the flow.

### 8.3.5. Insertion Angle, $\alpha$

The insertion angle,  $\alpha$ , is the angle the nasal spray device makes away from the horizontal position, ( $0^\circ$  in the x-y plane), when looking into the side of a person's face (Figure 8.7). Particle sizes of  $10\mu\text{m}$  to  $20\mu\text{m}$  were used at an initial velocity of  $10\text{m/s}$ . A uniform

surface injection released from the inlet was used to eliminate variables such as location of the nozzle tip, nozzle diameter and spray cone angle.

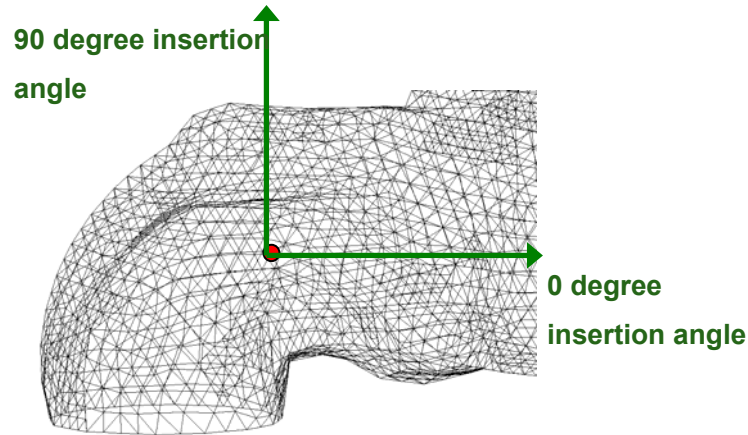


Figure 8.7 Side view of the nasal vestibule showing the insertion angle.

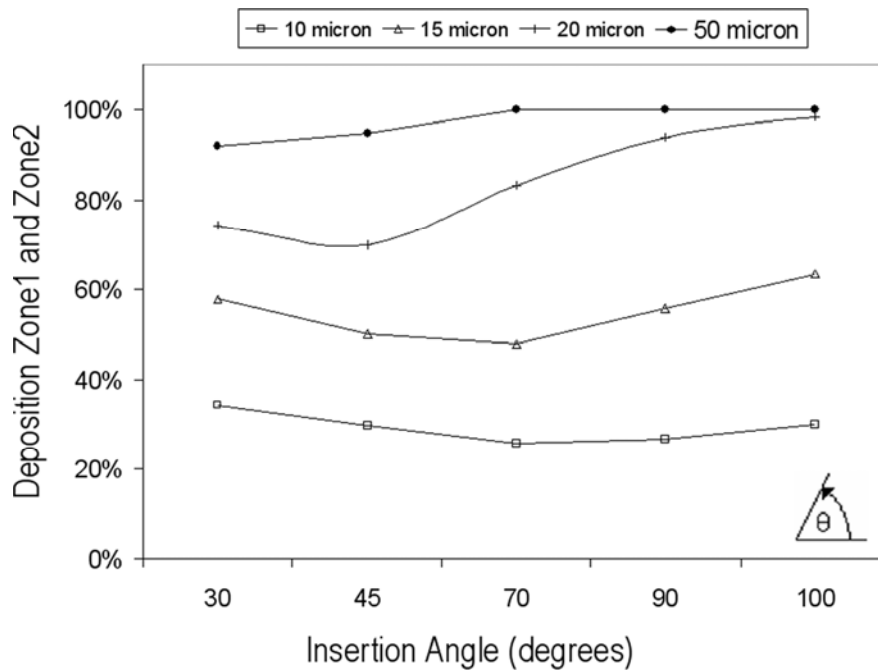
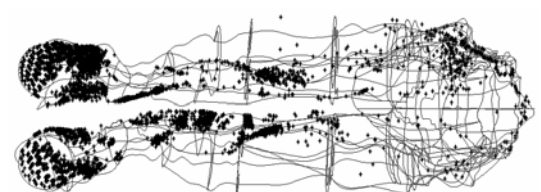
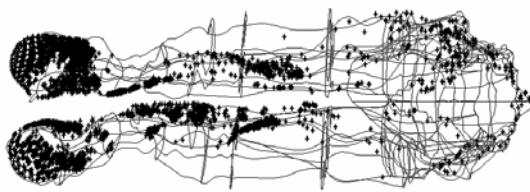
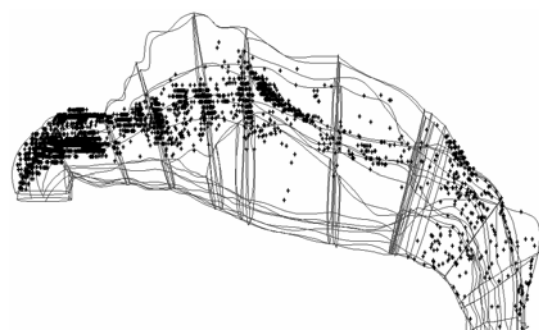
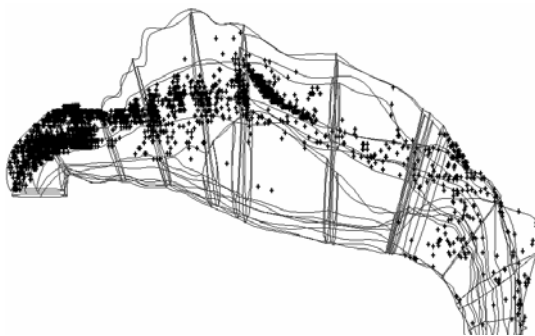
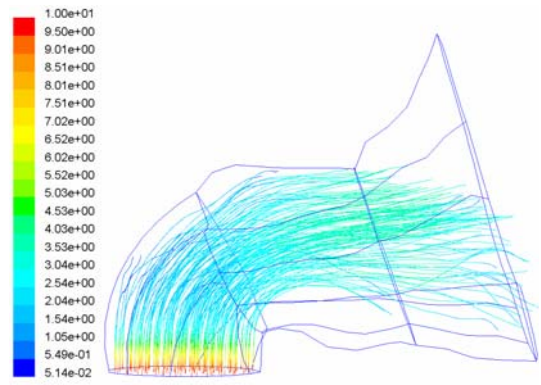
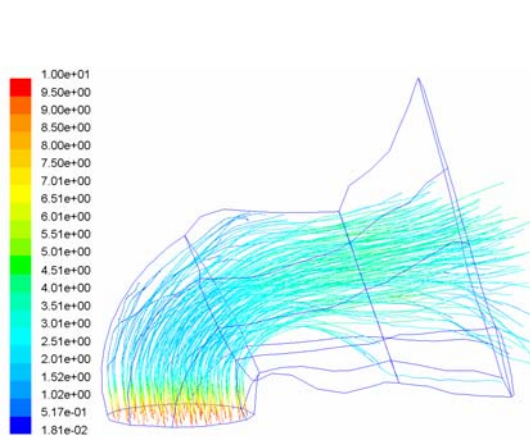


Figure 8.8 Deposition in zone1 and zone2 for monodispersed particles released uniformly from the inlet surface at different insertion angles.

Higher deposition occurred at  $100^\circ$  for most particles (Figure 8.8) as the gas phase velocity cannot overcome the initial injected velocity of 10m/s, which causes the particles to be discharged directly into the anterior-most walls of the nasal cavity. This concentration of particles can be seen in Figure 8.9 for  $15\mu\text{m}$  particles. Minimum deposition for smaller sized particles,  $10\mu\text{m}$  and  $15\mu\text{m}$ , was found when  $\alpha=70^\circ$ . The  $70^\circ$  direction of particles enhances the ability of turning, as more particles assume the streamlines on the inside of the curvature. Further decreases in  $\alpha$ , where the direction of discharge approaches the horizontal increases deposition of particles as a higher proportion of particles are now directed at the adjoining wall of the nostril, albeit at a small margin.

$20\mu\text{m}$  particles behave similarly but at lower  $\alpha$ . Minimum deposition in the two frontal zones was found at  $\alpha=45^\circ$ . Although more particles are directed into the adjoining wall, this is offset by more particles penetrating into the curvature instead of impacting straight into the roof of the vestibule as is the case when  $\alpha=90^\circ$ . These larger particles require a sharper angle of insertion to avoid impacting with the roof of the vestibule, thus aiding the alignment of the particles with the  $90^\circ$  bend and reducing the amount of deviation required in turning. The larger particle ( $20\mu\text{m}$  and  $50\mu\text{m}$ ), the more effective the decrease in  $\alpha$  is. Another insertion angle that can be considered is the orientation when looking into a person's face, front-on, in the  $y$ - $z$  plane. This wasn't investigated as the same ideas regarding the particle size with its dependency on initial flow conditions exist.





15µm at insertion angle  $\alpha = 100^\circ$ ,  $u = 10\text{m/s}$

15µm at insertion angle  $\alpha = 90^\circ$ ,  $u = 10\text{m/s}$

(a)

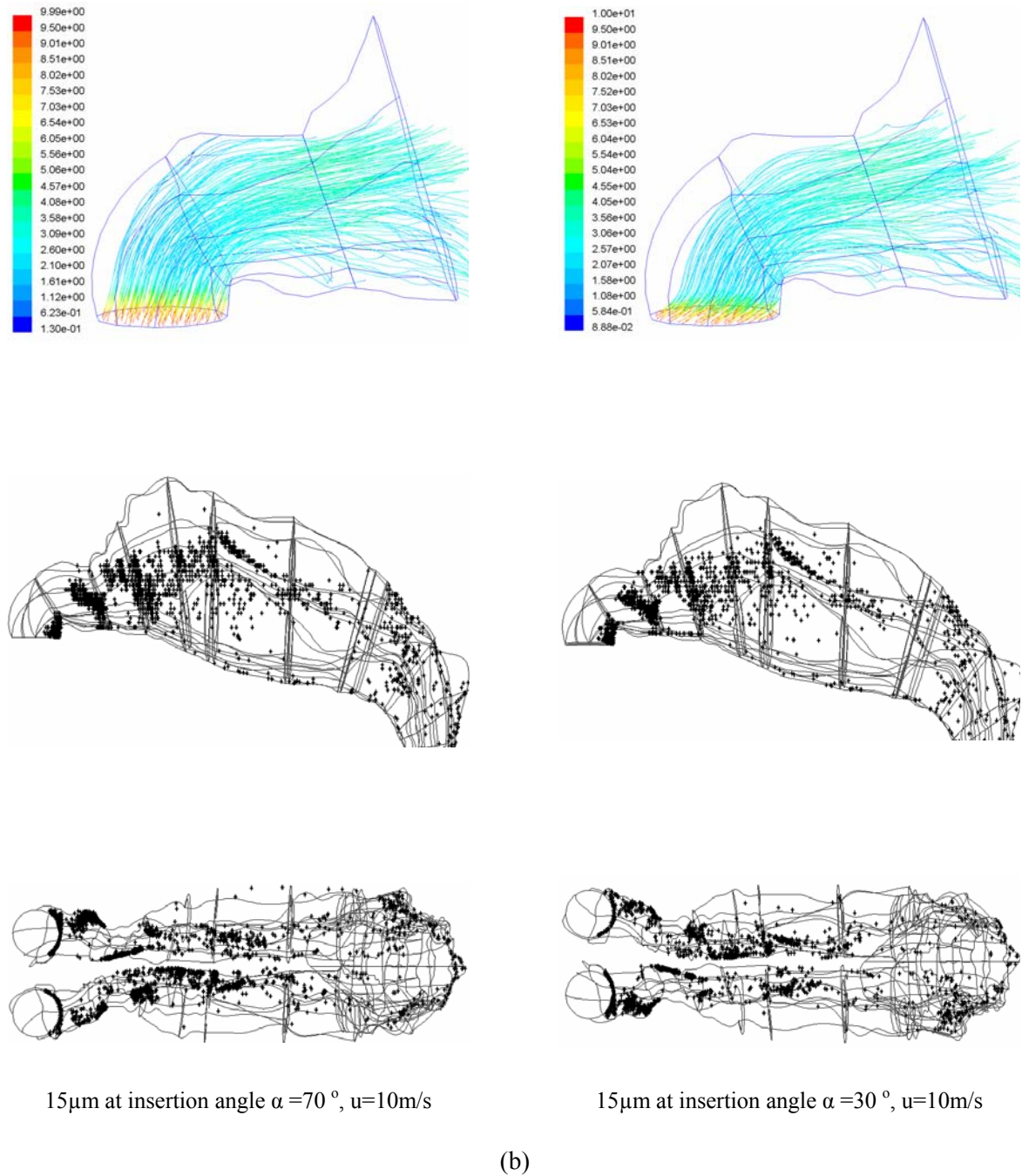


Figure 8.9 (a) Deposition patterns for  $15\mu\text{m}$  particles released uniformly from the inlet surface uniformly from the inlet surface at insertion angles  $100^\circ$  and  $90^\circ$ . (b) Deposition patterns for  $15\mu\text{m}$  particles released uniformly from the inlet surface uniformly from the inlet surface at insertion angles  $70^\circ$  and  $30^\circ$ .

### 8.3.6. Full Spray Cone Angle, $\beta$

The full spray cone angle,  $\beta$ , is the dispersion of particles exiting from the nozzle tip. It is twice the angle of the half spray cone angle (Figure 8.10). Particles were released from a small diameter compared with previous particle release methods which used a uniform surface inlet at the nostril openings. This allows observation of the physical differences when changing  $\beta$ . Particles were released at 10m/s from an internally fixed location with a diameter of 0.8mm and a range of  $\beta$  between 20° to 80°.

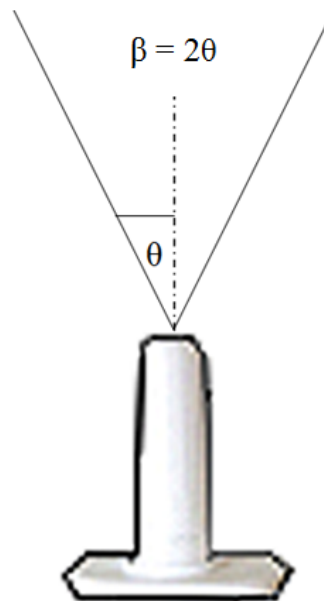


Figure 8.10  $\beta$  – full spray cone angle in comparison with  $\theta$  – half cone spray angle.

Deposition of 10 $\mu$ m particles in the two frontal zones are unaffected by the change in  $\beta$  (Figure 8.11). Again the significance of  $\beta$  is realized as particle size increases. The smaller ranged particles, that follow the gas phase velocity more readily, are optimised when released with a narrow  $\beta$ . A wider  $\beta$  gives rise to a larger range of dispersion due to the nature of a 360° spray cone. There is a low ratio of favourably dispersed particles (those pointing with the flow) to those being dispersed away from the curvature of the gas flow. Figure 8.12a shows the flow for 15 $\mu$ m being centralized when  $\beta=20^\circ$  and the increase in deviation from the centre when  $\beta=80^\circ$ . Deposition for  $\beta=20^\circ$  remains along the roof of the nasal cavity and near the septum walls with 33% depositing in the first two zones. At  $\beta=80^\circ$  a higher proportion of deposition is observed in the frontal zones.

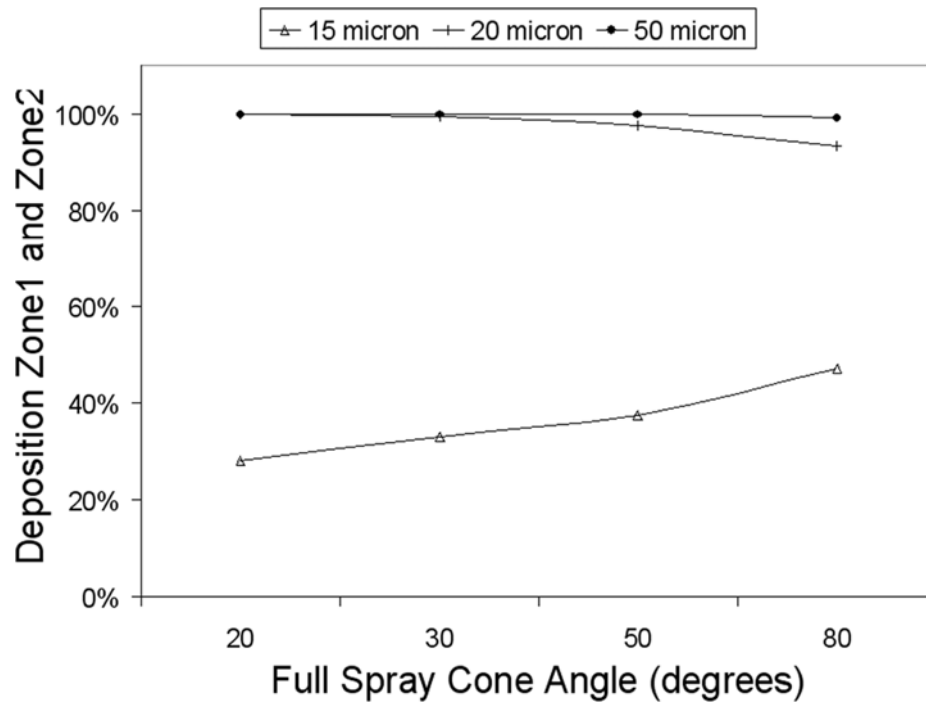
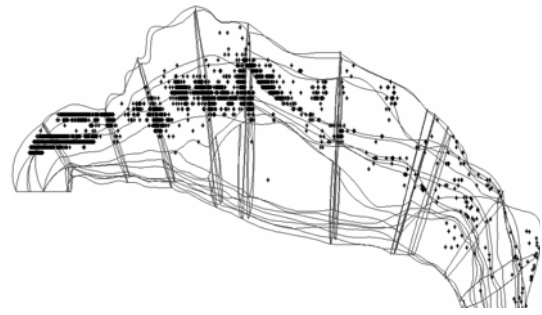
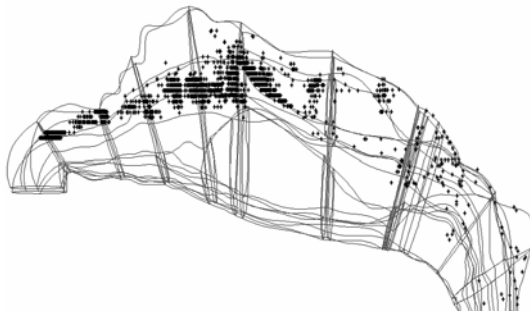
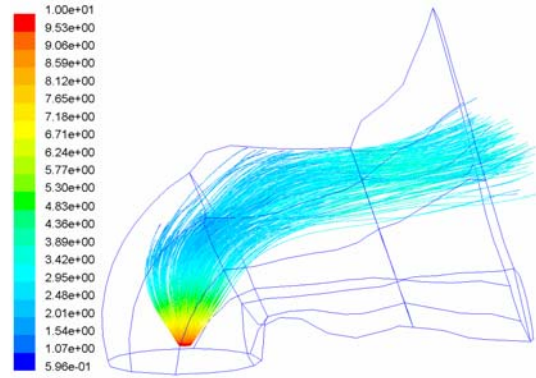
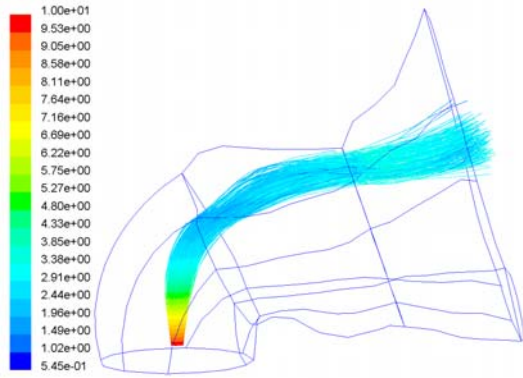


Figure 8.11 Deposition in zone1 and zone2 for monodispersed particles released at 10m/s from a small internal diameter at different spray cone angles.

The internal location of injection is closer to the roof of the vestibule than from the nostril inlet. This reduces the allowable distance for particles to relax their initial injected conditions to the gas phase conditions, thus enhancing impaction on the roof of the vestibule. This effect is more pronounced for larger particles, 20-50 $\mu$ m particles. As seen earlier these particles have near 100% deposition in the front two zones. Consequently any deviation that is favourable will project the particles into the already curved streamlines, allowing particles to travel further, albeit a small proportion. Figure 8.12b compares the two deposition patterns for 20 $\mu$ m particles at  $\beta=20^\circ$  and  $\beta=80^\circ$ . At  $\beta=20^\circ$ , impaction occurs directly above the injection release point in a concentrated area. When  $\beta=80^\circ$ , a wider area of deposition is observed in the frontal zones, whilst those particles projected favourably towards the nasal valve are able to travel beyond the  $90^\circ$  bend. However their deposition is imminent and this occurs within the middle sections of the nasal cavities. Particles in the 15-20 $\mu$ m range will exhibit an optimum  $\beta$ , which is based on the ratio of the change in favourably dispersed particles to the number of particles that are predestined to impact on the roof of the vestibule because of their particle size.



15µm at cone angle  $\beta = 20^\circ$ ,  $u = 10\text{m/s}$

15µm at cone angle  $\beta = 80^\circ$ ,  $u = 10\text{m/s}$

(a)



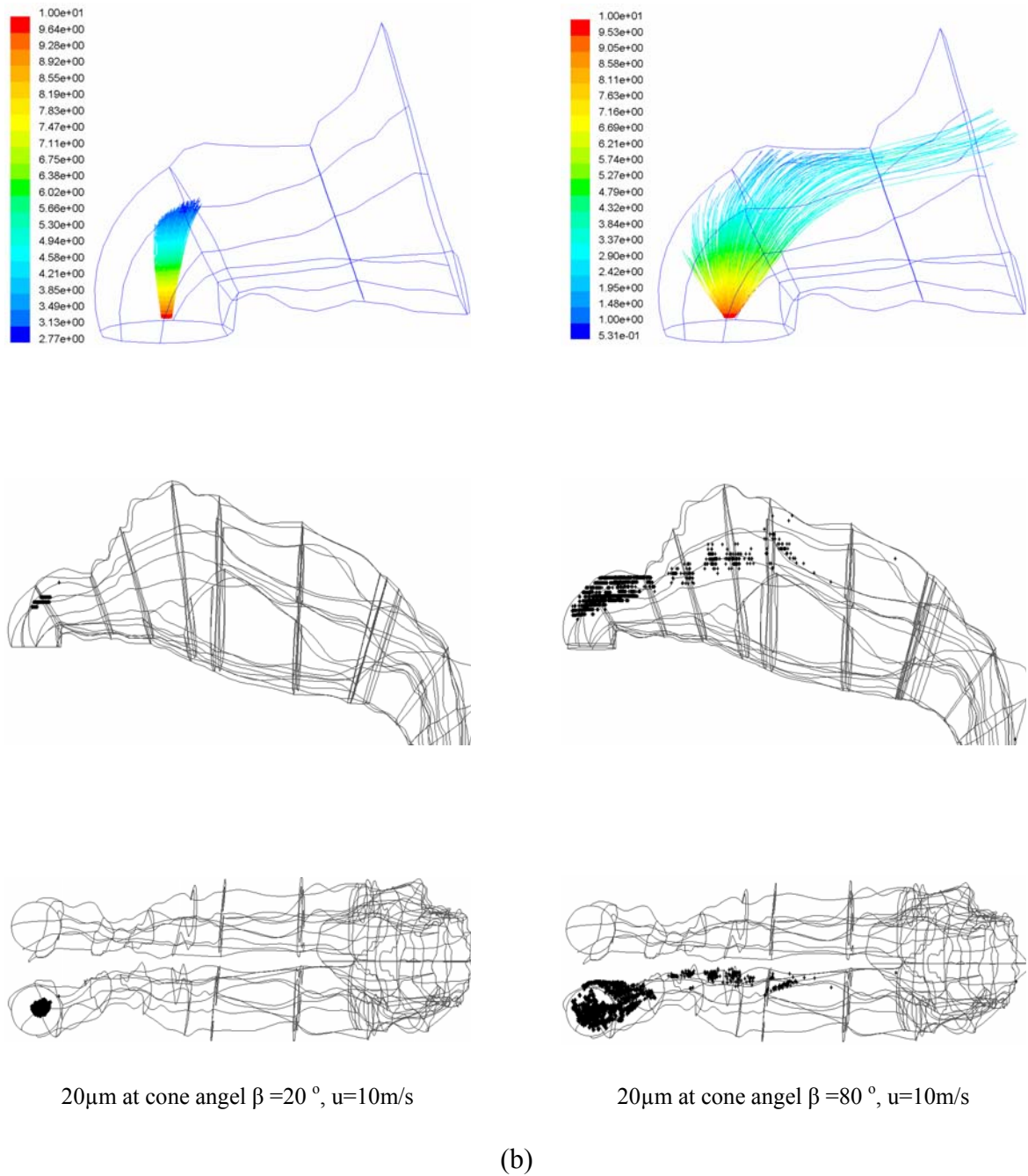


Figure 8.12 (a) Deposition patterns for 15  $\mu\text{m}$  particles released at 10 m/s from a small internal diameter at the centre of the nostril inlet surface. The spray cone angles ranged from  $20^\circ$  and  $80^\circ$ . (b) Deposition patterns for 20  $\mu\text{m}$  particles released at 10 m/s from a small internal diameter at the centre of the nostril inlet surface. The spray cone angles ranged from  $20^\circ$  and  $80^\circ$ .

### 8.3.7. Implications for Nasal Drug Delivery

The results from the present study were aimed at gaining a greater insight into what parameters are important in the design of nasal drug delivery devices. The results revealed high deposition occurring in the frontal regions of the nasal cavity. It is well recognized that one of the functions of the nose is to filter out foreign particles during inhalation which was mainly thought to be attributed to cilia (nasal hairs) movement within the nose. However the filtering function also extends to the airway geometry at multiple locations in the nasal cavity. In the frontal sections, Region 1 and 2, the flow experiences a curvature in the streamlines which acts similarly to inertial impactors that filter out high inertial, large particles. Another filter is the contraction of the nasal airway into the smallest cross-sectional area, the nasal valve region where particles are accelerated increasing their inertial property. Finally another  $90^\circ$  bend exists at the nasopharynx which acts as a final filter before particles enter the lower airways. This may be one explanation for why patients experience an undesirable 'taste' after taking drugs via the nasal cavity after patients continually sniff the drug further in.

The filtering curvature in the frontal sections along with the constricting nasal valve region is most significant for therapeutic drug delivery as it prohibits larger particles to penetrate into the middle cavity region for deposition onto the highly vascularised mucosal walls. One possible solution is to instruct users to insert the spray deeper or to develop spray devices that will naturally be inserted deeper with particles being released beyond the frontal curvature. The swirl fraction was used to create a vortical flow for the particles. It was found that high swirl fractions cause the particles to travel tangentially and that the spray penetration in the axial distance is very flat. This altered the particle trajectories since the particles reach equilibrium with the air flow field in different locations and hence different flow streamlines which produces different local deposition sites. This effect is significant for  $10\mu\text{m}$  and  $20\mu\text{m}$  particles that exhibit low and high inertial particles. In practical terms such an extreme swirl fraction may not be possible without the production of a wide spray cone angle in the design of the internal spray and optimisation studies would be required in the design process.

# CHAPTER 9

## Conclusion and Recommendations

Computationally reconstructing the nasal cavity provides extensive advantages related to fine, detailed analysis. A nasal cavity was obtained through a CT scan of the nose of a healthy 25 year old, non-smoking Asian male (170 cm height, 75 kg mass). This model became the basis of fluid dynamics analysis in order to investigate the inhalation of air and particles for toxicological and therapeutic cases. In this chapter, major findings, problems solved and research methods developed are discussed.

### 9.1. Airflow and Heat Transfer Analysis

To better understand the physiology of the nose, airflow patterns and distribution were investigated and compared with existing available data. The computational model was reconstructed from CT scans of an Asian male volunteer, who exhibited a narrower nasal valve region, wider turbinates and a shorter length in comparison with other models. Despite this, a general trend was observed for the cross-sectional area profile of the airway along the axial distance. The nasal resistance was found to contribute up to half of the total airway resistance within the first 2–3 cm of the airway. The flow patterns were captured through novel visualisation of planes in complex flow areas that depicted formations of vortices primarily in the upper olfactory region and just posterior to the nasal valve where the geometry begins to expand. The bulk flow travelled through the middle regions of the nasal valve and remained close to the septum walls. Only a small proportion reached the olfactory region and the outer meatus extensions that were created by the turbinate



protrusions in the main nasal passage. This leads to two highlighting issues: Firstly, low flow in the olfactory region provides a defence mechanism that prevents particles where the trajectory is heavily dependent on flow patterns being deposited onto the sensitive olfactory nerve fibres, while vapours are allowed to diffuse for olfaction. Secondly, the low flow in the meatus region brings into the question the efficiency of the turbinate protrusions to condition the inspired air.

In terms of the heat transfer, the airflow distribution was shown to affect the conditioning ability of the nose. The results suggested that the air is conditioned early in the front region for 25°C degree inhalation while for colder air at 12°C was heated up at a distance further downstream before the nasopharynx. Differences in the width of the airway were found to be critical, particularly in the frontal regions. The comparative temperature difference between the left and right airway was greatest in the frontal region. Heating of the air is therefore expedited when the air is surrounded by the hotter walls. Analysis of the airflow distribution through a plane that cuts through the turbinates showed a small percentage of air reaching the outer meatus region (2%). This suggests that the heating ability of the turbinates, due to the increase in surface area of the meatus regions, only affects 2% of the flow field. These results suggest the role of the turbinates to condition the air may not be solely reliant on the surface area contact but may in fact be influenced by the nature of the flow that the turbinates cause. For example, the protrusions create narrow meatus airways which affect the flow regime (laminar or turbulent), hence the existent heating capability. Further studies into this effect are needed.

## 9.2. Inhalation of Toxic Particles

In the human nasal cavity, the dominant mechanism of deposition is by inertial impaction, particularly for particles greater than 5µm at low flow rates (7.5-15L/min). Under these conditions, the inertial parameter was used to develop comparisons between particles that exist in this inertial regime. Particle morphology plays a significant role in the aerodynamic behaviour of the particle itself. The most significant particle characteristic is the shape factor, which greatly influences the particle drag coefficient. In this research, spherical, rough surface, and fibrous shaped particles were considered. In the case of spherical particles, the density of the particles has minimal affect on the aerodynamic flight. The deposition efficiency of the particles was determined over a range of diameters

and an empirical equation relating the deposition to the aerodynamic diameter and the flow rate was established. Rough surface particles were modelled by creating an agglomerate of spheres. This agglomerate acted as representatives of pollen particles. The well established general drag correlation for arbitrary particle shapes by Haider and Levenspiel (1989) was used and its correlation implemented as a custom function in FLUENT. Using this methodology, the resultant data indicated the deposition of pollen (rough surface) particles was smaller when compared with a sphere having the same aerodynamic diameter. This major finding indicates that the rough surface increases the drag coefficient of pollen when compared with a spherical particle. Fibrous particles, such as asbestos fibres were also considered. It was found that the general drag correlation by Haider and Levenspiel (1989) became less accurate as the particle shape deviated further from a spherical shape (i.e. when the shape factor decreased from 1  $\rightarrow$  0). The shape factor of a fibre is significantly low due to its natural elongated shape. Considering this, a more specific drag correlation by Tran-Cong et al. (2004) was applied in the methodology. The model loses some generality but is compensated by the better prediction of the fibre deposition patterns. In addition, the morphology of asbestos fibres was found to be significant. Given that the density and cross-sectional diameter is small, the asbestos fibre length became insignificant in the deposition efficiency. It was seen that the deposition increased from 8.7%-9.6% for an increase in fibre length of 10 $\mu$ m to 300 $\mu$ m. This simple geometrical property causes about 90% of the particles to travel through the nasal cavity and most likely to deposit deep in the lung causing severe health problems. Conversely, man-made fibres where the density and the cross-sectional diameter is higher, exhibit greater mass per unit length. This concentration of mass increases the fibre's inertia, leading to an increase in deposition. In addition, the fibre deposition increased from 14%-50% over the fibre length range from 10 $\mu$ m to 300 $\mu$ m. According to the results, it was evident that the mass per unit length was an important parameter, as it has a significant contribution to the fibre inertia. The mass per unit length parameter was therefore used to extrapolate the deposition curve against fibre length for different fibre configurations (e.g. different cross-sectional diameters, different densities). These significant results may assist in the design of new aerosols and guide practical clinical tests for toxicological.

### 9.3. Inhalation of Sprayed Particles

While it is indeed important to filter out toxic particles, there is an opportunity to exploit the highly vascularised walls that exist in the nasal cavity. Nasal sprays deliver atomised particles into the nasal cavity at high velocities. The structure of the atomised spray from a nasal spray was not known, which made the setting up of the initial particle boundary conditions for the CFD simulations difficult. This research designed a nasal spray test station to capture the spray characteristics that would allow intelligent settings of the particle boundary conditions. The experiment determined parameters that were important during the spray atomisation from a nasal spray device. Experimental images of a continuous spray formation were obtained through a high speed camera, PIV and PDPA systems. The experimental work provided a qualitative insight and obtained realistic range of values for the following parameters.

- ◆ Nozzle diameter
- ◆ Diameter at break-up length
- ◆ Spray cone angle
- ◆ Initial particle velocity
- ◆ Break-up length

It was found that a break-up length from the nozzle, which is caused by the internal atomiser of the nasal spray, was evident. Particles were formed at this break-up length at a cone diameter greater than the spray nozzle diameter. Findings indicated that a larger diameter at the break-up length led to an increase in particle deposition in the frontal sections of the nasal cavity. The swirl fraction determined how much of the velocity magnitude went into a tangential component.

These parameters then became the foundation for CFD studies into nasal drug delivery into the nasal cavity. The parameters were tested within their realistic ranges and subsequently, deposition patterns and deposition efficiencies were determined. For a flow rate of 20 L/min 10-20 $\mu$ m particles were sensitive to initial injection velocity, insertion angle, and spray cone angle as its size increased. Larger particles exhibited very high Stokes numbers (inertial parameter) causing it to be insensitive to these parameters. Current commercially available nasal sprays produce mean size particles of 45-60 $\mu$ m. This presents a problem as larger particles ( $\geq 20\mu$ m) are relatively insensitive towards initial injection conditions and are likely to deposit in the anterior portion of the nose

decreasing the drug delivery's efficiency. Producing smaller particles ( $\leq 20\mu\text{m}$ ) during atomisation is an option for designers, however smaller particles are more inclined to follow the gas phase flow and can lead to deposition beyond the nasal pharynx. In addition, the effect of the swirl fraction differed for  $10\mu\text{m}$  and  $20\mu\text{m}$  particles. The particles were severely altered by the swirl fraction and therefore local deposition sites are altered. By combining a swirling component along with a narrow spray into the main streamlines, greater penetration of larger particles into the nasal cavity may be possible.

The simulations also demonstrated that numerous variables exist during everyday nasal spray actuation which are significant given the order of magnitudes that the analysis deals within. Numerical studies are able to isolate parameters to investigate their effects, however in reality, these parameters and more are combined during an actuation, which maybe an explanation for the differences in literature data regarding spray cone angles and their effect on deposition efficiencies.

The ideas formulated can be used as a basis for improving the design of nasal spray devices to achieve better drug delivery such as (i) redirecting the release point of the spray (i.e. the insertion angle) to align with flow streamlines (ii) controlling the particle size distribution and (iii) controlling the particle's initial velocity. In the attempt to replicate actual nasal spray applications while isolating the investigating parameters, idealized injected conditions for the particles were used, along with the idealized nasal cavity. Further studies are needed to extend the results to other nasal cavities, to include the permeability effects of nasal hairs, and to establish more accurate initial particle conditions such as the instantaneous velocity at injection that can include swirl effects.

Finally, the airflow was simulated using a turbulence model. This implies that the particle dispersion should also be affected by the turbulent fluctuations. The most commonly used turbulent dispersion model is the stochastic process of the Discrete Random Walk model. This model is often coupled with RANS-based turbulence models which place the assumption of isotropic turbulence. In free shear flows this assumption is sufficient, however in wall-bounded flows; the anisotropic character at the near walls presents a problem. This was encountered in the current research, and a hybrid tracking technique applying a non-turbulent dispersion for low inertial particles and a turbulent dispersion for

high inertial particles was used. Currently models exist but the accessing the fluctuating velocity variables in the FLUENT code is not permitted.

## 9.4. Recommendations for Further Study

There are several further studies that can be performed to continue this research which encompasses both the experimental and simulation aspects.

The experiment provided a first step and insight into parameters associated with nasal spray design. The measurements were made from a continuous spray. In a new study currently being undertaken, an actuating device powered by pneumatics is being designed to repeatedly pump a nasal spray. This machine will be taken to the CSIRO laser laboratory for the PIV and PDPA laser analysis. This extension will provide further insights into the particle boundary conditions to give even more realistic simulations.

Analysis of airflow in the turbinate region found that the distribution of air passing within this region was constrained to the nasal septum, thus the wide, outer sections of the turbinates (meatus airway) were not exposed to the inhaled air. This raises questions regarding the role of the turbinates to heat the inhaled air through an increase in the surface area caused by the meatus or whether the geometry of the turbinates was to invoke turbulence within the airflow thereby increasing the heat convection process. A larger sample of nasal geometries is needed to clarify this issue, however obtaining CT scans, processing the images, and converting the data into a computational model is very time consuming.

Further studies may also involve running the simulations under transient flow. Since data has been established for steady simulations, an unsteady simulation will provide important comparisons into airflow structures and particle dynamics. The unsteady simulations may provide insight into types of inhalation such as high levels (sniffing) and the holding of breaths, which influence particle flow dynamics. Different breathing patterns may also be investigated by using unsteady simulations. The type of inhalation affecting the deposition patterns of particles will then determine whether one form of inhalation is more effective than another for drug delivery. Studies of abnormalities to the nasal cavity can also be performed to investigate possible surgical interventions. The simulations can provide

cause-and-effect results from ‘virtual surgery’ where walls and sections of the nasal cavity can be modified in the computational model to explore the effects on airflow and heat transfer. This concept is also highly applicable to sleep apnoea where the influence of airway geometries plays a critical role in the breathing ability.

Additionally, there has been little investigation into the influence of the movements of the nasal walls in terms during nasal obstruction and general physiological changes during breathing. In every study thus far, the walls have been assumed to be rigid in numerical simulations and replicate cast experiments. The study of fluid-structure interaction is still a difficult stream, as it involves both statics and dynamics equations that need to be coupled through an interface. This is especially difficult when dealing with highly complex geometries such as the nasal cavity.

The final recommendation is in terms of the numerical modelling technique. The effect of using a RANS based turbulence model is that it inherits the assumption of isotropic turbulent properties which creates problems when dealing with wall-bounded flows. The turbulence kinetic energy, (TKE) is too high for the normal fluctuating velocity. One possible solution is to apply a damping function to TKE within the near wall region by applying an exponential function related to the  $y^+$  of the cells near the walls (see Appendix). Other methods for this include the newly developed  $v^2$ -f turbulence model which accounts for the smaller normal wall fluctuation. This method is computationally efficient when compared with the other alternative method of Large Eddy Simulations.

## Appendix – User Defined Functions

```

/*****
User-Defined Function to verify, track and apply an alternative fibre drag correlation
(used in Chapter 6)
*****/
#include "udf.h"
#include "dpm.h"

DEFINE_INIT(Initiateki, domain)
{
    /* if memory for the particle variable titles has not been
    * allocated yet, do it now */

    if (NULLP(user_particle_vars)) Init_User_Particle_Vars();
    /* now set the name and label */
    strcpy(user_particle_vars[0].name, "drag_force");
    strcpy(user_particle_vars[0].label, "Drag Coefficient");

    strcpy(user_particle_vars[1].name, "Fluid-Re");
    strcpy(user_particle_vars[1].label, "Fluid Reynolds");

    strcpy(user_particle_vars[2].name, "Fluid-Re-Part");
    strcpy(user_particle_vars[2].label, "Fluid Reynolds Part");

    strcpy(user_particle_vars[3].name, "Cd_Trans-Cong");
    strcpy(user_particle_vars[3].label, "Cd_Trans-Conga");

    strcpy(user_particle_vars[4].name, "Particle_Re");
    strcpy(user_particle_vars[4].label, "Particle_Re");
} /* update the user scalar variables */

```

```

DEFINE_DPM_SCALAR_UPDATE(reynolds, c, t, initialize, p)
{
    real fluid_vel, visc_kine, d_charact;
    real x_position;
    visc_kine=0.0000146;

    /*****fluid velocitycalculation*****/
    fluid_vel=sqrt(pow(C_U(c,t),2)+pow(C_V(c,t),2)+pow(C_W(c,t),2));
    /*****fluid velocitycalculation*****/
    if (initialize)
    {
        /* this is the initialization call, set:
        * p->user[0] initialize to 0
        */
        p->user[0] = 0;
        p->user[1] = 0;
        p->user[2] = 0;
        p->user[3] = 0;
        p->user[4] = 0;
    }
    else
    {
        x_position = P_POS(p)[0];

        /*****fluid Re calculation*****/
        if (x_position < -0.0075)
            d_charact=0.00832;

        else if (x_position<0.0025)

```

```

    d_charact=0.00840;

    else if (x_position<0.0105)
    d_charact=0.00712;

    else if (x_position<0.02)
    d_charact=0.00486;

    else if (x_position<0.0265)
    d_charact=0.00481;

    else if (x_position<0.043)
    d_charact=0.00626;

    else if (x_position<0.057)
    d_charact=0.01045;

    else if (x_position<0.067)
    d_charact=0.02245;

    else if (x_position<0.073)
    d_charact=0.01603;

    else
    d_charact=0.014;

p->user[1] =fluid_vel*d_charact/visc_kine;
}
}
DEFINE_DPM_DRAG(particle_drag_force,Re,p)
{
    real drag_force;
    real dadn,circ_sqrt;
    real aa,bb,cc;
    real x_position, fluid_re, d_charact;
    real Cd_TranCong;

    /*****fluid Re calculation*****/
    x_position = P_POS(p)[0];

```

```

    if (x_position < -0.0075)
    d_charact=0.0079576;

    else if (x_position<0.0025)
    d_charact=0.0080547;

    else if (x_position<0.0105)
    d_charact=0.0070349;

    else if (x_position<0.02)
    d_charact=0.005193;

    else if (x_position<0.0265)
    d_charact=0.0051592;

    else if (x_position<0.043)
    d_charact=0.0060662;

    else if (x_position<0.057)
    d_charact=0.010711;

    else if (x_position<0.067)
    d_charact=0.02245;

    else if (x_position<0.073)
    d_charact=0.01603;

    else
    d_charact=0.014;
    /*****fluid Re calculation*****/
    fluid_re = Re*d_charact/P_DIAM(p);
    dadn = 1.1497;
    circ_sqrt = pow(0.91109,0.5);

    aa = 24*dadn/fluid_re;
    bb = 1 + (0.15/circ_sqrt) * pow((dadn*fluid_re),0.687);
    cc = 0.42*pow(dadn,2)/(circ_sqrt*(1+42500*pow((dadn*fluid_re),-1.16)));

    Cd_TranCong = aa * bb + cc;
    drag_force = (aa * bb + cc)*Re*0.75;
    p->user[0]=drag_force;

```



```

        p->user[2]=fluid_re;
        p->user[3] = Cd_TranCong;
        p->user[4] = Re;
        return (drag_force);
} /* calculates the drag coefficient for agglomerate of spheres that simulate pollen */

```

```

DEFINE_DPM_OUTPUT(Fluid_Re_out,header,fp,p,thread,plane)

```

```

{
    char name[100];
    if (header)
    {
        if (NNULLP(thread))
            par_fprintf_head(fp,"%s %d\n",thread->head->
                dpm_summary.sort_file_name,11);
        else
            par_fprintf_head(fp,"%s %d\n",plane->sort_file_name,11);
        par_fprintf_head(fp,"%10s %10s %10s %10s "
            "%10s %10s %10s %10s %10s %s)\n",
            "U", "V", "W", "diameter", "Cd_TranCong",
            "Particle_Re", "Fluid-Re", "Drag-Force", "Fluid-Re-fromPartRe", "name");
    }
    else
    {
        sprintf(name, "%s:%d",p->injection->name,p->part_id);
        #if PARALLEL
            /* add try_id and part_id for sorting in parallel */
            par_fprintf(fp,
                "%d %d (%10.6g %10.6g %10.6g "
                "%10.6g %10.6g %10.6g %10.6g %s)\n",
                p->injection->try_id, p->part_id,
                p->state.V[0], p->state.V[1], p->state.V[2],
                p->state.diam, p->flow_rate, p->user[1] p->state.time,
                p->user[0], name);
        #else
            par_fprintf(fp,
                "%10.6g %10.6g %10.6g "
                "%10.6g %10.6g %10.6g %10.6g %10.6g %10.6g %s)\n",
                p->state.V[0], p->state.V[1], p->state.V[2],
                p->state.diam, p->user[3], p->user[4],
                p->user[1], p->user[0],p->user[2], name);
        #endif
    }
}

```

```

    }
}

```

```

/***** UDF that computes
mass diffusivity as a function of Temperature
*****/
#include "udf.h"
DEFINE_DIFFUSIVITY(new_diffusivity,c,t,i)
{
    return 2.16e-05 * ((C_T(c,t)/278.15)^1.8);
}

```

## References

- ASHRAE. 2001. "Chapter 26 - Ventilation and Infiltration: Ventilation and Filtration." In ASHRAE handbook 2001 Fundamentals. Atlanta: American Society of Heating, Refrigeration and Air Conditioning Engineers, Inc.
- Babu, K.R., M.V. Narasimhan and K. Narayanaswamy. 1982. "Correlations for prediction of discharge rate, cone angle and aircore diameter of swirl spray atomisers." In Proceedings of the 2nd International Conference on Liquid Atomisation and Spray Systems. Madison, Wisc.
- Bailey, B. 1998. "Nasal function and evaluation, nasal obstruction." In Head and Neck Surgery: Otolaryngology. 2nd ed. New York, NY: Lippincott-Raven.
- Beekhuis, G.J. 1976. "Nasal obstruction after rhinoplasty: etiology, and techniques for correction." *Laryngoscope* 86(4):540-548.
- Beidler, L.M. 1980. "The chemical senses: gustation and olfaction." In *Medical Physiology*, ed. V.B. Mountcastle. St. Louis: C.V. Mosby Co.
- Berglund, B. and T. Lindvall. 1982. "Olfaction." In *The Nose: Upper Airway Physiology and the Atmospheric Environment*, eds. D.F. Proctor and I. Andersen. New York: Elsevier Biomedical Press.
- Bousquet, J., P. Van Cauwenberge, N. Khaltaev and W.H.O. 2001. "Allergic rhinitis and its impact on asthma." *J. Allergy and Clin. Immun.* 108(5):147-334.
- Calhoun, K.H., W. House, J.A. Hokanson and F.B. Quinn. 1990. "Normal nasal airway resistance in noses of different sizes and shapes." *Otolaryngol Head Neck Surg* 103:605-609.
- Carey, J.W. and A.T.J. Steegmann. 1981. "Human nasal protrusion, latitude, and climate." *Am J Phys Anthropol* 56:313-319.
- Cauna, N. 1982. "Blood and nerve supply of the nasal lining." In *The Nose* eds. D.F. Proctor and I. Anderson. New York: Elsevier Biomedical Press.
- Chang, H.K. 1989. "Flow dynamics in the respiratory tract." In *Respiratory Physiology, an Analytical Approach*, eds. H.K. Chang and M. Paiva. New York: Dekker.

Cheng, K.H., Y.S. Cheng, H.C. Yeh, A. Guilmette, S.Q. Simpson, Y.H. Yang and D.L. Swift. 1996. "In-vivo measurements of nasal airway dimensions and ultrafine aerosol deposition in the human nasal and oral airways." *J. Aerosol Sci.* 27(5):785-801.

Cheng, Y.S. 2003. "Aerosol deposition in the extrathoracic region." *Aerosol Sci. Tech.* 37:659-671.

Cheng, Y.S., T.D. Holmes, J. Gao, R.A. Guilmette, S. Li, Y. Surakitbanharn and C. Rowlings. 2001. "Characterization of nasal spray pumps and deposition pattern in a replica of the human nasal airway." *J. Aerosol Med.* 14(2):267-280.

Cheng, Y.S., H.C. Yeh, S.M. Smith, K.H. Cheng and D.L. Swift. 1998. "Deposition of ultrafine particles in the nasal and tracheo-bronchial airways." *J. Aerosol Sci.* 29(1):S941-S942.

Chung, K.Y.K, R.J. Cuthber, G.S. Revell, S.G. Wassel and N. Summer. 2000. "A study on dust emission, particle size distribution and formaldehyde concentration during machining of medium density fibreboard. ." *Annals of Occ. Hyg.* 44:455-466.

Churchill, S., L.L. Shackelford, N. Georgi and M. Black. 2004. "Morphological variation and airflow dynamics in the human nose." *Am J Human Biol* 16:625-638.

Cottle, M.H. 1955. "The structure and function of the nasal vestibule." *Arch Otolaryngol* 62:173-181.

Courtiss, E.H. and R.M. Goldwyn. 1983. "The effects of nasal surgery on airflow." *Plastic Reconstr Surg* 72:9-19.

Crawford, J.H. 1949. "Determination of the specific gravity of ragweed pollen (*Ambrosia elatior*) and conversion of gravity sample counts to volumetric incidence. ." *Publ. Health Rep.* 64:1195-1200.

Croce, C., R. Fodil, M. Durand, G. Sbirlea-Apiou, G. Caillibotte, J.F. Papon, J.R. Blondeau, A. Coste, D. Isabey and B. Louis. 2006. "In vitro experiments and numerical simulations of airflow in realistic nasal airway geometry." *Annals of Biomedical Engineering* 34(6):997-1007.

Crowder, T.M., J.A. Rosati, J.D. Schroeter, A.J. Hickey and T.B. Martonen. 2002. "Fundamental effects of particle morphology on lung delivery: Predictions of Stokes law and the particular relevance to dry powder inhaler formulation and development." *Pharama. Res.* 19(3):239-245.

Crowe, C.T., M. Sommerfeld and Y. Tsuji. 1998. *Multiphase flows with droplets and particles.* Boca Raton, Fla.: CRC Press.

Dai, Y.T., Y.J. Juang, Y.Y. WU, P.N. Breyse and D.J. Hsu. 2006. "In vivo measurements of inhalability of ultralarge aerosol particles in calm air by humans." *J. Aerosol Sci.*(37):967-973.

- Dayal, P., M.S. Shaik and M. Singh. 2004. "Evaluation of different parameters that affect droplet-size distribution from nasal sprays using Malvern Spraytec." *J. Phar. Sci.* 93:1725-1742.
- Doorly, D., D.J. Taylor, P. Franke and R.C. Schroter. 2008. "Experimental investigation of nasal flow." *Proc. of the Institution of Mechanical Engineers Part H - J Engineering in Medicine* 222(H4):439-453.
- Eck, C.R., T.F. McGrath and A.G. Perlwitz. 2000. "Droplet size distributions in a solution nasal spray." *Respir. Drug Deliv.* 7:475-478.
- Elad, D., R. Liebenthal, B.L. Wenig and S. Einav. 1993. "Analysis of air flow patterns in the human nose." *Medical & Biological Engineering & Computing* 31:585-592.
- Escudier, M. 1988. "Vortex breakdown: Observations and explanations." *Prog. Aerospace Sci.* 422(25):189-229.
- Etherington, G., J.R.H. Smith, M.R. Bailey, M.D. Dorrian, A.L. Shutt and M.J. Youngman. 1998. "Deposition and clearance of inhaled particles in the human nasal passage: Implications for dose assessment." *Radiation Protection Dosimetry* 79(1-4):249-252.
- Franciscus, R.G. and J.C. Long. 1991. "Variation in human nasal height and breadth." *Am J Phys Anthropol* 85:419-427.
- Fry, F.A. and A. Black. 1973. "Regional deposition and clearance of particles in the human nose." *Aerosol Sci.* 4(113-124).
- Gabitto, J. and C. Tsouris. 2007. "Drag coefficient and settling velocity for particles of cylindrical shape." *Powder Technol.* doi:10.1016/j.powtec.2007.1007.1031.
- Gao, J., D. Jiang, Z. Huang and X. Wane. 2005. "Experimental and numerical study of high-pressure-swirl injector sprays in a direct injection gasoline engine. Proceedings of the Institution of Mechanical Engineers. Part A." *J. Power Energy* 219(8):617-629.
- Garcia, G.J. M., N. Bailie, D.A. Martins and J.S Kimbell. 2007. "Atrophic rhinitis: a CFD study of air conditioning in the nasal cavity." *J Appl. Physiol.* 103:1082-1092.
- Girardin, M., E. Bilgen and P. Arbour. 1983. "Experimental study of velocity fields in a human nasal fossa by laser anemometry." *Ann. Otol. Rhinol. Laryngol.* 92:231-236.
- Gonda, I. and E. Gipps. 1990. "Model of disposition of drugs administered into the human nasal cavity." *Pharm. Res.* 7:69-75.
- Gradon, L. and A. Podgorski. 1992. "Experimental study on fibrous particle deposition in the human nasal cast." *J. Aerosol Sci.* 23(1):469-472.
- Guilmette, R.A., Y.S. Cheng, H.C. Yeh and D.L. Swift. 1994. "Deposition of 0.005-12 $\mu$ m monodisperse particles in a computer-milled, MRI-based nasal airway replica. ." *Inhal. Toxicol.* 6(S1):395-399.

- Hadfield, E.M. 1972. "Damage to the human nasal mucosa by wood dust." In *Inhaled Particles III*, ed. W.H. Walton: Unwin Bros. Old Working.
- Hahn, I., P.W. Scherer and M.M. Mozell. 1993. "Velocity profiles measured for airflow through a large-scale model of the human nasal cavity." *J Appl. Physiol.* 75(5):2273-2287.
- Haider, A. and O. Levenspiel. 1989. "Drag coefficient and terminal velocity of spherical and nonspherical particles." *Powder Tech.* 58:63-70.
- Harrington, J.B. and K. Metzger. 1963. "Ragweed pollen density." *American J. Botany* 50:532-539.
- Häußermann, S., A.G. Bailey, M.R. Bailey, G. Etherington and M.J. Youngman. 2001. "The influence of breathing patterns on particle deposition in a nasal replicate cast." *J. Aerosol Sci.* 33:923-933.
- Heyder, J. and G. Rudolf. 1977. "Deposition of aerosol particles in the human nose." In *Inhaled particles*, ed. W.H. Walton. Oxford UK: Pergamon Press.
- Hinze, J.O. 1975. *Turbulence*. New York: McGraw-Hill Publishing Co.
- Hornung, D.E., D.A. Leopold, S.L. Youngentob, P.R. Sheehe, G.M. Gagne, F.D. Thomas and M.M. Mozell. 1987. "Airflow patterns in a human nasal model." *Arch Otolaryngol Head Neck Surg* 113:169-172.
- Hörschler, I., M. Meinke and W. Schröder. 2003. "Numerical simulation of the flow field in a model of the nasal cavity." *Comp. Fluids* 32(39-45).
- Hounam, R.F., A. Black and M. Walsh. 1971. "Deposition of aerosol particles in the nasopharyngeal region of the human respiratory tract." *J. Aerosol Sci* 2:341-352.
- Inthavong, K., Z.F. Tian, H.F. Li, J.Y. Tu, W. Yang, C.L. Xue and C.G. Li. 2006. "A numerical study of spray particle deposition in a human nasal cavity." *Aerosol Sci. Technol.* 40(1034-1045).
- Isabey, D. and H.K. Chang. 1981. "Steady and unsteady pressure-flow relationships in central airways." *J. Appl. Physiol.* 51:1338-1348.
- Itoh, H., G.C. Smaldone, D. L. Swift and H.N.J. Wagner. 1985. "Mechanisms of aerosol deposition in a nasal model." *J. Aerosol Sci.* 16:529-534.
- Keck, T., R. Leiacker, A. Heinrich, S. Kuhneman and G. Rettinger. 2000a. "Humidity and temperature profiles in the nasal cavity." *Rhinology* 38(167-171).
- Keck, T., R. Leiacker, M. Klotz and J. Lindemann. 2000b. "Detection of particles within the nasal airways during respiration." *Eur Arch Oto-Rhino-L* 257:493-497.
- Keck, T., R. Leiacker, H. Riechelmann and G. Rettinger. 2000c. "Temperature profile in the nasal cavity." *Laryngoscope* 110:651-654.

- Kelly, J.T., B. Asgharian, J.S. Kimbell and Wong. B.A. 2004. "Particle deposition in human nasal airway replicas manufactured by different methods. Part 1: Inertial regime particles." *Aerosol Sci.Tech.* 38(1063-1071).
- Kelly, J.T., A.K. Prasad and A.S. Wexler. 2000. "Detailed flow patterns in the nasal cavity." *J Appl. Physiol.* 89:323-337.
- Kerr, A. 1997. "Rhinology." In *Scott-Brown's Otolaryngology* 6th Ed. Oxford: Butterworth-Heinemann.
- Kesavanathan, J., R. Bascom and D.L. Swift. 1998. "The effect of nasal passage characteristics on particle deposition." *J. Aerosol Med.* 11(27-39).
- Keyhani, K., P.W. Scherer and M.M. Mozell. 1995. "Numerical simulation of airflow in the human nasal cavity." *J.Biomech. Eng.* 117:429-441.
- Kimbell, J., J.D. Schroeter, B. Asgharian, B.A. Wong, R.A. Segal, C.J. Dickens, J.P. Southall and F.J. Miller. 2004. "Optimisation of nasal delivery devices using computational models." *Res. Drug Del.* 9(233-238).
- Kimbell, J.S., R.A. Segal, B. Asgharian, B.A. Wong, J.D. Schroeter, J.P. Southall, C.J. Dickens, G. Brace and F.J. Miller. 2007. "Characterization of deposition from nasal spray devices using a computational fluid dynamics model of the human nasal passages." *J. Aeros. Med.* 20(1):59-74.
- Kreplin, H-P. and H. Eckelmann. 1978. "Behaviour of the three fluctuating velocity components in the wall region of a turbulent channel flow." *Phys. Fluids* 22(7):1233-1239.
- Lefebvre, A.H. 1989. *Atomization and Sprays.* : Hemisphere Publishing Corporation.
- Leonard, B.P. and S. Mokhtari. 1990. "ULTRA-SHARP Nonoscillatory convection schemes for high-speed steady multidimensional flow." NASA Lewis Research Center.
- Lienar, K., R. Leiacker, J. Lindemann, G. Rettinger and T. Keck. 2003. "Nasal mucosal temperature after exposure to cold, dry air and hot, humid air." *Acta Otolaryngol* 123:851-856.
- Lindemann, J., T. Keck, K. Wiesmiller, B. Sander, H.J. Brambs, G. Rettinger and P. Pless. 2004. "A numerical simulation of intranasal air temperature during inspiration." *The Laryngoscope* 114:1037-1041.
- Lippman, M. 1990. " Effects of fibre characteristics on lung deposition, retention and disease." *Environ. Health Perspect.* 88:311-317.
- Lippman, M., D.B. Yeates and R.E. Albert. 1993. "Deposition, retention and clearance of inhaled particles." *J. Ind. Med.* 37:337-362.
- Macinnes, J.M. and F.V. Bracco. 1992. "Stochastic particle dispersion modeling and the tracer particle limit." *Physics of Fluids A* 4:2809-2823.

- Masing, H. 1967. "Investigations about the course of flow in the nose model." *Arch Klin Exp Ohren Nasen Kehlkopfheilkd* 189:371-381.
- Morsi, S.A. and A.J. Alexander. 1972. "An investigation of particle trajectories in two-phase flow systems." *J. Fluid Mech.* 55(2):193-208.
- Mumford, D. and J. Shah. 1989. "Optimal approximations by piecewise smooth functions and associated variational problems." *Comm.Pure and Appl. Mathem.* XLII:577-685.
- Myers, A.D. 1993. *Biological basis of facial plastic surgery*. New York, NY: Thieme Medical Publisher.
- Mygind, N., M. Pedersen and H. Nielsen. 1982. "Morphology of the upper airway epithelium." In *The Nose* eds. D.F. Proctor and I. Anderson. New York: Elsevier Biomedical Press.
- Naftali, S., M. Rosenfeld, M. Wolf and D. Elad. 2005. "The air-conditioning capacity of the human nose, ." *Annals of Biomedical Engineering*, 33:545-553.
- Naftali, S., R.C. Schroter, J. Shiner and D. Elad. 1998. "Transport phenomena in the human nasal cavity: A computational model." *Annals of Biomedical Engineering* 26:831-839.
- Newman, S.P., F. Moren and S.W. Clarke. 1998. "Deposition pattern of nasal sprays in man." *Rhinology* 26(111-120).
- Nucci, G., B. Suki and K. Lutchen. 2003. "Modeling airflow-related shear stress during heterogeneous constriction and mechanical ventilation." *J Appl Physiol* 95:348-356.
- Orive, G., R.M. Hernandez, A.R. Gascon, A. Dominguez-Gil and J.L. Pedraz. 2003. "Drug delivery in biotechnology: present and future." *Current Opinion in Biotechnology* 14:659-664.
- Park, K.I., C. Brucker and W. Limberg. 1997. "Experimental study of velocity fields in a model of human nasal cavity by DPIV." In *Laser Anemometry Advances and Applications: Proceedings of the 7th International Conference*, eds. B. Ruck, A. Leder and D. Dopheide. Karlsruhe, Germany: University of Karlsruhe.
- Pattle, R.E. 1961. "The retention of gases and particles in the human nose." In *Inhaled particles and vapors* ed. C.N. Davies. Oxford, UK: Pergamon Press.
- Piegl, L.A. and W Tiller. 1995. *The NURBS book*. New York, NY: Springer-Verlag.
- Proctor, D.F. 1982. "The upper airway." In *The Nose*, eds. D.F. Proctor and I. Anderson. New York: Elsevier Biomedical Press.

- Proetz, A.W. 1951. "Air currents in the upper respiratory tract and their clinical importance." *Ann Otol Rhinol Laryngol* 60:439-467.
- Richmond, C. 2004. "Sir Godfrey Hounsfield." *British Medical Journal* 329(7467):687.
- Rizk, N.K. and A.H. Lefebvre. 1985. "Internal flow characteristics of simplex swirl atomisers." *AIAA J. Propul. Power* 1(3):193-199.
- Robert, G.H. 2001. "Forced inspiratory nasal flow–volume curves: A simple test of nasal airflow." *Mayo Clin. Proc.* 76:990-994.
- Roland, N.J., R.K. Bhalla and J. Earis. 2004. "The local side effects of inhaled corticosteroids: Current understanding and review of the literature." *Chest* 126:213-219.
- Scherer, P.W., I.I. Hahn and M.M. Mozell. 1989. "The biophysics of nasal airflow." *Otolaryngol. Clin. North Am* 22:265-278.
- Schlichting, H. 1979. *Boundary-Layer Theory*. New York: McGraw-Hill.
- Schreck, S., K.J. Sullivan, C.M. Ho and Chang H.K. 1993. "Correlations between flow resistance and geometry in a model of the human nose." *J. Appl. Physiol* 75(4):1767-1775.
- Schroeter, J.D., J.S. Kimbell and B. Asgharian. 2006. "Analysis of particle deposition in the turbinate and olfactory regions using a human nasal computational fluid dynamics model." *J. Aerosol Med.* 19(3):301-313.
- Shi, H., C. Kleinstreuer and Z. Zhang. 2006. "Laminar airflow and nanoparticle or vapor deposition in a human nasal cavity model." *J. Biomech. Eng.* 128:697-706.
- Shi, H.W., C. Kleinstreuer and Z. Zhang. 2007. "Modeling of inertial particle transport and deposition in human nasal cavities with wall roughness." *J. Aerosol Sci.* 38:398-419.
- Shih, T.H., W.W. Liou, A. Shabbir, Z. Yang and J. Zhu. 1995. "A new  $k-\epsilon$  eddy viscosity model for high Reynolds number turbulent flows." *Comput. Fluids* 24:227–238.
- Stabl, W.H. 1992. "Experimental investigation of the vortex flow on delta wings at high incidence." *AIAA J.* 30(4):1027-1032.
- Stöber, W. 1972. "Dynamic shape factors of nonspherical aerosol particles." In *Assessment of airborne particles*, ed. T. Mercer et al. Springfield, IL: Charles C. Thomas.
- Straatsma, J., G. Van Houwelingen, A.E. Steenbergen and P. De Jong. 1999. "Spray drying of food products: 1. Simulation model." *J. Food Eng.* 42(2):67-72.
- Su, W.C. and Y.S. Cheng. 2005. "Deposition of fiber in the human nasal airway." *Aerosol Sci. Technol.* 39:888–901.



- Subramaniam, R.P., R.B. Richardson, K.T. Morgan, J. S. Kimbell and R.A. Guilmette. 1998. "Computational fluid dynamics simulations of inspiratory airflow in the human nose and nasopharynx." *Inhal. Toxicol.* 10(91-120).
- Sullivan, K.J. and H.K. Chang. 1991. "Steady and oscillatory trans-nasal pressure-flow relationships in healthy adults." *J. Appl. Physiol.* 71:983-992.
- Suman, J.D., B.L. Laube, T.C. Lin, G. Brouet and R. Dalby. 2002. "Validity of in vitro tests on aqueous spray pumps as surrogates for nasal deposition." *Pharma. Res.* 19:1-6.
- Sussman, R. G., B. S. Cohen and M. Lippmann. 1991. "Asbestos fiber deposition in human tracheobronchial cast. I.- Experimental." *Inhal. Toxicol.* 3:145-160.
- Swift, D.L. 1991. "Inspiratory inertial deposition of aerosols in human nasal airway replicate casts: Implication for the proposed NCRP lung model." *Radiat. Prot. Dosim.* 38(29-34).
- Swift, D.L. and J. Kesavanathan. 1996. "The anterior human nasal passage as a fibrous filter for particles." *Chemical Engineering Communications* 151(1):65-78.
- Swift, D.L. and D.F. Proctor. 1977. "Access of air to the respiratory tract." In *Respiratory Defense Mechanism*, eds. J.D. Brain, D.F. Proctor and L.M. Reid. New York: Marcel Dekker.
- Swift, D.L. and J.C. Strong. 1996. "Nasal deposition of ultrafine  $^{218}\text{Po}$  Aerosols in human subjects." *J. Aerosol Sci.* 27(7):1125-1132.
- Timbrell, V. 1982. "Deposition and retention of fibres in the human lung." *Ann. occup. Hyg.* 26:347-369.
- Tran-Cong, S., M. Gay and E.E. Michaelides. 2004. "Drag coefficients of irregularly shaped particles." *Powder Tech* 139:21-32.
- Tu, J.Y. 2000. "Numerical investigation of particle flow behavior in particle-wall function." *Aerosol Sci. Technol.* 32:509-526.
- Vandoormaal, J.P. and G.D. Raithby. 1984. "Enhancements of the SIMPLE method for predicting incompressible fluid flows." *Numer. Heat Transfer* 7(147-163).
- Vargaftik, N.B. 1975. *Tables on Thermophysical Properties of Liquids and Gases*. 2nd Edition. Washington, DC: Hemisphere.
- Wadell, H. 1933. "Sphericity and roundness of rock particles." *J. Geol.* 41:310-331.
- Wang, Y. and P.W. James. 1999. "On the effect of anisotropy on the turbulent dispersion and deposition of small particles." *Int. J. of Multiphase Flows* 25:551-558.
- Weiner, J.S. 1954. "Nose shape and climate." *Am J Phys Anthropol* 12:1-4.

- Weinhold, I. and G. Mlynski. 2004. "Numerical simulation of airflow in the human nose." *Eur. Arch. Otorhinolaryngol.* 261:452-455.
- Wiesmiller, K., T. Keck, R. Leiacker, T. Sikora, G. Rettinger and J. Lindemann. 2003. "The impact of expiration on particle deposition within the nasal cavity." *Clinical Otolaryngology & Allied Sciences* 28(4):304-307.
- Wilcox, D. 1993. *Turbulence Modeling for CFD*. 5354 Palm Drive, La Canada, California 91011: DCW Industries, Inc.
- Wolf, M. , S. Naftali, C. Schrotter and D. Elad. 2004. "Air-conditioning characteristics of the human nose." *J. Laryng. Otology* 118(2):87-92.
- Wolpoff, M.H. 1968. "Climatic influence on skeletal nasal aperture." *Am J Phys Anthropol* 29:405-424.
- Yan, J., A. Karanjkar and M. Branagan. 2004. "Dynamic modelling and simulation for nasal drug delivery." *PMPS-Drug Delivery* August:68-71.
- Zamankhan, P., G. Ahmadi, Z. Wang, P.H. Hopke, Y.S. Cheng, W.C. Su and D. Leonard. 2006. "Airflow and deposition of nanoparticles in a human nasal cavity." *Aerosol Sci. Technol.* 40:463-476.
- Zhang, Y., W.H. Finlay and E.A. Matida. 2004. "Particle deposition measurements and numerical simulation in a highly idealized mouth-throat." *J. Aerosol Sci.* 35(789-803).
- Zhang, Z., C. Kleinstreuer, J.F. Donohue and C.S. Kim. 2005. "Comparison of micro- and nano-size particle depositions in a human upper airway model." *J. Aerosol Sci.* 36:211-233.
- Zhang, Z., C. Kleinstreuer and C.S. Kim. 2002. "Cyclic micron-size particle inhalation and deposition in a triple bifurcation lung airway model." *Aerosol Sci.* 33:257-281.
- Zhao, B., Y. Zhang, X. Li, X. Yang and D.T. Huang. 2004. "Comparison of indoor aerosol particle concentration and deposition in different ventilated rooms by numerical method." *Building and Environment* 39:1-8.
- Zinreich, S.J., D.E. Mattox, D.W. Kennedy, H.L. Chisholm, D.M. Diffley and A.E. Rosenbaum. 1988. "Concha bullosa: CT evaluation." *J Comput Assist Tomogr* 12(5):778-784.
- Zwartz, G.J. and R.A. Guilmette. 2001. "Effect of flow rate on particle deposition in a replica of a human nasal airway." *Inhal. Toxic.* 13:109-127.